Issues 1-2
2025 | Volume 21

The Journal on Advanced Studies in Theoretical and Experimental Physics,
including Related Themes from Mathematics

PROGRESS IN PHYSICS

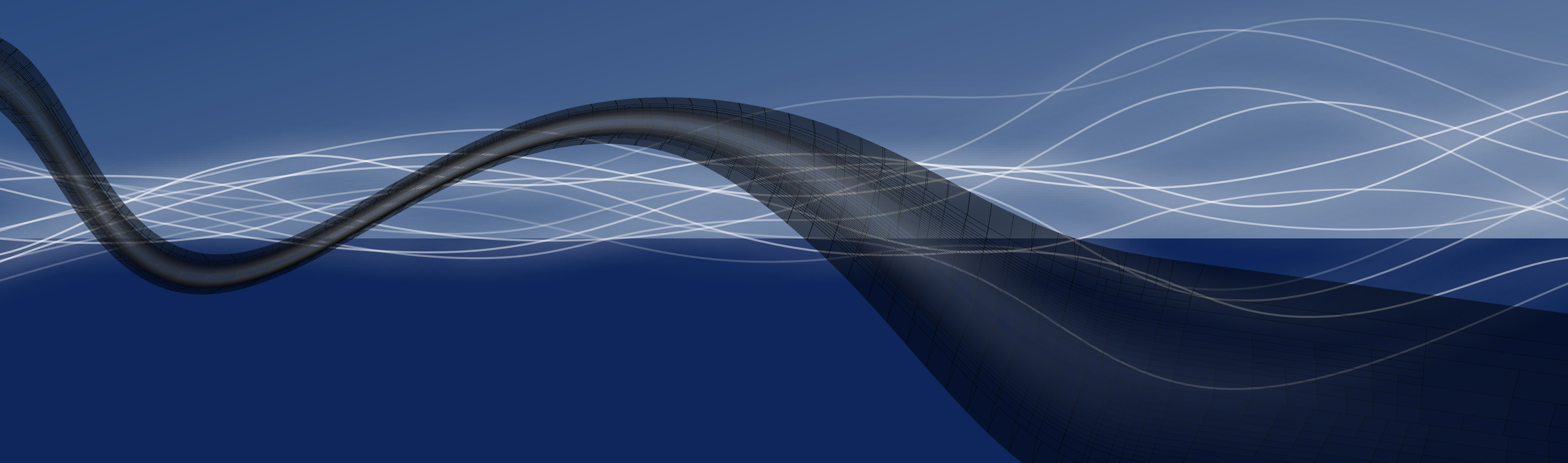

“All scientists shall have the right to present their scientific research results, in whole or in part, at relevant scientific conferences, and to publish the same in printed scientific journals, electronic archives, and any other media.” — Declaration of Academic Freedom, Article 8

ISSN 1555-5534

PROGRESS IN PHYSICS

A Scientific Journal on Advanced Studies in Theoretical and Experimental Physics, including Related Themes from Mathematics. This journal is registered with the Library of Congress (DC, USA).

Electronic version of this journal:
https://www.progress-in-physics.com

Postal Address

Department of Mathematics and Science,
University of New Mexico,
705 Gurley Ave., Gallup, NM 87301, USA

This journal is powered by LaTeX

A variety of books can be downloaded free from the Digital Library of Science:
http://fs.gallup.unm.edu/ScienceLibrary.htm

ISSN: 1555-5534 (print)
ISSN: 1555-5615 (online)

Standard Address Number: 297-5092
Printed in the United States of America

June 2025 **Vol. 21, Issue 1**

CONTENTS

Information for Authors

Progress in Physics has been created for rapid publications on advanced studies in theoretical and experimental physics, including related themes from mathematics and astronomy. All submitted papers should be professional, in good English, containing a brief review of a problem and obtained results.

All submissions should be designed in LaTeX format using *Progress in Physics* template. This template can be downloaded from *Progress in Physics* home page.

Preliminary, authors may submit papers in PDF format. If the paper is accepted, authors can manage LaTeXtyping. Do not send MS Word documents, please: we do not use this software, so unable to read this file format. Incorrectly formatted papers (i.e. not LaTeXwith the template) will not be accepted for publication. Those authors who are unable to prepare their submissions in LaTeXformat can apply to a third-party payable service for LaTeX typing. Our personnel work voluntarily. Authors must assist by conforming to this policy, to make the publication process as easy and fast as possible.

Abstract and the necessary information about author(s) should be included into the papers. To submit a paper, mail the file(s) to the Editor-in-Chief.

All submitted papers should be as brief as possible. Short articles are preferable. Large papers can also be considered. Letters related to the publications in the journal or to the events among the science community can be applied to the section *Letters to Progress in Physics*.

All that has been accepted for the online issue of *Progress in Physics* is printed in the paper version of the journal. To order printed issues, contact the Editors.

Authors retain their rights to use their papers published in *Progress in Physics* as a whole or any part of it in any other publications and in any way they see fit. This copyright agreement shall remain valid even if the authors transfer copyright of their published papers to another party.

Electronic copies of all papers published in *Progress in Physics* are available for free download, copying, and re-distribution, according to the copyright agreement printed on the titlepage of each issue of the journal. This copyright agreement follows the *Budapest Open Initiative* and the *Creative Commons Attribution-Noncommercial-No Derivative Works 2.5 License* declaring that electronic copies of such books and journals should always be accessed for reading, download, and copying for any person, and free of charge.

Consideration and review process does not require any payment from the side of the submitters. Nevertheless the authors of accepted papers are requested to pay the page charges. *Progress in Physics* is a non-profit/academic journal: money collected from the authors cover the cost of printing and distribution of the annual volumes of the journal along the major academic/university libraries of the world. (Look for the current author fee in the online version of *Progress in Physics*.)

Correct Solutions for Rotating Black Holes

Dmitri Rabounski
Puschino, Moscow Region, Russia. E-mail: rabounski@yahoo.com

This paper introduces correct solutions for rotating black holes and electrically charged rotating black holes. The solutions are based on the space metric of a rotating spherical body approximated by a mass-point, which is a new metric to General Relativity introduced and proved using Einstein's equations in the previous paper (Progr. Phys., 2014, v. 20, 79–99) as an extension of Schwarzschild's mass-point metric. According to the solutions, rotating black holes have the shape of an oblate spheroid, flattened at the poles, where its radius is equal to the gravitational radius of the body, and thickened at the equator. The introduced black hole solutions are mathematically and physically correct, because they have no limitations, unlike Kerr's solution and the Kerr-Newman solution, which, since they are obtained using the tetrad formalism, are valid only in an infinitely small vicinity of the surface of a rotating black hole.

1 Non-rotating black holes

Definition 1: A black hole is a type of cosmic body, the gravitational field of which is so strong that light cannot escape from its surface.

This is the original definition of black holes according to the founders of the black hole problem — the Reverend John Michell, who in 1783 wrote his article in which he first outlined his idea of such cosmic objects [1], and also Pierre-Simon Laplace, who in 1796, independently of Michell, in Chapter 6 of his *Exposition du Système du Monde* gave a definition of black holes [2, p. 305], and then in 1799 provided a mathematical justification for such objects in the framework of Classical Mechanics [3].

See the 2009 study of the history of the black hole problem [4] and the papers [5–7] referred therein.

In the General Theory of Relativity, the geometric basis is not a three-dimensional Euclidean space, as in Classical Mechanics, but a four-dimensional pseudo-Riemannian space (space-time), black holes are defined from the general formula of the Riemannian space (space-time) metric[*]

$$ds^2 = g_{\alpha\beta}\, dx^\alpha dx^\beta = \\ = g_{00}\, dx^0 dx^0 + 2\, g_{0i}\, dx^0 dx^i + g_{ik}\, dx^i dx^k, \qquad (1)$$

in which specific formulae for the components of the fundamental metric tensor $g_{\alpha\beta}$ determine the geometry and distribution of matter of the particular Riemannian space (space-time) that we are considering.

Usually, the definition of black holes in General Relativity is given in terms of the zero (time) component

$$g_{00} = \left(1 - \frac{\mathrm{w}}{c^2}\right)^2 \qquad (2)$$

of the fundamental metric tensor $g_{\alpha\beta}$, based on the assertion that the difference of g_{00} from 1 indicates the deviation of real time intervals $d\tau$ from ideal (unperturbed and homogeneous) time intervals dt, which is determined *only* by the potential of the acting gravitational field $\mathrm{w} = c^2 (1 - \sqrt{g_{00}})$.

This definition of black holes says:

Definition 2: A black hole is a type of cosmic body, on the surface of which $g_{00} = 0$ and, hence its physical radius is equal to the gravitational radius $r_g = 2GM/c^2$, calculated for its mass M. The entire mass of such a body is under its gravitational radius, which means that this body is in the state of gravitational collapse, i.e., the body is a *gravitational collapsar*.

This definition of black holes originates from the mass-point space metric introduced in 1916 by Karl Schwarzschild [8], which is known as the *Schwarzschild mass-point metric*. This metric[†]

$$ds^2 = \left(1 - \frac{r_g}{r}\right) c^2 dt^2 - \frac{dr^2}{1 - \frac{r_g}{r}} - r^2 \left(d\theta^2 + \sin^2\theta\, d\varphi^2\right) \qquad (3)$$

describes a spherically symmetric space filled with a gravitational field created by a massive spherical island of substance, which is approximated by a material point, where r is the radial distance from the barycentre of the massive island (which is the coordinate origin), and $r_g = 2GM/c^2$ is the gravitational radius of the island, calculated for its mass M. According to this metric, the non-zero components of the fundamental metric tensor $g_{\alpha\beta}$ of such a space are

$$\left.\begin{aligned} g_{00} &= 1 - \frac{r_g}{r}\,, \qquad & g_{11} &= -\frac{1}{1 - \frac{r_g}{r}} \\ g_{22} &= -r^2, & g_{33} &= -r^2 \sin^2\theta \end{aligned}\right\}. \qquad (4)$$

According to the views commonly accepted in the 1920–1930s among the scientists working in the field of General

---

[*] Here $\alpha, \beta = 0, 1, 2, 3$ are four-dimensional (space-time) indices, and $i, k = 1, 2, 3$ are three-dimensional spatial indices.

[†] The commonly accepted mathematical form of this metric given above was derived not by Schwarzschild himself, but immediately after his death in 1916 independently by Johannes Droste and David Hilbert [9, 10].

Relativity, real time intervals $d\tau$ are expressed through ideal (unperturbed, homogeneous) time intervals dt as

$$d\tau = \sqrt{g_{00}}\,dt\,, \tag{5}$$

see §84 on distances and time intervals in *The Classical Theory of Fields* by Landau and Lifshitz [11], the 1st edition of which was published in 1939.

Since $g_{00} = 1 - \frac{r_g}{r} = 0$ on the surface of a gravitational collapsar ($r = r_g$), physically observable time stops ($d\tau = 0$) on its surface from the point of view of an external observer and, hence, no signal can escape from this body. In other words, this is a cosmic object called a *black hole*.

Some criticism to the black hole concept is based on the fact that r in the formula of the Schwarzschild mass-point metric is a radial coordinate (as in any space metric written in spherical coordinates r, θ, φ), and not the physical radius of the massive spherical island of substance creating the gravitational field. For the details of this criticism, see [12, 13] and references therein. This is true, but this fact does not cancel the existence of a space breaking on a spherical surface of the radius $r_g = 2GM/c^2$ from the barycentre of the massive island (due to the breaking $g_{00} = 0$ in the space metric on this surface). Of course, a spherical massive island that creates a gravitational field described by the Schwarzschild mass-point metric can have any radius R. But if its radius is equal to the gravitational radius $R = r_g$ calculated for its mass M, then this body is definitely a gravitational collapsar (black hole). See my remarks [14] on the above criticism.

Gravitational collapsars are conceivable not only in the form of a collapsed spherical body, i.e., they are associated not only with the Schwarzschild mass-point metric. It can be any cosmic body, the physical radius of which is equal to its gravitational radius (and, therefore, $g_{00} = 0$ on its surface). So, in 2010 Larissa Borissova introduced a new cosmological model, according to which the entire observable Universe is a de Sitter collapsar — a de Sitter space (this is a constant curvature spherical space filled with the physical vacuum) in the state of gravitational collapse: its radius (which is the same as the curvature radius of space) is equal to its gravitational radius. She called this model the *de Sitter bubble* [15]. Also, in our common monograph on the internal constitution of stars, *Inside Stars* [16], we considered liquid black holes; the space inside such a collapsar is determined by Schwarzschild's metric of the space inside a liquid sphere.

2 The complete formula for real time

As was mentioned above, the key point of the black hole solution in General Relativity is the stopping of real time ($d\tau = 0$) on the surface of a black hole, which is usually determined from the formula for real time intervals $d\tau = \sqrt{g_{00}}\,dt$, commonly accepted in the 1920–1930s [11, §84].

At the same time, the problem of determining real time intervals is not trivial, and is a particular case of the general problem of determining physically observable quantities in the space-time of General Relativity.

Initially, only heuristic considerations were used for determining physical observable quantities in General Relativity. For example, physically observable (real) time intervals $d\tau$ were assumed to be the square root of the first (time) term $g_{00}\,dx^0 dx^0 = g_{00}\,c^2 dt^2$ of the square of the four-dimensional (space-time) interval ds^2, i.e., $d\tau = \sqrt{g_{00}}\,dt$. It was heuristically assumed that three-dimensional components of a four-dimensional vector form a three-dimensional observable vector, and its time component is the observable potential of the vector field. And so forth and so on, which generally does not prove that these quantities can be actually observed.

Only in 1944 Abraham Zelmanov developed a versatile mathematical method that unambiguously determined physically observable quantities in the space-time of General Relativity as the projections of four-dimensional quantities onto the time line and the three-dimensional spatial section, associated with an observer. Such projections are invariant throughout the spatial section of the observer (his observable three-dimensional reference space), i.e., they are "chrono-metric invariants" in his reference frame and depend on the properties of his reference space, such as the gravitational potential, rotation, deformation, curvature, etc. For this reason, Zelmanov called his mathematical method the *theory of chronometric invariants* or the *chronometrically invariant formalism*.

Although Zelmanov presented his work in 1944 in his lengthy doctoral dissertation and later in two short papers, one of which was published in English in 1956 [17], his chronometrically invariant formalism remained outside attention of the scientific community over decades. His main works were published in English only in the 2000s [18, 19]. See the comprehensive survey of the Zelmanov formalism [20], where I and Larissa Borissova collected almost everything that we know on this subject personally from Zelmanov and based on our own research studies.

In short, the chronometrically invariant projections of any four-dimensional quantity are calculated using operators of projection, which take the physical properties and geometric structure of the observer's physical space into account. Thus, the four-dimensional displacement vector dx^α ($\alpha = 0, 1, 2, 3$), projected onto the time line of an observer, represents the physically observable (real) chr.inv.-time interval

$$d\tau = \sqrt{g_{00}}\,dt - \frac{1}{c^2}\,v_i\,dx^i, \quad i = 1, 2, 3, \tag{6}$$

and the projection of dx^α onto the three-dimensional spatial section associated with the observer is the physically observable three-dimensional chr.inv.-displacement vector dx^i.

Here g_{00} is expressed through the physically observable chr.inv.-potential w of the gravitational field that fills the observer's space

$$\mathrm{w} = c^2\left(1 - \sqrt{g_{00}}\right), \qquad \sqrt{g_{00}} = 1 - \frac{\mathrm{w}}{c^2}\,, \tag{7}$$

and v_i is the three-dimensional vector of the linear velocity of rotation of the observer's space

$$v_i = -\frac{c\, g_{0i}}{\sqrt{g_{00}}}\,, \quad v^i = -c\, g^{0i}\sqrt{g_{00}}\,, \quad v_i = h_{ik}\, v^k. \tag{8}$$

The square of the three-dimensional physically observable chr.inv.-interval is determined as

$$d\sigma^2 = h_{ik}\, dx^i dx^k \tag{9}$$

using the three-dimensional chr.inv.-metric tensor h_{ik}

$$h_{ik} = -g_{ik} + \frac{1}{c^2}\, v_i v_k\,, \quad h^{ik} = -g^{ik}, \quad h^i_k = \delta^i_k\,, \tag{10}$$

which is the chr.inv.-projection of the fundamental metric tensor $g_{\alpha\beta}$ onto the spatial section associated with the observer and possesses all properties of $g_{\alpha\beta}$ throughout the spatial section (the observer's three-dimensional space).

Thus, the square of the four-dimensional (space-time) interval $ds^2 = g_{\alpha\beta}\, dx^\alpha dx^\beta$ is expressed in terms of chronometrically invariant (physically observable) quantities as

$$ds^2 = c^2 d\tau^2 - d\sigma^2. \tag{11}$$

The above has aftermaths for the black hole solution. The complete formula for physically observable (real) time intervals $d\tau = \sqrt{g_{00}}\, dt - \frac{1}{c^2}\, v_i dx^i$ (6) differs from $d\tau = \sqrt{g_{00}}\, dt$ (5) given in §84 of *The Classical Theory of Fields* by the second term, determined by the rotation of space. They coincide only if space does not rotate. Therefore, since the stopping of observable time ($d\tau = 0$) defines black holes in General Relativity ($d\tau = 0$ on the surface of a body means that no signal can leave this body), the condition

$$d\tau = \sqrt{g_{00}}\, dt - \frac{1}{c^2}\, v_i\, dx^i = 0 \tag{12}$$

which follows from the chronometrically invariant formalism should give a black hole solution for rotating black holes.

3 The correct solution for a rotating black hole

It is obvious that a correct solution for a rotating black hole should follow from the space metric of a rotating spherical body, approximated by a mass-point. Such a metric was introduced and proved using Einstein's field equations in the previous paper [21].

This metric was derived on the basis of the Schwarzschild mass-point metric (3) by assuming that the space rotates together with the body itself along the equatorial coordinate axis φ, i.e., along the geographical longitudes of the body, with the linear velocity $v_3 = \omega r^2 \sin^2\theta$. In addition, it was assumed that the rotation of space is stationary, i.e., the angular velocity ω of this rotation is constant ($\omega = const$). Since by definition of v_i (8) we have

$$v_3 = \omega r^2 \sin^2\theta = -\frac{c\, g_{03}}{\sqrt{g_{00}}}\,, \tag{13}$$

then the metric of a rotating spherical body approximated by a mass-point has the form

$$ds^2 = \left(1 - \frac{r_g}{r}\right) c^2 dt^2 - 2\,\omega r^2 \sin^2\theta\, \sqrt{1 - \frac{r_g}{r}}\, dt\, d\varphi - \\ - \frac{dr^2}{1 - \frac{r_g}{r}} - r^2 \left(d\theta^2 + \sin^2\theta\, d\varphi^2\right), \tag{14}$$

where, as is seen from the above formula,

$$\left.\begin{array}{l} g_{00} = 1 - \dfrac{r_g}{r}\,, \qquad g_{03} = -\dfrac{\omega r^2 \sin^2\theta}{c}\sqrt{1 - \dfrac{r_g}{r}} \\ g_{11} = -\dfrac{1}{1 - \frac{r_g}{r}}\,, \qquad g_{22} = -r^2, \quad g_{33} = -r^2 \sin^2\theta \end{array}\right\}, \tag{15}$$

and, hence, non-zero lower-index components of the chr.inv.-metric tensor h_{ik} (10) are

$$\left.\begin{array}{l} h_{11} = \dfrac{1}{1 - \frac{r_g}{r}}\,, \qquad h_{22} = r^2 \\ h_{33} = r^2 \sin^2\theta \left(1 + \dfrac{\omega^2 r^2 \sin^2\theta}{c^2}\right) \end{array}\right\}, \tag{16}$$

while its upper-index components h^{ik}, since the matrix h_{ik} is strict diagonal, i.e., all of its non-diagonal components (for which $i \neq k$) are zero, are $h^{ik} = (h_{ik})^{-1}$ just like the invertible matrix components to any diagonal matrix.

To check the above rotating metric, we calculate $v^2 = v_i v^i = h_{ik} v^i v^k$. Since $v^i = h^{ik} v_k$, we obtain the following

$$v^2 = v_i v^i = \frac{\omega^2 r^2 \sin^2\theta}{1 + \frac{\omega^2 r^2 \sin^2\theta}{c^2}}\,, \qquad v = \frac{\omega r \sin\theta}{\sqrt{1 + \frac{\omega^2 r^2 \sin^2\theta}{c^2}}}\,, \tag{17}$$

therefore, the dimension of v is [cm/sec] as it should be. If the space rotates slowly, then the above formula transforms to $v = \omega r \sin\theta$ [cm/sec] as in Classical Mechanics.

In fact, the space metric (14) describes a spherically symmetric space, which is filled with the gravitational field created by a rotating spherical island of substance (approximated by a mass-point) and rotates together with this body.

The introduced and proved metric (14) is a new space metric to General Relativity, which is a modern extension and replacement of the Schwarzschild mass-point metric (3), because in the space of the Schwarzschild metric a massive body creating gravitational field does not rotate. Moreover, this metric is the *basic space metric in the Universe*, characterizing the physically observable field of any real cosmic body, be it a planet, star, galaxy or something else (since all real cosmic bodies rotate).

Consider the black hole condition $d\tau = 0$ in the space of a rotating spherical body approximated by a mass-point, i.e., according to the space metric (14).

Independently of the specific metric of space, the black hole condition $d\tau = 0$ (12) can be transformed to the form

$$d\tau = \left(\sqrt{g_{00}} - \frac{1}{c^2}\, v_i u^i\right) dt = 0\,, \qquad u^i = \frac{dx^i}{dt}\,, \tag{18}$$

where ideal (unperturbed, homogeneous) time intervals are $dt \neq 0$ and, therefore,

$$\sqrt{g_{00}} - \frac{1}{c^2}\, v_i u^i = 0\,, \tag{19}$$

while u^i is the coordinate velocity of a source of signals (in this case — along the surface, on which physically observable time stops). Thus, the black hole condition $d\tau = 0$ (12) took its detailed form (19).

In the space of a rotating spherical body, approximated by a mass-point, i.e., in the space of the metric (14), the obtained detailed formula (19) of the black hole condition $d\tau = 0$ takes the particular form characteristic of this space metric

$$\sqrt{1 - \frac{r_g}{r}} - \frac{1}{c^2}\, v_3 u^3 = 0\,. \tag{20}$$

From this form of the black hole condition $d\tau = 0$, since $r_g = 2GM/c^2$ is the gravitational radius of the body, calculated for its mass M,* we then derive the *black hole solution*, which is a distance $r = r_c$ from the barycentre of the body at which physically observable time for signals stops, i.e., the signals disappear for an external observer.

So forth, assuming that the linear velocity with which the space rotates together with the body itself $v_3 = \omega r^2 \sin^2\theta$ is much less than the speed of light, and the source of signals rests on the body's surface, i.e., its coordinate velocity along the equatorial axis φ is $u^3 = \frac{d\varphi}{dt} = \omega$, we obtain the *black hole solution for a rotating black hole*

$$r_c = \frac{r_g}{1 - \frac{1}{c^4}\,\omega^4 r^4 \sin^4\theta} \simeq r_g \left(1 + \frac{1}{c^4}\,\omega^4 r^4 \sin^4\theta\right) \geqslant r_g\,. \tag{21}$$

According to the obtained black hole solution (21), since $\sin\theta = 0$ at the poles of a rotating black hole (as in the previous paper [21] we assume that the θ coordinate is the polar angle measured from the North Pole), the second term in the brackets vanishes at the poles and has no effect. As a result, the radius r_c of a rotating black hole coincides with its gravitational radius ($r_c = r_g$) at the North Pole and South Pole.

In contrast, $\sin\theta = 1$ at the equator and, hence, the equatorial radius of a rotating black hole is greater than its gravitational radius r_g by a length

$$\Delta r = r_g\, \frac{\omega^4 r^4}{c^4}\,, \tag{22}$$

which is greater the faster the black hole rotates.

Therefore, according to the black hole solution (21) that we have obtained, we arrive at the conclusion:

Conclusion: Rotating black holes are not spheres, but have the *shape of an oblate spheroid*, flattened at the poles, where its radius is equal to the gravitational radius of the body, and thickened at the equator, where its radius exceeds the gravitational radius (due to rotation). The faster a black hole rotates, the thicker its body is at the equator compared to the poles.

This means that, according to the black hole solution obtained above, signals arriving at the poles of a rotating gravitational collapsar disappear for an external observer when they arrive at its gravitational radius (as in the case of a non-rotating collapsar). However, if signals arrive at a rotating gravitational collapsar at latitudes other than the poles, then they disappear at a distance greater than its gravitational radius (this distance exceeding the gravitational radius is maximum at the equator).

For this reason, it is reasonable to reconsider the initial definition of black holes in General Relativity, which is based on the gravitational collapse condition $g_{00} = 0$ (see Definition 2 in the beginning of this article). Since, according to the solution obtained above for rotating black holes, the equatorial radius of a rotating black hole exceeds its gravitational radius, we must replace the initial definition of black holes with a more general one, according to which black holes are defined as objects, on the surface of which physically observable time stops:

Definition 3: A black hole is a type of cosmic body, on the surface of which time stops from the point of view of an external observer (the interval of physically observable time is zero $d\tau = 0$ on its surface) and, hence, no one signal can escape the surface of the body.

4 The correct solution for an electrically charged rotating black hole

Consider another case, where the considered spherical island of substance (approximated by a mass-point) possesses an electric charge q. In this case, the space of the mass-point is filled with not only the gravitational field created by it, but also a spherically symmetric electric (electromagnetic) field, i.e., is filled with distributed matter. The space of an electrically charged mass-point is described by the Reissner-Nordström metric

$$ds^2 = \left(1 - \frac{r_g}{r} + \frac{r_q^2}{r^2}\right) c^2 dt^2 - \\ - \frac{dr^2}{1 - \frac{r_g}{r} + \frac{r_q^2}{r^2}} - r^2\left(d\theta^2 + \sin^2\theta\, d\varphi^2\right), \tag{23}$$

which is an extension of the Schwarzschild mass-point metric, first considered in 1916 by Hans Reissner [22], and then,

---

*At the distance $r_g = 2GM/c^2$ from its barycentre the space has a breaking, which manifests itself in the form of the condition $g_{00} = 0$.

in 1918, by Gunnar Nordström [23]. The Reissner-Nordström metric uses the same denotations as the Schwarzschild mass-point metric, with an addition of

$$r_q^2 = \frac{Gq^2}{4\pi\varepsilon_0 c^4}\,, \tag{24}$$

where q is the electric charge of the massive island (source of the gravitational field and the electromagnetic field), G is the gravitational constant, and $\frac{1}{4\pi\varepsilon_0}$ is Coulomb's force constant.

We introduce the space metric of an electrically charged rotating body (approximated by a mass-point) analogous to the mass-point space metric of a rotating body (14), which together with its space stationary rotates with a constant angular velocity $\omega = const$ and the linear velocity $v_3 = \omega r^2 \sin^2\theta$ along the equatorial coordinate axis φ, i.e., along the geographical longitudes of the body. The resulting space metric of an electrically charged rotating soherical body approximated by a mass-point has the form

$$\begin{aligned} ds^2 &= \left(1 - \frac{r_g}{r} + \frac{r_q^2}{r^2}\right) c^2 dt^2 - \\ &- 2\omega r^2 \sin^2\theta \sqrt{1 - \frac{r_g}{r} + \frac{r_q^2}{r^2}}\, dt\, d\varphi - \\ &- \frac{dr^2}{1 - \frac{r_g}{r} + \frac{r_q^2}{r^2}} - r^2\left(d\theta^2 + \sin^2\theta\, d\varphi^2\right), \end{aligned} \tag{25}$$

where, as follows from the above formula,

$$\left.\begin{aligned} g_{00} &= 1 - \frac{r_g}{r} + \frac{r_q^2}{r^2} \\ g_{03} &= -\frac{\omega r^2 \sin^2\theta}{c}\sqrt{1 - \frac{r_g}{r} + \frac{r_q^2}{r^2}} \\ g_{11} &= -\frac{1}{1 - \frac{r_g}{r} + \frac{r_q^2}{r^2}} \\ g_{22} &= -r^2, \quad g_{33} = -r^2 \sin^2\theta \end{aligned}\right\}, \tag{26}$$

and, hence, non-zero lower-index components of the chr.inv.-metric tensor h_{ik} (10) are

$$\left.\begin{aligned} h_{11} &= \frac{1}{1 - \frac{r_g}{r} + \frac{r_q^2}{r^2}}\,, \qquad h_{22} = r^2 \\ h_{33} &= r^2 \sin^2\theta \left(1 + \frac{\omega^2 r^2 \sin^2\theta}{c^2}\right) \end{aligned}\right\}, \tag{27}$$

while its upper-index components are $h^{ik} = (h_{ik})^{-1}$ just like the invertible matrix components to any diagonal matrix.

The introduced space metric (25) describes a spherically symmetric space, which is filled with the gravitational field and the electromagnetic field, which are created by a rotating electrically charged spherical island of substance (approximated by a mass-point) and rotates together with this body.

The introduced metric (25) is a new space metric to General Relativity, which is a modern extension of the Schwarzschild mass-point metric (3), the recently introduced metric of a rotating spherical body approximated by a mass-point (14) and the Reissner-Nordström metric (23).

This metric is proved using Einstein's field equations absolutely analogous to the metric of a rotating spherical body approximated by a mass-point, which was introduced and proved in the recent paper [21], because it differs only by one additional term in g_{00}, which takes the electric charge q into account. The only difference in the proof is that the right-hand side of the Einstein equations in this case is non-zero and contains physically observable components of the energy-momentum tensor of the electromagnetic field, and the Riemannian conditions for the metric take the electromagnetic field into account. This proof is easy to repeat by anyone, following with the recent paper [21]. We therefore omit this proof in the present paper, since the main task here is to obtain solutions for black holes.

In the space of the rotating Reissner-Nordström metric (25) that we just introduced, the detailed general formula (19) of the black hole condition $d\tau = 0$ takes the form

$$\sqrt{1 - \frac{r_g}{r} + \frac{r_q^2}{r^2}} - \frac{1}{c^2}\, v_3 u^3 = 0\,. \tag{28}$$

From here, assuming that the effect created by the electromagnetic field of an electrically charged black hole (the third term under the square root) is much weaker than the effect of its gravitational field (the second term), which is a natural assumption for a gravitational collapsar due to its super-strong gravitational field, we then derive the black hole solution for an electrically charged black hole, which is a distance from its barycentre at which physically observable time for signals stops (they disappear for an external observer).

As above in the case of a regular rotating black hole, we assume that the linear velocity $v_3 = \omega r^2 \sin^2\theta$ with which the space rotates together with the electrically charged body itself is much less than the speed of light, and the source of signals rests on the body's surface ($u^3 = \frac{d\varphi}{dt} = \omega$). Thus, we obtain the formula of the *black hole solution for an electrically charged rotating black hole*

$$\begin{aligned} r_c &= \frac{r_g}{1 - \frac{1}{c^4}\,\omega^4 r^4 \sin^4\theta + \frac{r_q^2}{r^2}} \simeq \\ &\simeq r_g \left(1 + \frac{1}{c^4}\,\omega^4 r^4 \sin^4\theta - \frac{r_q^2}{r^2}\right). \end{aligned} \tag{29}$$

According to the obtained black hole solution (29), the radius of an electrically charged rotating black hole is shorter at its poles than the gravitational radius $r_g = 2GM/c^2$ calculated for its mass M, and is less thick at the equator than the equatorial radius of a regular rotating black hole. In other words, the electric charge (and the electromagnetic field) of an electrically charged rotating black hole makes its shape more flattened from the poles and less thick at the equator than a regular rotating black hole

$$r_{c\,(\text{poles})} = \frac{r_g}{1+\frac{r_q^2}{r^2}} \simeq r_g\left(1-\frac{r_q^2}{r^2}\right) < r_g\,, \tag{30}$$

$$r_{c\,(\text{equator})} = \frac{r_g}{1-\frac{\omega^4 r^4}{c^4}+\frac{r_q^2}{r^2}} \simeq r_g\left(1+\frac{\omega^4 r^4}{c^4}-\frac{r_q^2}{r^2}\right). \tag{31}$$

An electrically charged rotating black hole has a radius equal to its gravitational radius r_g at geographic latitudes in the northern and southern hemispheres, where the sine of the polar angle θ is

$$\sin\theta = \frac{c\sqrt{r_q}}{\omega\, r^{3/2}}\,, \qquad r_q^2 = \frac{Gq^2}{4\pi\varepsilon_0 c^4}\,. \tag{32}$$

Finally, the obtained black hole solution for electrically charged black holes (29) leads us at the conclusion:

Conclusion: Electrically charged rotating black holes are not spheres, but have the *shape of an oblate spheroid*, flattened at the poles, where its radius is shorter that the gravitational radius of the body, and thickened at the equator, where its radius exceeds the gravitational radius (due to rotation). The faster a black hole rotates, the thicker its body is at the equator compared to the poles. The greater its electric charge, the shorter its radius is at the poles compared to its gravitational radius and the less thick its equatorial radius.

That is, according to the obtained black hole solution, signals arriving at the poles of an electrically charged rotating gravitational collapsar disappear for an external observer at an altitude less than its gravitational radius. But, if signals arrive at such a collapsar at the equator, then they disappear at a distance greater than its gravitational radius. Signals disappear at a distance of the gravitational radius from the barycentre of an electrically charged rotating gravitational collapsar at geographic latitudes in the northern and southern hemispheres, where the effect of the collapsar's rotation is completely compensated by the effect of its electric charge.

P.S. It should be noted that the significance of the black hole solutions obtained in the present paper contrasts with Kerr's solution and the Kerr-Newman solution.

Kerr's solution for a rotating black hole [24] and the Kerr-Newman solution for an electrically charged rotating black hole [25] were introduced in the early 1960s, based on the respective space (space-time) metrics that they derived using a special version of the tetrad formalism called the Newman-Penrose formalism [26]. In the tetrad formalism, all quantities given in the four-dimensional pseudo-Riemannian space (space-time of General Relativity, which is generally curved, inhomogeneous and anisotropic) are projected onto a tangential space, which is a four-dimensional flat, homogeneous and isotropic space (space-time) tangential to the given Riemannian space at the point where you are looking for a solution. Thus, the tetrad formalism solves all problems of General Relativity in this tangential flat space.

The advantage of this mathematical formalism is that in the tangential flat homogeneous and isotropic space there are no singularities (space discontinuities), and complicated problems of General Relativity are expressed in a simple mathematical form. On the other hand, the tetrad formalism has a serious drawback that has prevented it from becoming the main mathematical tool of the researchers working in the field of General Relativity. Quantities associated with objects and the geometric structure of the Riemannian space can be projected onto a tangential flat space only in an infinitely small vicinity of the projection point (because they are absent in the tangential flat space). Therefore, all calculation results obtained using the tetrad formalism or any modification of it are valid only in an infinitely small vicinity of the projection point in the tangential flat space (and not in the Riemannian space itself), and these results are not integrable to another point of the Riemannian space.

Kerr's solution and the Kerr-Newman solution were derived using the Newman-Penrose formalism (a modification of the tetrad formalism) in the tangential flat space, in which objects of General Relativity do not actually exist. Therefore, the physical reality of their theoretical results is questionable. In addition, Kerr's solution and the Kerr-Newman solution have a serious limitation. Namely — these solutions are valid only in an infinitely small vicinity of the surface of a rotating black hole in the tangential flat space, and not in the Riemannian space itself (in which all objects of General Relativity exist, including gravitational collapsars).

In contrast, the solutions obtained here for rotating black holes and electrically charged rotating black holes are mathematically and physically correct, since they were derived in the Riemannian space itself, have no limitations, and are integrable over the entire space.

Submitted on December 19, 2024

References

1. Michell J. On the means of discovering the distance, magnitude, &c. of the fixed stars, in consequence of the diminution of the velocity of their light, in case such a diminution should be found to take place in any of them, and such other data should be procured from observations, as would be farther necessary for that purpose. *Philosophical Transactions of the Royal Society*, 1784, v. 74, 35–57.
2. Laplace P.S. Exposition du Système du Monde. Part II. Paris, 1796 (English translation by Rev. H. Harte, Dublin, 1830).

3. Laplace P.S. Beweis des Satzes, dass die anziehende Kraft bey einem Weltkörper so gross seyn könne, dass das Licht davon nicht ausströmen kann. *Allgemeine Geographische Ephemeriden*, July 1799, Bd. IV, 1–6.
4. Montgomery C., Orchiston W., and Whittingham I. Michell, Laplace and the origin of the black hole concept. *Journal of Astronomical History and Heritage*, 2009, v. 12, issue 2, 90–96.
5. Schaffer S. John Michell and black holes. *Journal for the History of Astronomy*, 1979, v. 10, 42–43.
6. Israel W. Dark stars: the evolution of an idea. In: *Three Hundred Years of Gravitation*. Cambridge Univ. Press, Cambridge, 1987, 199–276.
7. Hodges L. Michell, John. In: *The Biographical Encyclopedia of Astronomers*, Volume II (M-Z), Springer, New York, 2007, 778–779.
8. Schwarzschild K. Über das Gravitationsfeld eines Massenpunktes nach der Einsteinschen Theorie. *Sitzungsberichte der Preussischen Akademie der Wissenschaften*, *Physikalisch-Mathematische Klasse*, 1916, 189–196. English transl.: On the gravitational field of a mass point according to Einstein's theory. arXiv: physics/9905030.
9. Droste J. The field of a single centre in Einstein's theory of gravitation and the motion of a particle in that field. *Koninklijke Akademie van Wetenschappen te Amsterdam* (*KNAW*), *Proceedings of the Section of Sciences*, 1917, v. 19, no. 1, 197–215.
10. Hilbert D. Die Grundlagen der Physik. Zweite Mitteilung. *Nachrichten von der Gesellschaft der Wissenschaften zu Göttingen*, *Mathematisch-Physikalische Klasse*, 1917, 53–76.
11. Landau L. D. and Lifshitz E. M. The Classical Theory of Fields. First published in 1939 in Russian, and then in 1951 in English (Pergamon Press, Oxford). The section and pages are referred from the final, 4th, twice expanded and revised English edition (Butterworth-Heinemann, Oxford, 1979).
    Landau L. et Lifchitz E. Théorie des champs. Première édition en français, Éditions MIR, Moscou, 1964. Publié pour la première fois en 1939 en russe. Les références des sections et pages sont données à partir de la dernière 3ème édition française, révisée et augmentée deux fois (Éditions MIR, Moscou, 1970).
12. Abrams L.S. Alternative space-time for the point mass. *Physical Review D*, 1979, v. 20, 2474–2479 (arXiv: gr-qc/0201044); Black holes: the legacy of Hilbert's error. *Canadian Journal of Physics*, 1989, v. 67, 919–926 (arXiv: gr-qc/0102055); The total space-time of a point charge and its consequences for black holes. *Intern. Journal of Theor. Physics*, 1996, v. 35, 2661–2677 (arXiv: gr-qc/0102054); The total space-time of a point-mass when the cosmological constant is nonzero and its consequences for the Lake-Roeder black hole. *Physica A*, 1996, v. 227, 131–140 (arXiv: gr-qc/0102053).
13. Crothers S.J. On the general solution to Einstein's vacuum field and its implications for relativistic degeneracy. *Progress in Physics*, 2005, v. 1, issue 1, 68–73; On the ramifications of the Schwarzschild space-time metric. *Progress in Physics*, 2005, v. 1, issue 1, 74–80; On the geometry of the general solution for the vacuum field of the point-mass. *Progress in Physics*, 2005, v. 1, issue 2, 3–14; A brief history of black holes. *Progress in Physics*, 2006, v. 2, issue 2, 54–57.
14. Rabounski D. On the current situation concerning the black hole problem. *Progress in Physics*, 2008, v. 4, issue 1, 101–103.
15. Borissova L. De Sitter bubble as a model of the observable Universe. *The Abraham Zelmanov Journal*, 2010, v.3, 3–24.
16. Borissova L. and Rabounski D. Inside Stars. The 3rd edition, revised and expanded, New Scientific Frontiers, London, 2023 (the 1st edition was issued in 2013).
17. Zelmanov A.L. Chronometric invariants and accompanying frames of reference in the General Theory of Relativity. *Soviet Physics Doklady*, 1956, v. 1, 227–230 (translated from *Doklady Academii Nauk USSR*, 1956, v. 107, issue 6, 815–818).
18. Zelmanov A.L. On the relativistic theory of an anisotropic inhomogeneous universe. *The Abraham Zelmanov Journal*, 2008, vol. 1, 33–63 (translated from the thesis of the *6th Soviet Conference on the Problems of Cosmogony*, USSR Academy of Sciences Publishers, Moscow, 1957, 144–174).
19. Zelmanov A.L. Chronometric Invariants. English transl. of the 1944 dissertation, American Research Press, Rehoboth (New Mexico), 2006.
20. Rabounski D. and Borissova L. Physical observables in General Relativity and the Zelmanov chronometric invariants. *Progress in Physics*, 2023, v. 19, issue 1, 3–29.
21. Rabounski D. Introducing the space metric of a rotating massive body and four new effects of General Relativity. *Progress in Physics*, 2024, v. 20, issue 2, 79–99.
22. Reissner H. Über die Eigengravitation des elektrischen Feldes nach der Einsteinschen Theorie. *Annalen der Physik*, 1916, Bd. 50 (355), No. 9, 106–120.
23. Nordström G. On the energy of the gravitational field in Einstein's theory. *Koninklijke Akademie van Wetenschappen te Amsterdam* (*KNAW*), *Proceedings of the Section of Sciences*, 1918, vol. 20, no. 9–10, 1238–1245.
24. Kerr R.P. Gravitational field of a spinning mass as an example of algebraically special metrics. *Physical Review Letters*, 1963, v. 11, issue 5, 237–238.
25. Newman E. and Janis A. Note on the Kerr spinning-particle metric. *Journal of Mathematical Physics*, 1965, v. 6, issue 6, 915–917; Newman E., Couch E., Chinnapared K., Exton A., Prakash A., Torrence R. Metric of a rotating, charged mass. *Journal of Mathematical Physics*, 1965, v. 6, issue 6, 918–919.
26. Newman E.T. and Penrose R. An approach to gravitational radiation by a method of spin coefficients. *Journal of Mathematical Physics*, 1962, v. 3, issue 3, 566–768; Newman E.T. and Penrose R. Errata: An approach to gravitational radiation by a method of spin coefficients. *Journal of Mathematical Physics*, 1963, v. 4, issue 7, 998.

Fundamental Forces in Physics of Numerical Relations

Hartmut Müller
Rome, Italy. E-mail: hm@interscalar.com

According to the numerical-relational approach to physics proposed here, fundamental conservative forces such as gravity can be understood as a consequence of the logarithmic symmetry of fractal scalar fields of transcendental numerical attractors that arise in systems of coupled harmonic quantum oscillators.

Introduction

Modern physics attempts to explain every observed physical phenomenon by fundamental forces: gravitation, electromagnetism, the weak interaction, and the strong interaction. Each of the fundamental interactions can be described mathematically as a field. In the Standard Model [1] of fundamental interactions, matter consists of fermions, like electrons or protons, which carry fundamental properties called charges. They are thought to be field sources, which attract or repel each other by exchanging bosons. However, the origin of the charges and particles, and thus also the fields and forces is still poorly understood. So defining electric charge [2] as a fundamental property of matter that exhibits electrical attraction or repulsion in the presence of other electrically charged matter is essentially circular reasoning.

The explanation of observed physical phenomena by assuming the existence of elementary particles with charges that represent simply the physical properties required for interaction is a typical feature of the current paradigm. In this case, the question about the origin of the observed physical phenomena is only redirected, because also the question about the origin of the assumed particles and charges remains without answer. Basically, such relay-race-like explanation, in which the question is never answered but is passed like a stick from one model object to another, cannot satisfy the scientific mind in the long term.

Apropos, despite the appreciated success of the Standard Model in describing subatomic processes, the gravitational interaction defies this paradigm – already over more than 50 years. In my opinion, this circumstance indicates less the specificity of the gravitational interaction than the conceptual limitations of the paradigm.

In this context, the history of Newton's law of gravitation is quite revealing. In accordance with the historical legend, only 100 years after Newton, in 1797, Henry Cavendish came up with the idea to measure the mutual attraction of two bodies of known mass in an experiment with a sensitive rotating balance. Cavendish's measuring device is similar to the torsion balance that was invented by the geologist John Michell and used by Charles Augustin de Coulomb in 1785 to investigate electrostatic attraction and repulsion. Actually, until the second half of the 19th century, Newton's law of gravitation was described only in the form of proportionalities, no gravitational constant. In the explicit form that is used today, it was formulated 200 years after Newton in 1873 by Alfred Cornu and Jean-Baptist Baille, whose competence lay in the field of optics and electricity. Actually, they were inspired by Coulomb's law of electrostatic interaction, with the idea that gravitation must be something similar to electrostatic attraction, where the masses of the involved bodies act like the charges in Coulomb's law. In this way, Coulomb's law served as conceptional model of the current form of Newton's law of gravitation.

Electrostatic forces and gravitational forces actually share some fundamental properties: both are central, conservative, and obey an inverse-square law. Furthermore, the electrostatic and gravitational fields both act instantaneously.

In fact, it is well known that if a charged source moves at a constant velocity, the electric field experienced by a test particle points toward the source's instantaneous position rather than its retarded position.

Also in astronomical calculations of star and planetary movements, it is traditionally assumed that the effect of gravity occurs instantaneously. In fact, gravitation shows no aberration [3], such as the light of the stars. It is certainly true, although perhaps not widely enough appreciated, that observations are incompatible with gravitation having a light-speed propagation delay. Orbits in the solar system would shift substantially on a time scale on the order of a hundred years. By analyzing the motion of the Moon, Pierre Simon Laplace [4] concluded in 1805 that the speed of gravitation must be at least $7 \cdot 10^6$ times higher than 300.000 km/s. Using modern astronomical observations, Thomas Van Flandern [5] raised this limit to $2 \cdot 10^{10}\, c$.

The theoretical problem is that instantaneity contradicts the Standard Model, which considers fundamental interactions as mediated by force carrier particles limited by the speed of light in vacuum.

Actually, besides instantaneity, there is still a more serious problem: The hypothesis that G is a fundamental constant of physics is generally accepted, although it has not yet been experimentally confirmed [6]. In fact, Newton's law of gravitation cannot be verified in the scale of a planetary system, because the mass of a planet cannot be measured. By the way, the widely quoted claim that the orbit of the planet Neptune was discovered by calculation based on Newton's law of gravity is obviously false [7]. Apropos, Kepler's laws of planetary motion contain neither masses nor the G, and hence, they do not require Newton's law of gravitation for their derivation. Moreover, while Newton's theory of gravitation leads to inconsistencies already in the case of three interacting bodies, Kepler's laws of planetary motion do not have any N-body problem. However, despite perturbation models and parametric optimization, the stability of planetary systems is still a theoretical problem. In general, the stability of systems of a large number of coupled periodical processes is still a fundamental problem in physics [8].

In particular, there is no way to derive the current configuration of the solar system from Kepler's laws of planetary motion, and certainly not from Newton's law of universal gravitation, because there are infinitely many pairs of orbital periods and distances that fulfill Kepler's laws. Newer models of modified Newtonian dynamics have not changed this situation. Einstein's field equations do not reduce the theoretical variety of possible orbits, but increases it even more. General relativity does not provide solutions of the mentioned problems, because in the normal case of weak gravity and low velocities, Einstein's field equations obey the correspondence principle and reduce to Newton's law of gravitation.

Perhaps the concept of gravitation itself requires a revision. Obviously, it is not about details, but an important part of the hole is missing.

In previous publications [9, 10] I have applied a numeric-relational approach to the analysis of the ratios of the orbital and rotational periods of the planets and planetoids of the solar system and thousands of exoplanets [7], which led me to the hypothesis that the *avoidance* of orbital and rotational resonances by approximation of transcendental ratios is a basic forming factor and stabilizer of planetary systems [11].

In this article, I indent to show that this numeric-relational approach leads to a new understanding of gravitation based on fractal scalar fields of transcendental numerical attractors.

Theoretical Approach

It is well known [12] that orbital resonance can destabilize a planetary system. However, resonance is often confused with synchronization that occurs when coupled oscillators lock to a common period or phase. Once they are synchronized, they behave as one large oscillator. In either case, the frequencies of the coupled periodical processes coincide, or are related by a ratio of small integers like 1:2 or 2:3. However, only if the frequency of synchronization coincides with the *natural* frequency of an oscillator involved, resonance amplification occurs and can destabilize the system. For instance, asteroids cannot maintain orbits that are unstable because of their resonance with Jupiter [13]. These orbits form the Kirkwood gaps that are areas in the asteroid belt where asteroids are absent. In a similar way, resonances with the orbital motion of Saturn's inner moons give rise to gaps in the rings of Saturn.

In contrast to these cases, the 1:2:4 orbital synchronization of the moons Io, Europa and Ganymede does not destabilize the Jupiter system. There are many moons in the solar system that approximate orbital synchronization, for example, Enceladus-Dione = 1:2, Titan-Hyperion = 3:4, Phobos-Deimos = 1:4. Cases of extrasolar planets close to orbital synchronization are also fairly common. For instance, the 6 known exoplanets (b, c, d, e, f, g) of HD110067 approximate 54:36:24:16:12:9 synchronization ratios [14].

By the way, most known exoplanetary systems are similar in scale to the lunar system of Jupiter, because the predominantly used transit photometry method can detect only planets with short enough orbital periods in the range of days. This circumstance can create the impression that in their majority, exoplanetary systems are very small, and our solar system is quite exotic. Indeed, in contrast to moon systems and small exoplanetary systems, the planets of our solar system avoid orbital synchronization and resonances by approximation of transcendental ratios [10] of orbital periods.

Synchronization requires irreversibility, as is the case of dissipative, self-excited non-conservative oscillators, whose energy is not a conserved quantity. Their oscillations converge towards certain attractors, which are independent of initial values and are determined by a dynamic balance of energy supply and dissipation [15]. Even a weak coupling is enough to accelerate or slow down the oscillation phase. Therefore, even small periodic stimuli are able to adjust oscillations and frequencies, and oscillators can adjust their periods through weak interaction. Hence, synchronization can occur even with any weak interaction.

Coupled oscillators with slightly different frequencies exhibit a transition to equal period oscillations once the coupling strength exceeds a critical value that is proportional to the frequency difference. However, for frequency differences larger than some threshold, phase locking is not possible [16]. If the frequencies do not almost match, higher-order synchronization is possible, in which the oscillators lock into a rational frequency ratio. Simple cases with small integers usually occur. For example, oscillations can synchronize by exciting them with double or half frequency. As a rule, a larger excitation force or stronger coupling is required for higher-order synchronization.

The physical reason of synchronization is sharing energy between the oscillators according to Hamilton's principle in order to minimize the energy dissipation of the system. Synchronization requires feedback and self-regulation and can, in a sense, be viewed as a type of intelligent behavior.

Avoiding resonance is another type of intelligent behavior of real systems of coupled oscillators. The physical reason is lasting stability as strategy of survival. Already in 1799, Laplace [17] concluded that the solar system can be stable under periodic perturbations only if the ratios between the orbital parameters approximate irrational numbers. Irrational frequency ratios allow to avoid resonances [18, 19]. Resonance can be viewed as a special case of synchronization when the common oscillation frequency matches the natural frequency of an oscillator involved. The natural frequency can be defined as the rate at which a conservative free harmonic oscillator tends to oscillate with minimal excitation. In a certain range, this frequency does not depend on the excitation energy, but is determined by the physical properties of the oscillator, by its mass, size, atomic structure etc.

From the arithmetic point of view, coupled oscillators can avoid resonance by maintaining frequencies that are in irrational ratios to their natural frequencies. However, algebraic irrational numbers, being real roots of algebraic equations, can be converted to rational numbers by multiplication. Therefore, only frequency ratios that approximate transcendental numbers can prevent resonance in systems of coupled harmonic oscillators and sustain their stability [9].

Among all transcendental numbers, Euler's number $e = 2.71828\ldots$ is unique, because the real exponential function is its own derivative. For rational exponents, the natural exponential function is always transcendental [20]. This is why Euler's number and its rational powers allow avoiding mutual parametric resonance between any coupled harmonic periodic processes including their derivatives.

Integer and rational powers of Euler's number form a fractal scalar field of transcendental attractors – the *Euler field*, as I have shown in [10]:

$$\mathcal{E} = e^{\mathcal{F}}$$

The Euler field $\mathcal{E}$ is a k-dimentional projection of its fundamental fractal $\mathcal{F}$ that is given by finite canonical continued fractions of integer attractors $n_0, n_1, n_2, \ldots, n_k$:

$$\mathcal{F} = \langle n_0; n_1, n_2, \ldots, n_k \rangle = n_0 + \cfrac{1}{n_1 + \cfrac{1}{n_2 + \cdots + \cfrac{1}{n_k}}}$$

Figure 1 shows the first and the second layer of $\mathcal{F}$ in comparison. As we can see, reciprocal integers $\pm 1/2, \pm 1/3, \pm 1/4, \ldots$ are the attractor points of the fractal. In these points, the attractor distribution density reaches local maxima. Integer logarithms $0, \pm 1, \pm 2, \ldots$ define the main attractors having the widest ranges. Half logarithms $\pm 1/2$ form smaller attractor ranges, third logarithms $\pm 1/3$ form the next smaller attractor ranges and so forth.

Fig. 1: Two layers $k=1$ (above) and $k=2$ (below) of the fundamental fractal $\mathcal{F}$ in the range $-1 \leqslant \mathcal{F} \leqslant 1$.

These attractors are islands of stability in the sense that they define the frequency ratios which allow to avoid destabilizing parametric resonance in systems of coupled harmonic oscillators. For instance, two coupled harmonic periodical processes A and B with the angular frequencies ω_A and ω_B can avoid parametric resonance, if they obey the condition:

$$\ln(\omega_A/\omega_B) = \mathcal{F}$$

In other words, coupled harmonic oscillators can avoid mutual parametric resonance, if the ratios of their natural frequencies approximate attractors of the Euler field. In the case of harmonic *quantum* oscillators [21], the same is valid for the ratio of their natural wavelengths $\lambda = c/\omega$, and energies $E = \hbar\omega$, where c is the speed of light in vacuum, and $\hbar$ is the Planck constant.

The spatial projection of the Euler field $\mathcal{E}$ of coupled harmonic quantum oscillators is a fractal set of embedded spherical equipotential surfaces. The logarithmic scalar potential difference $\Delta\mathcal{F}$ of sequent equipotential surfaces:

$$\Delta\mathcal{F} = \langle n_0; n_1, \ldots, n_k \rangle - \langle n_0; n_1, \ldots, n_k + 1 \rangle$$

defines a gradient [7] always directed to the center of the attractor n_{k-1} of the next higher level that finally creates the effect of an existing field source (charge) at the center of the Euler field. However, the Euler field is of pure arithmetic origin, and there is no particular physical mechanism required as field source.

Since the frequency ratio $x = \omega_A/\omega_B$ is always a real number, the first derivative of $\ln x$ equals the reciprocal of its argument:

$$\frac{d}{dx} \ln x = \frac{1}{x}$$

Therefore, the larger the frequency ratio $x = \omega_A/\omega_B$, the slower the velocity of its change. Consequently, the velocity of change of the frequency ratio x increases always in the direction to an attractor of the Euler field $\mathcal{E}$. In this way, the logarithmic symmetry of the Euler field causes an acceleration of the frequency ratio x in the direction to the center of the field. In fact, the 2^{nd} derivative of $\ln x$ equals the negative reciprocal square of its argument:

$$\frac{d^2}{dx^2} \ln x = -\frac{1}{x^2}$$

If we substitute $x = E_A/E_B$ we can realize that the energy of the coupled quantum oscillators increases in the direction to an attractor of the Euler field. Therefore, the physical reason of the accelerated free fall of coupled quantum oscillators to the center of the Euler field is to gain energy from the field.

Now we can recapitulate the behavior of coupled harmonic quantum oscillators caused by the Euler field: In order to reach collective stability, coupled harmonic quantum oscillators adjust the ratios of their frequencies in a way that they approximate numerical attractors of the Euler field. Then, by approximating an attractor, the quantum oscillators experience a frequency blueshift that allows them to gain energy from the field. In this way, the numerical Euler field turns out to be an energy source, and fundamental interactions like gravity or electromagnetism could turn out to be physical effects caused by numerical attractors.

In their famous experiment of 1959, Robert Pound and Glen Rebka [22] verified the gravitational frequency shift. Sending gamma rays over a vertical distance of $\Delta h = 22.56$ m, they measured a blueshift of $\Delta f / f = 2.46 \cdot 10^{-15}$ that corresponds precisely with Earth's surface gravity 9.81 m/s^2.

$$\frac{\Delta f}{f} = g \, \frac{\Delta h}{c^2}$$

However, because of the fractal logarithmic hyperbolic metric of the Euler field $\mathcal{E}$, every equipotential surface is an attractor where potential differences decrease and processes can gain stability. While integer logarithms $\mathcal{F}$ define main equipotential surfaces at $k = 0$, rational logarithms define equipotential surfaces at deeper layers $k > 0$. Therefore, one can expect that gravity does decrease parabolically fractal with the distance to an attractor of the Euler field. The closer to an attractor, the more evident this effect of fractal inhomogeneity of the gravity field becomes. The strongest inhomogeneities are expected near the main attractor in the center of the field.

In fact, Stacey, Tuck, Holding, Maher and Morris [23, 24] reported anomalous measures of the gravity acceleration in deep mines and boreholes. In [25] Frank Stacey writes that "geophysical measurements indicate a 1% difference between values at 10 cm and 1 km (depth); if confirmed, this observation will open up a new range of physics."

In [26] was shown that the Euler field reproduces the 2D profile of the Earth's interior confirmed by seismic exploration. Also the stratification layers in planetary atmospheres correspond with equipotential surfaces of the Euler field [27].

Exemplary Applications

Compared to the majority of known particles, electron and proton are exceptionally stable quantum oscillators. Indeed, their life-spans top everything that is measurable, exceeding 10^{28} years [28]. This is why normal matter is formed by nucleons and electrons. For this reason, in a previous publication [11] I introduced a model of matter as fractal chain system of oscillating protons and electrons.

In order to be bound in atoms, the proton and the electron must avoid mutual resonance. This is why the proton-to-electron frequency ratio approximates an integer power of Euler's number and its square root:

$$\ln\left(\frac{\tau_e}{\tau_p}\right) = \ln\left(\frac{1.28809 \cdot 10^{-21}\ \text{s}}{7.01515 \cdot 10^{-25}\ \text{s}}\right) \simeq 7 + \frac{1}{2} = \mathcal{E}\langle 7; 2\rangle$$

$\tau_e = \lambda_e / c = 1.28809 \cdot 10^{-21}$ s is the angular oscillation period of the electron, λ_e is the Compton wavelength of the electron, c is the speed of light in vacuum, and $\tau_p = 7.01515 \cdot 10^{-25}$ s is the angular oscillation period of the proton. In order to avoid proton and electron resonance, also planetary systems have to obey the Euler field. In [10] I have shown that Venus' distance from Sun approximates the main equipotential surface $\mathcal{E}\langle 54\rangle$ of the Euler field of the *electron* that equals the 54^{th} power of Euler's number multiplied by the Compton wavelength of the electron λ_e. The aphelion 0.728213 AU = $1.08939 \cdot 10^{11}$ m delivers the upper approximation of $\mathcal{E}\langle 54\rangle$:

$$\ln\left(\frac{A(Venus)}{\lambda_e}\right) = \ln\left(\frac{1.08939 \cdot 10^{11}\ \text{m}}{3.86159 \cdot 10^{-13}\ \text{m}}\right) = 54.00$$

The perihelion 0.718440 AU = $1.07477 \cdot 10^{11}$ m delivers the lower approximation:

$$\ln\left(\frac{P(Venus)}{\lambda_e}\right) = \ln\left(\frac{1.07477 \cdot 10^{11}\ \text{m}}{3.86159 \cdot 10^{-13}\ \text{m}}\right) = 53.98$$

This means that Venus' orbit derives from the Euler field of the electron. In other words, Venus' orbit is of subatomic origin. This is not a random coincidence. Jupiter's distance from Sun approximates the main equipotential surface $\mathcal{E}\langle 56\rangle$ of the Euler field of the electron. The aphelion 5.45492 AU = $8.160444 \cdot 10^{11}$ m delivers the upper approximation of $\mathcal{E}\langle 56\rangle$:

$$\ln\left(\frac{A(Jupiter)}{\lambda_e}\right) = 56.01$$

The perihelion 4.95029 AU = $7.405528 \cdot 10^{11}$ m delivers the lower approximation:

$$\ln\left(\frac{P(Jupiter)}{\lambda_e}\right) = 55.91$$

This fact suggests that quantumness is conserved in macroscopic scales up to planetary systems. Indeed, in [29] the quantumness of macroscopic large masses was verified, in particular, the mass-independent irreducible quantumness of harmonic oscillator systems.

Also Jupiter's orbital period 4332.59 days derives from the Euler field of the electron. In fact, it equals the 66^{th} power of Euler's number multiplied by the oscillation period $2\pi \cdot \tau_e$ of the electron:

$$\ln\left(\frac{T(Jupiter)}{2\pi \cdot \tau_e}\right) = \ln\left(\frac{4332.59 \cdot 86400\ \text{s}}{2\pi \cdot 1.28809 \cdot 10^{-21}\ \text{s}}\right) = 66.00$$

The same is valid for the orbital period 686.98 days (1.88 years) of the planet Mars that equals the 66^{th} power of Euler's number multiplied by the *angular* oscillation period τ_e of the electron:

$$\ln\left(\frac{T(Mars)}{\tau_e}\right) = \ln\left(\frac{686.98 \cdot 86400\ \text{s}}{1.28809 \cdot 10^{-21}\ \text{s}}\right) = 66.00$$

Consequently, the ratio of the orbital periods of Jupiter and Mars equals 2π:

$$T(Jupiter) = 2\pi \cdot T(Mars)$$

This transcendental ratio allows Mars to avoid parametric orbital resonance with Jupiter and evidences that Jupiter and Mars are not planets of different systems, but bound together in the same conservative system (the solar system).

In [10] I introduced the Archimedes field $\mathcal{A} = \pi^{\mathcal{F}}$ and have shown how it connects orbital periods with rotational periods. Stable orbital speeds [30] derive from the speed of light divided by integer and reciprocal integer powers of e or π. This circumstance drastically reduces the diversity of preferred orbits, orbital periods, and speeds, increasing the likelihood of matches in different planetary or lunar systems. Furthermore, it indicates a transcendental duality of Euler- and Archimedes-orbits in the solar system.

In the Jupiter lunar system, we can observe both strategies of stabilization, avoidance of resonance and synchronization. The orbital period of the Galilean moon Io approximates the attractor $\mathcal{E}\langle 60\rangle$ of the *Euler* field of the *electron*:

$$\ln\left(\frac{T(Io)}{\tau_e}\right) = \ln\left(\frac{1.7691378 \cdot 86400\,\mathrm{s}}{1.28809 \cdot 10^{-21}\,\mathrm{s}}\right) = 60.03$$

Simultaneously, it approximates also the attractor $\mathcal{E}\langle 59\rangle$ of the *Archimedes* field of the *proton*:

$$\mathrm{lp}\left(\frac{T(Io)}{\tau_p}\right) = \mathrm{lp}\left(\frac{1.7691378 \cdot 86400\,\mathrm{s}}{7.01515 \cdot 10^{-25}\,\mathrm{s}}\right) = 59.01$$

τ_p is the angular oscillation period of the proton. We use the symbol "lp" for the logarithm to the base $\pi = 3.14159\ldots$

$$\mathrm{lp}(x) = \frac{\ln(x)}{\ln(\pi)}$$

The Galilean moons Europa and Ganymede are in 1:2:4 orbital synchronization with Io in order to save orbital kinetic energy. Callisto is not synchronized with the other Galilean moons, but avoids *proton* resonance by approximation of the attractor $\mathcal{E}\langle 68\rangle$ of the *Euler* field:

$$\ln\left(\frac{T(Callisto)}{2\pi \cdot \tau_p}\right) = \ln\left(\frac{16.689 \cdot 86400\,\mathrm{s}}{2\pi \cdot 7.01515 \cdot 10^{-25}\,\mathrm{s}}\right) = 67.96$$

and the attractor $\mathcal{E}\langle 61\rangle$ of the *Archimedes* field of the *proton*:

$$\mathrm{lp}\left(\frac{T(Callisto)}{\tau_p}\right) = \mathrm{lp}\left(\frac{16.689 \cdot 86400\,\mathrm{s}}{7.01515 \cdot 10^{-25}\,\mathrm{s}}\right) = 60.97$$

Obviously, in order to reach the centers of these attractors, Callisto still has to extend its orbital period by half a day. This prediction is consistent with alternative approaches [31].

However, not only Euler's number $e = 2.71828\ldots$ and Archimedes' number $\pi = 3.14159\ldots$ define fractal scalar fields of their integer and rational powers, but in general, every prime, irrational and transcendental number does it. While the fundamental fractal $\mathcal{F}$ is always the same distribution of rational logarithms, the structure of the corresponding fundamental field changes with the logarithmic base. Here it is important to notice that no fundamental field can be transformed in another by stretching, because $\log_a(x) - \log_b(x)$ is a nonlinear function of x. In this way, every prime, irrational or transcendental number generates a unique fundamental field of its own integer and rational powers that causes physical effects which are typical for that number. Figure 2 shows the Euler field and the Archimedes field in comparison.

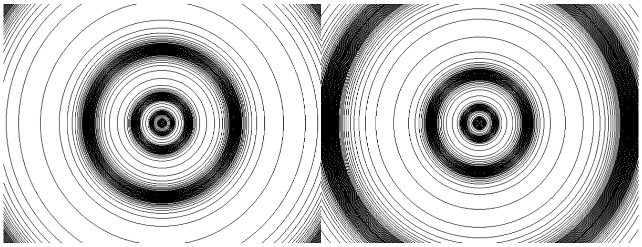

Fig. 2: The 2D projection of the first layer ($k = 1$) of equipotential surfaces of the Euler Field $\mathcal{E} = e^{\mathcal{F}}$ (left), and the Archimedes Field $\mathcal{A} = \pi^{\mathcal{F}}$ (right). The fields are shown to the same scale.

Conclusion

According to our numeric-physical approach presented in this paper, numeric fields like $\mathcal{A}, \mathcal{E}$ are primary. When formed in systems of coupled harmonic quantum oscillators, they define numerical attractors that act as islands of stability and avoid destabilizing mutual resonances.

In order to reach collective stability, coupled harmonic quantum oscillators adjust the ratios of their frequencies in a way that they approximate transcendental attractors of the numeric fields.

Then, in order to gain more energy from the numeric field by approaching always more powerful attractors, the coupled harmonic quantum oscillators are forced to move in the direction of the center of the numeric field.

Since the fractal scalar fields of transcendental numerical attractors are logarithmically symmetric, locally this movement appears as accelerated free fall caused by a conservative central force that obeys an inverse-square law.

However, because of the fractal logarithmic hyperbolic metric of the numeric field, every equipotential surface is an attractor, so that the closer to an attractor, the more evident the effect of fractal inhomogeneity of the numeric field becomes. These inhomogeneities appear as local deviations from the inverse-square law of free fall. In this way, no additional (fifth) force or physical field is required to explain the observed violations [24] of Newton's gravity in depth.

We are aware that no physical principle can explain the origin of energy, because every physical process presupposes the existence of another physical process that serves as its energy source. This non ending chain of energy converters suggests that the imperishability of motion and interaction, and the inexhaustibility of energy must have a non-physical cause. On the one hand, our approach seems to draw on Pythagoras, but on the other hand, it is intended to encourage us to break the vicious circle of the current paradigm.

Within the presented here approach, fundamental physical forces are caused by numerical relations. This approach allows to derive physical effects from non-physical i.e. numerical relations. In particular, this approach leads us to the conclusion that motion and interaction, including energy as well as other constants of motion are caused by attractors of numeric fields. Perhaps a new relational paradigm could lead us to a deeper understanding of physics and help us overcome our current inability to invent new energy sources.

Acknowledgements

The author is grateful to Alexandr Beliaev, Alexey Petrukhin, Ulrike Granögger, Clemens Kuby, Michael Kauderer, Erwin Müller and Leili Khosravi for valuable discussions.

Submitted on December 19, 2024

References

1. Langacker P. The Standard Model and Beyond. *CRC Press*, ISBN 978-1-4200-7907-4, (2009).
2. Electric charge, Overview. *en.wikipedia.org* (2023).
3. Carlip S. Aberration and the Speed of Gravity. arXiv:gr-qc/9909087v2 (1999).
4. Laplace P. S. Sur les altérations que le mouvement des planètes et des comètes par la résistance des milieux qu'elles traversent, et par la transmission successive de la pesanteur. Traité de mécanique céleste. Partie IV, livre X, chapitres VII, pp. 313–326, Paris, (1805).
5. Flandern Van T. The Speed of Gravity – What the Experiments Say. *Physics Letters A*, 1998, v. 250, 1–11.
6. Neumann L. Experimental Verification of Gravity Dynamics: Horizontal Chaos. *European Journal of Applied Sciences*, 2023, v.,11, no. 5, 222–258.
7. Müller H. Physics of Transcendental Numbers meets Gravitation. *Progress in Physics*, 2021, v. 17, 83–92.
8. Hansson J. The 10 Biggest Unsolved Problems in Physics. *International Journal of Modern Physics and Applications*, 2015, v. 1, no. 1, 12–16.
9. Müller H. The Physics of Transcendental Numbers. *Progress in Physics*, 2019, v. 15, 148–155.
10. Müller H. Physics of Irrational Numbers. *Progress in Physics*, 2022, v. 18, 103–109.
11. Müller H. Physics of Transcendental Numbers as Forming Factor of the Solar System. *Progress in Physics*, 2022, v. 18, 56–61.
12. Malhotra R. Orbital Resonances and Chaos in the Solar system. // *Solar System Formation and Evolution ASP Conference Series*, 1998, v. 149, 37–63.
13. Minton D. A., Malhotra R. A record of planet migration in the main asteroid belt. *Nature*, 2009, v. 457, 1109–1111.
14. Luque R., Osborn H. P. et al. A resonant sextuplet of sub-Neptunes transiting the bright star HD 110067. *Nature*, 2023, v. 623(7989), 932–937; arXiv:2311.17775.
15. Parlitz U. et al. Schwingungen im Gleichtakt. *Physik Journal*, 2006, v. 5, no. 10, 33.
16. Pantaleone J. Synchronization of metronomes. *Am. J. Phys.*, 2002, v. 70, 992–1000.
17. Laplace P. S. Valeurs numériques des différentes grandeurs qui entrent dans les expressions des inégalités planétaires. Traité de mécanique céleste. Partie II, livre VI, chapitres VI–VII, pp. 61–94, Paris, (1799).
18. Dombrowski K. Rational Numbers Distribution and Resonance. *Progress in Physics*, 2005, v. 1, 65–67.
19. Ruzza di S. Some results on the dynamics of conservative and dissipative systems with applications to Celestial Mechanics. Dottorato di Ricerca in Matematica, p. 60; Rome University, (2010).
20. Hilbert D. Über die Transcendenz der Zahlen e und π. *Mathematische Annalen*, 1893, v. 43, 216–219.
21. Müller H. Gravity as Attractor Effect of Stability Nodes in Chain Systems of Harmonic Quantum Oscillators. *Progress in Physics*, 2018, v. 14, 19–23.
22. Pound R. V., Rebka Jr. G. A. Gravitational Red-Shift in Nuclear Resonance. *Physical Review Letters*, 1959, v. 3(9), 439–441.
23. Stacey F. D. et al. Constraint on the planetary scale value of the Newtonian gravitational constant from the gravity profile within a mine. *Phys. Rev. D*, 1981, v. 23, 1683.
24. Holding S. C., Stacey F. D., Tuck G. J. Gravity in mines. An investigation of Newton's law. *Phys. Rev. D*, 1986, v. 33, 3487.
25. Stacey F. D. Gravity. *Science Progress*, 1984, v. 69, no. 273, 1–17.
26. Müller H. Quantum Gravity Aspects of Global Scaling and the Seismic Profile of the Earth. *Progress in Physics*, 2018, v. 14, 41–45.
27. Müller H. Global Scaling of Planetary Atmospheres. *Progress in Physics*, 2018, v. 14, 66–70.
28. R.L. Workman et al. (Particle Data Group), *Progr. Theor. Exp. Phys.*, 2022, 083C01.
29. Debarshi D. et al. Mass-Independent Scheme to Test the Quantumness of a Massive Object. *Phys. Rev. Lett.*, 2024, v. 132, 030202.
30. Müller H. Fractal Quantization of Speed in Physics of Numerical Relations. *Progress in Physics*, 2023, v. 19, 153–155.
31. Lari G. et al. Long-term evolution of the Galilean satellites: the capture of Callisto into resonance. *Astronomy and Astrophysics*, 2020, v. A639, A40.

The Time Machine

Patrick Marquet

Calais, France
E-mail: patrick.marquet6@wanadoo.fr

Gödel's metric (1949) describes a homogeneous and rotating universe unveiling the existence of closed time-like curves (CTCs) which make it feasible to go on a journey into one's own past. In the first part of this paper we follow Gödel's initial work and its conclusions but we show that his metric as it stands does not represent a cosmological model. Introducing a simple conformal factor readily induces a pressure term that straightforwardly leads to a perfect fluid field equation. This term was wrongly interpreted by Gödel as the ad hoc cosmological constant he was forced to introduce in order for his solution to satisfy Einstein's field equations. The theory is now endowed with a physical meaning and the dynamics no longer apply to the space but to a fluid which can be acted upon. In the second part, we investigate the possibility of creating a time machine materialized by a specific warp drive device travelling along a Gödel closed curve. The third part is devoted to highlighting the properties resulting from our model and some conjectures as to reversed CTCs.

Introduction

In the science fiction novel *The Time Machine* by H. G. Wells (1895), an English scientist constructs a machine which allows him to travel back and forth in time. He used this device to visit the world far in the future but returned from his journey only a few hours after he has started it. The history of the scientific controversy about the possibility of time travel can be traced back to the ingenious logician Kurt Gödel. In a paper published in 1949 to honour his close friend Albert Eistein on the occasion of his 70th birthday, he described a homogeneous and rotating universe unveiling the existence of closed time-like curves (CTCs) which make it feasible to go on a journey into one's own past.

In the first part of this paper we follow Gödel's initial work and its conclusions but we show that his metric as it stands does not represent a cosmological model. Introducing a simple conformal factor readily induces a pressure term that straightforwardly leads to a perfect fluid field equation. This term was wrongly interpreted by Gödel as the *ad hoc* cosmological constant he was forced to introduce in order for his solution to satisfy Einstein's field equations. The theory is now endowed with a physical meaning and the dynamics no longer apply to the space but to a fluid which can be acted upon. In the second part, we investigate the possibility of creating a time machine materialized by a specific warp drive device traveling along a Gödel closed curve. The third part is devoted to highlighting the properties resulting from our model and some conjectures as to reversed CTCs.

Notations

Space-time indices: $\mu, \nu = 0, 1, 2, 3$;
Spatial indices: $a, b = 1, 2, 3$;
Space-time signature: -2 (unless otherwise specified);
Newton's constant of gravitation: G.

Part I

1 The Gödel universe

1.1 General considerations

In his original paper [1], Kurt Gödel has derived an exact solution to Einstein's field equation which describes a homogeneous and non-isotropic universe where matter takes the form of a shear free fluid. This metric exhibits a rotational symmetry which allows for the existence of closed time-like curves (previously called CTCs).

The Gödel space-time has a five dimensional group of isometries (G5) which is transitive (an action of a group is transitive on a manifold $(\mathrm{M}, \boldsymbol{g})$, if it can map any point of the manifold into any other point of this manifold. It admits a five dimensional Lie algebra of Killing vector fields generated by a time translation ∂_{ct}, two spatial translations ∂_x,∂_y plus two further Killing vector fields

$$\partial_z - y\,\partial_y\,, \quad 2\,e^x\,\partial_{c\,t} + y\,\partial_z + \left(e^{2x} - \frac{1}{2}\,y^2\,\partial_y\right).$$

The Weyl tensor of the standard Gödel solution has Petrov type D

$$C^{\alpha\beta}_{\mu\nu} = R^{\alpha\beta}_{\mu\nu} + \frac{1}{3}\,R\,\delta^{\alpha}_{[\mu}\delta^{\beta}_{\nu]} + 2\,\delta^{[\alpha}_{[\mu}R^{\beta]}_{\nu]}\,.$$

The presence of the non-vanishing Weyl tensor prevents the Gödel metric from being Euclidian, unlike the Friedmann-Lemaître-Robertson-Walker metric, which can be shown to reduced to a conformal euclidian metric implying that its Weyl tensor is zero [2].

The Gödel model is dismissed because it has a cosmological constant and also since its rotation would conflict with observational data. In what follows we are able to relax our demand that Gödel's metric be the description of our actual Universe which is expanding.

1.2 Gödel's metric

The classical Gödel line element is given in Cartesian coordinates by

$$ds^2 = a^2\left(c^2dt^2 + \frac{1}{2}\,e^{2x}dy^2 - 2\,e^x c\,dt\,dy - dx^2 - dz^2\right), \quad (1.1)$$

where $a > 0$ is a constant. The components of the metric tensor $g_{\mu\nu}$ and $g^{\mu\nu}$ are, respectively,

$$\left.\begin{aligned} g_{\mu\nu} &= \begin{pmatrix} a^2 & 0 & a^2e^x & 0 \\ 0 & -a^2 & 0 & 0 \\ a^2e^x & 0 & \frac{1}{2}\,a^2e^{2x} & 0 \\ 0 & 0 & 0 & -a^2 \end{pmatrix} \\ g^{\mu\nu} &= \begin{pmatrix} a^{-2} & 0 & 2\,a^{-2}e^{-x} & 0 \\ 0 & -a^{-2} & 0 & 0 \\ 2\,a^{-2}e^{-x} & 0 & -2\,a^{-2}e^{-2x} & 0 \\ 0 & 0 & 0 & -a^{-2} \end{pmatrix} \end{aligned}\right\}. \quad (1.2)$$

Owing to the fact that only $\partial_1\, g_{22} \neq 0$ and $\partial_1\, g_{02} \neq 0$, one easily computes

$$\Gamma^0_{01} = 1\,, \qquad \Gamma^0_{12} = \Gamma^1_{02} = \frac{1}{2}\,e^x,$$

$$\Gamma^1_{22} = \frac{1}{2}\,e^{2x}, \qquad \Gamma^2_{01} = -e^{-x}.$$

The Ricci tensor is very simplified

$$R_{\beta\gamma} = \partial_1\,\Gamma^1_{\beta\gamma} + \Gamma^1_{\beta\gamma} - \Gamma^\delta_{\alpha\beta}\Gamma^\alpha_{\delta\gamma}\,, \quad (1.3)$$

the components of which are reduced to

$$R_{00} = 1\,, \quad R_{22} = e^{2x}, \quad R_{02} = R_{20} = e^x,$$

therefore the Ricci scalar is

$$R = \frac{1}{a^2}\,.$$

The normalized unit vector $\boldsymbol{u}$ of matter has components

$$u^\mu = \left(a^{-1}, 0, 0, 0\right), \quad u_\mu = (a,\, 0,\, ae^x,\, 0)\,, \quad (1.4)$$

thus the Ricci tensor takes the formulation

$$R_{\mu\nu} = u_\mu u_\nu\, a^{-2} \quad (1.5)$$

and the Ricci scalar takes the form

$$R = u^\mu u_\mu = a^{-2}. \quad (1.6)$$

Since R is a constant, the field equations (with the x^0-lines as world lines of matter)

$$R_{\mu\nu} - \frac{1}{2}\,g_{\mu\nu}R = \frac{8\pi G}{c^4}\,\rho c^2 u_\mu u_\nu + \Lambda\, g_{\mu\nu} \quad (1.7)$$

are satisfied (for a given value of the density ρ), if we put

$$a^{-2} = \frac{8\pi G\rho}{c^2}\,, \quad (1.8)$$

$$\Lambda = -\frac{1}{2}\,R = \frac{1}{2a^2} = -\frac{4\pi G\rho}{c^2}\,. \quad (1.9)$$

The sign of the cosmological constant Λ here is the opposite of that occurring in Einstein's field equations. Bearing in mind that a is a constant, fine tuning the density of the universe with the cosmological constant and the Ricci scalar appears as a dubious result. It then becomes clear that such cosmological constraints are physically irrelevant.

2 Rotation of Gödel's model

As primarily assumed by Gödel, the stationary space-time of his model is homogeneous. For every point A of the manifold $(\mathrm{M}, \boldsymbol{g})$, there is a one-parameter group of transformations of M carrying A into itself. In addition, the manifold $(\mathrm{M}, \boldsymbol{g})$ is endowed with a rotational symmetry and the flow lines have a vorticity magnitude $\boldsymbol{\omega}$ orthogonal to $\boldsymbol{u}$.

2.1 Vorticity vector

Let u_α be a 4-unit vector everywhere tangent to the flow line on $(\mathrm{M}, \boldsymbol{g})$. The covariant derivative $u_{\alpha;\mu}$ of this time-like vector may be expressed in a invariant manner in terms of tensor fields which describe the kinematics of the congruence of curves generated by the velocity vector field u^α [3]

$$u_{(\alpha;\mu)} = \sigma_{\alpha\mu} + \omega_{\sigma\mu} + \frac{1}{3}\,\theta h_{\alpha\mu} + {}^*u_{(\alpha}u_{\mu)}\,, \quad (2.1)$$

where θ is the scalar expansion

$$\theta = u^\alpha_{;\alpha}\,, \quad (2.2)$$

and ${}^*u_\alpha$ is the 4-acceleration vector of the flow lines

$${}^*u_\alpha = u_{\alpha;\mu}u^\mu, \quad (2.3)$$

while $h_{\mu\nu}$ is the projection tensor determined as

$$h_{\mu\nu} = g_{\mu\nu} - u_\mu u_\nu\,.$$

Besides ${}^*u_\alpha$ and θ, one can define the vorticity tensor

$$\omega_{\alpha\mu} = h^\sigma_\alpha h^\nu_\mu\, {}^*u_{[\sigma;\nu]} = u_{[\alpha;\mu]} + {}^*u_{[\alpha}u_{\mu]}\,, \quad (2.4)$$

and also the quantity

$$\sigma_{\alpha\mu} = \theta_{\mu\nu} - \frac{1}{3}\,h_{\alpha\mu}\theta$$

which is the symmetric trace free shear tensor, where

$$\theta_{\mu\nu} = h^\sigma_\alpha h^\nu_\mu\, u_{(\sigma;\nu)}$$

is the expansion tensor.

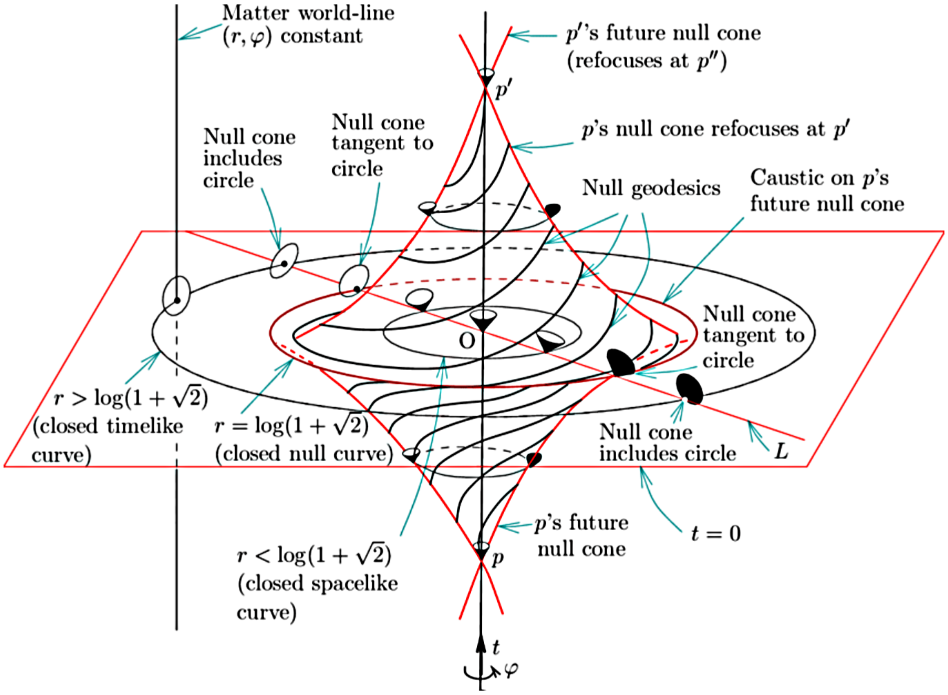

Fig. 1: With increasing $r > r_G$, the light cones continue to tip over and their opening angles increase until their future parts reach negative values of t'. Thus $\partial/\partial\phi$ becomes a timelike vector, and circles of constant r and t' are closed time-like curves.

Thus the components of the 4-vorticity vector $\boldsymbol{\omega}$ of the flow lines tangent to u^μ are expressed by

$$\omega^\beta = \frac{1}{6}\,\eta^{\beta\gamma\sigma\rho} u_\gamma \omega_{\sigma\rho}\,, \tag{2.5}$$

where $\eta^{\beta\gamma\sigma\rho}$ is the Levi-Civita tensor indicator

$$\eta^{\beta\gamma\sigma\rho} = \frac{\varepsilon^{\beta\gamma\sigma\rho}}{\sqrt{g}}\,.$$

The kinematic quantities $\omega_{\sigma\mu}$, ω_μ and ${}^*u_\mu$ are completely orthogonal to u^μ, i.e.,

$$\omega_{\sigma\mu} u^\mu = \omega_\mu u^\mu = {}^*u_\mu u^\mu = h_{\mu\nu} u^\mu = 0\,.$$

In the Gödel model the shear tensor is zero, therefore

$$\sigma_{\alpha\mu} = u_{(\alpha;\mu)} - \frac{1}{3}\,\theta h_{\alpha\mu} - \omega_{\sigma\mu} - {}^*u_{(\alpha}u_{\mu)} = 0 \tag{2.5bis}$$

(shear free flows of a perfect fluid in relation with the Weyl tensor have been extensively investigated by A. Barnes [4]).

Knowing that $\sqrt{g} = a^4\sqrt{\frac{1}{2}e^{2x}}$, we compute the contravariant components of the 4-vorticity vector $\boldsymbol{\omega}$

$$\omega^\alpha = \left(0,\,0,\,0,\,\frac{\sqrt{2}}{a^2}\right) \tag{2.6}$$

and we find

$$\omega = \sqrt{g_{\alpha\beta}\,\omega^\alpha\omega^\beta} = \frac{\sqrt{2}}{a}\,. \tag{2.7}$$

Taking into account (1.8) the magnitude of this vector is

$$\omega = \sqrt{\frac{1}{2}\left(\frac{8\pi G}{c^2}\right)\rho}\,. \tag{2.8}$$

2.2 Closed time-like curves

Following Gödel we introduce cylindrical coordinates (t', r, θ)

$$e^x = \cosh 2r + \cosh\phi\,\sinh 2r\,,$$

$$y\,e^x = \sqrt{2}\sinh\phi\,\sinh 2r\,,$$

$$\tan\frac{1}{2}\left[\phi + \left(ct - \frac{2t'}{2\sqrt{2}}\right)\right] = e^{-2r}\tan\frac{\phi}{2}$$

thus the Gödel metric reads now

$$\begin{aligned} ds^2 = 4a^2\Big[dt'^2 - dr^2 + \left(\sinh^4 r - \sinh^2 r\right)d\phi^2 + \\ + 2\sqrt{2}\sinh^2 r\,d\phi\,dt'\Big] \end{aligned} \tag{2.9}$$

(with the inessential coordinate z suppressed).

In its original formulation, the Gödel universe describes a set of masses (stars and planets) rotating about arbitrary axes. The metric (2.9) manifests a rotational symmetry with respect to the axis t', and $r = 0$ since we clearly see that the components of the metric tensor do not depend ϕ.

For $r \geqslant 0$, we have $0 \leqslant \phi \leqslant 2\pi$. If a curve r_G is defined by $\sinh r = 1$ that is $r_G = \log\,(1+\sqrt{2})$, then such a curve

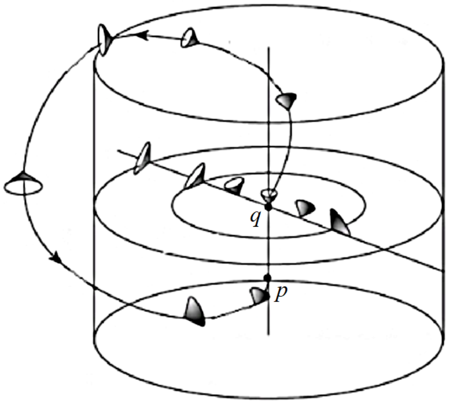

Fig. 2: The Gödel trajectory loops back in the past at p after crossing a Cauchy-like "horizon".

which materializes in the "plane" $t' = const$ is a closed lightlike curve. The radius r_G referred to as the Gödel radius, thus induces a closed null curve where the light cones are tangent to the plane of constant t'.

With increasing $r > r_G$, the light cones continue to tip over and their opening angles increase until their future parts reach negative values of t'. Thus $\partial/\partial\phi$ becomes a timelike vector, and circles of constant r and t' are closed time-like curves (see Fig. 1). Starting from the centre of the axis at q, the Gödel trajectory loops back in the past at p after crossing a Cauchy-like "horizon" (see Fig. 2).

3 The Gödel model as a homogeneous perfect fluid

3.1 Reformulation of the Gödel metric

In our publication [5], we assumed that a is slightly spacetime variable and we set

$$a^2 = e^{2U}. \tag{3.1}$$

The positive scalar $U(x)$ will be explained below. The Gödel metric thus becomes

$$ds^2 = e^{2U} \times \times \left(c^2dt^2 + \frac{1}{2}\, e^{2x} dy^2 - 2\, e^x\, c dt\, dy - dx^2 - dz^2 \right). \tag{3.2}$$

We see that it is conformal to the Gödel metric with the constant $a = 1$

$$(ds^2)_G = c^2dt^2 + \frac{1}{2}\, e^{2x} dy^2 - 2\, e^x\, c dt\, dy - dx^2 - dz^2. \tag{3.3}$$

It is clear that this solution retains the properties related to CTCs of the initial Gödel metric (1.1).

3.2 Differential geodesic system

Let us consider the manifold $(\mathrm{M}, \boldsymbol{g})$ on which is defined a vector tangent to the curve C

$$^*x^\alpha = \frac{dx^\alpha}{d\zeta}\,,$$

where ζ is an affine parameter. In these local coordinates, we consider the scalar function $f(x^\alpha, {}^*x^\alpha)$, which is homogeneous and of first degree with respect to $^*x^\alpha$. To the curve C joining the points x_1 and x_2 one can always associate the integral $\mathcal{A}$ such that

$$\mathcal{A} = \int_{\zeta_1}^{\zeta_2} f(x^\alpha, {}^*x^\alpha)\, d\zeta = \int_{x_1}^{x_2} f(x^\alpha, {}^*x^\alpha)\, dx^\alpha. \tag{3.3}$$

We now want to evaluate the variation of $\mathcal{A}$ with respect to the points ζ_1 and ζ_2

$$\delta\mathcal{A} = f\,\delta\zeta_2 - f\,\delta\zeta_1 - \int_{\zeta_1}^{\zeta_2} \delta\, d\zeta\,.$$

Classically we know that

$$\int_{\zeta_1}^{\zeta_2} \delta\, d\zeta = \left(\frac{\partial f}{\partial\, {}^*x^\alpha} \right) \delta x^\alpha - \int_{\zeta_1}^{\zeta_2} E_\alpha\, \delta x^\alpha\, d\zeta\,,$$

where E_α is the first member of the Euler equation associated with the function f.

With E_α as the components of $\boldsymbol{E}$, we infer the expression

$$\delta\mathcal{A} = [w(\delta)]_{x_2} - [w(\delta)]_{x_1} - \int_{\zeta_1}^{\zeta_2} \boldsymbol{E}\, \delta x\, d\zeta\,, \tag{3.5}$$

where $w(\delta)$ has the form

$$w(\delta) = \frac{\partial f}{\partial\, {}^*x^\alpha}\, \delta x^\alpha - \frac{x^\alpha\, \partial f}{\partial\, {}^*x^\alpha - f}\, \delta\zeta\,.$$

Due to the homogeneity of f it reduces to

$$w(\delta) = \frac{\partial f}{\partial\, {}^*x^\alpha}\, \delta x^\alpha.$$

Let us apply the above results to the function

$$f = e^U\, \frac{ds}{d\zeta} = e^U \sqrt{g_{\alpha\beta}\, {}^*x^\alpha\, {}^*x^\beta}\,, \tag{3.6}$$

where e^U is defined everywhere on $(\mathrm{M}, \boldsymbol{g})$.

We first differentiate $f^2 = e^{2U} (g_{\alpha\beta}\, {}^*x^\alpha\, {}^*x^\beta)$ with respect to $^*x^\alpha$ and x^α

$$\frac{f\,\partial f}{\partial\, {}^*x^\alpha} = e^{2U} g_{\alpha\beta}\, {}^*x^\beta, \tag{3.7}$$

$$\frac{f\,\partial f}{\partial x^\alpha} = e^U \sqrt{g_{\beta\mu}\, {}^*x^\beta\, {}^*x^\mu} \times \times \left[\partial_\alpha e^U \sqrt{g_{\beta\mu}\, {}^*x^\beta\, {}^*x^\mu} + \frac{1}{2}\, e^U\, \partial_\alpha \left(g_{\beta\mu}\, {}^*x^\beta\, {}^*x^\mu \right) \right]. \tag{3.8}$$

We now choose s as the affine parameter ζ on the curve C, so the vector $^*x^\beta$ is here regarded as the 4-unit vector u^β tangent to C whose curvilinear abscissa is noted s. Equations (3.7) and (3.8) then reduce to the following

$$\frac{\partial f}{\partial\, {}^*x^\beta} = e^U u_\beta\,, \tag{3.9}$$

$$\frac{\partial f}{\partial x^\beta} = \partial_\beta e^U + \frac{1}{2}\, e^U \partial_\beta g_{\alpha\mu} u^\alpha u^\mu = \\ = \partial_\beta e^U + e^U \Gamma_{\alpha\beta,\mu} u^\alpha u^\mu \,, \tag{3.10}$$

where $\Gamma_{\alpha\beta,\mu}$ denote here the Christoffel symbols of the first kind. Expliciting the Euler equations $f(x^\alpha, du^\alpha)$

$$E_\beta = \frac{d}{ds}\frac{\partial f}{\partial u^\beta} - \frac{\partial f}{\partial x^\beta}\,, \tag{3.11}$$

we obtain

$$\begin{aligned} E_\beta &= \frac{d}{ds}\, e^U u^\beta - e^U \Gamma_{\alpha\beta,\mu} u^\alpha u^\mu - \partial_\beta e^U = \\ &= e^U \left(u^\mu \partial_\mu u_\beta - \Gamma_{\alpha\beta,\mu} u^\alpha u^\mu\right) - \partial_\alpha e^U \left(\delta^\alpha_\beta - u^\alpha u_\beta\right) \\ &= e^U \left[\left(u^\mu \nabla_\mu u_\beta\right) - \partial_\beta U - \partial_\alpha U \left(\delta^\alpha_\beta - u^\alpha u_\beta\right)\right]. \end{aligned} \tag{3.12}$$

Equation (3.5) becomes

$$\delta\mathcal{A} = [w(\delta)]_{x_2} - [w(\delta)]_{x_1} - \int_{x_1}^{x_2} \langle \boldsymbol{E}\,\delta x\rangle\, ds\,, \tag{3.13}$$

where locally we have $w(\delta) = e^U u_\alpha dx^\alpha$. When the curve C varies between two fixed points x_1 and x_2, the local variations $[w(\delta)]_{x_2}$ and $[w(\delta)]_{x_1}$ vanish.

Applying the variation principle to (3.13) simply leads to

$$\delta\mathcal{A} = -\int_{x_1}^{x_2} \langle \boldsymbol{E}\,\delta x\rangle\, ds = 0\,, \tag{3.14}$$

i.e., $\boldsymbol{E} = 0$, and since $e^U \neq 0$, we obtain

$$u^\mu \nabla_\mu u_\beta - \left(\delta^\alpha_\beta - u^\alpha u_\beta\right) \partial_\alpha U = 0\,. \tag{3.15}$$

The equation (3.15) is formally identical to the differential system obeyed by the flow lines of a perfect fluid of density ρ and pressure P with an equation of state $\rho = f(P)$ and where

$$U(x^\mu) = \int_{P_1}^{P_2} \frac{dP}{\rho c^2 + P}$$

accounts for the fluid indice [6]. Pressure P_1 and P_2 are referred to x_1 and x_2 [7, 8]; see Appendix. The resulting field equation is [9]

$$R_{\mu\nu} - \frac{1}{2}\, g_{\mu\nu} R = \frac{8\pi G}{c^4}\left[\left(\rho c^2 + P\right) u_\mu u_\nu - P g_{\mu\nu}\right]. \tag{3.16}$$

Here, the 4-unit vector u^μ of the fluid is the real 4-velocity defined in Gödel's metric (3.3):

$$u^\mu = (1, 0, 0, 0)\,, \quad u_\mu = (1, 0, e^x, 0)\,. \tag{3.17}$$

3.3 Fluid rotation in the framework of the Gödel model

The wave vector $k^\mu = dx^\mu / d\lambda$ determines the propagation of ligh rays tangent to the light cone (λ is a given parameter varying along those rays). The equation of propagation is here

$$\frac{dk^\mu}{d\lambda} + \Gamma^\mu_{\alpha\nu} k^\alpha k^\nu = 0\,.$$

Substituting $\partial_\mu \psi$ (here ψ is the eikonal) in this expression, one finds the eikonal equation

$$g^{\mu\nu} \partial_\mu \psi\, \partial_\nu \psi = 0\,.$$

Let us now examine the case of the light cone for closed lines, when the Gödel radius is reached. To this effect, we revert to the metric (2.9) which reads now

$$ds^2 = 4\, e^{2U}\Big[dt'^2 - dr^2 + \left(\sinh^4 r - \sinh^2 r\right) d\phi^2 + \\ + 2\sqrt{2}\, \sinh^2 r\, d\phi\, dt'\Big]. \tag{3.18}$$

The wave vectors k^μ tangent to the light cone follow les closed lines located to the plane orthogonal to the time axis $t' = const$: the integral U performed over the closed path has no endpoints

$$U(r) = \int \frac{dP}{\rho c^2 + P} + const. \tag{3.19}$$

Beyond r_G, the fluid trajectory does not loop up at the same point but in the past, and the magnitude of the time shift will depend on the pressure difference ΔP.It is now easy to compute the vorticity tensor $\omega_{\mu\nu}$ which is derived from u^μ

$$\omega_{\mu\nu} = \partial_\mu u_\nu - \partial_\nu u_\mu\,. \tag{3.20}$$

The components of the 4-vorticity vector $\boldsymbol{\omega}$ of the fluid flow lines are

$$\omega^\beta = \frac{1}{6}\, \eta^{\beta\gamma\sigma\rho} u_\gamma \omega_{\sigma\rho}\,.$$

For calculating the Levi-Civita tensor $\eta^{\beta\gamma\sigma\rho} = \varepsilon^{\beta\gamma\sigma\rho}/\sqrt{g}$, the $g_{\mu\nu}$ determinant is now $g = \frac{1}{2}\, e^{2x}$. A simple calculation leads to the Gödel rotation which remains constant

$$\boldsymbol{\omega} = \sqrt{g_{\alpha\beta}\, \omega^\alpha \omega^\beta} = \sqrt{2}\,. \tag{3.21}$$

We note that the Kretschmann scalar is still invariant

$$R_{\mu\nu\alpha\beta} R^{\mu\nu\alpha\beta} = 12\,\omega\,.$$

Part II

4 Warp drive

4.1 The (3 + 1) formalism or ADM technique

Arnowitt, Deser and Misner (ADM) suggested a technique which leads to decompose the space-time into a family of spacelike hypersurfaces and parametrized by the value of an arbitrarily chosen time coordinate x^0 [10]. This *foliation* displays a proper time element $d\tau$ between two nearby hypersurfaces labeled

$$x^0 = const, \qquad x^0 + dx^0 = const,$$

and the proper time element $cd\tau$ must be proportional to dx^0, thus we write

$$cd\tau = N(x^a, x^0)\, dx^0.$$

The line element corresponding to the hypersurfaces separation is therefore written in the form

$$\begin{aligned}(ds^2)_{\text{ADM}} = &-N^2 (dx^0)^2 + \\ &+ g_{ab}\,(N^a dx^0 + dx^a)(N^b dx^0 + dx^b).\end{aligned} \tag{4.1}$$

In the ADM terminology, N is called the *lapse function*. Let us now evaluate the 3-vector whose spatial coordinates x^a are lying in the hypersurface $x^0 = const$, which is normal to it, on the second hypersurface $x^0 + dx^0 = const$, and where these coordinates now become $N^a dx^0$. The N^a vector is called the *shift vector*. The 4-metric tensor covariant and contravariant components $(g_{\alpha\beta})_{\text{ADM}}$ and $(g^{\alpha\beta})_{\text{ADM}}$ are

$$\left.\begin{aligned}(g_{\alpha\beta})_{\text{ADM}} &= \begin{pmatrix} -N^2 - N_a N_b\, g^{ab} & N_b \\ N_a & g_{ab} \end{pmatrix} \\ (g^{\alpha\beta})_{\text{ADM}} &= \begin{pmatrix} -N^{-2} & \dfrac{N^b}{N^2} \\ \dfrac{N^a}{N^2} & g^{ab} - \dfrac{N^a N^b}{N^2} \end{pmatrix}\end{aligned}\right\}. \tag{4.2}$$

The line element corresponding to the hypersurfaces separation is therefore written as

$$\begin{aligned}(ds^2)_{\text{ADM}} &= \\ &= -N^2 (dx^0)^2 + g_{ab}\,(N^a dx^0 + dx^a)(N^b dx^0 + dx^b) \qquad (4.3)\\ &= -N^2 + N_a N^a\,(dx^0)^2 + 2N_b\, dx^0 dx^b + g_{ab}\, dx^a dx^b,\end{aligned}$$

where g_{ab} is the 3-metric of the hypersurfaces. As a result, the hypersurfaces have a unit time-like normal with contravariant components

$$u^\alpha = N^{-1}(1, -N^a). \tag{4.4}$$

If the universe is approximated to the Minkowski space within an orthonormal coordinates frame of reference and where the fundamental 3-tensor satisfies $g^{ab} = \delta^{ab}$, the metric (4.3) becomes

$$(ds^2)_{\text{ADM}} = -(N^2 - N_a N^a)\, c^2 dt^2 + 2N^a dx\, cdt + dx^a dx^b, \tag{4.5}$$

$$(ds^2)_{\text{ADM}} = -N^2 dt^2 + (dx + N^a cdt)^2 + dy^2 + dz^2. \tag{4.5bis}$$

The Einstein action can be written in terms of the 4-metric tensor $(g_{\alpha\beta})_{\text{ADM}}$ according to [11] as follows

$$S_{\text{ADM}} = \int cdt \int N\left({}^{(3)}R - K^a_b K^b_a + K^2\right) \sqrt{{}^{(3)}g}\, d^3x + \\ + \text{boundary terms},$$

where $K^a_a K^b_b = K^2$, and ${}^{(3)}R$ is the 3-Ricci scalar and stands for the *intrinsic curvature* of the hypersurface

$$x^0 = const,$$

$$\sqrt{{}^{(3)}g} = \sqrt{\det \|g_{ab}\|} \;\longleftrightarrow\; \sqrt{{}^{(4)}{-g}} = N\sqrt{{}^{(3)}g}\,,$$

while

$$K_{ab} = (2N)^{-1}(-N_{a;\,b} - N_{b;\,a} + \partial_0\, g_{ab}) \tag{4.6}$$

represents the *extrinsic curvature*, and as such describes the manner in which the hypersurface $x^0 = const$ is embedded in the surrounding space-time. The rate of change of the 3-metric tensor g_{ab} with respect to the time label can be decomposed into "normal" and "tangential" contributions:

— The normal change is proportional to the extrinsic curvature $2K_{ab}/N$ of the hypersurface;

— The tangential change is given by the Lie derivative of g_{ab} along the shift vector N^a

$$\mathbf{L}_N\, g_{ab} = 2N_{(a;\,b)}\,. \tag{4.7}$$

With the choice of $N^a = 0$, we have a particular coordinate frame called *normal coordinates* according to which is called an *Eulerian gauge*.

Inspection shows that

$$K_{ab} = -u_{a;b}\,, \tag{4.8}$$

which is sometimes called the *second fundamental form* of the 3-space. Six of the ten Einstein equations imply for K^a_b to evolve according to

$$\begin{aligned}\frac{\partial K^a_b}{c\partial t}\,\mathbf{L}_N K^a_b &= \nabla^a \nabla_b N + \\ &+ N\left[R^a_b + K^a_a K^a_b + 4\pi\,(T - C)\,\delta^a_b - \frac{8\pi G}{c^4}\,T^a_b\right],\end{aligned} \tag{4.9}$$

$$C = T_{\alpha\beta}\, u^\alpha u^\beta, \tag{4.10}$$

where C is the matter energy density in the rest frame of normal congruence (time-like vector field) with $T = T^a_a$.

With the Gauss-Codazzi relations [12] we can express the Einstein tensor as a function of both the intrinsic and extrinsic curvatures. At this stage it is convenient to introduce the 3-momentum current density $I_a = -u_c T^c_a$. Thus, the remaining four equations finally form the so-called *constraint equations*

$$H = \frac{1}{2}\left({}^{(3)}R - K^a_b K^b_a + K^2\right) - \frac{8\pi G}{c^4}\, C = 0, \tag{4.11}$$

$$H_b = \nabla_a \left(K^a_b - K\delta^a_b \right) - \frac{8\pi G}{c^4}\, I_b = 0\,. \tag{4.12}$$

Therefore, another way of writing (4.10) eventually leads to

$$C = \frac{c^4}{16\pi G} \left({}^{(3)}R - K_{ab}K^{ab} + K^2 \right). \tag{4.13}$$

4.2 Alcubierre's theory

In 1994, M. Alcubierre showed that a superluminal velocity can be achieved without violating the laws of General Relativity [13]. He considered a perturbed space-time region likened to bubble (called "warp drive") which could transport a machine in a surfing mode: inside the bubble, the proper time element $d\tau$ is the coordinate time element dt measured by an external observer called "Eulerian". The motion is only achieved by the space wave, so that the occupant of the machine is at rest and would not suffer any acceleration nor time dilation in the displacement. This process requires a front contraction of the space and a rear expansion.

The distance of the machine centre located in the bubble

$$r_s(t) = \sqrt{\left[y - y_s(t) \right]^2 + x^2 + z^2}$$

varies until R_e, which is the external radius of the bubble. With respect to the distant observer the apparent velocity of the machine is

$$\mathrm{v}_s(t) = \frac{dy_s(t)}{dt}\,,$$

where $y_s(t)$ is the coordinate of the bubble's trajectory along the y-direction. Within the ADM formalism in the signature +2, the Alcubierre metric is defined on a flat space-time thus the lapse vectors and shift vectors reduce to

$$\left. \begin{aligned} & N = 1 \\ & N^1 = -\mathrm{v}_s(t) f(r_s, t) \\ & N^2 = N^3 = 0 \end{aligned} \right\}. \tag{4.14}$$

The shape of the function $f(r_s, t)$ induces both a volume contraction and expansion ahead and behind of the bubble. This can be checked by using the scalar expansion $\theta = u^\alpha_{;\alpha}$

$$\theta = \mathrm{v}_s \frac{df}{(dy)_{\mathrm{Al}}}\,. \tag{4.15}$$

Alcubierre chooses the following step function $f(r_s, t)$

$$f(r_s, t) = \frac{\tanh \sigma(r_s + R_e) - \tanh \sigma(r_s - R_e)}{2\tanh\,(\sigma R_e)}\,, \tag{4.16}$$

where $R_e > 0$ is the external radius of the bubble, and σ is a "bump"parameter used to tune the wall thickness of the bubble: the larger the parameter σ, the greater the contained energy density, for its shell thickness decreases. Moreover, the absolute increase of σ means a faster approach of the condition

$$\lim_{\sigma\to\infty} f(r_s, t) = 1 \quad \text{for} \;\; r_s \in [-R_e, R_e]$$

and is 0 everywhere else.

Here the expansion scalar becomes

$$\theta = \partial_1 N^1 = -\mathrm{trace}\, K_{ab}\,.$$

With (4.16) one finally gets

$$\theta = \mathrm{v}_s \frac{df}{dr_s} \frac{y_s}{r_s}\,. \tag{4.17}$$

The Natàrio warp drive evades the problem of contraction/expansion, by imposing the divergence free constraint to the shift vector $\nabla[\mathrm{v}_s^2 f^2(r_s, t)] = 0$ [14].

The distant observer is called *Eulerian* [15], and his 4-velocity relative to the bubble has components

$$(u^\alpha)_{\mathrm{E}} = \left[c,\, \mathrm{v}_s\, c\, f(r_s, t),\, 0,\, 0 \right], \tag{4.18}$$

$$(u_\alpha)_{\mathrm{E}} = [-c, 0, 0, 0]\,. \tag{4.18bis}$$

The Eulerian observer is a special type of observer which refers to the Eulerian gauge defined above but with $N^1 \neq 0$, and as such, it follows timelike geodesic orthogonal to euclidean hypersurfaces. Such an observer starts out just inside the bubble shell at its first equator with zero initial velocity.

Once during his stay inside the bubble, this observer travels along a time-like curve $y = y_s(t)$ with a constant velocity nearing the machine local velocity $\mathrm{v}_s = dy_s/dt$. The Eulerian observer's velocity will always be less than the bubble's velocity unless $r_s = 0$, i.e. when this observer is at the centre of the machine located inside. After reaching the second region's equator, this observer decelerates and is left at rest while going out at the rear edge of the bubble. The Eulerian observer's velocity is needed to evaluate the energy density required to create the bubble (see below).

The Alcubierre metric is:

$$(ds^2)_{\mathrm{Al}} = -c^2dt^2 + \left[dy - \mathrm{v}_s f(r_s, t)\, c dt \right]^2 + dx^2 + dz^2 \tag{4.19}$$

or, in the framework of signature −2,

$$(ds^2)_{\mathrm{Al}} = c^2dt^2 - \left[dy - \mathrm{v}_s f(r_s, t)\, c dt \right]^2 - dx^2 - dz^2. \tag{4.19bis}$$

Let us now write the Alcubierre metric in the equivalent form which puts in evidence the covariant components of the metric tensor

$$\begin{aligned} (ds^2)_{\mathrm{Al}} = & \left[(1 - \mathrm{v}_s^2 f^2(r_s, t) \right] c^2dt^2 + \\ & + 2\,\mathrm{v}_s f(r_s, t)\, c dt dy - dx^2 - dz^2, \end{aligned} \tag{4.20}$$

$$\left. \begin{aligned} & (g_{00})_{\mathrm{Al}} = \left[1 - \mathrm{v}_s^2 f^2(r_s, t) \right] \\ & (g_{01})_{\mathrm{Al}} = (g_{10})_{\mathrm{Al}} = 2\,\mathrm{v}_s f(r_s, t) \\ & (g_{11})_{\mathrm{Al}} = (g_{22})_{\mathrm{Al}} = (g_{33})_{\mathrm{Al}} = -1 \end{aligned} \right\}. \tag{4.21}$$

With the components (4.21) the Einstein-Alcubierre tensor reads

$$(G^{\alpha\beta})_{\rm Al} = (R^{\alpha\beta})_{\rm Al} - \frac{1}{2}\,(g^{\alpha\beta})_{\rm Al}\,R\,, \tag{4.22}$$

$$(T^{\alpha\beta})_{\rm Al} = \frac{c^4}{8\pi G}\,(G^{\alpha\beta})_{\rm Al}\,. \tag{4.23}$$

The weak energy conditions stipulate

$$C_{\rm Al} = (T^{\alpha\beta})_{\rm Al}\,(u_\alpha)_{\rm E}\,(u_\beta)_{\rm E} \geqslant 0\,. \tag{4.24}$$

Considering (4.13), we see that in the Alcubierre spacetime ${}^{(3)}R = 0$, hence

$$C_{\rm Al} = \frac{c^4}{16\pi G}\left(K^2 - K_{ab}\,K^{ab}\right), \tag{4.25}$$

$$C_{\rm Al} = \frac{c^4}{16\pi G}\times \\ \times\left[(\partial_1 N^1)^2 - (\partial_1 N^1)^2 - 2(\partial_2 N^2)^2 - 2(\partial_3 N^1)^2\right], \tag{4.26}$$

$$(T^{00})_{\rm Al}\,(u_0)_{\rm E}\,(u_0)_{\rm E} = (T^{00})_{\rm Al} = \\ -\frac{c^4}{32\pi G}\,{\rm v}_s^2\left[\left(\frac{\partial f}{\partial x}\right)^2 + \left(\frac{\partial f}{\partial z}\right)^2\right] < 0\,. \tag{4.27}$$

Taking into account (4.16), one eventually finds the energy tensor:

$$(T^{00})_{\rm Al} = -\frac{c^4}{32\pi G}\,{\rm v}_s^2\left(\frac{\partial f}{dr_s}\right)^2\frac{x^2+z^2}{r_s^2} < 0 \tag{4.28}$$

This expression is unfortunately negative as measured by the Eulerian observer and therefore it violates the weak energy conditions (WEC) [16]. Notwithstanding this violation, one is nevertheless forced to introduce a way to obtain a negative energy density. This possibility is examined below.

4.3 Nature of the negative energy

The machine has a shell whose thickness is: $R_e - R_i$, where R_e is the external radius while R_i is the inner radius. R_e coincides with the Alcubierre bubble which thus constitutes the whole machine contour. The mass has a charge μ circulating within the shell thus giving rise of a 4-current density $j^\alpha = \mu u^\alpha$. This current is coupled to a co-moving electromagnetic field with the 4-potential A^α, which yields the interacting energy-momentum tensor

$$(T^{\alpha\beta})_{\rm elec} = \frac{1}{4\pi}\left(\frac{1}{4}\,g^{\alpha\beta}F_{\gamma\delta}F^{\gamma\delta} + F^{\alpha\nu}F_{\nu\cdot}^{\cdot\beta}\right) + g^{\alpha\beta}j_\nu A^\nu - j^\alpha A^\beta,$$

and the extracted energy density is

$$(T^{00})_{\rm elec} = \frac{1}{4\pi}\left(\frac{1}{4}\,F_{\gamma\delta}F^{\gamma\delta} + F^{0\nu}F_{\nu\cdot}^{\cdot 0}\right) + j_\nu A^\nu - j^0 A^0. \tag{4.29}$$

Since we chose an orthonormal basis, we have

$$(T^{00})_{\rm elec} = \frac{1}{8\pi}\left(\boldsymbol{E}^2 + \boldsymbol{B}^2\right) + \frac{1}{4\pi}\,\Delta(\Phi\boldsymbol{E}), \tag{4.30}$$

where $\boldsymbol{E}$ and $\boldsymbol{B}$ are respectively the electric and magnetic field strengths derived from the Maxwell tensor

$$F_{\gamma\delta} = \partial_\gamma A_\delta - \partial_\delta A_\gamma$$

(we assume that the field potential $A^\alpha(\Phi, \boldsymbol{A})$ is given in the Lorentz gauge). The charge density is derived from

$$\Delta\boldsymbol{E} = 4\pi\mu, \tag{4.31}$$

which is just the time component of the 4-current density inferred from Maxwel's equations

$$\nabla_\alpha F^{\alpha\beta} = \frac{4\pi}{c}\;j^\beta. \qquad (4.32))$$

Therefore negative energy density may be shown explicitly by the interaction tensor

$$(T^{00})_{\rm elec-int} = \frac{1}{4\pi}\,\boldsymbol{E}\,\Delta\Phi + \mu\Phi, \tag{4.33}$$

$$(T^{00})_{\rm elec-int} = \frac{1}{4\pi}\left[\,-\Delta\Phi - \frac{1}{c}\,\partial_t\boldsymbol{A}\right]\Delta\Phi + \mu\Phi \tag{4.34}$$

since $\boldsymbol{E} = -\Delta\Phi - \frac{1}{c}\,\partial_t\boldsymbol{A}$.

In (4.34) the first term in the brackets is always negative. As to the last term, it is made negative when the time varying charge density μ and the scalar potential Φ are 180° out of phase (method reached by the use of phasors).

We now assume that the positive free radiative energy density

$$(T^{00})_{\rm elec-rad} = \frac{1}{8\pi}(\boldsymbol{E}^2 + \boldsymbol{B}^2) \tag{4.35}$$

is confined within the machine, i.e., right to the inner side of the shell wall.

The interacting tensor $(T^{00})_{\rm elec-int}$ is set so as to exhibit its energy density part on the *external* side of the shell. Now, we see that negative energy production can be achieved with such a configuration. The higher the charge density and the higher the scalar potential, then the most effective negative energy density. The local field equations read

$$G_{\mu\beta} = \frac{8\pi G}{c^4}\left[\left(\rho c^2 + P\right)u_\mu u_\beta - P g_{\mu\beta} + (T_{\mu\beta})_{\rm elec}\right]. \tag{4.36}$$

The energy density level $(T^{00})_{\rm elec-int}$ is now remaining and is anticipated to be very huge. There is however a possible drastic reduction which adequately exploits the contribution of the electromagnetic field interacting with the charges.

4.4 The energy required for the propulsion

The machine is externally charged surrounded by a comoving electromagentic field. Thus, it follows the *Finsler geodesic* [17] provided that the ratio $\mu/\rho c^2$ remains constant along the trajectory

$$(ds)_{\rm shell} = ds + \frac{\mu}{\rho c^2}\,A_\alpha\,dx^\alpha, \quad ds = \sqrt{\eta_{\alpha\beta}\,dx^\alpha dx^\beta}\,. \tag{4.37}$$

Neglecting the non quadratic terms, the metric reads

$$(ds^2)_{\text{shell}} = ds^2 + \left(\frac{\mu}{\rho c^2} A_\alpha dx^\alpha\right)^2. \tag{4.38}$$

For the energy density of the machine, the spatial components $(\mu/\rho c^2)A_\alpha dx^\alpha$ in (4.38) do not come into play. The interaction term reduces to its time component

$$\frac{\mu}{\rho c^2} A_0 dx^0 = \frac{\Phi\mu}{\rho c^2} c dt, \tag{4.39}$$

where Φ is the scalar potential.

If $g_{\alpha\beta}$ is approximated to the Minkowski tensor $\eta_{\alpha\beta}$, the metric (4.38) reads

$$ds^2 = \left(1 + \frac{\Phi\mu}{\rho c^2}\right)^2 c^2 dt^2 - dz^2 - dx^2 - dy^2.$$

In this case, we notice that the time component of the metric tensor

$$g_{00} = \left(1 + \frac{\Phi\mu}{\rho c^2}\right)^2 \tag{4.41}$$

formally corresponds to the expression of the ADM formalism (signature −2)

$$M = (1 + N)\,, \tag{4.42}$$

where the lapse function is defined as

$$N = \frac{\Phi\mu}{\rho c^2}\,. \tag{4.43}$$

The Alcubierre metric (4.20) is now

$$\begin{aligned}(ds^2)_{\text{Al}} = \left[M^2 - \mathrm{v}_s^2 f^2(r_s)\right] c^2 dt^2 + \\ + 2\mathrm{v}_s f(r_s) c dt dy - dx^2 - dz^2.\end{aligned} \tag{4.44}$$

The interaction term should be only function of r_s, R_e, σ, and of the thickness $(R_e - R_i)$, but not depending on the velocity v_s.

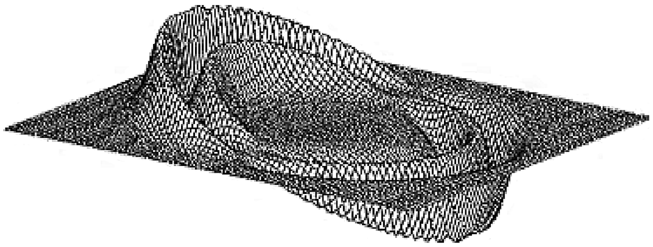

Fig. 3: 2D representation of the warped region propagating from left (expansion) to right (contraction). The groove corresponds to the shell thickness determined by the function N.

Here, our analysis is not too dissimilar to the approach detailed in [18, 19].

From the metric (4.43), it is now easy to derive the components of the Eulerian observer's velocity. We write

$$c^2 = c^2\left(M^2 - \mathrm{v}_s^2 f^2\right)\left(\frac{dt}{d\tau}\right)^2 + 2\mathrm{v}_s f c\left(\frac{dt}{d\tau}\right)\boldsymbol{u}_{\text{E}} - \boldsymbol{u}_{\text{E}}^2.$$

Travelling along a geodesic the observer "sees"

$$\frac{dt}{d\tau} = M^{-1}, \tag{4.45}$$

therefore

$$0 = \boldsymbol{u}_{\text{E}}^2\, 2\mathrm{v}_s f c M^{-1} \boldsymbol{u}_{\text{E}} + \mathrm{v}_s^2 f^2 c^2 M^{-2}. \tag{4.46}$$

Hence we find the velocity

$$\boldsymbol{u}_{\text{E}} = \mathrm{v}_s f c M^{-1}, \tag{4.47}$$

the components of which are easy to compute

$$(u^\mu)_{\text{E}} = \left[cM^{-1}, \mathrm{v}_s f c M^{-1}, 0, 0\right], \tag{4.48}$$

$$(u_\mu)_{\text{E}} = [cM, 0, 0, 0]\,. \tag{4.49}$$

By inserting M into (4.24), the expression

$$C_{\text{Al}} = (u_0)_{\text{E}} (u_0)_{\text{E}} (T^{00})_{\text{Al}} \tag{4.50}$$

leads to the new required energy density

$$(T^{00})_{\text{Al}} = -\frac{c^4}{32\pi G} \frac{\mathrm{v}_s^2 (x^2 + z^2)}{M^4 r_s^2} \left(\frac{df}{dr_s}\right)^2. \tag{4.51}$$

Therefore we may choose the factor N (thereby M) arbitrarily large so as to substantially reduce the required energy density for the machine frame.

Looking at (4.43), the higher the charge and the potential, the lower the energy requirement. In the closed volume V of the machine shell one can inject a flow of electrons according to the constant ratios

$$\frac{\mu}{\rho} = \frac{\sum_{\text{V}} e}{\sum_{\text{V}} m}\,.$$

We see that the leptonic electron lightweight has the capacity to lower the negative energy even further.

The negative energy supply is fnally expressed by

$$\left[\Delta\Phi + \frac{1}{c}\partial_t \boldsymbol{A}\right]\Delta\Phi + \mu\Phi = \frac{c^4}{8G} \frac{\mathrm{v}_s^2 (x^2 + z^2)}{\left(1 + \frac{\Phi\mu}{\rho c^2}\right)^4 r_s^2} \left(\frac{df}{dr_s}\right)^2. \tag{4.52}$$

Part III

5 The generalized Gödel metric

5.1 Dynamics of the fluid

The splitting shell/inner part of the spacecraft frame, is really the hallmark of the theory here. It implies that the proper time τ of the inner part of the machine is not affected by the term

N. We now set the machine to follow the trajectory $y_s(t)$ *tangential* to a CTC beyond the Gödel radius r_G. Hence, we may write down the Gödel-Alcubierre metric that was generalized (3.3) in the following form

$$ds^2 = e^{2U(1-f)} \left\{ \left[\left(1+\frac{\Phi\mu}{\rho}\right)^2 - \mathrm{v}_s^2 f^2 \right] c^2 dt^2 - \right.$$
$$- \left[f - \frac{1}{2}(1-f)\, e^{2x} \right] dy^2 - \tag{5.1}$$
$$\left. - 2\left[\mathrm{v}_s f + (1-f)\, e^{x} \right] c\,dt\,dy - dx^2 - dz^2 \right\}.$$

The shell of the machine has a volume V and the total energy required for the propulsion along y is

$$E = -\int_{\mathrm{V}} \frac{c^4}{32\pi G} \frac{\mathrm{v}_s^2 (x^2+z^2)}{\left(1+\frac{\Phi\mu}{\rho c^2}\right)^4 r_s^2} \left(\frac{df}{dr_s}\right)^2 . \tag{5.2}$$

From the machine's perspective, the space-time can be regarded as *globally hyperbolic* since for $f = 1$, it is always defined by the metric (4.43) and the occupant of the machine will never know whether he moves along a CTC.

In the absence of charge, beyond R_e (i.e., where $R > R_e$ and $R \to \infty$), we have $f = 0$ implying $M = 1$ outside of the machine and we thus retrieve Gödel's original modified metric (3.3) in this case.

It is now easy to determine the acceleration of the flow lines carrying the machine.

Let us revert to equation (2.1bis)

$$\sigma_{\alpha\mu} = u_{(\alpha;\mu)} - \frac{1}{3}\,\theta h_{\alpha\mu} - \omega_{\sigma\mu} - {}^{*}u_{(\alpha}u_{\mu)} = 0\,, \tag{5.3}$$

$${}^{*}u_{(\alpha}u_{\mu)} = -\left(u_{[\alpha;\mu]} + {}^{*}u_{[\alpha}u_{\mu]}\right) - \frac{1}{3}\,\theta h_{\alpha\mu} + u_{\alpha;\mu}\,. \tag{5.4}$$

In our case, the scalar expansion is

$$\theta = \mathrm{v}_s \frac{df}{dr_s} \frac{y_s}{r_s}\,,$$

see (4.17). In the equation (A7), see Appendix, we found

$${}^{*}u_{\alpha} = h_{\alpha\mu}\,\partial^{\mu} U,$$

therefore we have

$${}^{*}u_{\mu} h_{\alpha\mu} \partial^{\mu} U = -\left(u_{[\alpha;\mu]} + {}^{*}u_{[\alpha}u_{\mu]}\right) -$$
$$- \frac{1}{3}\, h_{\alpha\mu}\, \mathrm{v}_s \frac{df}{dr_s} \frac{y_s}{r_s} + u_{(\alpha;\mu)}\,. \tag{5.5}$$

This equation is fundamental: it displays all elements related to the dynamics of the fluid described by the Gödel-Alcubierre metric (5.1): the pressure and density of the fluid as function of its rotation along a flow line subjected to the Alcubierre local deformation.

5.2 A thermodynamic aspect

Consider a fluid that consists of n particles in motion within a given region. The primary variables are:

— The particle current

$$I^{\mu} = n u^{\mu}\,; \tag{5.6}$$

— The energy-momentum $T^{\mu\nu}$ and the entropy flux S^{μ}. These quantities are conserved

$$T^{\mu\nu}_{;\nu} = 0, \qquad I^{\mu}_{;\mu} = 0\,.$$

In a relativistic case, the second law of thermodynamics requires

$$S^{\mu}_{;\mu} \geqslant 0\,. \tag{5.7}$$

For equilibrium states we have

$$S^{\mu} = n s u^{\mu}, \tag{5.8}$$

where s is the entropy per particle. Denoting Q as the chemical potential and T the heat quantity of the medium, the Euler relation reads

$$n\,s = \frac{\rho + P}{\mathrm{T}} - \frac{\mathrm{Q}n}{\mathrm{T}}\,, \tag{5.9}$$

where ρ and P are respectively the density and pressure of the medium.

We also have the fundamental thermodynamic equation of Gibbs

$$\mathrm{T}ds = ds\,\frac{\rho}{n} + P d\left(\frac{1}{n}\right) \tag{5.10}$$

or

$$\mathrm{T}n ds = d\rho - \frac{\rho + P}{n} + dn\,. \tag{5.11}$$

From (5.9), we get

$$S^{\mu} = -\frac{\mathrm{Q}I^{\mu}}{\mathrm{T}} + \frac{(\rho + P)u^{\mu}}{\mathrm{T}}\,. \tag{5.12}$$

Since in the rest system, the matter energy flux must vanish, we have

$$u_{\lambda} T^{\lambda\mu} = \rho u^{\mu} \tag{5.13}$$

and thus, we find the following expression for the entropy vector in equilibrium

$$S^{\mu} = -\frac{\mathrm{Q}I^{\mu}}{\mathrm{T}} + \frac{u_{\lambda}T^{\lambda\mu}}{\mathrm{T}} + \frac{P u^{\mu}}{\mathrm{T}}\,. \tag{5.14}$$

Let us consider our machine moving along a Gödel trajectory. We obviously neglect the chemical potential of the machine's bodyframe as well as the pressure and the entropy vector reduces to

$$S^{\mu} = \frac{u_{\lambda}T^{\lambda\mu}}{\mathrm{T}}\,. \tag{5.15}$$

This vector must be measured by the Eulerian observer which travels along the trajectory tangent to u^{λ} and (5.15) becomes

$$(S^{\mu})_{\mathrm{E}} = \frac{(u_{\lambda})_{\mathrm{E}}\,(T^{\lambda\mu})_{\mathrm{Al}}}{\mathrm{T}}\,. \tag{5.16}$$

Keeping in mind our definition of the Eulerian velocity

$$(u^{\mu})_{\rm E} = \left[cM^{-1},\, {\rm v}_s f cM^{-1},\, 0,\, 0\right], \tag{5.17}$$

$$(u_{\lambda})_{\rm E} = [cM,\, 0,\, 0,\, 0]\,, \tag{5.18}$$

and since we are interested in the entropy scalar part we have

$$(S^0)_{\rm E} = \frac{(u_0)_{\rm E}\,(T^{00})_{\rm Al}}{\rm T} \tag{5.19}$$

with

$$(T^{00})_{\rm Al} = -\frac{c^4}{32\pi G}\,\frac{{\rm v}_s^2\,(y^2+z^2)}{M^4 r_s^2}\left(\frac{df}{dr_s}\right)^2, \tag{5.20}$$

$$(u_0)_{\rm E} = cM\,. \tag{5.21}$$

We clearly see that the entropy $(S^0)_{\rm E}$ of the system attached to the machine is seen negative with respect to the Eulerian observer which measures a "negentropy". While travelling to the past, the occupant of the machine experiences a positive entropy, i.e., he is ageing in his own proper time.

5.3 The voyage home

The above analysis has been extended to the backwards time travel as initially detailed by Gödel. Once this voyage is completed, the machine should be able to return to its own epoch. Therefore, the reversed oriented loop is obviously to be envisaged although it should be emphasized that it does not represent a future travel.

To this end it is useful to refer to our publication [20], where we recalled that the Einstein tensor is derived from the second Bianchi identity verified by the Riemann tensor $R_{\alpha\beta\nu\gamma}$. A particular form of the latter is described by the *Landau-Lifchitz superpotential*

$$H^{\alpha\beta\nu\gamma} = -g\left(g^{\alpha\nu}g^{\beta\gamma} - g^{\beta\nu}g^{\gamma\alpha}\right) \tag{5.22}$$

The second order tensor

$$H^{\alpha\beta\nu\gamma}_{\;\;,\beta\gamma} = \partial_\beta\left\{\partial_\gamma\left[-g\left(g^{\alpha\nu}g^{\beta\gamma} - g^{\beta\nu}g^{\gamma\alpha}\right)\right]\right\} \tag{5.23}$$

is a special choice of the Ricci tensor in which all first derivatives of the metric tensor vanish at the considered point. The corresponding field equations read

$$H^{\alpha\beta\nu\gamma}_{\;\;,\beta\gamma} = \frac{16\pi G}{c^4}\left[-g\left(T^{\alpha\nu} + t^{\alpha\nu}_{\rm L-L}\right)\right], \tag{5.24}$$

where $T^{\alpha\nu}$ is the energy-momentum tensor of matter with its gravitational field described by the *Landau-Lifchitz energy-momentum pseudo-tensor* $t^{\alpha\nu}_{\rm L-L}$

$$\begin{aligned}(-g)\,t^{\alpha\nu}_{\rm L-L} = \frac{c^4}{16\pi G}\Big\{&\boldsymbol{g}^{\alpha\nu}_{\;,\lambda}\boldsymbol{g}^{\lambda\mu}_{\;,\mu} - \boldsymbol{g}^{\alpha\lambda}_{\;,\lambda}\boldsymbol{g}^{\nu\mu}_{\;,\mu} + \frac{1}{2}\,g^{\alpha\nu}g_{\lambda\mu}\,\boldsymbol{g}^{\lambda\theta}_{\;,\rho}\boldsymbol{g}^{\rho\mu}_{\;,\theta} - \\ &- \left(g^{\alpha\lambda}g_{\mu\theta}\,\boldsymbol{g}^{\nu\theta}_{\;,\rho}\boldsymbol{g}^{\mu\rho}_{\;,\lambda} + g^{\nu\lambda}g_{\mu\theta}\,\boldsymbol{g}^{\alpha\theta}_{\;,\rho}\boldsymbol{g}^{\mu\rho}_{\;,\lambda}\right) + g_{\mu\lambda}\,g^{\theta\rho}\,\boldsymbol{g}^{\alpha\lambda}_{\;,\theta}\boldsymbol{g}^{\nu\mu}_{\;,\rho} + \\ &+ \frac{1}{8}\left(2g^{\alpha\lambda}g^{\nu\mu} - g^{\alpha\lambda}g^{\lambda\mu}\right)\left(2g_{\theta\rho}g_{\delta\tau} - g_{\rho\delta}g_{\theta\tau}\right)\boldsymbol{g}^{\theta\tau}_{\;,\lambda}\boldsymbol{g}^{\rho\delta}_{\;,\mu}\Big\},\end{aligned}$$

where $\boldsymbol{g}^{\alpha\nu} = \sqrt{-g}\,g^{\alpha\nu}$.

In this way, the right hand side of (5.24) is conserved

$$\partial_\nu\left[-g\left(T^{\alpha\nu} + t^{\alpha\nu}_{\rm L-L}\right)\right] = 0\,.$$

Besides equation (5.24), there exists a second field equation having the form

$$H^{\alpha\beta\nu\gamma}_{\;\;,\gamma\alpha} = \frac{16\pi G}{c^4}\left[-g\left(T^{\beta\nu} + t^{\beta\nu}_{\rm L-L}\right)\right]. \tag{5.25}$$

A quick inspection at (5.22), shows that field equations (5.24) and (5.25) differ from a sign and are linked by a common index but they are not necessarily symmetrical. The intertwined metrics are

$$ds^2 = g_{\mu\nu}\,dx^\mu dx^\nu, \tag{5.26}$$

$$^{(-)}ds^2 = -g_{\mu\lambda}\,dx^\mu dx^\lambda. \tag{5.27}$$

In our case, the time coordinate $x^0 = ct'$ is chosen to be the cosmic time-axis of the expanding universe described by the positive metric (5.26). It is then pertinent to identify x^0 with the common index

$$ds^2 = g_{0\nu}\,dx^0 dx^\nu, \tag{5.28}$$

$$^{(-)}ds^2 = -g_{0\lambda}\,dx^0 dx^\lambda. \tag{5.29}$$

The Gödel solution (3.18) corresponding to (5.27) can be expressed by

$$\begin{aligned}^{(-)}ds^2 = -4e^{2U}\Big[&dt'\,(2\sinh r - 1)^2 - dr^2 + \\ &+ \left(\sinh^4 r - \sinh^2 r\right)d\theta^2 + 2\sqrt{2}\,\sinh^2 r\,d\theta\, dt'\Big].\end{aligned} \tag{5.30}$$

One notices that t' is negative which means that the trajectory of the machine derived from (5.30) is reversed with respect to the one resulting from the solution (3.18). Starting from the point p (see Fig. 2 on page 19) the machine reaches the Gödel radius r_G for $\sinh r = 1$, while it is still being governed by the equation (5.30). As soon as $r = 0$ after crossing the plane containing r_G, then ds^2 becomes positive again and reconnects to the cosmic time t' at the departure point q. In order to come back to its epoch, our machine can then legitimately exploit the second field equation whose solution is given by (5.30).

Conclusions

When Gödel introduced his metric, he was led to introduce a distinctive constant factor a in order to retranscript the field equations with a cosmological constant along with additional constraints. Our theory is free of all theses constraints and moreover, it provides a physical meaning to the a term.

The Gödel space-time is no longer a cosmological model but a limited domain wherein takes place the dynamics of a physical fluid which retains all basic properties related to closed time-like curves. The modified Gödel metric can be locally replicated and this fact naturally sheds new light on time travel possibility.

Our theory, which relies on the Alcubierre metric propulsion, has some similarities with the one suggested by B. Tippett and D. Tsang (University of British Columbia, Okanagal and MacGill University, Montreal, respectively). The essence of their paper is to describe an Alcubierre bubble which travels backwards and forwards along a loop in flat space-time [21]. In this geometry, the bubble is referred to as a *Traversable Achronal Retrograd Domain in Space-Time* or TARDIS, in short. The TARDIS is also an acronym for *Time and Relative Dimensions in Space*, a fictional hybrid of a time machine and spacecraft that appears in the British science fiction television series *Doctor Who* and its various spin-offs. See also [22].

Historically, it seems that the first model exhibiting CTCs was pioneered by the German mathematician C. Lanczos, assistant to Einstein in 1924 [23] and later re-discovered in 1937 in an improved form by the Dutch physicist W. J. Van Stockum [24].

A typical example of a time machine was first proposed in 1974 by the American F. J. Tipler, Prof. of Physics at the Tulane University, New Orleans [25]. It describes an infinitely long massive cylinder spinning along its longitudinal axis which gives rise to the *frame dragging effect*. If the rotation rate is fast enough the light cones of objects in cylinder's vicinity becomes tilted. Tipler claimed that a finite cylinder could also produce CTCs which was objected by S. Hawking who argued that any finite region would require negative energy and at the same time, vacuum fluctuation mechanism would impede any attempts to travel in time [26]. Several authors have however challenged this last conclusion and rejected Hawking's statement [27, 28].

At the same time, travelling backwards in time highlights many paradox problems. Among them is the well-known *grandfather paradox*: a person travelling to the past and causing the death of his ancestor beforehand is thus never born and it would not be possible for him to undertake such an act in the first place. In fact, you can not fix your issues by travelling back in time: you go back in time to prevent something that happened in the past and arrive just before the event. You race to stop it, yet in doing as such, directly or indirectly cause it to happen in the first place. This can be illustrated by the predestination paradox where a billiard ball is sent in the past through the time machine:

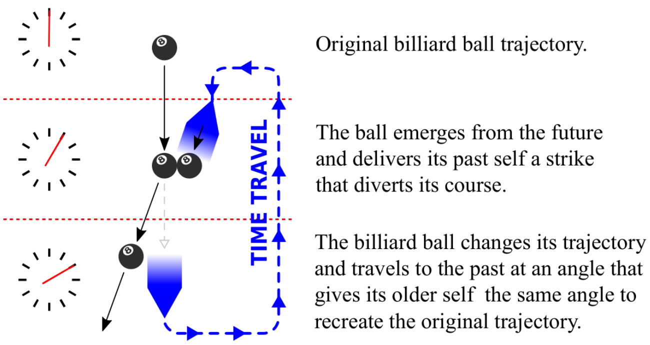

Fig. 4: The predestination paradox where a billiard ball is sent in the past through the time machine.

In other words one cannot change the past (at least major events): this is confirmed by the famous *Self Consistency Principle* introduced in 1990 by the physicist I. Novikov [29]. The principle asserts that if an event exists that would cause a paradox or any change to the past whatsoever, then the probability of that event is zero. This principle does not exclude the predestined fate of our history if some actions from the future would have marked the successive events of our evolution.

A typical example is the so-called *writer's paradox*, when the inventor of the time machine sends his calculations to a selected scientist in his own past. The question naturally arises: who could be this scientist?

Fig. 5: Albert Einstein and Kurt Gödel at the Princeton Institute for Advanced Study, Princeton, New Jersey, December 5, 1947. Photo by Oskar Morgenstern.

Submitted on January 1, 2005

References

1. Gödel K. An example of a new type of cosmological solutions of Einstein's field equations of gravitation. *Review of Modern Physics*, 1949, v. 21, no. 3, 447–450.
2. Marquet P. Gödel's universe revisited. *Progress in Physics*, 2014, v. 10, no. 4, 259–262.
3. Straumann N. General Relativity and Relativistic Astrophysics. Springer-Verlag, 1984.
4. Barnes A. On shear free flows of a perfect fluid. *General Relativity and Gravitation*, 1973, v. 4, 105–129.
5. Marquet P. The exact Gödel metric. *Progress in Physics*, 2021, v. 17, no. 2, 133–138.
6. Eisenhart L.P. Space-time continua of perfect fluids in general relativity. *Trans. Amer. Math. Soc.*, 1924, v. 26, 205–220.
7. Synge J.L. Relativistic hydrodynamics. *Proc. London Math. Soc.*, 1937, v. 43, 376–416.

8. Lichnerowicz A. Les Théories Relativistes de la Gravitation et de l'Electromagnétisme. Masson et Cie, Paris, 1955.
9. Landau L., Lifshitz E. The Classical Theory of Fields. Addison-Wesley, Reading, 1962.
10. Arnowitt R., Deser S., Misner C. Dynamical structure and definition of energy in general relativity. *Physical Review*, 1959, v. 116, no. 5, 1322–1330.
11. Kuchar K. Canonical methods of quantization. In: *Quantum Gravity 2: A second Oxford symposium*, Clarendon Press, Oxford, 1981, 329–374.
12. Wald R. General Relativity. University of Chicago Press, 1984.
13. Alcubierre M. The warp drive: hyper fast travel within General Relativity. *Classical and Quantum Gravity*, 1994, v.11, L73–L77.
14. Natario J. Warp drive with zero expansion. arXiv: gr-qc/01.10086 (2002).
15. Marquet P. The generalized warp drive concept in the EGR theory. *The Abraham Zelmanov Journal*, 2009, v. 2, 261–287.
16. Kramer D., Stephani H., Hertl E., Mac Callum M. Exact Solutions of Einstein's Field Equations. Cambridge University Press, 1979.
17. Marquet P. Geodesics and Finslerian equations in the EGR theory. *The Abraham Zelmanov Journal*, 2010, v. 3, 90–100.
18. Loup F., Waite D., Halerewicz E. Jr. Reduced total energy requirements for a modified Alcubierre warp drive spacetime. arXiv: gr-qc/010.70975 (2001).
19. Loup F., Waite D., Held R., Halerewicz E. Jr., Stabno M., Kuntzman M., Sims R. A causally connected superluminal Warp Drive spacetime. arXiv: gr-qc/020.2021 (2002).
20. Marquet P. Twin universes confirmed by General Relativity. *Progress in Physics*, 2022, v. 18, no. 1, 89–94.
21. Tippett B.K., Tsang D. Traversable achronal retrograd domain in spacetime. arXiv: gr-qc/1310.7985 (2013).
22. Marquet P. Gödel Time travel with warp drive propulsion. *Progress in Physics*, 2022, v.18, no. 1, 82–88.
23. Lanczos C. Über eine Stationäre Kosmologie im Sinne der Einsteinischer Gravitationstheorie. *Zeitschrift für Physik*, 1924, Bd.21, 73–110.
24. Van Stockum W.J. The gravitationnal field of a distribution of particles rotating around an axis of symmetry. *Proc. Roy. Soc. Edinburgh*, 1937, v.57, 135-154.
25. Tipler F.J. Rotating cylinders and the possibility of global causality. *Phys. Rev. D*, 1974, v. 9, no. 8, 2203–2206.
26. Hawking S.W. Chronology protection conjecture. *Phys. Rev. D*, 1991, v. 46, no. 2, 603–610.
27. Kim Sung Won, Thorne K.S. Do vacuum fluctuations prevent the creation of closed time-like curves? *Phys. Rev. D*, 1991, v. 43, no. 12, 3029–3947.
28. Li Li-Xin. Must time machines be unstable against vacuum fluctuations? arXiv: gr-qc/9703024 (2006).
29. Friedmann J., Morris M.S., Novikov I., Echeverria F., Klinkhammer G., Thorne K.S., Yurtzever U. Cauchy problem in space-times with closed time-like curves. *Phys. Rev. D*, 1990, v. 42, no. 6, 1915–1930.
30. Hawking S.W., Ellis G.F.R. The Large Scale Structure of Space-Time. Cambridge University Press, 1973.

Appendix

The 4-unit vector u^μ is normalized on $(\mathrm{M}, \boldsymbol{g})$

$$g_{\mu\nu}\, u^\mu u^\nu = g^{\mu\nu} u_\mu u_\nu = 1.$$

By differentiating it we get

$$u^\nu\, \nabla_\mu\, u_\nu = 0\,. \tag{A1}$$

Let us define the vector L_ν by the relation

$$\nabla_\mu\, P\, \delta^\mu_\nu = \mathbf{r}\, L_\nu \tag{A2}$$

having set $\mathbf{r} = \rho c^2 + P$.

The conservation law for $T_{\mu\nu} = \mathbf{r}\, u_\mu u_\nu - P g_{\mu\nu}$ is expressed by $\nabla_\mu\, T^\mu_\nu = 0$ or

$$\nabla_\mu\, (\mathbf{r}\, u^\mu u_\nu) = \mathbf{r}\, L_\nu\,, \quad \nabla_\mu\, (\mathbf{r}\, u^\mu)\; u_\nu + \mathbf{r}\, u^\mu\, \nabla_\mu\, u_\nu = \mathbf{r}\, L_\nu\,. \tag{A3}$$

Multiplying through this relation with u^ν and taking into account (A1), after substituting it into (A3) and then dividing by $\mathbf{r}$, we obtain

$$u^\mu\, \nabla_\mu\, u_\nu = \left(g_{\mu\nu} - u_\mu u_\nu \right) L^\mu \tag{A4}$$

or

$$^*u_\nu = h_{\mu\nu}\, L^\mu. \tag{A5}$$

Setting $L_\nu = \partial_\nu\, U$, the equation (A5) takes the form $^*u_\nu = h_{\mu\nu}\, \partial^\mu\, U$ and (A2) reads

$$\left(\rho c^2 + P \right) L_\nu = \nabla_\mu\, P\, \delta^\mu_\nu\,, \quad L_\nu = \frac{\partial_\nu P}{\rho c^2 + P}\,.$$

As a result we find

$$U = \int_{P_1}^{P_2} \frac{dP}{\rho c^2 + P}\,.$$

The flow lines of the fluid everywhere tangent to the vector u^μ are determined by the differential system (3.15)

$$u^\mu\, \nabla_\mu\, u_\beta = \left(\delta^\alpha_\beta - u^\alpha u_\beta \right) \partial_\alpha U\,.$$

These flow lines are time-like geodesics of the conformal metric

$$\mathscr{A} = s' = \int_{S_1}^{S_2} e^U\, ds\,. \tag{A6}$$

The 4-vector

$$^*u_\nu = h_{\mu\nu}\, \partial^\mu U \tag{A7}$$

must be regarded as the 4-acceleration $^*u_\nu$ of the flow lines given by the pressure gradient orthogonal to those lines; see [30, p. 70].

LETTERS TO PROGRESS IN PHYSICS

Does the Macroworld Need Quantum Mechanics?

Anatoly V. Belyakov

Tver, Russia. E-mail: belyakov.lih@gmail.com

In a series of articles, the author explained some phenomena and calculated a number of parameters related to the microworld using the non-quantum methods of the geometrodynamics (introduced by J. A. Wheeler). Thus, the nature of the electric charge has been revealed, its value and the proton/electron mass ratio have been calculated, the light quarks mass have been determined, etc. This publication gives a short survey of the obtained results.

Initial provisions

Developing an adequate physical model of the microworld is a primary task. The Standard Model of fundamental interactions (SM) is replete with abstractions that are understandable only to a few theorists. Over the last century, many researchers attempted to construct physical models of the microroworld based on non-quantum methods. Currently, despite some positive results obtained in this field, these results are not yet recognized by the scientific community.

However, contrary to the generally accepted views on the impossibility of adequately representing the microworld phenomena with visual images and analogies from the reality surrounding us, such analogies undoubtedly exist, since the basic physical laws are reproduced at various large-scale levels of the organization of matter. And if non-quantum methods can explain at least some of the microworld phenomena, then this will remove the mystery layer from it, allow us to look at microphenomena from a different angle and accelerate progress in their study and understanding.

The author has solved this problem to some extent, and this is proven by the definition of many properties and parameters of the microworld, and, unlike the works of other researchers, the author's model made it possible to determine many more of the mentioned parameters, moreover, using simpler methods. To solve this problem, the author's physical model was based on:

a) A mechanistic interpretation of John Wheeler's geometrodynamic, where the materiality of space itself is postulated, and the initial one-dimensional spatial elements are vortex structures that can form a continuous two-dimensional network [1] and then, when deforming, three-dimensional objects are formed [2–4]. Charged microparticles according to Wheeler are special points on the three-dimensional surface of our world, where, for example, a proton and an electron are connected by a "wormhole" or a vortex current tube of the drain-source type in an additional dimension. As a result, a *closed contour* is formed which the material environment circulates along;

b) The concept of elementary particles as unipolar vortices with a funnel on the surface (*analogous to a fermion*, conventionally along the X-axis in our world) and a vortex thread under the surface in depth (*analogous to a boson*, conventionally along the Y-axis in an additional dimension), which, according to a well-known physical analogy, spirally fills the current tube with an electron radius r_e. These forms, during oscillations, can transform into each other. Fermions retain part of the boson mass, bringing in a half spin. Boson masses cannot be stable in principle, as well as their physical analogues — vortex formations in a continuous medium, if they do not lean on the phase boundary. The boson mass is one-dimensional one and proportional to the vortex tube length. The bosons vortex elements rotate relative to the longitudinal axis with a circumferential velocity v_0, determined from the balance of dynamic and magnetic forces (see below). This velocity is constant, does not depend on the rotation radius, so many bosons can be located coaxially, that is, in one place;

c) The existence of a "hidden" mass, which in one way or another introduces *gravity into the microworld*, no matter whether it is an additional dimension, a "wormhole" or simply a topological feature, which for an external observer is some additional degree of freedom associated with electromagnetism; it is this that determines the electron charge and spin.

In this model, the electron volume with mass m_e and radius r_e is taken as an element of the mentioned material medium, and the quantity that replaces the charge in the well-known formulas of Coulomb and Ampere is $m_e c$; then the electric and magnetic constants ε_0 and μ_0 in the Coulomb-free form take the form:

$$\varepsilon_0 = \frac{m_e}{r_e} = 3.233 \times 10^{-16} \text{ kg/m}, \tag{1}$$

$$\mu_0 = \frac{1}{c^2 \varepsilon_0} = 0.03441 \text{ 1/N}. \tag{2}$$

Thus, ε_0 becomes the linear density of the vortex tube, and μ_0 becomes the value of the inverse centrifugal force, and the formulas for electrical, magnetic, gravitational and dynamic (inertial) forces are written as:

$$F_e = \frac{1}{\mu_0}\left(\frac{r_e}{r_0}\right)^2 z_{e_1} z_{e_2}\,, \tag{3}$$

$$F_m = \frac{1}{\mu_0}\frac{l}{2\pi r_0}\left(\frac{r_e}{c\times[\text{sec}]}\right)^2 z_{e_1} z_{e_2}\,, \tag{4}$$

$$F_g = \frac{1}{\mu_0}\frac{1}{f}\left(\frac{r_e}{r_0}\right)^2 z_{g_1} z_{g_2}\,, \tag{5}$$

$$F_i = \frac{1}{\mu_0}\frac{r_e}{r_0}\left(\frac{\upsilon_0}{c}\right)^2 z_g\,, \tag{6}$$

where υ_0, r_0, l, z_e, z_g, f are, respectively, the circumferential velocity, circumferential radius or distance between vortex tubes, the length of a vortex tube (thread) or contour, the relative values of charge and mass in the charges and masses of an electron, and the electrical forces to gravitational forces ratio, equal to $c^2/\varepsilon_0\gamma$.

The balance of these forces leads to the emergence of structures that are necessary for the microworld and beyond. Based on the model, the microworld properties are unexpectedly easily and naturally clarified and important parameters are calculated, which proves the complete correspondence of the model to physical reality. The most important results have been the determination of the electron nature and its charge nature [5], as well as other parameters that *were not explained or calculated by quantum methods within the SM framework*, namely: the proton/electron mass ratio [6], the proton structure and the quarks mass [6, 7], the neutrino mass [8], etc.

The electron charge

The **electron charge** in a simple mechanistic interpretation of Wheeler's idea becomes proportional to the amount of medium motion along the vortex current tube contour, the spin, accordingly, to the angular momentum relative to its longitudinal axis, and the magnetic interaction between conductors is analogous to the forces acting between vortex current tubes.

Assuming a charge to be a momentum, we are convinced that many bizarre electrical and magnetic dimensions are simplified in a striking way and take on a meaningful and physically obvious form: the current strength becomes simply a force [kg × m/sec^2] or [N], the potential — a velocity [m/sec], the capacitance — the mass of electrons accumulated on the capacitor plates [kg], the conductivity — the mass velocity [kg/sec], the inductance — the value reciprocal of the mass acceleration [sec^2/kg], the magnetic field strength — the mass acceleration [kg/sec^2], the solenoid magnetic induction — the winding density of its turns [1/m], etc. [9].

Moreover, the established nature of the charge reveals the Boltzmann constant and temperature essence. It is known the exact value k_B to give by the ratio of Planck's constant to the speed of light and the electron charge, $k_\text{B} = h/ce_0$, but the reason for this is not clear, since the dimension of k_B is completely different. However, if we consider the electron charge as a momentum, then the dimension of k_B becomes [sec], which is equal in magnitude to the time it takes light to travel the distance close to the electron size. Then the temperature dimension turns out to be physically understandable and obvious, namely, the microparticles chaotic motion kinetic power [J/sec].

To determine the **charge magnitude** e_0, it is sufficient to introduce a unit of potential (velocity υ) in the Coulomb-free system

$$1\ [\text{m/sec}] = \frac{m_e \upsilon^2}{e_0}\,, \tag{7}$$

and for the contour with the maximum energy of a single charge write:

$$\upsilon\ [\text{m/sec}] = \frac{m_e c^2}{e_0}\,. \tag{8}$$

It is necessary to take into account that the charge magnitude and other microworld parameters are projected from the additional dimension onto our three-dimensional world surface with distortions at a certain angle q. In the work [5] this angle is determined, and it almost exactly coincides with the Weinberg mixing angle in weak interaction $q_\text{W} = 28.7°$. As a result, the observed electron charge magnitude, taking into account (7) and (8), is equal to:

$$e_0 = m_e c_0^{4/3} \cos q_\text{W} \times [\text{m/sec}] = 1.602\times 10^{-19}\ \text{kg}\times\text{m/sec}, \tag{9}$$

where the dimensionless speed of light is $c_0 = c/[\text{m/sec}]$.

Since the charge (momentum) is by definition equal to $M\upsilon$, then in (9) the first factor is the contour mass $M = 4.48\times 10^5\ m_e$, and the second is the vortex current tube longitudinal velocity $\upsilon = 4.48\times 10^5$ m/sec. A contour having an energy $M\upsilon^2$, which is equal to the energy of a "point" electron $m_e c^2$ (i.e. at the point where the contour intersects our world surface) can be called "standard", for it $n = 4.884$; but here and below the parameter n does not have any special quantum properties, but simply determines the contour size.

The "hidden" mass of the standard contour approximately corresponds to the W, Z-bosons total mass. Therefore, it can be stated that the vortex tube of current is formed by three vortex threads rotating around a common longitudinal axis. These threads necessarily have right, left, and the last, obviously double, total zero rotation. They can be associated with the vector bosons W^+, W^-, Z^0.

In the work [5] the indicated thermodynamic constants of Boltzmann, Wien, Stefan-Boltzmann are determined, if we correlate the energy of a "point" electron per photon $m_e c\upsilon/z$ with the energy of thermal motion kT (the average energy of the radiation oscillator) for some characteristic conditions; and it is also established the unit oscillator energy $k_\text{B} b/\lambda_\text{C}$ at the Compton wavelength to be equal to the kinetic energy of the electron rotating along a circular trajectory, $2m_e(c/\pi)^2$.

Thus, the identification of the electron nature at the same time establishes its connection with both the weak interaction in the SM and the molecular-kinetic properties of atoms and molecules.

The proton/electron ratio

The **proton/electron ratio** is determined on the basis of the adopted model of microparticles and the proton-electron contour. As shown in [5], for any contour with an arbitrary quantum number n, with constant values of the electric and magnetic constants, charge and spin, the contour mass, its length, velocity and radius of the vortex thread, filling the contour tube, in units of m_e, r_e and c have the form:

$$M = m_y = l = (an)^2, \tag{10}$$

$$v = \frac{c_0^{1/3}}{(an)^2}\,, \tag{11}$$

$$r = \frac{c_0^{2/3}}{(an)^4}\,, \tag{12}$$

where a is the inverse fine structure constant.

Note that by analogy with natural vortex structures (in the case of the formation of subsequent spiral structures of radius r inside of a contour tube of radius r_e), the vortex thread can be extremely "compressed", i.e. shortened by a multiple of $1/r$. In this case, its mass-energy in units of $m_e c^2$ will be

$$L = lr = \frac{c_0^{2/3}}{(an)^2}\,, \tag{13}$$

or, conversely, extremely "stretched", i.e. extended by a multiple of $1/r$.

It is assumed that the contour to contain structural units (waves or photons), and their number z is the ratio of the "stretched" contour total length to the wavelength λ. In [5], the number of photons in the contour is determined, and in the standard contour $z \approx a = 137$, and for the case of contour decay (ionization) for the transition $n \to \infty$ the number of photons $z \approx n^4$.

In this model, the elementary particle has both point (intersection region) and wave properties, since the vortex funnel creates ring waves or second-order contours on the surface, which one can assign proper quantum numbers to that determine other parameters in accordance with formulas (10–13). In [6] it is defined:

$$\text{for a proton} \quad n_p = \left(\frac{2c_0}{a^5}\right)^{1/4} = 0.3338, \tag{14}$$

$$\text{for an electron} \quad n_e = \left(\frac{2c_0}{a^5}\right)^{1/8} = 0.5777. \tag{15}$$

It is accepted that a one-dimensional boson thread in the process of oscillations along the Y-axis is capable of packing extremely tightly into a fermion form along all four degrees of freedom, increasing the fermion relative linear size along the X-axis proportionally to $l_y^{1/4}$ and, as shown in [6], as a result, any i-th fermion mass in relation to the electron mass is determined by the ratio:

$$m_i = \left(\frac{n_e}{n_i}\right)^{14}. \tag{16}$$

For a proton, $m_p = (n_e/n_p)^{14} = 2160$, and the proton boson mass $(an_p)^2 = 2092$ is almost equal to its fermion mass, which is one of the conditions of its stability (the difference in values is due to simplifications in the formula for n) and, when corrected by the cosine of the Weinberg angle, it almost exactly coincides with the relative mass of the proton $2092\cos q_\text{W} = 1835$.

Zitterbewegung, i.e. electron oscillations with amplitude λ_C are revealed by a simple non-quantum method, without recourse to solving the Schrödinger equation, since the parameter n_e determines the electron contour length $l_y = (an_e)^2$, which envelops three inscribed circles with diameter d_y, which the vortex threads rotate inside; this also confirms the three-zone structure of the electron, noted in [10]. From geometric considerations it follows:

$$d_y = \frac{(an_e)^2 \sin 60^\circ}{2\pi} = 863.8\, r_e \quad \text{or} \quad 2.43 \times 10^{-12}\ \text{m}, \tag{17}$$

which exactly corresponds to the Compton wavelength.

Three generations of elementary particles naturally exist in this model, since a microparticle is considered as a contour itself, therefore any contour connecting charged particles can be likened to a particle included in a larger contour, assuming the mass of the smaller contour to be the mass of a hypothetical fermion (a proton analog) for the larger one. Thus, interconnected contours can exist. For the contour of the third generation and the last, extremely excited one, $v \to 1$, $r \to 1$ and $n = 0.189$.

The structure of the photon

The **structure of the photon**, as well as various virtual abstractions of quantum theory in the SM (such as quarks, partons, color, confinement, etc.) in this model naturally acquire physical content or become unnecessary [6].

A proton in a proton-electron contour as a special (singular) point is the place where the medium flow crosses the boundary between the regions X (fermions) and Y (bosons), where, by analogy with liquid or gas flows, phase inversion occurs and the medium parameters acquire critical values. It is clear that in the critical section their densities are compared.

Assuming the volume of fermions to be a sphere $w_x = (r_x)^3$, and the one-dimensional volume of the boson thread to be a cylinder $w_y = r^2 l_y$ and equating their densities, we obtain the quantum number belonging to the critical section, $n_q = 0.480$. This averaged parameter can be attributed to a certain particle — a quark, existing only in the region of the phase transition.

In accordance with (24) its mass $m_{qx} = 12.9$, which is the total mass, since the ratio of the boson mass of the electron to the boson mass of the proton, bearing in mind (10), $M_e/M_p = (n_e/n_p)^2 = 3.0$. That is, to satisfy the conditions of continuity of the flow and constancy of the charge in any critical section, the general contour flow must split in the proton region into *three parts* and *reverse circulation currents must arise*, i.e. there, in the proton, must be zones with different charge signs, as shown in Fig. 1:

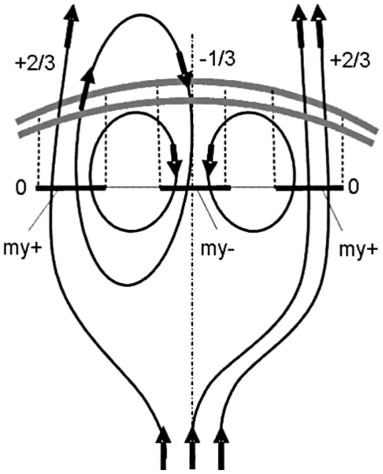

Fig. 1: A scheme of the proton: distribution of the current lines inside the proton.

In fact, quarks should be associated with stable ring currents containing, as follows from Fig. 1, one or two closed unit contours intersecting three critical sections. Therefore, the quark masses are 1/3 or 2/3 of the total mass, i.e. $4.3\,m_e$ and $8.6\,m_e$, which coincides with the masses of light quarks. The phenomenon of confinement or "non-escape" of quarks seems self-evident, since in this model the proton has no constituent parts, it only has the peculiarities of its structure.

Thus, the proton internal structure is characterized by a set of parameters that find their virtual analogues in the SM: vector bosons (three vortex threads connecting the proton and electron in an additional dimension), fractional charge (projection of current lines onto the outer surface of the proton), quarks (ring currents), "color" (three different critical sections), antiquarks and "anticolor" (opposite to the direction of currents and rotation of vortex tubes), partons (zones of increased velocity pressure), mesons (pairs of boson tubes with a total mass of $\sim 270\,m_e$). Here they all find their physical representation [6, 7]. The proposed proton structure in the form of a unique configuration of field lines does not require the existence of a "sea" of virtual quarks and gluons.

The **anomalous magnetic moment of the proton** is also explained in [6]. By definition, μ_p = (charge×velocity×path). This product agrees well with the known value of μ_p if we take the velocity to be υ, the path to be πr, and calculate these parameters using (11) and (12) with the proton parameter n_p.

The neutrino mass

The **neutrino mass** is determined by *introducing gravity into the microworld*, whose rôle is erroneously denied in the SM. Neutrinos are released in weak interaction processes, for example, in the case of *e*-capture; in this case, quarks and vector bosons participate in the process, but even in this complex case there is a macroanalogy — something similar to the charge and spin separation — a phenomenon recorded in ultra-thin conductors [11]. In the applied model [8], all virtual participants find a physical correspondence.

Let us recall that here the electron does not rotate around the proton and is not "smeared" over the orbits, while the proton-electron contour exists due to the *gravimagnetic balance*, when $F_m = F_g$, from which it follows in units of r_e:

$$L_x = l\,r = \frac{z_{g_1} z_{g_2}}{z_{e_1} z_{e_2}} \,(2\pi\gamma\rho_e) \times [\mathrm{sec}^2], \tag{18}$$

where the value L, according to (13), is the mass-energy of the compressed contour, z_{g_1} is the mass of the proton active part (i.e. the quark) entering the circulation contour, z_{g_2} is the electron mass, ρ_e is the electron specific density, equal to m_e/r_e^3.

In the work [8] it is shown when particles to approach each other at a certain distance, the contour connecting them transfers energy-momentum to the proton internal structure, losing charge, deforms and reorients into the Y-region, releasing in the form of a one-dimensional neutrinos vortex tube, carrying away the electron spin. This occurs under the condition the quark mass-energy to reach the Y-vortex tube mass-energy in its compressed state, formula (13). At the same time $r_x = l_y$, see Fig. 2. This makes it possible to determine the neutrino quantum parameter n_υ.

As a result, in [8] it was obtained

$$n_\upsilon = \frac{c_0^{1/9}(2\pi\gamma\rho_e \times [\mathrm{sec}^2])^{1/3}}{a} = 1.643, \tag{19}$$

and then, according to (16), the neutrino fermion mass is determined

$$m_\nu = \left(\frac{n_e}{n_\nu}\right)^{14} = \left(\frac{0.5777}{1.643}\right)^{14} = 4.39\times10^{-7}\ (0.225\ \mathrm{eV}). \tag{20}$$

Next, the quark mass $m_q = 8.84\,m_e$ (4.51 MeV) was calculated, which agrees well with the previously calculated quark mass when considering the proton structure, and in general it agrees with the **d-quark mass** (4.8 MeV); and the mass-energy of the X-contour $L_x = 1.51\times10^5$ (77 GeV) was calculated, which turns out to be close to the ***W*-bosons mass** (80 GeV), see Fig. 2. See [12] for more detail. Moreover,

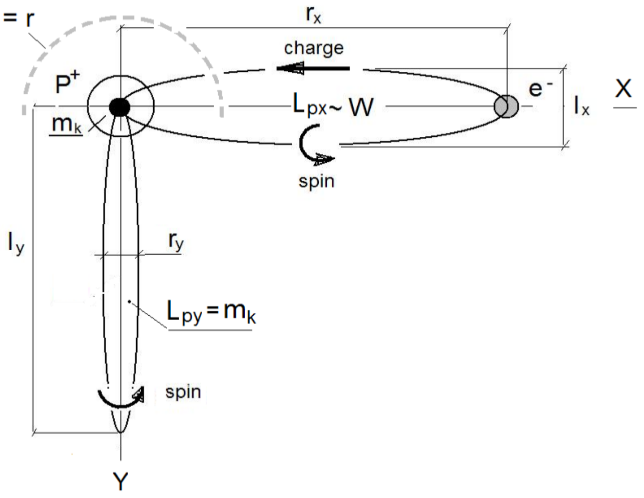

Fig. 2: Scheme of formation of the neutrino.

in [8] exactly the same neutrino mass value was obtained as the gravitational mass, i.e. as the value $z_{g_1} = z_{g_2} = z_g$, when considering the contour consisting of a pair of closed vortex threads having the Planck size $r_\hbar = (\hbar\gamma/c^3)^{1/2}$ and each having 1/4 of the electron charge

$$m_\nu = z_g = \frac{c_0^{1/6} r_\hbar^{1/4}}{(32\pi\gamma\rho_e \times [\text{sec}^2])^{1/2}} = 4.31\times10^{-7}\ (0.220\ \text{eV}). \qquad (21)$$

Thus, two different neutrino states with identical masses were obtained — at the moment of birth in the form of a vortex Y-tube fermionic part and in its final state in the closed structure form having a gravitational mass. Such duality, as shown in [8], possibly explains **neutrino oscillations**.

The obtained values of the neutrino mass are consistent with the estimate of Adam Moss and Richard Battye, where the upper limits on the sum of neutrino masses are about 0.320 ± 0.081 eV [13].

The **difference in the proton and neutron masses, the neutron lifetime and energy of beta decay**, which are undetermined in the SM, are found due to the gravimagnetic balance, which allows the contour to have various configurations and, when the proton passes into the neutron, to become axisymmetric at the intersection of the regions X and Y, see Fig. 2. Then, with equal axes, its relative length and mass are equal to $c_0^{2/9}$. In [6] it is shown the symmetric contour, replacing the quark contour, to increase the nucleon mass by the desired value:

$$\Delta m = r\left(c_0^{2/7} - \frac{m_q^{9/7}}{2}\right)\cos q_{\text{W}} = 2.53\, m_e\,, \qquad (22)$$

here r is the electron vortex thread radius, determined by (16) at n_e.

The **lifetime of a neutron** is determined by the time of deformation and decay of the same symmetrical contour due to the proper rotation of the vortex threads relative to the longitudinal circular axis, which gives the time constant $\pi l/v_0$, where v_0 is determined from the *magnetodynamic balance* at $F_m = F_i$ and is a fundamental constant. For unidirectional vortex threads, taking into account (4) and (6), at $z_{e_1} = z_{e_2}$ and at $z_g = l/r_e$:

$$v_0 = \frac{r_e}{(2\pi)^{1/2}\times[\text{sec}]} = 1.12\times10^{-15}\ \text{m/sec}, \qquad (23)$$

then the time constant for $\pi l = \pi c_0^{2/9}$ has the form:

$$\tau = 2^{1/2}\pi^{3/2} c_0^{2/9} \times [\text{sec}] = 603\ \text{sec}. \qquad (24)$$

The obtained value agrees with the half-life of the neutron $\tau_{1/2}$. By definition, $\tau_{1/2} = \ln 2 \times \tau_n$, where τ_n is the neutron lifetime; its value is 878.5 sec [14], then $\tau_{1/2} = 609$ sec. In [6], this time is also determined in another way.

In *beta decay*, the energy of the excited contour is transferred to the electron and antineutrino released in this process. The paper [6] provides examples of calculating the beta decay energy E_β, which by definition is the ratio of the acquired momentum (charge) square to the released particles mass. In particular, for the highest of beta decay (for isotopes) energy value, it was obtained

$$E_{\beta\,(\text{lim})} = \frac{c_0^{1/3}\cos q_{\text{W}}}{18} = 32.6\, m_e c^2\ (16.7\text{MeV}). \qquad (25)$$

Indeed, the highest value of E_β among various isotopes was recorded for the 12N → 12C transition (16.6 MeV), which coincides with the value (25) calculated within the framework of this model.

The model of the atomic nucleus

The **model of the atomic nucleus** is continuously updated, and various hypotheses about its structure are still being put forward. And here, at the level of the atomic nucleus, the non-quantum method demonstrates its applicability and effectiveness [15].

The **coupling constant** a, which in the SM determines the intensity of the exchange of specific quanta between microparticles, actually indicates the bonds strength between the elements of the proton structure (quarks) and is determined by the formula:

$$a_s = \frac{m_e c_0^{2/3} v_0^2/r_e}{\gamma m_e^2/r_e^2} = 26.25, \qquad (26)$$

where the ratio of the inertial forces arising from the rotation of the boson mass of a standard contour vortex tube of radius r_e with the circumferential velocity v_0 and acting toward the periphery to the gravitational forces acting between masses of size m_e at a distance r_e can serve as an equivalent of the coupling constant. In this case, coupling particles (π-mesons) are not needed.

The proton has a complex structure, therefore the interaction energy increasing, i.e. "deepening" along the proton Y-axis and, accordingly, decreasing the distance between quarks, it is perceived by an external observer as a nuclear forces changing.

At *low energies* of interacting particles (small "depth" along Y), the peripheral inertial forces exceed the attractive forces, so the quarks are weakly bound to each other, can move away from their original position and interact with the quarks of nearby nucleons.

At *high energies* ($\sim$100 GeV, a large "depth" along Y), the attractive forces hold the quarks within the nucleon, which reduces the microparticles interaction efficiency with each other. In [15], a_s were calculated, which coincide with the values accepted for these types of interactions [16].

The **radius of the proton** is calculated at $a_s = 1$, when there is a balance between the forces of attraction and the peripheral forces of inertia. From (26), assuming that the quarks are located at the corners of an equilateral triangle, at $m = m_e$ and $r = r_e$ we obtain

$$r_p = \frac{(8\pi\gamma\rho_e)^{1/2} \times [\text{sec}]}{3^{1/4} c_0^{1/3}} = 0.297, \quad \text{i.e.}\ 0.836 \times 10^{-15}\ \text{m}, \tag{27}$$

which exactly coincides with the proton charge radius value (0.833 femtometers, with an uncertainty of ±0.010 femtometers [17]). Thus, **nuclear forces** as a special interaction may not exist at all. At high energies and small distances, when the internal structures of nucleons overlap, the interaction between nucleons occurs *within their common quark bag* between quarks with charges $+1$ and -1 at a distance equal to the quark vortex tube size r_q. Outside the quark bag, the Coulomb interaction takes place between fractional charges of different signs located *on the nucleons outer surface*. The attractive potential decreases sharply in this case, for protons — proportionally to the product $\frac{1}{3} \times \frac{2}{3}$.

In [15, 18], the depth of the attractive potential for single charges, the binding energies for the deuteron, tritium, tetraneutron and alpha particle were calculated. At the same time, within the SM framework, these quantities are almost impossible to calculate. For example, the authors of the work studying the tetraneutron (see [18]) admit that "*More recent state-of-the-art theoretical calculations have concluded that without altering fundamental characteristics of the nuclear forces, the tetraneutron should not be bound. More theoretical calculations were performed, all of them agreeing that a bound tetraneutron is not supported by theory*".

Within the framework of the proposed model, these parameters are calculated because it takes into account the quarks mass-energy's changing in accordance with the contour size, the distance between quarks or charges, and the geometry of objects. Moreover, for example, the binding energy of an alpha particle (28.2 MeV) was determined in two ways — on the basis of the quark masses and on the basis of the quarks energy, see Fig. 3 [15]:

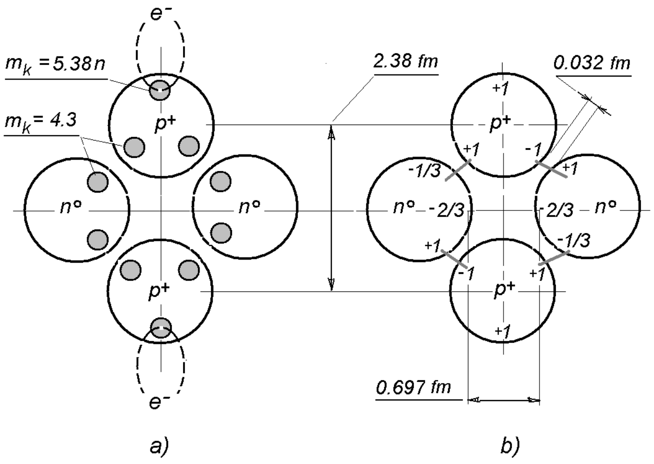

Fig. 3: Settlement scheme of the alpha particle: a — on the basis of the quark masses, b — on the basis of energy of the quarks.

Atomic nuclei are the system of nucleons and alpha clusters that are in dynamic equilibrium [19]. Their packing density in the nucleus increases toward the center, since electrons located in more distant orbits are associated with protons located at nucleus deeper levels, while the distance between the vortex tubes of the $p^+ - e^-$ contours decreases and their length increases, formula (18); thus, *layers or shells similar to electron ones are formed in the nucleus*.

Since r cannot be less than the alpha particle size $1.42\, r_e$ (4 fm), this limits the number of the shell whose electrons can bind to protons included in alpha clusters. In [15] it is shown that the *fourth layer or shell is the last one in the nucleus*; alpha clusters are not formed closer to the center of the nucleus. A similar condition for the nucleon size also determines the largest possible atom electron shell number and, if $r \leqslant 2r_p$, then $n_{\max} \geqslant 8$. As calculated in [15], the alpha particle maximum energy is achieved during the transfer of energy from protons located in the nucleus center, which are bound to the last seventh shell (27.5 MeV), which exactly coincides with the maximum energy value of alpha particles determined in the study of the fission of heavy nuclei [20].

Also, in the work [15] the stable isotope of lead detailed calculation was performed, which gave its exact mass $A = 207$. It turned out that for elements heavier than lead, protons associated with electrons of the fifth and subsequent electron shells no longer completely "fit" into the nucleus core, limited by the fourth filled shell. With an increase in the number of protons, the fourth nuclear shell expands, additional neutrons are included in it, and the nucleus radius increases. Neutrons that are not included in clusters (for ${}_{82}\text{Pb}^{207}$ there are 65 such neutrons) are located in the remaining free volume, being forced out into the outer shells.

In [15] a relation was obtained between the number of nucleons in the nucleus core and in the adjacent shell, which the nuclear density of nucleons in them is the same at. This *homogeneity condition* is observed very precisely for lead: 22 nucleons in the core correspond to 64 nucleons in the 4th shell (32 protons and 32 neutrons) and also approximately for xenon, neodymium, iron and for some other elements, and that for the nuclei of such elements the observed *electric quadrupole moments are close to zero* [21]. For lighter nuclei, the core can be considered the volume of the inner shell, including protons and neutrons.

So the reason for the deviation of the electric charge distribution in the atomic nucleus from spherically symmetrical is the non-uniformity in the "packing" of nucleons inside the atomic nuclei, so for most elements their nuclei can have a non-spherical shape. In addition, to fill the outer nuclear shells, neutrons are usually insufficient, and for some nuclei their outer shell must shrink, lose the spherical layer shape and take the polyhedron shape, in the corners of which alpha clusters are located [22].

It is interesting that the obtained homogeneity condition makes it possible to calculate the number of protons Z and neutrons N for superheavy elements of the hypothetical "island of stability". Thus, if we accept that the fourth shell is replenished with neutrons up to the number of nucleons necessary to fill the fifth shell, i.e. up to $2\times2\times25 = 100$, then, according to the homogeneity condition, it turns out that for such an element $Z = 112$, $N = 184$. The latter just coincides with the expected "magic" number N, which was proposed by physicist Vitaly Goldansky in 1966.

The **binding energies of nuclei** in this model (in contrast to the well-known semi-empirical Weizsäcker formula) are calculated with no less accuracy, without resorting to empirical coefficients. It is determined by the mass-energy of nucleon quarks 4×2.2, all proton quarks included in the $p^+{-}e^-$-circulation contours $2.75\,(m_1{+}2m_2{+}3m_3{+}\dots)$ and the energy of the potential barrier (the energy of the first unfilled shell) $2.75\,z$. The final sum has the form:

$$E_n = 8.8\,z_p + 2.75\,(m_1 + 2m_2 + 3m_3 + \dots + z)\ \text{MeV}, \quad (28)$$

where z_p is the number of protons in the first to fourth shells, z is the total number of protons, m_i is the number of electrons in the i-th shell of the atom, 2.2 is the mass-energy of one quark in MeV.

The **mass number** is calculated based on the energy balance and using the already obtained relationships:

$$A = z_p + 0.625\,(m_1 + 2m_2 + 3m_3 + \dots - z) + (4)_{A<140}\,. \quad (29)$$

For A, in some cases, a correction is necessary that takes into account the presence of four alpha-cluster nucleons on the first shell, which are split off when the nucleus reaches a certain mass. In [15], actual and calculated data on the binding energy and mass numbers for stable isotopes of some elements are given according to formulas (28) and (29), where their good agreement is obvious.

The gravitational constant

The **gravitational constant** is calculated based on the scheme of a single radiation cell of a surface transverse-longitudinal wave, where a medium with an arbitrary mass m circulates along the toroid contour of radius R and at the same time has a spiral rotation with a radius r relative to the toroid longitudinal annular axis [23].

Circulation along R occurs under the action of gravitational forces with acceleration υ^2/R, and spiral rotation with r — under the action of surface tension forces with acceleration υ^2/r. The components of the surface wave are logically correlate to longitudinal gravitational waves and transverse electromagnetic waves. The ratio of electrical forces to gravitational forces is $c^2 r_e/\gamma m_e$, and it will be such when the elements of the medium circulate along the contour with the largest radius R with the lowest speed and spirally rotate with the smallest radius r with the highest speed, which gives the corresponding equality.

For the transverse component $\upsilon = c$, and the smallest dimension r is the diameter of the circumscribed circle around three Planck dimensions $r_\hbar$. For the longitudinal component, the smallest velocity and the largest radius (length of the contour) are determined by formulas (11) and (10) with the use of the largest quantum number $n_m = 390$, determined from (19) under the condition that the entire proton mass $m_p/\cos q_\text{W}$ is involved in the circulation contour. As a result, the following formula is obtained:

$$\gamma = \left(1 + \frac{2}{3^{1/2}}\right)^{\frac{2}{13}} a^{1/13} c_0^{16/39} \left(\frac{\cos q_\text{W}}{2\pi m_p}\right)^{\frac{12}{13}} w_e \left(\frac{c}{r_e}\right)^{\frac{2}{13}} \times \\ \times [\text{sec}^{-24/13}], \quad (30)$$

where w_e is the specific volume of an electron, equal to r_e^3/m_e.

The **speed of light** was determined in [24] using the well-known equation for the wave speed on the liquid surface as applied to the above-mentioned radiating cell (toroid), where the first term in the equation reflects the influence of gravity on the wave speed (parameter g), the second — the influence of surface tension (parameter σ)

$$\upsilon^2 = \frac{g\lambda}{2\pi} + \frac{2\pi\sigma}{\rho\lambda}\,. \quad (31)$$

A gravitational wave is a compression deformation of the surface wave longitudinal component and its length can be determined by taking $\upsilon = c$; in [23] from (31) it is derived (the positive radical expression is taken)

$$\lambda = \frac{\pi r_e a^6 n^6}{c_0^{2/3}} \left[1 + \left(1 - \frac{4c_0^{2/3}}{a^2 n^2 m_p}\right)^{1/2}\right]. \quad (32)$$

Within the parameters of the contour $n = 1\dots\ n_m$, the wavelength is very large (here the parameter n determines the physical size of the radiating cell, in contrast to the proton-electron system), and the wave becomes effectively longitudinal one with negligible electromagnetic "capillary ripples" (the second term under the root in (32) tends to zero). Since longitudinal waves are the result of gravitational forces, they can be considered gravitational waves.

This is confirmed by the discovery of gravitational waves by the LIGO and VIRGO collaborations [23]. On February 11, 2016, oscillations with the frequency of 30–500 Hz were detected, which corresponds to wavelengths of 600,000–10,000,000 m [25, 26]. And these results correspond exactly to the middle of the range of circulation cell emissions at $n = 115$–180.

The cosmological constant

The **cosmological constant** Λ, its origin and nature remain a subject of discussion to this day [27–29]. It defines non-Newtonian gravitational forces and characterizes the curvature of empty space, as if additional mass or energy were introduced into it, and has a dimension of m^{-2}.

However, Λ can be determined taking into account in the Universe to be some constant vortex motion of particles relative to each other, and to be the rotation of unidirectional vortex threads (bosons) with the circumferential velocity v_0, caused by magnetogravitational equilibrium, see formula (23). It creates the background component of energy, which has not attracted any attention of physicists until now. This rotation introduces additional energy into the vacuum, which can be likened to a kind of cosmic "Brownian motion" creating pressure on the "walls" of space (which is perceived by an external observer as the manifestation of non-Newtonian forces) and must be compensated by gravitational forces [30]. The *balance of pressures* from these forces is

$$\frac{M\varepsilon_0\gamma}{L^3} = \frac{Mv_0^2}{L\Lambda^{-1}}\,, \tag{33}$$

The balance does not depend on the mass of the Universe M, but depends on its parameter L. The main parameter of the Universe L is determined in [4] from the *electromagnetic balance* and, provided that r is equal to the Bohr radius, i.e. the size of the most common hydrogen atom. Finally, the Universe's parameter L takes the following value

$$L = \frac{2\pi c^2}{R_\mathrm{B}} \times [\mathrm{sec}^2] = 1.06 \times 10^{28}\ \mathrm{m}. \tag{34}$$

In the end

$$\Lambda = \frac{\varepsilon_0\gamma}{(Lv_0)^2} = (2\pi)^{-1}\left(\frac{a}{c}\right)^4 \varepsilon_0\gamma \times [\mathrm{sec}^{-2}] = = 1.49 \times 10^{-52}\ \mathrm{m}^{-2}, \tag{35}$$

and such a value should correspond to the equilibrium state of the Universe. At present, based on the assumed age of the Universe, the value of Λ is estimated at 10^{-52} m^{-2} [31].

Conclusion

All the above results are obtained on the basis of the model that does not have any empirical coefficients, and the numerical results are ultimately the combination of fundamental quantities. Macroanalogies applied to the microworld in this model are similar to physical natural laws that are reproduced at various large-scale levels of matter organization. Thus, it is proven the microworld physical model can be built on the basis of existing physical realities without using the sophisticated mathematical apparatus of the Standard Model of Fundamental Interactions (SM), which inevitably masks the physical essence of phenomena with virtual abstractions. The new realistic model will provide an opportunity to look at microphenomena from a different angle and make them accessible to a wider range of researchers.

Submitted on December 12, 2024

References

1. Dewitt B.S. Quantum Gravity. *Scientific American*, Dec. 1983, v. 249, 112–129.
2. Peano G. Sur une courbe, qui remplit toute une aire plane. *Mathematische Annalen*, 1890, v. 36, issue 1, 157–160.
3. Berera A., Buniy R.V., Kephart T.W., Päs H., and Rosa J.G. Knotty inflation and the dimensionality of spacetime. arXiv: 1508.01458.
4. Belyakov A.V. On the independent determination of the ultimate density of physical vacuum. *Progress in Physics*, 2011, v. 7, issue 2, 27–29.
5. Belyakov A.V. Charge of the electron, and the constants of radiation according to J. A. Wheeler's geometrodynamic model. *Progress in Physics*, 2010, v. 6, issue 4, 90–94.
6. Belyakov A.V. Macro-analogies and gravitation in the micro- world: further elaboration of Wheeler's model of geometrodynamics. *Progress in Physics*, 2012, v. 8, issue 2, 47–57.
7. Belyakov A.V. The substantive model of the proton according to J. Wheeler's geometrodynamic concept. *Progress in Physics*, 2021, v. 17, issue 1, 15–19.
8. Belyakov A.V. Determination of the neutrino mass. *Progress in Physics*, 2016, v. 12, issue 1, 34–38.
9. Belyakov A.V. On the uniform dimension system. Is there the necessity for Coulomb? *Progress in Physics*, 2013, v.9, issue 3, 142–143.
10. *New Scientist*, 1998, no. 2119, 36.
11. Jompol Y., Ford C.J.B., Griffiths J.P., Farrer I., Jones G.A.C., Anderson D., Ritchie D.A., Silk T.W., and Schofield A.J. Probing spin-charge separation in a Tomonaga-Luttinger liquid. *Science*, 31 July 2009, v. 325, no. 5940, 597–601.
12. Belyakov A.V. Gravity in the microworld. Progress in Physics, 2020, v.16, issue 1, 58–61.
13. Battye R.A., Adam M. Evidence for massive neutrinos from CMB and lensing observations. arXiv: 1308.5870, August 27, 2013.
14. Serebrow A.P. The Measurement of the neutron lifetime with the use of gravitational traps of ultra-could neutrons. *Uspekhi-Physics*, 2005, v. 175, no. 9, 905–923.
15. Belyakov A.V. Nuclear power and the structure of a nucleus according to J.Wheeler's geometrodynamic concept. *Progress in Physics*, 2015, v. 11, issue 1, 89–98.
16. Krivokhizhin V.G., Kotikov A.V. The structure functions of nucleons and the definition of the coupling constant of the strong interaction. *Particle Physics and Nuclear Physics*, 2009, v. 40, issue 7.

17. Bezginov N., Valdez T., Horbatsch M., Marsman A., Vutha A.C., Hessels E.A. A measurement of the atomic hydrogen Lamb shift and the proton charge radius. *Science*, 6 Sep. 2019, v. 365, issue 6457, 1007–1012.
18. Belyakov A.V. Calculating the Parameters of the Tetraneutron. *Progress in Physics*, 2017, v. 13, issue 2, 123–124.
19. Kadmensky S.G. Clusters in the Nucleus. Soros Educational Journal, 2000, issue 3.
20. Perfilov N.A., Romanov Y.F., Solovyov Z.I. Fission of heavy nuclei with the emission of longrange α-particles. *Physics-Uspekhi*, July I960, v. LXXI, issue 3.
21. Nuclear electric quadrupole moment. http://nuclphys.sinp.msu.ru/enc/e189.htm?ysclid=m61vt4e21c308850051
22. Dudek J., Curien D., Dubray N., Dobaczewski J., Pangon V., Olbratowski P., and Schunck N. Island of rare-Earth nuclei with tetrahedral and octahedral symmetries: possible experimental evidence. *Phys. Rev. Lett.*, 2006, v. 97, 072501.
23. Belyakov A.V. Space and gravity. Progress in Physics, 2023, v.19, issue 1, 50–54.
24. Belyakov A.V. On the speed of light and the continuity of physical vacuum. *Progress in Physics*, 2018, v. 14, issue 4, 211–212.
25. LIGO Scientific Coll. and Virgo Coll. Observation of gravitational waves from a binary black hole merger. *Phys. Rev. Lett.*, v. 116, 11 February 2016, 061102; arXiv: 1602.03837.
26. Blair D., Li Ju et al. Gravitational wave astronomy: the current status. arXiv: 1602.02872.
27. Weinberg C.S. The cosmological constant problem. *Reviews of Modern Physics*, 1989, v. 61, 1–23.
28. Carroll S.M. The cosmological constant. *The Living Reviews in Relativity*, 2001, v. 4, 1–56.
29. Yermolenko Yu. The cosmological constant problem. http://cdn.scipeople.ru/materials/55751/The_cosmological_constant_problem.pdf
30. Belyakov A.V. On the nature and values of the gravitational and cosmological constants. *Progress in Physics*, 2018, v. 14, issue 4, 233–235.
31. Borissova L., Rabounski D. Fields, Vacuum and the Mirror Universe. The 3rd revised edition, New Scientific Frontiers, London, 2023, Ch. 5, §5.4.

Krogh Quantum Gravity Explicitly Predicts Hubble Redshift Curve and JWST Findings without Expansion

John Howard Drake

6179 N Channing Lane, Meridian, ID 83646. E-mail: howarddrake@comcast.net

JWST finds too many galaxies, too bright, and mature, while surface brightness and angular diameter distance support Euclidean geometry without expansion. Redshift fits an exponential time decay equation perfectly, inconsistent with expansion. We propose a cosmology replacing GR with Krogh gravity theory, where gravity changes quantum vacuum rather than geometry. Using cosmological principle and gravity dependency of terms in governing differential equation, we solve for time variable potential since matter creation. Redshift occurs at emission at earlier potential and light speed. The exponential redshift equation is explicitly derived. It is not tired light. We predict wavelength of past spectral lines, which when measured reveal emission time. Using solved variable light speed, we integrate to calculate distance to present explicitly deriving new Hubble curve. No other cosmology can make this claim remaining free of *ad hoc* parameters. Gravity propagation begins after hot matter creation determining variable light speed, particle mass, and physical constants. Cooling is achieved by increasing mass with momentum conservation. Galaxies form over about 450 billion atomic years or 49 billion present years after CMB recombination surface of last scattering. Krogh gravity as updated remains consistent with successful GR tests and predicts testable new dynamics not predicted by GR. These include observed acceleration anomalies for Earth flybys, JUNO Jupiter orbiter, Pioneer Probe, superluminal galactic jet acceleration, galaxy dynamics, and faster black hole accretion. Spiral star paths explain MOND illusion and ring galaxy formation. JWST mature galaxies require older universe, while galactic jets confirm predicted past higher light speed. Required mass density supports prolific star formation. Many stars and galaxies are likely now dead or consumed by black holes, so invisible baryon mass is expected to be greater than visible mass.

1 Introduction

We propose a new cosmology framework without expansion based on revisions to General Relativity. For such a paradigm change to be accepted we must recognize that existing Big Bang cosmology based on General Relativity is not supported by recent JWST (James Webb Space Telescope) observations. Our new framework adopts Kris Krogh gravity theory removing inconsistencies without requiring any *ad hoc* parameters. The new gravity theory satisfies tests previously thought to confirm General Relativity. In addition, it makes new testable dynamic predictions that General Relativity does not. Despite the unquestionable success of General Relativity, it appears to have flaws in approach resulting in failures especially important as applied to the entire universe.

The cosmology we propose is not new to us. It was developed mostly about two decades ago, however until now remained unpublished. Since it replaces General Relativity and consensus Big Bang-based cosmology both accepted science for about a century, it was clear that a very compelling case was required for such a new paradigm to become accepted. The change at some point will also affect particle physics. Particle properties change with gravity potential, and according to Krogh theory energy no longer gravitates, therefore particle masses have no energy contribution to mass since General Relativity no longer applies. Since the new gravity theory is linked to quantum vacuum change rather than curvature of space, it is consistent with a quantum approach to gravity. Considering JWST findings, a new approach not in tension with observations but instead predicting them is due. We will show that our framework supports these observations. Compelling evidence justifies a new paradigm which is the purpose of this work.

To understand what we propose it will be necessary to have at least a working understanding of revisions to General Relativity adopted here from the work of Kris Krogh [1, 2]. This new cosmology framework would not have been possible without the Krogh gravitational theory with his new approach and perspective. We will not try to repeat here any complete discussion of the Krogh theory but will adopt important features and perspectives needed to develop a more rigorous cosmology solution. In some respects, the Krogh theory of gravity is presently incomplete in its published form notably that the original presentation does not include frame dragging predicted by GR and confirmed since by Gravity Probe B. This will be corrected and updated later but fortunately these changes will not affect our cosmology solution. We will provide further conclusions not mentioned in Krogh's original papers but useful in this discussion to support the cosmology.

In the Krogh approach, most physical constants including the speed of light change with the intensity of the gravity potential both locally and cosmologically for the entire universe over time. Krogh does not presently include how every physical constant varies, so the theory needs some additions for completeness. The most important addition we need is the universal gravity constant G. It turns out that for us to have a consistent cosmology solution including our new Hubble constant counterpart for the redshift versus distance relationship we require that the product GM be constant in an absolute sense even though it is a dimensional quantity. Since mass of bodies or particles are not constant with changing gravity potential in his theory, we require that G varies inversely with mass. Krogh concurs with this though using different arguments, so this addition is a necessary assumption we adopt here.

The Krogh gravity theory has outcomes consistent with GR for past successful predictions. It however has an entirely different perspective in its approach. GR was essentially developed with the view that all physics is local while the effect of gravity is to curve the geometry of space. Its effects extend everywhere in surrounding space time. Included in this perspective is the shrinking of measuring sticks and expansion of geometric space. The Big Bang cosmology rests on solutions to the entirety of space time essentially extending the locally based perspective to infinity. The present Lambda Cold Dark Matter consensus cosmology includes *ad hoc* gravity contributions from non-existent dark matter and dark energy for no other reason other than it would otherwise fail. We claim that the GR perspective still has remaining serious flaws when extended to the entirety of the universe. The most notable flaw is that it requires expansion of space at all where now we have evidence this cannot be the case despite the observed redshift.

In the Krogh theory physical measuring sticks still change as do emitted spectral wave lengths as the gravity potential changes in space or time, but space itself does not change. Space is defined only by mathematical coordinates which are absolute. Geometry of space is always flat, consists of nothing, and does not care what the gravity potential is. The vacuum as we know from quantum theory is not empty but teaming with virtual particles with fleeting existence. The vacuum does care what gravity potential is and its particles reflect the potential energy as does any real matter in space.

Applying a new viewpoint, the Krogh theory comes from the perspective that all physics depends on the entire universe. It is more Mach-like since inertia depends on the entirety of all gravitational mass. We cannot extend the apparent local constancy of speed of light to the entire universe over all time, but instead the light speed depends on the increasing size and location of the observable mass in the entire universe. The gravitationally observable universe has a very large but finite maximum size determined by the unknown extremely high primordial light speed at the matter creation epoch. We cannot observe radiation from anything further than the last scattering surface of the CMB. This observable radiation sphere is a small fraction of the volume of the gravitation observation horizon for all mass in the entire universe. The universe can never collapse because any location in the universe cannot be influenced beyond the symmetric finite gravity horizon sphere. Gravity gradients can only be from more local and nearby mass concentrations. All the above are automatic consequences coming as a direct result of the exact solution to the governing gravity equation. It is not based on speculations. We see that this perspective is entirely different from GR as applied to the whole universe.

With the Krogh perspective, gravity does not curve space time, but the gravity potential changes vacuum properties including particle energy and mass, speed of light and physical constants. In effect the laws of physics though similar are different at different locations and times. The particle mass increases while speed of light decreases in a manner such that the rest energy of the particles reflects any loss of potential energy. For this reason, energy not in the form of mass is not a source of gravitation as in GR since energy conservation arguments do not require it. We claim that photons are massless and not a source of gravity. Light is still redshifted in transit from mass sources because there is a light speed gradient associated with a gravity potential gradient.

All particles under the influence of a gravity potential, including vacuum virtual ones, change not only by increasing mass but also shrink in size as in GR theory. Similarly, there is a slowing rate of atomic time with increasing potential. We could say from this perspective that the vacuum particles are the carriers of the gravity potential. A gradient in potential is not a force, but apparently causes acceleration of masses due to their interaction with a quantum vacuum gradient. Apparently, the gravity potential field residing in space is a direct result of this interaction of matter with the quantum vacuum. The speed of light change results from changes in the vacuum state and gravity propagates at the same speed.

We see further from the new perspective that since particles shrink with increasing gravity potential, measuring sticks used to determine the distance between points in space also shrink. This is consistent with GR, but in the revised view we do not claim that space has shrunk with the sticks. If we use sticks to measure distance between points in space, where in our case potential is increasing negatively forever in time cosmologically, we would conclude that space is expanding, which is not the case.

If we use the wavelength of a spectral line in the current time and gravity potential it does not have the same length as a past much earlier emission. If we observe a distant spectral line and falsely assume it had the same wavelength as a local one, we would perceive that it has stretched in length, but in reality it was longer when emitted. When we measure the emitted length, it tells us the time of emission since we have the solution for how potential varies with time, we also know how light speed varies with time and can therefore calculate the distance from emission exactly by integration. This is a tremendous advantage of this perspective, which is testable and depends on only one free parameter, the average matter density, or the equivalent Hubble constant. Distance versus redshift is inherently non-linear without the need for dark energy. No competing cosmology can make this claim. We now have a perfect explanation for how the universe exists in flat Euclidean space while producing a redshift of spectral lines from the past without requiring tired light in transit or expansion.

Cosmologies based on GR Big Bang expansion have for many decades been the only cosmologies that could come close enough to satisfying observational tests, but only at the expense of introduction of *ad hoc* assumptions, which themselves have no empirical basis for existence were it not for the need for an acceptable cosmology outcome. These include inflation, dark matter, and dark energy, No one knows what these are or can verify their existence despite great expense invested.

The *ad hoc* entities needed to sustain Big Bang-based cosmologies remain as consensus for the sole reason that all previous alternatives have not withstood observational requirements. To some extent, the situation can be justified because we could not abandon the scientific need to understand the nature and history of our universe and working models were needed in order that research in this regard could continue. Cosmology cannot legitimately claim to fulfill the normal scientific process of adopting a hypothesis that is testable and predicting outcomes of observations. Instead, we have for the most part hypothesized things not proven but needed to sustain a working theory of cosmology. The current Lambda Cold Dark Matter consensus has so many *ad hoc* free parameters that it is little more than a curve fit of the observations rather than a prediction from theory. Without introduction of new unsupported parameters, the Big Bang model fails to adequately match observations. Cosmology is a science which does not support introduction of new experiments since we have only one universe. All events occurred in the past and we only observe the present location and time resulting in limited ability to test any theory.

We claim that our proposed cosmology framework has no *ad hoc* parameters. The only free parameters are primordial speed of light and average matter density of the universe. These are simply the initial boundary conditions necessary to apply the general solution of the governing gravity differential equation to the real universe. As it turns out the cosmology is only sensitive to average density if initial speed of light is sufficiently high. Average density determines the effective Hubble constant for the redshift versus distance but other effects on the dynamics of bodies in motion cause important changes in long time frames and high velocities such as in galaxy rotation. There is no longer any need for dark matter or dark energy within our new framework.

The cosmology must withstand observational tests including redshift versus distance and observed uniform smooth black body radiation from the CMB. The proposed framework has no *ad hoc* inflation like the Big Bang required to explain smoothness of CMB since the initial order of magnitude higher light speed would automatically smooth the background observed. The matter epoch must be hot in either case since particle creation can have no preferred inertial frame and is limited only by the speed of light. With a very high speed limit and no preferred direction, creation of particles inevitably results in a very hot plasma. If nucleosynthesis is involved extremely hot initial conditions are required. It can be noted that the universal light speed with no preferred direction establishes a universal rest frame based on the average velocity of zero as for the observed CMB background radiation.

Although matter is created hot it cannot remain so and still produce stars and galaxies. Prior to that it must cool to recombination temperature to produce a surface of last scattering for the observed CMB. There is no expansion as in the Big Bang to cool the universe rapidly, but instead all created particles will slow by conservation of momentum as the universal gravity potential increases. Mass of particles increases which requires their velocity to decrease. The result is cooling but it takes many Hubble times, far longer than the Big Bang. Particles not only have decreasing rest energy, but also decreasing kinetic energy. Eventually the last scattering surface becomes observable as the CMB after recombination temperature is reached and its spectrum is black body radiation not spectral lines. The emitted wavelength is far longer than expected because light speed is orders of magnitude higher. If we know the recombination temperature, we know both the light speed and the time, so we can again integrate for the current distance at today's light speed. It is observed as 2.7 K black body radiation proportional to light speed ratio at recombination temperature.

The solution is gravitationally stable but time dependent. It requires a finite age after the matter epoch. Finite age with a matter epoch is a condition also shared with any Big Bang-based cosmology. It should be pointed out here that finite age should be considered the only acceptable assumption for any cosmology, since we still have stars burning today and they have finite age. If matter were continually created to provide newer stars, then infinite age would produce infinite matter. Any notion of expanding space does not change the proportional density of dead stars. Similarly, we exclude any recycling star assumptions because the process could not be reversible. Infinite age would also make the CMB observation problematic. We do expect in our case that most stars are already dead or consumed by black holes because of the extremely old universe we predict.

With these arguments, only cosmologies with finite age can rationally be considered as candidates. This leaves us with the proposed framework we introduce here, or some variation of Big Bang-based concepts. The distinction between the two is that the Big Bang and General Relativity require that space is expanding and the cause of observed cosmological redshift. Furthermore, it requires that the finite age must not be greater than the time going back to the singularity where space vanishes. This limits the age to the classical Hubble time on the order of 13.8 billion years. Our new framework conversely requires that age is an order of magnitude greater, several Hubble times long, just to set up conditions we observe. It also has a cause for redshift vs distance relationships that are natural results of direct solutions to the governing gravity theory and integration of light speed since emission.

We claim especially from observations of the recently deployed JWST that the Big Bang cosmologies are no longer sustainable. We anticipated this would occur, since we have known our solution for over two decades before the telescope launch. It has long been unlikely that the Big Bang consensus could be broken without sufficient evidence to exclude it. One failure now clear is that massive mature galaxies have been observed by JWST including older generation stars and these structures did not have sufficient time to form since the Big Bang as reported by Labbe *et al* [3]. See also Asencio *et al* [4] showing that large galaxy clusters exist with mergers at excessive velocity for consensus cosmology. Since universe age is not severely limited in the proposed framework, these older mature galaxies and clusters are expected, and it is likely that others even older and more distant may be found depending only on the limits of the sensitivity of the telescope.

Another finding of the telescope is an unexpectedly high population of distant galaxies and the appearance that insufficient gas was available to produce the massive galaxies. The cosmology we propose requires far more baryon mass density providing more available mass for stars. Very distant black holes are found with insufficient time in the Big Bang context to form. In the proposed context there is adequate time and new dynamics associated with the revised gravity theory are in play for rapid accretion of matter into black holes. With the Krogh gravity model these high concentrations of mass still exist but are not totally black. Due to the cosmological gravity potential change we will show that entire galaxies will eventually be accreted into their center black hole.

While the above are features of age and available mass that exclude the Big Bang, other observations are available now which exclude expansion at all as a feature of the universe. Based on observed surface brightness with distance shown by Lovyagin *et al* [5] the universe appears consistent with normal Euclidean non-expanding space which is a feature of our cosmology. Similarly, the angular diameter distance appears to be Euclidean [5] which would exclude expansion. The unexpected massive galaxies appearing to be too small as seen by JWST are not unexpected in our cosmology with Euclidean geometry. These are just normal galaxies, not unlike the local ones we see nearby. Another feature of the universe long known is spatial flatness. This is inherent to the revisions to General Relativity adopted here from Krogh [1] . Gravitational lensing still occurs due to changes in refractive index from non-uniform mass distributions. It is not space curvature with this gravity model but refraction as in an optical lens due to light speed variation in space.

Finally, Marosi [6] extends the Hubble curve for higher redshifts versus distance including distant gamma ray bursts concluding that data perfectly fit an exponential equation with time for redshift of spectral lines. While this is normally associated with rejected past tired light proposals, we show this exact equation can be derived from time variation of gravity potential with our cosmology solution. It is not tired light. A further conclusion of Marosi is that the exponential form of the equation cannot be consistent with expansion. Laviolette [5] also performs several cosmology model tests showing that a tired light model is best of those studied. Our cosmology would perform the same as the tired light model. This becomes a strong confirmation of our proposed cosmology and a rejection of Big Bang expansion.

We conclude a case for exclusion of Big Bang expansion cosmologies creates a crisis in cosmology which requires a new paradigm as proposed in this new framework. Conversely, we see at least in these early stages that the proposed cosmology does not share any of the concerns identified with the Big Bang and makes promising testable predictions. There is much work needed to flesh out further analysis and perform extensive testing and modeling before this can become the consensus working model. There remain some details that need to be added before this can be considered a complete theory of the history of the universe which is why we choose to call it a new framework.

This requires the work of many others with necessary modeling and observational assets which we do not have. We strongly encourage others to participate within this framework and to propose additions or modifications. This work cannot move forward without the help of many experts having capabilities and assets up to the task. The solution has been developed with the knowledge of only a couple of now-retired contributors that are advancing in age. We believe that current cosmology has reached a crisis which cannot be fixed within the space expansion paradigm and those invested in that framework need to expand the scope of their efforts in another direction. Similarly, if we find this framework becomes accepted it may be time to reconsider efforts directed toward dark matter and dark energy.

2 Exact cosmology solution

To develop a more rigorous exact cosmology solution, we will begin with the Krogh [1] original governing equation for the gravitational potential. Although Krogh had a proposed solution for the universal time dependent cosmological gravity potential, it is only the asymptotic solution valid for late time epochs near the present. This approximate solution does not satisfy the governing differential equation. In the end his solution is fully adequate for most things we need, but it is useful to show the proof of his approximate solution previously not shown and fully understand its limitations and how it derives from the exact solution. The governing equation for the gravity potential given by Krogh is:

$$\nabla^2\Phi - \frac{1}{c^2}\frac{\partial^2\Phi}{\partial t^2} = 4\pi G\rho\,. \tag{1}$$

Our new cosmology framework derives directly from the application of this differential equation with appropriate assumptions and boundary conditions. The gravity potential Φ represents the resulting potential produced by the mass density ρ. Speed of light is c and gravity constant is G, but in accord with the Krogh gravity theory ρ, c, and G are all dependent on the gravity potential such that the differential equation is nonlinear. We first simplify the equation by assuming that the cosmological principle applies to the universe on large scales since it can be assumed for our purposes to have a uniform mass density everywhere in space at any given universal time.

The existence of a universal time since the beginning of matter creation is a necessary assumption to solve the equation with appropriate boundary conditions. Since we will end up primarily using only the asymptotic solution it should not make much difference if matter was created everywhere instantaneously. It is presumed that the matter epoch had to occur like a state change spreading almost instantaneously. It could for instance be an event such as a change from a false vacuum to a more stable present one.

Just as is the case for the Big Bang cosmologies, there is no detailed explanation for how matter creation occurred or what initiated it. In the context of this theory the primordial light speed had to be so large that even if matter creation began at some local point triggering a state change, the new state bubble would spread so fast that it would be nearly instantaneous. For our purpose then we assume matter was created everywhere in an infinitely large space. Since we assume the cosmological principle, spatial derivatives vanish, universal time is the only remaining independent variable. This eliminates the first term of the governing equation which results in an ordinary differential equation:

$$\frac{d^2\Phi}{dt^2} = -4\pi G\rho c^2\,. \tag{2}$$

The last three terms on the right are all dependent on the gravity potential so we need to apply the other requirements of the Krogh gravity theory to show the correct scaling relationships for these parameters before we can solve the equation. To simplify the equations further we will define the dimensionless gravity potential and what will be shown to be the equivalent Hubble constant as:

$$\phi = \frac{\Phi}{c_0^2}\,; \qquad H_0 = \sqrt{2\pi G_0\rho_0}\,.$$

We will generally use the subscript, 0, throughout to mean the value existing initially when the matter epoch occurred, where in the beginning there was no gravity potential before gravity had propagated over time. Parameters without the subscripts are the time dependent non-constant terms which depend on the gravity potential in accord with the tenets of the Krogh gravity theory. The newly defined equivalent Hubble constant will generally be shown with the subscript, 0, in equations primarily because we want it to be understood that it is in fact a constant with dimensions of inverse time. The solution of the governing differential equation will be dependent on the product of the Hubble constant and time which in effect is dimensionless time.

Atomic time itself depends on the gravity potential in accord with Krogh gravity theory so we must choose a fixed universe time that ticks at a uniform rate for the differential equation to have meaning. When we find the solution, we need to differentiate with respect to time to verify the solution. It is this universal time and not atomic time that is defined in the equation so when differentiating the solution to verify it satisfies the governing equation the product of Hubble constant and time must treat the Hubble constant as a true constant. The subscript definition reminds us to do this. Technically this also implies that the universal time is taken as the time clock rate that existed at matter creation so that the dimensionless time product cancels out the time units. The important thing is that the choice of linear universal time in differentiation or integration uses time units that are at the same epoch assumed for the Hubble constant.

When we address the problem of deriving the Hubble curve for distance versus redshift, we use the present epoch instead of the primordial one. This is convenient in that case because we are looking back from the present to the past emission time and will integrate the light speed forward to the present to determine the distance. We prefer also in this case to use a Hubble constant defined with the current definition of time units of measure. Note that our choice of how the Hubble constant is defined ends up requiring that the matter density of the universe is 4/3 of classical big bang expansion critical density. There is nothing critical here, however, since the choice simply uses the grouping of terms on the right-hand side of the equation which will end up being compatible with how the Hubble constant has been defined classically in the Hubble curve equation shown later.

Listed below we show the scaling of the terms in our differential equation with respect to the dimensionless gravity potential to be substituted into the final form. The speed of light and matter density are directly from the Krogh paper while the gravity constant G is scaled inversely to the density which we have determined is required and in agreement per discussions with Kris Krogh. Primarily what it means is that the mass charge equivalent to electric charge is also to be conserved and the Krogh theory is taken to be gauge invariant such that the laws of physics are the same at any epoch time:

$$c = c_0 e^{2\phi}\,; \qquad G = G_0 e^{3\phi}\,; \qquad \rho = \rho_0 e^{-3\phi}\,.$$

We can now substitute the defined scaling relationships and definitions for terms in the simplified governing equation to write an even simpler form below which includes only the unknown time-dependent dimensionless potential and constant linear universal time variables. The resulting equation is nonlinear but fortunately has an exact solution:

$$\frac{d^2\phi}{dt^2} = -2H_0^2 e^{4\phi}\,.$$

The exact solution below can be verified directly by differentiating the potential twice with respect to time and substituting the solved potential function into the right-hand side:

$$\phi = \frac{1}{2}\ln \operatorname{sech} 2H_0 t\,.$$

We also can substitute our solution for the potential into the scaling relationship for light speed to define the equation for the history of light speed with respect to time obtaining:

$$c = c_0 \operatorname{sech} 2H_0 t\,. \tag{3}$$

Figure 1 illustrates how the universal dimensionless potential varies with respect to the dimensionless time Ht. It is approximately $-Ht$ as was assumed by Krogh [1]. Figure 2 shows how the dimensionless ratio of light speed c/c_0 varies with universe age in Hubble times.

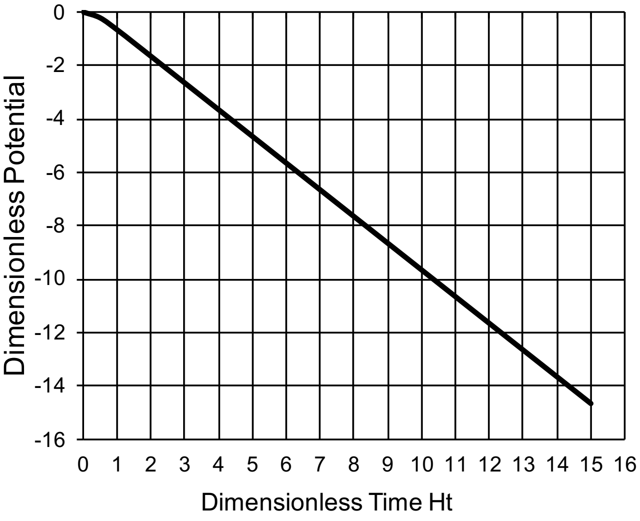

Fig. 1: History of Dimensionless Gravity Potential

Later when we develop the derivation of the Hubble curve resulting from our cosmology framework, we will use a simpler approximate asymptotic equation to integrate the light speed from emission since the exact solution is unnecessarily complex for late present epoch times. It is useful however to integrate the exact light speed solution from the matter creation epoch to the current time to show the size of the matter horizon from any point in the universe. This is in effect the size of the universe having any effect on any location in the universe. Understanding the enormous distance to the matter horizon is useful to get an understanding for how the average density of matter can be considered constant because it is averaged over a scale far larger than any structural clumping of matter can be. In effect the high light speed at the matter creation epoch was so high that it has a smoothing effect much like the concept of inflation in Big Bang cosmology. This distance is not observable by any means other than this expanding matter horizon is the cause of the present cosmological change in gravity potential. The distance R below from integration of light speed over the history of the universe is:

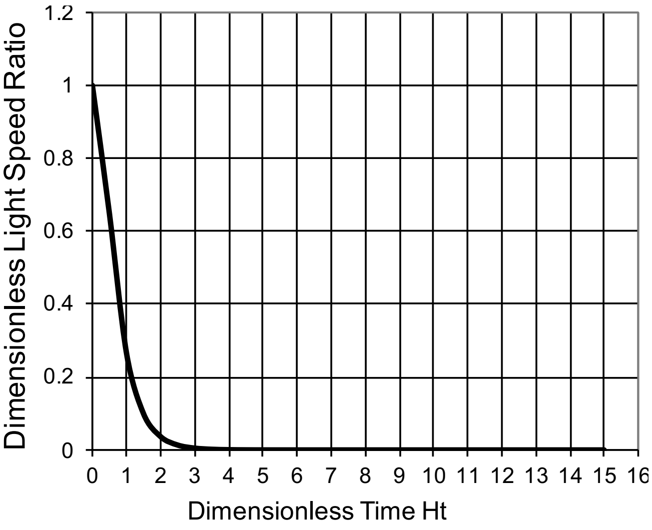

Fig. 2: History of Dimensionless Light Speed c/c_0

$$R = \frac{c_0}{2H_0} \arctan \sinh 2H_0 t\,. \tag{4}$$

Interestingly the matter horizon has a maximum radius which cannot be exceeded in infinite time. In the limit as time goes to infinity, the maximum distance light or gravity can travel is:

$$R_{max} = \frac{\pi}{4}\,\frac{c_0}{H_0}\,. \tag{5}$$

It is useful particularly since the primordial light speed is unknown to write the result in non-dimensional form. A plot of the dimensionless ratio of radius over the maximum possible radius, given by (8), is shown in Figure 3. It illustrates how the matter horizon growth causes continual change

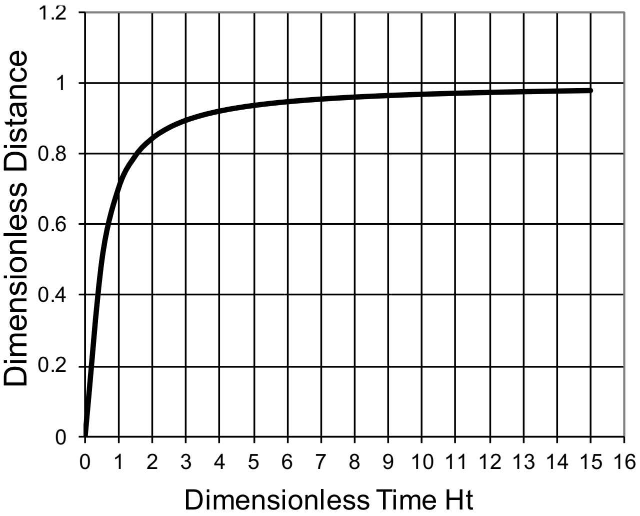

Fig. 3: History of Dimensionless Gravity Horizon

in universal gravity potential:

$$\frac{R}{R_{max}} = \frac{2}{\pi} \arctan \sinh 2H_0 t\,. \qquad (6)$$

3 Cosmological redshift types

Now that we have an exact solution for the history of the cosmological gravity potential which results from a matter creation epoch in flat non-expanding space, we can further explain cosmological redshifts which in the past have been the core support for the Big Bang notion that space is expanding in accord with General Relativity. We have adopted the Krogh gravity theory replacing GR where now the effect of gravity does not change the geometry of space but rather the quantum vacuum itself which in turn is fully in charge of the laws of physics, physical constants, light speed, particle mass, etc. Krogh in his original paper [1] defines how atoms residing in the cosmological potential of all the mass in the universe change their atomic spectral emissions. The light speed at emission is directly related to cosmological red shift in accord with scaling of energy at emission along with the associated light speed and gravitational potential. This derives from the Krogh energy equation, which defines energy of past emissions. This implies absolute frequency of emission is higher (blue shifted) at emission due to the lower gravitational potential and higher energy of atoms proportional to the square root of light speed, but the wavelength at emission is stretched in direct proportion to higher light speed. The net result is a red shift in proportion to the square root of light speed. Wavelengths are constant in transit over time at variable light speed since leading and trailing waves move at the same varying light speed. The resulting equation defining the net red shift of atomic spectral emissions with the usual definition for red shift factor z is:

$$\sqrt{\frac{c_e}{c_n}} = \frac{e^{\phi_e}}{e^{\phi_n}} = 1 + z\,. \qquad (7)$$

A second kind of redshift comes from the observed 2.7 K blackbody temperature of the CMB. In Big Bang cosmology, this is attributed to expansion of space since emission of a blackbody spectral distribution from the surface of last scattering began following recombination of electrons with atomic nuclei causing the plasma to become transparent following cooling. In the context of the proposed cosmology framework, there is no expansion of space and therefore no rapid cooling of hot primordial plasma is possible. In this case, we will show that cooling still occurs very slowly because all atomic particles are increasing in mass because of the increasingly negative universal gravity potential. To conserve momentum all moving particles will slow down as their mass increases. This is the cause of the observed Pioneer deceleration, so we have confirmation of such cosmological dynamics still occurring at the precent epoch. Since there was no preferred reference frame for the universe at the matter creation epoch, velocities of particles were universally distributed limited only by the speed of light. It is inevitable then that the beginning would be hot with such high particle velocities. We will discuss the changes in dynamics predicted by the Krogh theory of gravity in a later section, but for now we claim that cooling of the primordial plasma continued over many Hubble times before the recombination of atoms occurred to form a surface of last scattering in Big Bang-like fashion.

The blackbody emissions from the surface of last scattering are not associated with any specific spectral lines of atoms as was the case for the previous type of redshift of spectral lines, but instead is an apparent observed temperature obtained from the wavelength peak of a perfect blackbody curve. We need a different model for interpreting what is apparent redshift in the current cosmology framework. The longer wavelengths still occur at emission, but the governing equation is different. Blackbody radiation is defined by a distribution of wavelengths with a peak corresponding to the maximum energy flux. The wavelength at peak intensity for Planck blackbody radiation obeys Wien's law which has the known numerical solution:

$$\lambda_{max} = \frac{hc}{xkT}\,. \qquad (8)$$

We know x is a numerical constant and h and k are believed to be independent of gravity potential in the Krogh theory even though they are dimensional quantities. We see from the blackbody law that the peak wavelength depends only on the ratio c/T. Since the peak wavelength cannot change in transit to the observed blackbody temperature of 2.7 K and it was emitted at a presumed temperature of recombination normally taken as 3 000 K, we can write the relationship between light speed and temperature as:

$$\frac{c_e}{c_n} = \frac{T_e}{T_n}\,. \tag{9}$$

Since we know how light speed varies with the universal gravity potential, we can integrate for the distance to spectrally observed redshifted galaxies using (9) and the distance to the CMB from (11)

3.1 Derivation of Hubble curve

Since the exact solution for light speed variation includes the hyperbolic secant, it is unnecessarily complex for simple integration of the light speed to get distances from time of emission to the present observation of redshift based on observations when a much simpler exponential asymptotic solution approximation to the hyperbolic secant is extremely accurate for any emission later than a few Hubble times from the matter creation epoch. It takes many Hubble times to cool the primordial plasma to the recombination temperature for neutral atoms to allow a transparent interstellar space to observe any redshift or for that matter the CMB surface of last scattering beyond which nothing is observable. Thus for purposes of estimating distance versus redshift, we are justified in replacing the hyperbolic secant in the equation for light speed with the exponential asymptotic approximation:

$$c = c_0 \operatorname{sech} 2H_0 t \cong 2c_0\, e^{-2H_0 t}\,. \tag{10}$$

We can determine the theoretical distance to any observation as the integral of light speed from emission to observation. Using our approximation for the hyperbolic secant above we determine the integral:

$$D = \int_{t_e}^{t_n} 2c_0\, e^{-2H_0 t} dt\,. \tag{11}$$

We will use subscripts e for emission and n for now the present time of observation. Since we do not know the time of emission directly, we need to change the result to something we observe or know for the two types of redshifts. The integral of the exponential function just yields the same exponential function as the integrand again, which can then be replaced with the light speed from (12) when evaluating the integral upper and lower limits. The result expressed between limits in terms of light speed ratios becomes:

$$D = \frac{c_0}{2H_0}\left(\frac{c_e}{c_0} - \frac{c_n}{c_0}\right) = \frac{c_n}{2H_0}\left(\frac{c_e}{c_n} - 1\right). \tag{12}$$

We know current light speed and the emitted to present light speed ratio for either type of redshift above. For spectral redshifts of distant galaxies we use (9) to substitute for the observed redshift factor z and obtain the relation for distance versus redshift corresponding to the classic Hubble curve:

$$D = \frac{c_n}{H}\left(z + \frac{z^2}{2}\right). \tag{13}$$

This is like the historical Hubble relationship for distance vs redshift except for the last quadratic term in z. We dispense with using the subscript for H here because H is a dimensional constant with inverse time units, and we must use the same time units for H and the current light speed in the leading term. So, this is the Hubble constant expressed in the units we are familiar with at the current time. We have derived the Hubble curve directly from the new cosmology solution for the time varying universal gravity potential. Note that the extra quadratic term explains the non-linearity of the curve previously thought to be caused by dark energy when GR was used in consensus cosmologies. We do not need any such *ad hoc* parameter here to get the exact solution deriving from the Krogh gravity theory. As a preliminary check for our result, we show in Figure 4 a plot of distance modulus versus redshift obtained using this equation with some old observed distance estimates based on standard candle analysis including supernovas and redshifts for gamma ray bursts. It may be the case that standard candle energy fluxes need to be corrected for evolution with respect to the variable universal gravity potential with time at emission. Nevertheless, we are encouraged to find that we appear to have a credible model for the cosmological redshift of spectral lines without any expansion of space as a cause.

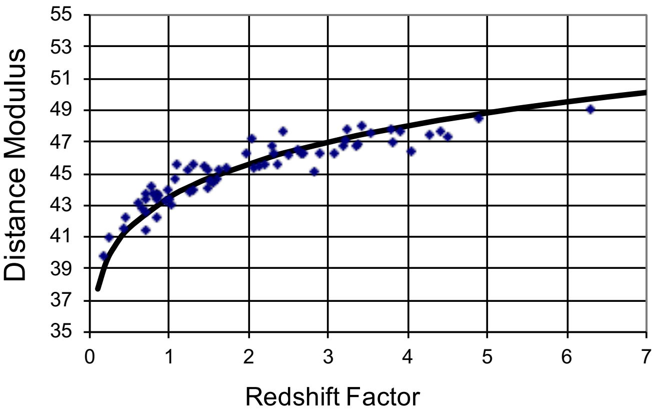

Fig. 4: Distance vs Redshift Factor

3.2 Distance to CMB surface

Using integration of light speed from emission to the present time given in (14) we can substitute the observation implied by temperature of recombination assumed in (11) for apparent redshift of blackbody radiation coming from the surface of last scattering which yields the distance to the CMB. Using the general integration of light speed from emission to the present given in (14) we can substitute the observation implied by temperature of recombination assumed in (11) for the apparent redshift of the blackbody radiation coming from the surface of last scattering which yields the distance to the CMB surface:

$$D = \frac{c_n}{2H}\left(\frac{T_e}{T_n} - 1\right). \tag{14}$$

Assuming temperature of recombination unchanged, the surface of last scattering has a temperature of 3 000 K and the CMB is 2.7 K blackbody radiation. Using (16) we calculate the distance to the CMB surface is about 555 Hubble time light-years at todays speed of light. This is about 7.8 trillion light-years with an assumption of Hubble time of 14 billion years. Present consensus cosmology based on the Big Bang would estimate this surface as about 40 billion light-years away. Our much greater distance estimate occurs because the light speed at emission from the surface of last scattering is orders of magnitude higher than today. The higher light speed is in fact the cause of the apparent redshift. Our use of light-years distance here is just a convention for historical reference. The 7.8 trillion light-years is not the light travel time, which is much shorter due to the earlier higher light speed. We have now set the stage for how much time is available for galaxy formation and distance to the CMB surface giving a visual picture of what we are looking at.

3.3 CMB relationship to Hubble constant

Previous investigations of the angular power spectrum structure of the CMB, according to what we predict, must now consider the surface is orders of magnitude more distant than thought. The universe is not expanding with respect to CMB observed structure. Past modeling of acoustic oscillations would now have to consider far higher speed of sound caused by lower mass of atoms in the plasma. The higher light speed also allows causal contact for far greater distance. Because of the great distance to the CMB surface, observed structures are enormously larger than thought. It also restricts the ability of instruments deployed to resolve smaller structural features of the CMB.

Cosmologists currently in the consensus Big Bang context have tried to estimate the Hubble constant by relating the CMB structure to the expansion of the universe which has resulted in a Hubble constant crisis due to disagreement between estimates based on the CMB versus more direct estimates based on the nearby distance ladder studies. Our new cosmology framework sets a stage which would invalidate prior estimates of the Hubble constant based on the CMB. It may be possible in the new context to estimate the distance to the CMB based on comparison of structure in the present universe compared to the scale of the structure in the CMB. The comparison would have to be made at a very large scale. According to (16), the distance to the CMB surface is inversely proportional to the Hubble constant.

3.4 Cause of uniformity of CMB

The extreme uniformity of the CMB has previously been used to support the concept of inflation as an addendum to the notion of the Big Bang. The argument is that there is a horizon problem due to lack of causal contact at required distances. We have no horizon problem here because the primordial light speed was sufficiently high and there is gravitational contact extending for many Hubble times distance from the CMB surface. Cooling of the primordial plasma as we will discuss later is a very slow process which results from the increasing gravity potential as the gravitational matter horizon grows. The resulting temperature cools very uniformly because it depends on the average density of gravitational matter over enormous distances far away from the CMB. The great length of time for equilibrium is also a benefit.

3.5 Age since CMB surface formation

We calculated the distance of the CMB surface using (16) but our distance of trillions of light-years was not the light transit time which is normally the case with constant light speed. The light transit time with the variable light speed can be calculated from (11) along with the cosmology solution for light speed versus time. Using simpler (12) for a sufficiently accurate relationship for light speed as a function of time and the known ratio of temperatures in (11) we get about 3.5 Hubble times for the required light speed change since the CMB surface formed which gives the light transit time of about 49 billion years. Interestingly this is not greatly different than the 40 billion years expected distance at constant light speed with consensus Big Bang cosmology but in that case the age since the CMB formation is believed to be close to 14 billion years and the distance accounts for presumed expansion. Here it was 49 billion years ago in today's time units in absolute years taken as constant over history. So this is our estimated age of the CMB surface formation time. This means we had 49 billion present years for galaxies to form since the universe cooled. It also means that JWST observed early galaxies had an abundance of time to form and grow old in some cases as well.

3.6 Early time dilation

We are a long way toward setting the stage for what we are in the process of observing in the universe today, however there is an important additional consideration which is significant. The teaching of the Krogh theory of gravity we have adopted along with our cosmology solution says that not only the speed of light and mass of particles was changing with our universal time reference, but atomic clocks have also slowed continuously since the matter creation epoch. This means that processes in the distant past occurred at a much faster pace in atomic time. If we observe an event such as a light curve of an explosion it would appear to be slower because the light speed change is faster than the rate of change speeding up the event in our universal time reality. So events that are actually happening more quickly are observed to be slower or time dilated due to the stretching effect of higher light speed. If we are looking at something caused by age, or which simply takes time like the death of stars it in reality occurs more rapidly in the past. We should not be surprised if things look too old or don't appear to have time to form. We also have seen apparent time dilation in distant events formerly attributed to general relativistic time dilation. Time dilation is a feature of this cosmology as well coming instead from the Krogh gravity theory.

To understand better what we are seeing when observing the most distant galaxies, and therefore the youngest, it is instructive to calculate atomic ages of things we observe. We can now do this by applying our cosmology framework and the Krogh gravity theory teachings. According to the theory, the rate of atomic clocks is greater in the past when the dimensionless potential was a lower negative value. The difference in the potential is positive if we are looking backward to earlier times. Defining atomic time as τ, the relationship for the instantaneous atomic clock differential time interval elapsed in the past compared to the universal constant present time intervals can be written using approximate late time gravity potential as:

$$d\tau = e^{Ht} dt\,. \tag{15}$$

The Hubble constant is in current universal time. Time in the exponent is the time as in years ago past. The total elapsed atomic time can be found by integrating forward to the present:

$$\Delta\tau = \int_0^t e^{Ht} dt = \frac{e^{Ht} - 1}{H} = \frac{z}{H}\,. \tag{16}$$

We obtain our result in terms of the spectral redshift originated from emission at the past time t by applying what we know from (9). This simple result shows elapsed atomic time is given by the product of redshift and the Hubble time. If we apply this equation assuming a Hubble time of 14 billion years, a galaxy observed by JWST at redshift 13 emitted its light about 182 billion years ago in atomic time. In §3.5, we found the distance to the CMB surface of last scattering based on the assumed temperature of recombination is estimated to be at a light travel time of about 49 billion years in constant present years. If spectral emissions were possible at the time of recombination when the CMB surface formed, we can use (11) substituted into (9) to predict that such an emission would have a redshift of about 32. This is the maximum redshift possible if the recombination temperature is 3 000 K. Computing the atomic time elapsed since the recombination time we get about 453 billion years. The difference in atomic time from recombination to the time of a redshift 13 galaxy gives us about 271 billion years available for the formation of the galaxy since the universe cooled to allow formation of stars. We would not be at all surprised if galaxies at this time appeared to be matured in form with signs of age.

4 Impacts of universe age and rate of physical processes

Because we do not know the primordial light speed at zero gravity potential before creation of matter initiated propagation of gravity throughout the universe, we cannot determine its total age. We predict about 49 billion years of current absolute length just since the CMB cooled to recombination temperature. We do expect the matter creation to be very hot if for no other reason that there cannot be a preferred reference frame for the velocity of mass particles created. The cooling process occurs only from conservation of momentum with increasing mass of particles. The cooling model applies from creation through the history of the universe. The mechanism in the absence of expansion is discussed further in §5 as part of a larger narrative about interstellar dynamics resulting from the Krogh gravity theory.

There are profound consequences of orders of magnitude increase in universe age and the accelerated rate of all physical processes at earlier lower gravity potential. The most significant effects occur in the 49 billion absolute years since formation of the CMB surface. After some additional cooling the formation of stars and galaxies begins, and these are the only things we can observe today. Since the rate of physical processes is much faster at early times, the effect of time dilation causes everything we observe today to age more quickly so we can expect evidence of more than 49 billion present years available from our perspective. We determine the 49 billion absolute years by using dimensionless time Ht which comes from the cosmology solution directly. We use units of Hubble constant based on the present which means that the number of Hubble times provides an estimate of age in current years. The number of Hubble times since the beginning is very close to the dimensionless gravity potential as well. Due to nothing else but the coefficients on the right-hand-side of (2) and the definition of the Hubble constant, we know that the total matter density of the universe is 4/3 of the classical Big Bang critical density. There is nothing critical here about the matter density since it is still an arbitrary initial boundary condition for solution of the governing equation. Since we require much more matter than can be accounted for as visible luminous stars, we require that most matter is invisible, but we do not believe that dark matter not consisting of baryons is needed because the effects of advanced age and rate of aging including new interstellar dynamics can be sufficient to produce the total matter density required.

Attempts to find supposed dark matter not made from ordinary baryons have failed to succeed regardless of extensive time and resources expended. So, while mysterious dark matter is not necessarily excluded in our new cosmology framework, it is not required. We will show in §5 that we believe new galaxy dynamics resulting from the Krogh gravity theory can account for galaxy rotation dynamics without any exotic type of matter.

4.1 Real baryonic dark matter

We claim that formation of real baryonic dark matter is a natural process in our new framework caused by both greater actual age predicted, but also from accelerated aging from the time dilation effect of lower gravity potential at earlier times beginning just after formation of CMB surface of last scattering and sufficient cooling to form stars and galaxies. Real dark matter is made up of products of star and galaxy formation and aging along with interstellar gas and dust which has so far not formed stars or been consumed in black holes. The principal products are discussed in the next subsections.

4.2 Star death

We have long known a great deal about how stars form from interstellar gas and dust. Depending on the makeup and mass, stars have various finite ages. Those which become unstable explode producing interstellar dust and remnants. Those which collapse or explode can exist in another state for extended times, but in any case, can remain luminous for only a finite time. The most common stars such as our sun will end up as very dense small white dwarfs which will ultimately cool to dark dwarfs. In the context of current Big Bang age-constrained cosmologies, it is thought that dark dwarfs do not exist in the universe yet because the cooling of a white dwarf star takes many billions of years. The age constraint of 14 billion years from the Big Bang is not sufficient. Dark dwarfs are not likely to be detected if existing because they would no longer be luminous and are only earth-sized very dense objects. With our new framework having 49 billion years available since CMB formation plus highly accelerated aging in the earlier years with far faster atomic time, we would expect to produce prolific populations of dark dwarfs and other types of dark remnants and dust. In fact, it is conceivable that what is thought to be dust in some galaxy photos with back lighting may actually contain large populations of dark dwarfs and remnants as well. We also know that many stars are formed which escape their galaxies and are adrift in interstellar space. These would die of old age in the time available during our 49 billion years and would remain undetectable at present. They would contribute to what may now be perceived as dark matter but there would be no need to claim it is not baryonic. Dead stars are one of the contributors for non-luminous matter we require. Due to accelerated atomic time at ancient times early stars did not last long before they died and became non-luminous. From further discussions we will see that new interstellar dynamics provides mechanisms to further dispose of ancient stars in black holes more quickly than allowed with present dynamic models. These can never be detected or seen again in any form.

4.3 Galaxy death

Astronomers have found galaxies which have stopped forming stars are common. It normally happens whenever there is insufficient interstellar gas remaining in the vicinity of a galaxy to support star formation. Many of these failed galaxies also have supermassive black holes at their centers. In the context of our new framework these galaxies will ultimately die and with sufficient time will be consumed by their black hole center in accord with what we will show. This will be more apparent after we discuss interstellar dynamics changes predicted by the Krogh theory. We have the same situation brought on by advanced universe age and time accelerated aging that we have with individual stars. Here we have entire galaxies collapsing into massive black holes that become undetectable except for gravitational effects such as affected galaxy clusters. It should be noted that gravitational lensing still occurs with Krogh gravity theory, so this is still consistent with observations.

4.4 Black hole formation and growth

The Krogh gravity theory still predicts that highly compact massive objects will form and for all intents and purposes have the characteristics we attribute to black holes in General Relativity. The only difference here is that they are just very gray and not black. They do not radiate sufficiently to be detectable but there is no event horizon. The speed of light can never quite be zero in Krogh gravity. The collapse of massive stars can still result in such black (gray) holes, which we, just for convenience and historical purposes, will refer to as black holes. It is also the case that matter can escape such holes forming galactic jets.

An inherent feature of the new gravity theory is that conservation of momentum will cause orbiting bodies to slow as their mass increases in the intense gravity potential of a black hole. This will cause matter to be accreted by black holes more rapidly than is the case for conventional GR theory. The new dynamics will be discussed in more detail in §5. With the new dynamics predicted not only will black holes accrete matter more quickly, but so also will the motion of stars in galaxies tend to spiral into the gravity well of the galaxy itself. The formation of a black hole at galaxy centers is inevitable with this dynamic if the galaxy is sufficiently large. Cosmological increase in potential also causes stars to spiral into galaxies as a normal process contributing to feeding center black holes. The fate of any galaxy not actively continuing to create stars is to cause stars to spiral into the center black hole. Our new cosmology framework predicts multiple processes have continued throughout the history of the universe which create prolific amounts of invisible baryonic matter. Since non-baryonic dark matter has not been detected, and we require total matter density of 4/3 of classical Big Bang critical density determined by the Hubble constant, it is believed that actual invisible baryonic matter exists in the various invisible forms discussed. We do not believe that any exotic non-baryonic matter is necessary to provide the required total matter density, since the universe is so old that a great deal of matter today cannot be detected other than through gravitational effects.

4.5 JWST findings

Our cosmology framework sets the stage for what we expect to observe with the recently deployed James Webb Space Telescope. We see no findings since JWST went operational that are considered unexpected. In the first year of operation a prolific number of galaxies were seen at great distance. Many were unexpectedly massive or bright, small, old, mature in form, contained older stars, and appeared to have insufficient time to form since the supposed Big Bang. Clearly Big Bang consensus cosmology is not consistent with JWST findings. There is a crisis in cosmology today which cannot be resolved without replacing the GR paradigm which leads to the Big Bang limitation on age of the universe since recombination formed the CMB surface. An extensive discussion of cosmological model tests using JWST findings was done by Lovygin *et al* [5] and further by LaViolette [7]. The key findings are that angular diameter distance and surface brightness do not support an expanding universe paradigm. Euclidean geometry and an alternative explanation for redshift are implied. We provide a new cause for redshift here without tired light.

We have shown here with our new framework that an observed galaxy at redshift 13 has an estimated 271 billion years of atomic time since recombination to form such a galaxy. It seems likely that many galaxies would exist at this redshift detectable by the telescope which are mature and massive, having had more than sufficient time to mature and grow. Furthermore, since we predict far more baryonic gas was available initially, there was no shortage as has been supposed in consensus cosmology models. In fact, based on other considerations of our new interstellar dynamics, black holes would have formed as well. We would expect prolific star formation with plenty of available gas and many star deaths due to both earlier formation and accelerated atomic age. Due to availability of gas, galaxy deaths would be expected to be less common at the earliest times compared to the present.

We predict that galaxies formed at times far more distant than JWST can detect. A key mission of the telescope was to explore the first galaxies formed in the universe. It appears to us that this goal cannot be achieved. Galaxies continue to form through the history of the universe so there will always be some new ones, but we do not expect that the telescope can see the first ones. It is likely that JWST will find fully mature massive galaxies as far away as the limits of its sensitivity allow. This is the inevitable consequence of the much older universe we predict.

5 Interplanetary and interstellar dynamics

We have shown that solving the governing equation for Krogh gravity theory results in a cosmology framework that solves the current crisis between observations and consensus Big Bang cosmology. General Relativity has been the consensus gravity theory for about a century. While providing superior cosmology, the Krogh gravity replacement still satisfies previous GR tests. We also predict new testable dynamics not predicted by GR. Predicting new outcomes in addition to satisfaction of prior tests is necessary to gain acceptance. With that in mind we will discuss the modeling of new dynamics in several examples to follow. The Mercury orbit is included to show that our dynamics model obtains the identical result as GR though it is based on an entirely new paradigm.

There are different approaches that can be taken when following the teachings of the Krogh gravity theory to model the dynamics of bodies in motion under the influence of gravity. The one we will use here is based on strict conservation of momentum while modeling the variation in mass under the influence of a gravity potential as required by the Krogh theory. The rest energy is not conserved because the combination of light speed change and mass results in rest energy changing to reflect the change of potential energy from gravitational potentials produced by either local masses or average cosmological mass density. The fact that all masses in the universe keep track of their potential energy is a key feature of the Krogh gravity paradigm. Conservation of momentum has always been a stronger mandate in physics. Using this mandate results in a slightly different anomalous acceleration math model than previously reported but observable anomalous effects previously not predicted are still indicated. The correct Mercury orbit supports our approach.

The continual growth of the gravitational matter horizon causes a cosmological deceleration of any mass in motion in the universe. This cosmological effect is one type of new dynamics not predicted by GR but clearly required by the Krogh theory. The second type of modified dynamics results from the transport of any mass in motion through a gravity gradient caused by local masses, which alters the universal background time dependent potential satisfying our cosmology solution. A mass in motion does not know the difference between time rate of change of mass from incoming gravity just arriving from the matter horizon since matter creation began or from change due to motion in a local gravity gradient. In the latter case, the gravity potential can either increase or decrease so it can cause either deceleration or acceleration not predicted by GR. Fortunately these predicted modifications to dynamics are testable with sufficiently accurate measurements and in fact have already produced observed anomalous effects. Our choice of modeling new dynamics from conservation of momentum alone works universally for all types of anomalous accelerations which will be discussed next. The approach for motion in local gravity gradients generalizes the fact that anomalous accelerations are caused by the total time derivative of the dimensionless potential locally causing masses to vary with the potential.

5.1 Cosmological deceleration

Cosmological deceleration is an inherent consequence of our cosmology solution from Krogh gravity theory along with its required variation of mass under the influence of the universal gravity potential. If momentum is to be conserved, the velocity must change inversely with the mass change at least in the non-relativistic case. We will develop our dynamic model with the requirement of conservation of momentum including consideration for special relativistic momentum which still applies. This leads to more generality and makes additional predictions of interest.

Beginning with the Lagrangian applicable for the Krogh gravity theory [1] and taking the partial derivative with respect to velocity yields the equation for the relativistic momentum:

$$p = \frac{vE_{00}\, e^{-3\phi}}{c_0^2 \sqrt{1-(v^2/c_0^2)\, e^{-4\phi}}}\,. \tag{17}$$

In accord with the Krogh definition E_{00} is the rest energy at zero gravity potential and c_0 is light velocity at zero potential. We similarly have the dimensionless gravity potential ϕ as defined. In the cosmology solution, masses are only free of gravity instantaneously at the matter epoch which is an instructive starting point. We can later generalize to more arbitrary epochs. Writing the momentum in terms of mass rather than energy originating from the Lagrangian, the momentum becomes:

$$p = \frac{vm_{00}\, e^{-3\phi}}{\sqrt{1-(v^2/c_0^2)\, e^{-4\phi}}}\,. \tag{18}$$

From the cosmological solution for the dimensionless potential, we found that it asymptotically became an effective dimensionless time since it converged to $-Ht$. So, our expression for momentum looks like momentum as a function of time for a free particle in straight line motion. But we require that momentum is conserved because there is no external force or acceleration in play. If we take the epoch of the motion as zero potential or time, we require that the momentum is constant. We require the equality:

$$\frac{v_0}{\sqrt{1-(v_0^2/c_0^2)}} = \frac{v\, e^{-3\phi}}{\sqrt{1-(v^2/c_0^2)\, e^{-4\phi}}}\,. \tag{19}$$

Terms with subscript zero can be considered as values at an epoch corresponding to zero gravity potential. For now, we will consider how changes affect the motion of all particles in the universe following the matter epoch beginning with zero dimensionless potential. To describe the motion, we can solve for the time-dependent velocity at any arbitrary potential at a time later than the epoch. The velocity at epoch is arbitrary representing all possible velocities that may have existed. We solve for velocity and obtain the function describing the trajectories of particles:

$$v = \frac{v_0\, e^{3\phi}}{\sqrt{1-(v_0^2/c_0^2)+(v_0^2/c_0^2)\, e^{2\phi}}}\,. \tag{20}$$

Another useful form is obtained by dividing by the local velocity of light on the left side and using the same light velocity scaled from c_0 with the dimensionless potential on the right side to obtain the relationship for the dimensionless velocity ratio:

$$\frac{v}{c} = \frac{(v_0/c_0)\, e^{\phi}}{\sqrt{1-(v_0^2/c_0^2)+(v_0^2/c_0^2)\, e^{2\phi}}}\,. \tag{21}$$

It is clear from (22) that all particles or bodies in motion are forever slowing as the potential becomes increasing negative in accord with our cosmology solution. The dimensionless potential plays the role of negative dimensionless universal time. Interestingly, (23) shows further that highly relativistic particle velocities near the speed of light tend to slow in proportion to the slowing light speed such that the velocity ratio v/c tends to be more constant. A particle moving at light speed would slow with light speed over time behaving more like a photon. Since there could be no preferred frame for matter creation, some original particles would be highly relativistic and in principle, barring collisions, would still be relativistic at the present time. If it were possible for some particles to survive in the rarified low particle density for many billions of years it would result in a cosmic ray background. In any case, any relativistic particles created later in the universe tend to remain relativistic for as long as they can survive. We will show that there exists a predicted means to create such particles that is a part of our new gravity model.

5.1.1 Cosmological cooling

Our first example of cosmological deceleration is cosmological cooling. We have discussed previously that cosmological cooling plays an important role in our new cosmology framework. Since we no longer have expansion to provide the rapid cooling after matter was created as is the case for the Big Bang, another means is required. Extremely hot matter creation seems to be an inevitable requirement as we have claimed, and cooling is required to form the surface of last scattering for the CMB in similar fashion as supposed in the Big Bang cosmologies. We also require that the universe must cool first to the recombination temperature of the last scattering surface and then additional cooling to allow star and galaxy formation at later times.

Temperature is assumed to be proportional to average kinetic energy of particles which is proportional to mv^2. Both mass and velocity depend on dimensionless potential given by the cosmology solution and our dynamic model conserving momentum. Eq. (22) provides the full relativistic model for velocity dependence on the potential. Since most particles are not at relativistic velocities, we will simplify our cooling model to consider that the average velocities are not relativistic. With this assumption, (22) simplifies to show variation of velocity with the dimensionless potential to become:

$$v = v_0\, e^{3\phi}\,. \tag{22}$$

So, while velocity decreases with increasing negative potential, mass scales inversely in accord with the Krogh theory. Since velocity is squared for kinetic energy, we can conclude that the temperature of the universe can be expected to cool over time in an otherwise adiabatic universe as the negative gravity potential increases in accord with the cosmology solution so that temperature will obey the scaling equation:

$$T = T_0\, e^{3\phi}\,. \tag{23}$$

Since the dimensionless potential is basically measured in Hubble times of approximately 14 billion years, after the few Hubble time non-linear start when matter was created, cooling would continue to reduce temperature by a factor of 1 000 over about every 30 billion years. We of course do not know the temperature of the universe at creation except that it had to be extremely high. We therefore can expect that the universe may have taken hundreds of billions of years to cool to the recombination temperature forming the surface of last scattering for the CMB. Because of the high primordial light speed, we can conclude that the matter horizon was already trillions of light-years at present speed from the last scattering surface. We conclude that the great length of time for the universe to reach equilibrium before this surface began and the great distance to the matter horizon source of the gravity potential would result in a very uniform smooth surface dependent on the average density over trillions of light-years. We propose that this rationale explains why the CMB is observed to be remarkably uniform in structure. Neither inflation nor expansion is necessary in the new cosmology framework.

5.1.2 Pioneer probe deceleration anomaly

Although it is unlikely we could observe cosmological cooling to test our dynamic model arising from the Krogh gravity theory and the cosmology solution, we have a surrogate for the effect by virtue of the anomalous observed deceleration of the Pioneer probes. The model applies equally to material bodies, spacecraft, or interstellar particles in motion. Analysis of observed anomalous deceleration is discussed extensively by Anderson [8]. Krogh [2] also has addressed the deceleration as a cosmological effect which we also claim here. Unfortunately, the Pioneer spacecraft are less than perfect as a test of the cosmological effect we predict. The deceleration is very small and can be contaminated by other forces coming from the spacecraft and as we will show there are opposing accelerations which are also predicted to occur from motion through gravity gradients existing in the solar system. Thorough analysis of the Pioneer data is ongoing which will add more than we can discuss here, but for now we want to show from the conservation of momentum model we propose here what the cosmological contribution would be.

We can use (24) which is what conservation of momentum requires for velocity in the non-relativistic free body case to derive the cosmological deceleration contribution for our cosmology model. The acceleration implied by the velocity (24) can be derived by differentiating velocity with respect to time which gives:

$$\frac{dv}{dt} = 3v_0\, e^{3\phi}\,\frac{d\phi}{dt}\,. \tag{24}$$

Using (24) we can effectively update the epoch for velocity to the local one by substitution:

$$\frac{dv}{dt} = 3v\,\frac{d\phi}{dt}\,. \tag{25}$$

Since it is sufficient to approximate the dimensionless potential at the present epoch as $-Ht$ according to the cosmology solution, we can write this in terms of the Hubble constant as:

$$\frac{dv}{dt} = -3vH\,. \tag{26}$$

This result is slightly different than the result given by Krogh [1] since we now have an integer factor 3 as opposed to 4 previously reported. It's clear since we have conserved momentum that the alternative derivation conserving energy did not conserve momentum which is the preference here. We will show modeling motion within the Sun's gravity gradient by planet Mercury that using the factor 3 duplicates the GR result for the rotation of the orbit ellipse. A full treatment of the anomalous acceleration of the Pioneer probes must include effects for motion within solar system gravity gradients.

5.2 Motion modified by gravity gradients

We have shown for the non-relativistic case in (27) that a cosmological deceleration results from the time rate of change of the time dependent dimensionless potential predicted by our cosmology solution. The cosmology solution applied the cosmological principle assuming a uniform average matter density throughout the universe. This of course implies there are no spatial gravity gradients from local gravitational bodies. A body in motion would experience a change in gravity potential due to passage through a local gravity gradient. The body would not know the difference between a change resulting from motion in a local gradient or a time rate of change from the cosmology.

The cause of the anomalous accelerations predicted by the Krogh gravity model arises from conservation of momentum in the presence of changing mass of a moving body. When massive bodies are immersed in a space subject to a spatial gradient of the gravity potential, they also experience gravitational accelerations which are independent of mass since all masses fall at the same acceleration. While the gravitational acceleration can cause momentum to change such that it is no longer conserved as we had assumed in previous derivations, we can still predict that the anomalous accelerations predicted by momentum conservation in the absence of external accelerations will occur because the mass still changes in accord with the Krogh gravity theory as a function of the dimensionless potential regardless of the cause. This effect of momentum conservation from changing mass occurs instantaneously and would be superimposed on accelerations arising from gravity gradients. It follows of course that cosmological deceleration predicted never goes away and is also superimposed as a perturbing anomalous source affecting the total acceleration of any body.

Before we go further, we should address an issue arising because we wish to superimpose dimensionless gravity sources coming from different gauges of reference. We could call this the near far and past present terms in the total gravitational potential. This problem results from the fact that the cosmological time dependent term has a primordial light speed which represents the light speed of an empty universe with no gravity potential and the gravity potentials of local bodies such as the sun or earth generally refer to a light speed far from local gravity fields. It is important to separate the definitions of the light speeds which are regarded to be free of gravity in local settings from the cosmological one where space was only free from gravity at the matter epoch long ago. We need to add non-dimensional potentials which are normally calculated by dividing by the square of light speed from different reference gauges. We do not even know the primordial light speed used to form the non-dimensional cosmological potential. Once potentials are made non-dimensional, the time rate of change must be calculated in the local reference time associated with the acceleration. Failure to make appropriate distinctions may result in exponential scaling terms in the acceleration equation that do not belong.

We saw when calculating trajectories in local space from cosmological changes, the dimensionless potential takes on the role of dimensionless time. For purpose of calculating accelerations locally it is a good practice to consider the instantaneous epoch of the trajectory in time and space should also be the reference for zero gravitational potential. Since potentials always have some normally arbitrary reference energy, this is permissible. We are only interested in changes in dimensionless potential. Whenever the dimensionless potential is differentiated, the zero base for the potential goes away, but we always end up with a light speed squared in the denominator to make potentials dimensionless. The local gravity potential must be made non-dimensional by dividing by light speed calculated locally with the same units of measure as the local gauge. The time rate of change must similarly be calculated for the local time reference for the trajectory.

For purposes of discussion and calculation it is useful to define three distinct light speeds as follows:

c_0 = Light speed of an empty primordial universe with zero potential;

c_n = Light speed now far from local gravitational bodies at present cosmological time;

c = Light speed in local space and time of body in motion.

Regarding the cosmological deceleration we have already discussed, it should be clear that there must be a universal frame of reference established when mass was created in the universe. The argument for this is clear. When particles consisting mostly of protons were created at the beginning of the universe, the particles had random velocities in all directions, i.e. no preferred direction. None of the particles had speeds greater than the then light speed of the previously empty universe. Since the random velocity distribution has uniform velocity densities in all directions, the average velocity is zero establishing a universal rest frame forever. The acceleration equation derived for the Pioneer cosmological effect causing deceleration proportional to velocity applies equally to either the universal reference frame or the local solar system frame, because the entire solar system or for that matter the galaxy motion with respect to the universal frame is decelerating. We can therefore focus on just the relative velocity with respect to the solar local frame of reference when determining the cosmological deceleration with respect to that body of reference.

We now predict additional previously un-modeled accelerations caused by motion in a local gravity gradient. We restrict for now our discussion to one local gravitational body of interest using our definitions of the various light speeds. We define the total non-dimensional gravitational potential to be used in exponential scaling terms in the Krogh theory including cosmological and local potentials as:

$$\phi = \frac{\Phi_u}{c_0^2} + \frac{\Phi_g}{c_n^2} = \phi_u + \phi_g\,, \tag{27}$$

where Φ_u is the potential of the observable universe, and Φ_g is the potential of the local gravitational body in both cases expressed in whatever units are used for the respective light speeds. We of course do not know c_0 but we know the time rate of change of that dimensionless term from the cosmology solution. To include the perturbing acceleration contribution of motion by transport through the gravity gradient, we must use the total time derivative of the dimensionless potential by adding the dot product of the velocity and the gravity gradient to the time derivative in (27). We can write the total perturbing anomalous acceleration from cosmological and gravity gradient contributions as:

$$a_p = 3v\,\frac{d\phi}{dt} = -3vH + \frac{3v}{c_n^2}\,(v \cdot \nabla\Phi_g)\,. \tag{28}$$

It is understood that the velocity is a vector. The first term on the right is the Pioneer anomaly cosmological acceleration term. The final term is added due to the requirement to use the total time derivative of the potential. Both terms contribute to anomalous accelerations for the Pioneer probes, but presumably the second becomes small when far from the Sun. A full treatment of the Pioneer anomaly needs to include this term especially for movement in the early stages in the inner solar system. The second term affects the orbits of planets or other bodies moving within the solar system. The later portion of the Pioneer trajectory far from the Sun would depend mostly on the first term cosmological effect and has so far been the only one considered.

5.2.1 Mercury orbit

We will now show that the second term on the right of (30) predicts the motion of planet Mercury identical with previous General Relativity predictions. If we restrict the discussions to just the Sun's gravity gradient for our purposes and ignore the small cosmological contribution of the first term, the perturbing acceleration can be written:

$$a_p = \frac{3v}{c_n^2}\,(v \cdot \nabla\Phi_s)\,. \tag{29}$$

Defining μ as GM_s for the Sun's gravity we know its radial gravity gradient and terms forming the scalar dot product with the velocity in (31). The perturbing acceleration in the direction of the velocity vector becomes:

$$a_p = \frac{3v}{c_n^2}\left(\frac{\mu}{r^2}\frac{dr}{dt}\right). \tag{30}$$

This acceleration caused by passage through the gravity gradient directed along the velocity vector is either positive or negative depending on the radial velocity direction. It will be immediately clear to those familiar with orbit maneuvers used to change argument of perigee for earth satellite orbits that pairs of accelerations in opposite directions before and after perigee will rotate the orbit ellipse. We need only to analyze the integrated effect of this perturbing acceleration to show that it duplicates the change predicted by GR. Note that no curvature of space is involved in the new gravity theory. The effect here is caused only by the conservation of instantaneous momentum in response to mass changes in the variable gravity potential along the orbit path as predicted by the new gravity theory.

A time-honored way to do this type of analysis is to use the Gauss planetary equations to calculate the cumulative integrated effect of small acceleration perturbations departing from normal Newtonian orbit mechanics. To use the Gauss planetary equations, we need components of perturbing accelerations in the radial and in plane tangential direction perpendicular to the radius. At this point we can dispense with the subscripts for light velocity since we can just use the light speed consistent with the location of the Mercury orbit. We begin by writing the components as:

$$a_r = \frac{3}{c^2}\,\frac{\mu}{r^2}\left(\frac{dr}{dt}\right)^2; \tag{31}$$

$$a_\theta = \frac{3}{c^2}\,\frac{\mu}{r}\,\frac{d\theta}{dt}\,\frac{dr}{dt}\,. \tag{32}$$

Before we can integrate the appropriate Gauss equation with substitution of these acceleration components, we need to express them only in terms of the orbit true anomaly θ because the integration will be over θ for one orbit revolution. We want both components written in terms of functions of θ times the time derivative of θ. We need the following orbit mechanics identities to make substitutions in terms:

$$r = \frac{a\,(1-e^2)}{1+e\cos\theta}; \tag{33}$$

$$\frac{dr}{dt} = \frac{r^2 e\sin\theta}{p}\,\frac{d\theta}{dt} = \sqrt{\frac{\mu}{p}}\,e\sin\theta; \tag{34}$$

$$\left(\frac{dr}{dt}\right)^2 = \sqrt{\frac{\mu}{p^3}}\,e\sin^2\theta\,\frac{d\theta}{dt}\,. \tag{35}$$

Using these orbit identities substituted for the appropriate terms for the perturbing accelerations to obtain the forms dependent only on true anomaly θ, we now have the alternative forms desired:

$$a_r = \frac{3}{c^2}\sqrt{\frac{\mu^3}{p^3}}\,e\sin^2\theta\,\frac{d\theta}{dt}; \tag{36}$$

$$a_\theta = \frac{3}{c^2}\sqrt{\frac{\mu^3}{p^3}}\,e\sin\theta(1+e\cos\theta)\,\frac{d\theta}{dt}\,. \tag{37}$$

The appropriate Gauss planetary equation expressing the time rate of change of argument of perihelion with radial and tangential perturbing accelerations is given as:

$$\frac{d\omega}{dt} = \frac{\sqrt{1-e^2}}{nea}\left[-a_r\cos\theta + \left(\frac{2+e\cos\theta}{1+e\cos\theta}\right)a_\theta\sin\theta\right]. \tag{38}$$

Substituting perturbing accelerations from (38) and (39) into (40) and replacing n and p with the relations:

$$n = \sqrt{\frac{\mu}{a^3}}; \tag{39}$$

$$p = a(1-e^2)\,, \tag{40}$$

$$\frac{d\omega}{dt} = \frac{3\mu}{c^2 a(1-e^2)}\left[-\sin^2\cos\theta + \sin^2(2+e\cos\theta)\right]\frac{d\theta}{dt}\,. \tag{41}$$

Integrating over one revolution for the change in argument of perihelion we have the result:

$$\Delta\omega = \frac{6\pi\mu}{c^2 a(1-e^2)}\,. \tag{42}$$

This is identical to the prediction from General Relativity and consistent with observations of the Mercury orbit. We show in this example testing our methodology of conservation of instantaneous momentum with changing mass dependent on gravitational potential along the path of the orbit, that our dynamic model is confirmed. This prediction is made without any need to require that space is curved. The motion is duplicated by accelerations along the velocity vector direction only.

5.2.2 JUNO orbit anomaly

The JUNO spacecraft has been orbiting Jupiter in a highly eccentric orbit. Because Jupiter is so massive and the spacecraft passes through strong gravity gradients near the planet with substantial radial velocity, it experiences similar anomalous accelerations as predicted in the previous section for Mercury's orbit around the Sun. We have already shown that our new dynamics model works for the Mercury orbit by replicating rotation of the orbit ellipse as observed and consistent with prior GR predictions. In the case of JUNO, we have an additional and unique opportunity to test our new theory and show that it is superior to GR since it predicts more than just the global observation that the ellipse rotates. The opportunity arises because we have precision doppler tracking data for the spacecraft which was not available for the planet. The perturbing accelerations produce velocity variations which should be directly observable with doppler tracking which are predicted by the new dynamics and not by GR. Anomalous unpredicted velocity variations have already been reported by Acedo *et al* [9].

Unfortunately, currently we have neither the data nor the resources to confirm that our new dynamics correctly models the JUNO discrepancies in observed trajectory. The fact that anomalies are predicted, exist, and are currently unexplained suggests that such test are clearly warranted. To do the work correctly will require careful attention to all the gravity models in the Jupiter environment including moons and the non-spherical planet models. We have provided a proposed model for the anomaly source which would have to be added to existing models by the appropriate investigators. We encourage that this effort take place.

5.2.3 Earth flyby anomalies

Several examples of Earth flyby velocity anomalies have been reported. Earth flybys are common practice for giving spacecraft a gravity-assisted boost to higher velocity primarily to reach the outer solar system or to exit the solar system such as for the Pioneer probes. The observed anomaly is generally described as a difference between the asymptotic velocity solution from Earth approach and Earth exit as reported by Acedo [10]. The effect causes an inability to fit the tracking data for the whole trajectory connecting both approach and exit. The anomaly varies substantially depending on the nature and geometry of the Earth gravity encounter.

The new dynamic model we have proposed here would obviously produce discrepancies of the type observed in Earth flybys. The effect is entirely based on the variation in mass of the spacecraft as it is in transit through the gravity potentials of all the bodies involved including Sun, Moon, and Earth. Since we require momentum to be conserved the velocity increases or decreases depending on whether gravity potential decreases or increases with respect to all gravitational bodies in play. We have shown how to model the perturbing unmodeled accelerations, which could be added to the tracking reduction fitting models in detail. We of course do not have the data or assets to do this but suggest it would be appropriate to make such a test.

Another simpler method is suggested as well just for purposes of explaining the cause of the anomaly. Since the gravitational accelerations from the bodies are well modeled already, and they are the only thing that can change the momentum along the trajectory of the spacecraft, we would have already accounted for momentum change from ordinary accelerations correctly. It would be instructive and perhaps sufficient to simply determine the total dimensionless gravity potential of all gravitational bodies at the positions of asymptotic Earth approach and the asymptotic Earth exit. From this we can calculate the difference in dimensionless potential between the two points in space comparing approach to exit points. Using the Krogh gravity theory, we can then calculate the predicted ratio of spacecraft masses between approach and exit by evaluating the exponential function with the difference in dimensionless potential in the exponent. The ratio of velocity at exit observed to expected should be the inverse of the predicted mass ratio. The prediction could be expressed by the relations:

$$\frac{V_a}{V_e} = \frac{M_e}{M_a} = e^{3\Delta\phi}\,; \tag{43}$$

$$V_a = V_e e^{3\Delta\phi}\,, \tag{44}$$

where V_a is the actual exit velocity and V_e is the expected exit velocity while $\Delta\phi$ is the difference in gravity potential divided by c^2. It is important that the spatial positions at both approach to Earth and exit asymptotes are actual best estimates. The integrated gravity accelerations must be over the actual trajectory between these points in space. This shortcut approach is suggested only as a simpler approximate method which has some possibility of success, but it does not replace integrating the correct instantaneous perturbing accelerations according to the dynamics model. To remove current errors in spacecraft navigation it will be necessary to include the corrections for the integrated accelerations to fit tracking data correctly and minimize residuals.

5.2.4 Pioneer outgoing transient

The Pioneer cosmological deceleration anomaly is discussed in §5.1.2. When the probe was sufficiently far from the Sun and solar system bodies, the continuous cosmological deceleration anomaly may be dominant, but it should be recognized that other perturbing accelerations were present and may at times be significant during the outgoing trajectory as the probe left the solar system. The model for modified dynamics caused by passage of a body through gravity gradients has been discussed in a prior section with the perturbing acceleration given by (31) where we proved the validity of the model for the orbit of planet Mercury. The Pioneer probes would experience anomalous accelerations near Earth flybys, passage near other planets, and particularly the entire escape from the Sun's gravity potential. During exit from the Sun's potential the effect will be an acceleration which would oppose the cosmological deceleration which is present continuously. Since the anomalous acceleration is also proportional to velocity, the effects would be more pronounced during periods of higher velocity, generally occurring in earlier phases before the deceleration from Sun escape slowed the probe. The acceleration would diminish with distance from the Sun both as the velocity slowed and the Sun's gravity gradient became weaker. The cosmological deceleration is abated only by the lower velocity far from the Sun so the presence of proportionately higher perturbing acceleration closer to the Sun would flatten the observed net perturbed deceleration. There is no intent here to analyze the trajectories in detail but to make the claim that these effects are predicted, and a model has been provided. The effects were not predicted by General Relativity but are direct consequences of the new gravity theory proposed by Krogh including the resulting cosmology solution provided here.

5.2.5 Cosmological orbit decay

An additional prediction of the proposed cosmology and the Krogh gravity theory is that all orbits will decay under the influence of the increasing cosmological potential and conservation of momentum with changing mass of the orbiting bodies. Cosmological deceleration occurs in any orbiting body like what was observed for the Pioneer probes. We will for simplicity consider circular orbits of a small mass around a much larger central body as in planetary orbits. Because the satellite body is in orbit, any small reduction in tangential velocity from a cosmological deceleration will result in a deficiency in the centripetal acceleration, causing the body to accelerate radially toward the central gravitational body. The resulting trajectory is a shallow nearly circular spiral continually reducing the orbit radius. In the process the angular momentum must be conserved as the radius decreases and the mass increases. Because there is a small radial velocity the intensity of the negative gravity potential increases further due to the reduction in radial distance to the central body. This gravity potential change is in addition to the cosmological change causing the orbit to decay an additional amount. For weak gravity gradients the additional amount is small while in the presence of very strong gravity gradients the orbit will become unstable with a steep spiral.

Consider then a small body spiraling toward a much more massive central body. We assume the orbit radius changes only a very small amount per revolution so that the velocity vector is considered perpendicular to the radius vector and equal to circular orbit velocity. With this assumption we can calculate the rate of decay of the orbit over a cosmological time interval with our cosmology providing the measure of the gravity potential change. We further include the potential change resulting from reduction of orbit radius in the gravity gradient, which provides a method of testing if a given example can be considered as a stable near circular weak gravity case. With our assumptions and the requirement that angular momentum is conserved as the mass of the orbiting body increases with changing potential, we can easily calculate the elapsed cosmological time required for any given reduction in orbit radius. Conservation of angular momentum requires:

$$m_0 v_0 r_0 = m v r\,; \tag{45}$$

$$\frac{m}{m_0} = \frac{v_0 r_0}{v r} = \sqrt{\frac{r_0}{r}} = e^{-3\Delta\phi}\,; \tag{46}$$

$$\frac{r_0}{r} = e^{-6\Delta\phi}\,, \tag{47}$$

where we have substituted for circular velocity at both radii and applied the Krogh gravity theory for scaling the change in orbital mass. Since GM remains constant at the times for both radii, it cancels out for the ratio of the starting and ending radii. The product GM will remain in the equation for total change in dimensionless potential $\Delta\phi$, which will affect our test for the weak gravity assumption for orbit stability. We can write the total change in dimensionless potential which applies to the exponential scaling of mass ratio as:

$$\Delta\phi = -Ht + \frac{GM}{r_0 c_0^2} - \frac{GM}{r c_0^2}\,, \tag{48}$$

where the time t is the time from the starting radius to the ending radius. Substituting this total potential change in the exponent of (49) and taking the natural logarithm of both sides:

$$\ln\frac{r_0}{r} = -6\Delta\phi = 6\left(Ht - \frac{GM}{r_0 c_0^2} + \frac{GM}{r c_0^2}\right). \tag{49}$$

Solving for transit time to go from the initial radius to the final one we have the result:

$$t = \frac{1}{H}\left[\frac{1}{6}\ln\frac{r_0}{r} - \left(\frac{GM}{r c_0^2} - \frac{GM}{r_0 c_0^2}\right)\right]. \tag{50}$$

For our assumption of near circular and stable orbits to be valid the difference in potentials in parenthesis must be small compared to the logarithmic term to its left in the brackets or otherwise stable near circular orbits cannot be sustained and the orbit will go into a steep spiral into the central body. This would be an example of very strong gravity fields resulting from either very large central mass or small orbit radius. For strong gravity fields a more complex integration of the dynamic model would be required to describe the trajectory. In the case of Earth orbit around the Sun at its present radius, the term on the right is many orders of magnitude smaller than the term on the left and can be neglected. An interesting conclusion for weak gravity fields is that the orbit radius decay is very similar to nuclear decay where it can be defined as a half-life. This is a direct result of the exponential relationship and the linear change in universal potential with time given by the applicable late term solution for our cosmology framework.

It is also important to consider that the solution obtained assumes that the central body GM is constant which is not strictly true for example if it is a star like our Sun. The Sun is losing mass from nuclear fusion and expulsion of solar wind particles. If we try to measure the distance to the Sun with the Earth diameter to measure parallax, we will have to understand that the Earth diameter is shrinking cosmologically which would mask some of the change in orbit diameter. The energy radiated by the Sun is also changing as well. According to the cosmology and the Krogh gravity theory the rest mass energy of the Sun is falling as the universal gravity potential is increasingly negative. Depending on what the net effect is, it is conceivable that global warming could be affected, but because changes occur so slowly it is unlikely to be significant.

5.2.6 Galaxy rotation and decay

Galaxy dynamics has long been a complex N-body problem difficult to model including unknown distribution of collective mass density from all the stars and other matter present. The present consensus theory includes the supposed existence of non-baryonic dark matter halos. It is not in the scope of this paper to develop necessary new galaxy simulation models that will be needed in the context of the new cosmology framework proposed. What is worthwhile is to point out how models developed with prior cosmology and gravity models are no longer valid in the new context. Prior observational methodologies are incorrect without knowledge provided by the new paradigm. The cosmological deceleration required by our solution becomes the same order of magnitude as the radial gravity gradient acceleration at large distances from galactic center, so dynamics cannot be understood without these terms.

We have just discussed in the prior section how orbits are subject to cosmological decay as the universal potential becomes increasingly negative because of continuous arrival of gravity from the most distant mass density just arriving since matter was created. Entire galaxies are also subject to this decay with the difference that galaxies rotate very slowly and have enormous size. Because the time for even one rotation is so large, the notion of circular orbits around the galaxy center is inherently flawed since conservation of angular momentum of the galaxy contents will cause the entire content of the galaxy to decay toward the center as the mass of these contents is forever increasing with the cosmological potential change. Since a black hole normally will exist at the center, the dynamics of the new framework will continually feed the galaxy contents into the black hole. Unless a galaxy continues to create new stars from infalling interstellar matter, it will be destined with sufficient time to turn into a supermassive black hole and no longer exist as visible matter. We showed that as orbiting matter gets closer to a massive center with very strong gravity gradients, it will become unstable causing it to spiral more rapidly and become consumed by an existing black hole.

Because of slow rotation and size, near circular orbits cannot exist inside galaxies at all, because cosmological dynamics will dominate the motion. Newtonian dynamics cannot describe their motion correctly. It can be said that galaxies are accretion disks around a black hole center. Since we already know galaxies no longer producing stars are common, we can expect that some galaxies may have already been consumed by supermassive black holes or at least their stars have since gone dead. These would contribute to dark baryonic matter throughout the universe. Galaxy clusters may have more dead galaxies than visible ones. Since atomic time moved more rapidly in the past, we can expect that stars would not have lived as long then.

Returning to live observable star producing galaxies we know that such galaxies have infalling interstellar matter continually producing those stars. With our new dynamics, the age of the visible stars says little about the age of the galaxy because oldest stars would have spiraled into and been consumed by the massive center black hole. A better indicator of galaxy age is the mass of the central black hole which requires time to produce and continually grows. Considering what we now claim about galaxy dynamics, the notion that galaxy rotation curves can be observed by assuming stars are in circular orbit around galaxy centers and the redshifts of stars can be used as a measure of orbital velocity is fundamentally flawed. The Hubble space telescope has had sufficient time and resolution to track the actual motion of stars in the Small Magellanic Cloud, a satellite galaxy of the Milky Way. NASA [11] found a pronounced inward spiral flow of stars towards the center which is consistent with what we propose to be the normal galaxy dynamics expected.

Expecting spiral motion is the norm, it is incorrect to assume stars are in circular orbits about galaxy centers when projecting line of sight doppler measurements. Since stars moving at higher velocity have higher cosmological deceleration from changing mass, effects are pronounced. Velocities near escape are expected for infalling interstellar gas sufficiently far from galaxy centers. Even stars which are measured to have velocity higher than escape velocity after formation will still be captured by the galaxy potential due to cosmological deceleration. The diameter of galaxies is so large that it takes considerable time just to pass by, so the cosmological effects are far more pronounced than for smaller planetary orbits. Integration of a free coast trajectory of a mass initially at escape velocity results in deceleration to circular velocity from cosmological increase of gravity potential predicted in about 1.6 billion years, a time comparable to galaxy rotation period in the outer extremes of the galaxies.

Because of this new cosmological capture process, there is a transition region which applies to galaxies in their outermost regions. These regions consist of infalling matter and stars which remain initially near Newtonian escape velocity or higher. The escape-like infalling outer region transitions to a quasi-circular stable body of the galaxy in the mid regions. It is never circular but will have a near circular tangential component of velocity, which has been misinterpreted by incorrect doppler projection. Because the infalling matter has inherent rotation with respect to the galaxy center, we know that as infalling stars decrease their radius the tangential rotation component of velocity will increase to conserve angular momentum. The cosmological deceleration from the potential change will act to reduce the velocity vector magnitude as it acts in the direction of the velocity vector. At the same time, the tangential component of velocity affecting the line-of-sight doppler measurements increases to conserve angular momentum, so the combination results in a near constant tangential component with radius observed in the doppler as interpreted. The spiral motion winds up as the radius decreases and the spiral flattens out. When the radius is small enough, the path becomes quasi circular regarding the tangential component like the inner galaxy region. The assumption of circular orbit has misled us to believe Newtonian dynamics is in play in the interior while something else controls the outer extremes of the galaxy. This led to either the MOND or dark matter halo incorrect conjectures.

We claim that a transition capture process is the MOND effect. There is no change in Newtonian gravity acceleration as supposed in the MOND interpretation. The problem occurs because doppler redshift distribution maps assume that line of sight doppler shifts come from circular velocities tangent to orbit rings centered on the galaxy center. Instead, what we have are spiral arm-like paths which begin steep in the outermost regions and are wound up tighter and flatter as the spirals approach the quasi-circular inner region. What it reflects is a capture process where the infalling matter is slowed cosmologically and captured by the galaxy. We believe that simulations of the transition region with dynamics we propose will result in apparent motion like MOND empirical interpretations of galaxy rotation based on the incorrect circular orbit projection assumption. We now have direct observational evidence of galaxy spiral star motion from NASA [11] proving this assumption incorrect. Since the speed of light is not constant, additional care should also be taken in measuring velocity from doppler redshifts.

5.2.7 Cosmological replacement for MOND

Based on the foregoing discussion we claim that the MOND galaxy dynamics conjecture is explained in its entirety by the dynamics and cosmology of our proposed framework. It should be recognized that we do not require dark matter to obtain the correct observed velocity rotation curves. This will occur naturally by updating future dynamics models with the perturbing accelerations required by Krogh gravity and our cosmology solution. Our objective here is only to provide the required framework, while we presently lack the computer models required to fully implement necessary changes. Instead, we apply conservation of angular momentum alone as we did in §5.2.5 for near circular orbit decay to the dynamics of galaxy capture of infalling matter beginning near escape velocity and spiraling into quasi circular orbit at capture. Quasi circular is defined here to mean that the tangential component of spiral motion equals circular orbit velocity normally expected with Newtonian gravity. We show that this occurs at what would formerly be interpreted as the MOND radius where the centripetal acceleration became consistent with Newtonian gravity potential of the galaxy. This is the region where flat galaxy rotation velocities are observed which led to the MOND conjecture for modified gravity. We can make significant conclusions and replace the MOND conjecture entirely by using conservation of angular momentum in the new framework. We assume a flat tangential velocity curve in the outer galaxy capture region and consider the transition to quasi circular tangential velocity. This is a special but representative case of a capture scenario which enables a simple solution consistent with observed rotation curves.

We must first correct the law of conservation of angular momentum in the variable mass context of the cosmology. We require conservation of angular momentum at different times where mass depends on the changing cosmological potential in accord with our solution. The angular momentum is taken with respect to rotation with respect to the galaxy center in question and applies to all interstellar mass engaged in free fall into a single isolated galaxy. Since the galaxy is an accretion disk, the size of the galaxy is all the mass inside the radius of some arbitrary mass such as a star in motion just outside of this radius. The effect of gravity is an acceleration vector toward the galaxy center in the radial direction. The tangential component of velocity provides an opposing centripetal acceleration in the radial direction, and we also have deceleration along the negative radial velocity vector required by the cosmology and confirmed by Pioneer probes. Cosmological deceleration occurs for both radial and tangential velocity components. There is a decay of angular momentum with respect to unit mass caused by cosmological mass change. Angular momentum of cosmological origin is the source of galaxy rotation and radial motion changes the tangential velocity component of any incoming mass. The radial acceleration depends on gravity acceleration, centripetal acceleration, and cosmological deceleration. Both mass change and radial motion dictates the tangential component of velocity by conservation of angular momentum. Angular momentum conservation for infalling masses requires:

$$v_t r m = v_{0t} r_0 m_0 \,. \tag{51}$$

Mass change from the cosmologically dependent gravity potential depends only on the Hubble constant which requires:

$$\frac{m_0}{m} = e^{-3Ht} \,. \tag{52}$$

Accounting for mass ratio dependence on cosmological time and substituting above we have a new general theory of angular momentum conservation that requires a time dependency of angular momentum per unit mass in the form:

$$v_t r = v_{0t} r_0 e^{-3Ht} \,. \tag{53}$$

We can now show that our conservation of angular momentum equation can be used to define the conditions which allow a flat tangential velocity to exist with respect to radius in an infalling region just prior to transition to a quasi-circular tangential velocity at radii below this transition. It is this region which previously has resulted in either the MOND interpretation of dynamics or the dark matter conjectures. Based on the actual observation of galaxies where this has been observed by projection of line-of-sight doppler measurements, we impose the existence of such a region at least as a potential scenario in such a transitional region. Differentiating (55) angular momentum conservation requirement with respect to time:

$$r \frac{dv_t}{dt} + v_t \frac{dr}{dt} = -3Hv_{0t}\, r_0\, e^{-3Ht} \,. \tag{54}$$

Substituting from (55) this becomes:

$$r \frac{dv_t}{dt} + v_t \frac{dr}{dt} = -3Hv_t r \,. \tag{55}$$

Solving for the rate of change of tangential velocity we have:

$$\frac{dv_t}{dt} = v_t \left(-3H - \frac{1}{r} \frac{dr}{dt} \right) . \tag{56}$$

To require a flat tangential velocity during some transition region we require that this derivative vanishes. This can be satisfied if:

$$\frac{dr}{dt} = -3Hr \,. \tag{57}$$

We also derive the radial acceleration required for acceleration balancing which by differentiation and substitution can be written:

$$\frac{d^2 r}{dt^2} = -3H \frac{dr}{dt} = 9H^2 r \,. \tag{58}$$

We can also express the time dependence of the radius in the transition region from the differential of the natural log implied by (59) as:

$$r = r_0\, e^{-3Ht} \,. \tag{59}$$

We have thus determined by conservation of angular momentum alone in the context of the new cosmology framework how the radial velocity component must vary in some transition region at the exterior region of a galaxy where we presume the tangential velocity is flat with respect to time and therefore with radius as infalling matter is captured by the galaxy from interstellar space. The matter is falling in spiral motion with both radial and tangential velocity and we need to find how it occurs that the tangential component becomes equal to the velocity of a Newtonian circular orbit. It is this condition which has been erroneously interpreted to mean that the motion is circular in the interior of the galaxy. Due to the appearance of the Hubble constant, we see that the motion in the transition region formerly thought to be the MOND region has a cosmological origin which cannot be determined without our cosmology solution.

To define how transition to quasi-circular tangential velocity occurs where the dependence on radius is no longer flat, we must investigate what the radial equation of motion requires for the balance of centripetal acceleration with the negative gravitational acceleration. We no longer have the Newtonian equation alone because the descending radial component of velocity in the region is subject to the cosmological deceleration, the same as we found for the Pioneer anomaly. This deceleration is $-3Hv$ which is the same as the result given by (60). We require the sum of the cosmological deceleration of the radial velocity plus centripetal acceleration minus gravitational acceleration must equal the net deceleration given by (60). We can write the equation balancing radial accelerations as:

$$-3H \frac{dr}{dt} + \frac{v_t^2}{r} - \frac{GM}{r^2} = -3H \frac{dr}{dt} \,. \tag{60}$$

The far-left term of this acceleration equation is the cosmological deceleration of the radial velocity. The right-hand term is the total radial acceleration which must be the same as we have just required for the flat tangential velocity curve derived from conservation of angular momentum. The far left and right terms are equal and cancel out of the radial acceleration balance. The center two terms are apposing centripetal acceleration and gravitational downward acceleration which must also cancel each other because we require that the radius chosen will be the one that satisfies this condition simultaneously with what we required for radial velocity just before the transition. We can substitute the radius in terms of radial velocity from (59) as:

$$r = -\frac{dr/dt}{3H}\,. \tag{61}$$

Since the center two terms must sum to zero for the circular tangential component velocity requirement, we require:

$$v_t^2 = \frac{GM}{r}\,. \tag{62}$$

Using the radius required by (63) in (64) we must have:

$$v_t^2 = \frac{3HGM}{-dr/dt}\,. \tag{63}$$

We can satisfy this requirement if we require the negative radial velocity is the same magnitude as the tangential component so that the flat tangential transit velocity equals to circular velocity at the transition point. The sum of the two components results in a total velocity equal to Newtonian escape velocity. The flight path angle of the spiral path would be 45 degrees at transition to quasi circular tangential velocity. The tangential velocity required which satisfies the requirement for our assumed flat velocity curve scenario is given by the relationship between velocity and galaxy mass:

$$v_\infty = (3HGM)^{\frac{1}{3}}\,. \tag{64}$$

We can also write the relationship for the radius where the transition to quasi circular spiral motion occurs as:

$$r_m = \left(\frac{GM}{9H^2}\right)^{\frac{1}{3}}\,. \tag{65}$$

where we now use subscripts for the tangential flat velocity value and the transition to quasi circular Newtonian velocity to be consistent with the conventional terms used for the past MOND conjecture. Note that the relations are similar but not identical to those obtained for MOND. We do not require the transition to a minimum acceleration constant of the universe as required by MOND but instead have only the Hubble constant because the effect can be explained in total by the cosmology proposed. The scenario we used in the derivation is only strictly valid for a truly flat velocity curve in the external transition zone formerly representing the onset of MOND dynamics. We also do not have actual circular orbits anywhere in the entire galaxy. The galaxies have spiral flow everywhere and the motion cannot be understood without the proposed cosmology. Motion is not defined by Newtonian or GR dynamics, but only by the modified dynamics introduced here. This conclusion is supported by evidence reported by NASA [11] where actual tracking of stars in a small galaxy by Hubble Space Telescope resolved the actual spiral path of individual stars.

We found in our discussion of circular orbit decay that the radial apparent orbit exponential decay with time is at twice the rate prior to the MOND-like transition to quasi circular behavior, so there is a higher negative radial velocity after the transition occurs. The decay internal to the galaxy is only influenced by mass of the galaxy internal to the radius of the tangential velocity in question, so the velocity curves act in accord with Newtonian assumptions, but it is important to recognize the radial component of the internal spiral motion because it feeds the entire galaxy into its center. Another observation of the proposed dynamics is that we can explain the existence of relatively rare observed ring galaxies. A ring will occur if a galaxy experiences a prolonged period without being able to capture interstellar gas outside the galaxy. During such a period the galaxy radius shrinks toward the center with the spiral inflow. If interstellar gas capture inflow then resumes much later, new star formation will occur at the former radius dictated by the galaxy mass inside and a now isolated ring can form well outside of the now much smaller disk of the galaxy after star formation and gas capture had ceased. Normally when galaxies are continually producing stars, the galaxy will grow from the outside and accrete toward the center.

5.2.8 Black hole formation accretion and growth

In §5.2.5, we found that circular orbits about massive bodies in strong gravity gradients cannot exist since they are subject to being triggered into a spiral inflow path by even the small cosmological deceleration inherent to our new cosmology solution. The resulting decay of the orbit causes a runaway mass increase in a strong gravity gradient such that conservation of angular momentum will not allow high enough velocity to sustain the necessary centripetal acceleration for orbit. So, we have a situation where cosmological decay of orbit radius ensures that any orbit will ultimately reach a critical radius ending in spiral inflow into a black hole. There is thus a dynamic mechanism that assures accretion and growth of center black holes in galaxies with a supply of low radius stars or gas. Furthermore, the cosmological decay of all orbits ensures that orbiting material is doomed to reach that critical orbit radius with sufficient cosmological time. The age of stars in a visible galaxy is limited because supermassive black hole growth is a natural evolution of galaxies. Accretion of material into a black hole is much more efficient than gravity wave radiation to deplete angular momentum even though this still occurs with the Krogh gravity theory. This explains why supermassive black holes have more than adequate time to form even in the earlier universe now seen by the James Webb Space Telescope.

5.2.9 Superluminal galactic jet acceleration

Several galaxies have been observed to have Active Galactic Nucleus (AGN) particle jets generally perpendicular to the galaxy disks and apparently having a source near the center where a massive black hole is present. Many of the observed jets extend to great distances from the galactic center and appear to continue to accelerate far from the center while achieving superluminal velocities more than light speed. Examples of such AGN galaxy jet observations are discussed extensively by Meyer *et al* [12]. Present theory does not provide a cause for why a stream of particles would accelerate in the process of escaping powerful gravity gradients associated with a concentrated massive black hole, much less that they would reach velocities exceeding the speed of light we know in the process. We will show here that this is a natural result of our new dynamics and the Krogh gravity theory resulting directly from conservation of relativistic momentum with decreasing particle mass as the potential changes. It is the most extreme example of the same cause we found for the Earth flyby anomaly upgraded to relativistic momentum and relativistic epoch velocity.

Krogh discusses how massive objects which, with GR theory would be black holes, are never quite black regardless of how massive they are, since a small amount of light and even particles can escape from the mass. See for example his paper, "Galactic Nuclei and Jets in Wave Gravity" [13]. With the description, atomic particles like electrons and protons still exist sustaining the mass of the object but as is required by the theory, the particle size has shrunk to allow a highly compact volume which is not a singularity. A small fraction of charged particles with sufficiently high relativistic velocity can escape directly from the central mass along magnetic field lines at poles north and south and generally perpendicular to the spinning galactic disk. An accretion disk is not required to supply the escaping particles.

We need now to extend our conservation of momentum equations to relativistic speeds for this specific case to explain the observed acceleration that drives the jets. We return now to (22) beginning by repeating it here only with a new definition of how it applies at the local epoch. The equation originally was written to show how velocity changes with universal potential for originally created particles at the matter epoch of the cosmology solution. We write it again as:

$$v = \frac{v_0\, e^{3\phi}}{\sqrt{1 - (v_0^2/c_0^2) + (v_0^2/c_0^2)\, e^{2\phi}}}\,. \tag{66}$$

This equation was derived by equating the relativistic momentum to different points in time where the potential had changed from the epoch where velocity was v_0 to a later time where dimensionless potential ϕ resulted in a mass change in accord with the exponential scaling law given by Krogh theory. In effect it is a coast trajectory which would apply to any time dependent potential change. The dimensionless potential becomes the time variable describing the motion. We want to apply this equation much like we did successfully for the Mercury orbit in the non-relativistic case where conservation of momentum provides a contribution to acceleration in addition to any other accelerations resulting from local gravitational bodies. We no longer have the luxury of selecting a local speed of light which is close enough to consider a constant for the trajectory as for the planet Mercury or an Earth flyby. For a galactic jet escaping from a black hole, the speed of light changes rapidly with motion in the strong gravity gradient and we need to define the dimensionless potential by dividing by light speed squared to apply our gravity theory. For this discussion, we only need to tease out the instantaneous acceleration model for any location and time chosen as the instantaneous epoch of the trajectory.

Consider then (68) as a means to account for how much velocity would change if relativistic momentum is conserved as mass increases for a particle escaping from a massive galactic center. The total acceleration would need to include the deceleration from the local gravity gradient toward the mass center while the conservation of momentum from (68) would account for the reduction in mass as the particle moves radially outward. In the equation, the dimensionless potential is assumed to be made non-dimensional by dividing by c_0^2 which is the light velocity at the instantaneous epoch where velocity is v_0. The dimensionless potential varies with radial outward movement where we are only interested in the incremental change in the gravity gradient from motion at radial velocity v_0. With this understanding, we differentiate (68) with respect to time to obtain the acceleration from momentum conservation only. The resulting complex equation can now be simplified with the consideration that we can choose the dimensionless potential to be zero at epoch where we are evaluating the acceleration. If we do that, all the terms with exponentials become unity and we tease out the instantaneous acceleration resulting from conservation of momentum alone which is given by the simple equation:

$$\frac{dv}{dt} = v_0 \left(3 - \frac{v_0^2}{c_0^2}\right) \frac{d\phi}{dt}\,. \tag{67}$$

We see that if the velocity ratio v_0^2/c_0^2 is negligible, the result is the same as the previous perturbing accelerations used. In the relativistic case the initial velocity becomes large so that this cannot be considered a small effect any longer. If we substitute for the derivative of the dimensionless potential the appropriate dot product of velocity with the gravity gradient, we have the result for momentum conservation with changing mass only:

$$\frac{dv}{dt} = \frac{v_0^2}{c_0^2} \left(3 - \frac{v_0^2}{c_0^2}\right) \nabla \Phi_g\,. \tag{68}$$

It is immediately clear from this result that the leading factors multiplied times the gravity gradient can result in an acceleration radially outward due to decreasing mass greater than unity with a sufficiently high relativistic initial velocity. This means that highly relativistic particles will have a net acceleration greater than the attractive acceleration toward the gravitational body. Particles moving at light speed have the greatest factor of two times the gravity gradient so the particles accelerate at the same rate we would normally expect them to fall towards the body with Newtonian gravity. When the central body is a black hole, the gravity gradient is very large, and the acceleration will be substantial.

We have explained why relativistic galactic jets accelerate but the question of apparent superluminal speeds needs further explanation. In accord with the Krogh gravity theory, the speed of light is near zero at a sufficiently massive body. Light speed increases as the radial distance from the body increases. We can do the same differentiation of the required change in light speed with the dimensionless potential with the result that light speed accelerates at the instantaneous rate:

$$\frac{dc}{dt} = 2c_0\,\frac{d\phi}{dt}\,. \tag{69}$$

Again, substituting for the derivative of the dimensionless potential at some velocity υ_0 we have the result for acceleration of light speed:

$$\frac{dc}{dt} = 2\left(\frac{\upsilon_0}{c_0}\right)\nabla\Phi_g\,. \tag{70}$$

Comparing factors in (70) and (72), we conclude that light speed accelerates faster than jet escaping particles for any velocity. Eq. (70) is the perturbing acceleration not including the gravity potential acceleration toward the black hole. There is no scenario where the accelerating particle can exceed light speed, which is what we should expect from special relativity. We thus have explained why the particles accelerate, but the observation of superluminal velocity is an illusion caused by the fact that the cosmology tells us that light speed in the past is greater than present. By squaring both sides of (9), we know from our cosmology solution that the light speed ratio from emission in the past compared to the present is given by:

$$\frac{c_e}{c_n} = (1+z)^2\,. \tag{71}$$

We see for example that at a galaxy redshift of 1.5 the light speed at time of emission from a distant galaxy is 6.25 times current light speed. We therefore predict that a galactic particle jet that leaves the center at relativistic speeds and accelerates can be expected to appear superluminal when we are assuming the wrong light speed. This is a remarkable confirmation of our new cosmology framework. We saw previously the redshift itself requires a light speed increase contribution.

5.2.10 Source of cosmic rays

Galactic jet acceleration provides a continuous supply of relativistic particles in the universe. We now have from Krogh [13] that black holes are always capable of producing and leaking relativistic particles in the form of jets following magnetic field poles north and south. From our discussion of superluminal jet accelerations, which are observed from active galactic nuclei, we further have explained how these jets accelerate and remain relativistic through escape from the black hole center and for that matter from the galaxy as well. We also expect from our previous cosmology discussions that the universe is so old that dead galaxies which have run out of interstellar gas and in some cases may have been totally consumed by the black hole center are likely to exist and may even well exceed the number of active visible galaxies. According to arguments from Krogh [13], the jets are expected even in the absence of any accretion disk, so the jets should exist for isolated unobservable black holes throughout the universe. We know from (23) that relativistic particles that survive collisions will remain relativistic with conservation of momentum as the speed of light slows cosmologically. We can with these arguments claim a continuous source of cosmic ray particles is predicted in our cosmology framework.

6 Concluding discussions

We have shown a new cosmology framework which explains why distant galaxies are redshifted without universe expansion while not requiring tired light decay in transit. By direct integration of variable light speed as known from our solution of the gravity potential differential equation and Krogh gravity theory, we derive a new Hubble curve equation consistent with observed redshift versus distance. The exponential form of the equation for the redshift factor derived directly from the theory agrees exactly with the same equation derived empirically from observations and ruled inconsistent with consensus universe expansion.

Solution of the governing equation for the time dependent universal gravity potential implies a matter creation epoch boundary condition with a gravitational matter observational horizon expanding at the variable speed of light derived from our solution. The matter creation was necessarily hot if for no other reason that there could be no preferred reference frame. We can speculate that matter creation occurred from a vacuum phase change, although just as for the Big Bang, there can be no specific cause of origin which is common to any theory of origins. Cooling occurred from conservation of momentum as particle masses increase with increasing time dependent gravity potential. A CMB surface of last scattering began after cooling to recombination temperature occurred. The surface is uniform because the density to the matter gravitational horizon is averaged over distances in the trillions of light-years at today's speed. The primordial plasma was fully thermalized and mixed over many Hubble times before recombination temperature was reached.

Assuming 3 000 K recombination temperature, time since the CMB surface formed was approximately 49 billion current length years, corresponding to about 453 billion years atomic time. There has been more than sufficient time for massive mature galaxies and black holes to form as observed by JWST. In fact, from the theory the relation between the Hubble constant and average matter density requires that density is 4/3 of classical Big Bang critical density. The age since CMB formation and higher matter density suggests prolific star formation. It is likely that many stars and galaxies are long since dead and unobservable except for their gravity. There is no reason to require non-baryonic dark matter which has never been found to exist. We believe that observed galaxy rotation can be fully explained without non-baryonic dark matter using the proposed dynamics here replacing the MOND interpretation as well. Dark energy and associated expansion are not relevant or necessary to have a valid Hubble curve shape.

Primordial light speed remains an unknown order of magnitude higher than present which would be necessary due to the exponential scaling equation which it obeys according to the Krogh theory. The dimensionless exponent is in number of Hubble times. Cooling of the plasma would require many Hubble times to reach the assumed recombination temperature of the CMB. There has been about 3.5 Hubble times making up the 49 billion current years since recombination. Primordial light speed is not particularly important to the cosmology if it is sufficiently high, because it only affects how much time the universe existed only in the plasma state. It also scales the distance to the matter horizon and is the cause for smoothness of the CMB because of the enormous distances over which the matter density is averaged. It essentially replaces inflation in consensus cosmology without *ad hoc* assumptions.

The Hubble constant is the most important constant of the cosmology. This constant essentially defines the dimensionless Hubble times which are required as the independent variable for the cosmology solution equations. We know exactly from the theory how it can be determined from the average matter density of the universe, but that is not an observable quantity especially since most of the matter is invisible. Three methods come to mind as alternatives. The first is to develop the conventional distance ladder as in the past and try to find the Hubble constant that best fits the redshift versus distance. It would be necessary in this process to ensure that any analysis involved with processing the various types of data used such as standard candles removes any prior possibility of embedded assumptions of universe expansion with redshift. We also need to look at each type of observation that may be affected by the evolution of physical constants and atomic time with cosmological dimensionless potential. This could change the brightness of supposed standard candles at different cosmological times. We showed in Figure 4 that data previously obtained by others can be fit reasonably well with only a single Hubble constant as an unknown. We cannot say that the assumptions embedded in the old data are any longer correct in the new context. Development of the distance ladder revisions as necessary would be beyond the scope of our goal of providing only a new framework here. We caution that this method would best be done by investigators with custody of the raw data who would need to process that data with knowledge of the new context and gravity theory.

A second method which is entirely new is to measure the Hubble constant directly from observed cosmological deceleration, such as observed for the Pioneer probes. Unfortunately, the accelerations are small and can be contaminated by other small acceleration causes. We have already pointed out here that there are other small perturbing accelerations resulting from transit through local gravity potentials from any and all gravitational bodies. We do believe that the local potentials are well known and the trajectories of the probes as well so that it should be relatively easy to model these and subtract them out. The remaining non-cosmological contributors would still need to be removed as effectively as possible. We would encourage investigators to make such and effort with the goal of teasing out a Hubble constant from data that already exists. A better application of this new approach would be to design and launch a new probe tailored for this purpose alone. The probe should be launched at the highest velocity which can reasonably be obtained since the cosmological acceleration is proportional to velocity. It should include the best possible tracking technology for detecting the small anomalous acceleration and should be designed to minimize any external causes of acceleration. This may provide an alternative allowing direct measurement of the Hubble constant.

A third method might be to take another look at the CMB radiation structure we already have and see if we can deduce the Hubble constant from the CMB structure. We no longer have expansion in play if comparing past structure to present universe structure, and we need to know for sure what the recombination temperature was because it too could scale with the past cosmological potential. The temperature determines the redshift and redshift plus Hubble constant determines distance of the surface required to understand the scale of structure. Any modeling of acoustic oscillations would have to be reworked because the speed of both light and sound is different at CMB time. Speed of light is tied to the black body temperature ratio and speed of sound is tied to both temperature and scaled lower particle masses, so both speeds are much higher than we have now. If this method has any credibility it needs to be determined by experts in this area.

Since the entire cosmology framework proposed rests on adopted new Krogh gravity theory which replaces General Relativity, we have included discussions of numerous predictions for gravitational dynamics changes implied by use of the teachings of Krogh theory of gravity. Since the new theory no longer involves curvature of space as with GR, but rather is restricted to flat Euclidean space, it requires modeling of any accelerations not a part of Newtonian gravity dynamics formerly replaced by GR. It still must replace GR dynamics where previously successful, but we found other predictions not predicted by GR which strongly support the Krogh theory. Since the Krogh theory requires changes to physical constants with the dimensionless gravity potential and these include rest mass, rest energy, and light speed.

It is not a trivial matter to tease out what the accelerations should be especially in relativistic dynamics. Krogh has used a few different approaches with at least limited success. Because mass and rest energy change, the usual conservation assumptions are risky. In this paper we have taken the approach uniformly that the only reliably conserved entity is momentum. We use this approach alone to tease out non-Newtonian acceleration dynamics. We confirm the methodology by proving that resulting Mercury orbit dynamics are consistent with confirmed General Relativity predictions.

Using conservation of momentum as our only assumption, we develop predictions not predicted previously by GR, but which have testable observational information. These include Earth flybys, JUNO Jupiter orbiter, Pioneer Probe, apparent superluminal galactic jet acceleration, galaxy rotation and spiral flow, and more rapid formation of black holes through faster accretion. All have been observed but those in possession of the observational data and modeling tools needed for adequate testing of our theory do not have the benefit of our model changes required. Perhaps the most remarkable is superluminal galactic jets, since the cosmology itself predicts that this is possible for relativistic starting velocities because the speed of light is far higher at distant galaxies. We predict the mechanism of acceleration through momentum conservation, while the changing light speed that the cosmology requires explains and enables apparent superluminal velocities for distant galaxies.

We have further shown that galaxy dynamics cannot be explained in the Newtonian or GR context where near circular orbits are presumed to describe the motion. Instead, all masses in the galaxy structure are engaged in spiral flow paths such that the entire galaxy is an accretion disk flowing into the center black hole. The outer region can exhibit flat tangential velocity which we can fully explain as a transition capture cosmological process without requiring MOND or dark matter *ad hoc* assumptions. Ring galaxies can also be explained by an interruption of interstellar matter inflow for an extended period followed by a resumption forming a ring of new star formation.

If the Krogh gravity theory is accepted as it must for this cosmology to have merit, there are consequences beyond cosmology. Cosmology was the primary objective in this work. Besides replacing General Relativity, Krogh's theory has further consequences for quantum theory and particle physics. Energy no longer gravitates, so it cannot be a contributor to mass of particles. It may imply that the Higgs mechanism accounts for all the particle mass. It might suggest that the Higgs energy is an indicator of the universal gravity potential since the Krogh theory requires particle masses and rest energies to change with the gravity potential.There is no longer a cosmological constant problem. Energy does not gravitate so the vacuum energy can be very large without creating a problem. The theory requires that the gravity potential changes the quantum vacuum state including speed of light and virtual particles. Models have already been introduced as for example Marcei Urban *et al* [14] which show how virtual particles could change light speed. Since all particles shrink and have reduced rest energy per particle in accord with Krogh theory, this can require a higher virtual particle density which would be expected to slow light speed. The gradient of the potential may be tied to a gradient in particle density.

As a further speculation we can note that if gravity causes the vacuum state to change as proposed, then it is the vacuum state which causes the acceleration of gravity. It is an acceleration and not a force, like principles shared by General Relativity. If there are a greater number of smaller vacuum particles deeper into a gravity well, then the gravity gradient is related to the virtual particle density gradient. If the real particles of an immersed test body are annihilated by virtual vacuum antiparticles they would be replaced by real particles from the vacuum in a preferential direction toward the higher particle density gradient. It seems plausible that the entire body could have all its particles replaced in a preferred direction toward the density gradient, resulting in an apparent acceleration. There would be no force explaining why a body in free fall experiences weightlessness rather than acceleration inertial forces.

If this is the mechanism of gravity acceleration, and we had a means to change the local vacuum state artificially, we could produce antigravity and we could accelerate objects or even occupants without experiencing inertia forces even for high accelerations. Obviously, we don't know how to do that artificially now, but we can certainly speculate that this mechanism could arise from the Krogh approach to gravity as a change of the quantum vacuum state and it shows how his theory leads to quantum gravity. Without a force there would not seem to be a need to require a new particle like the graviton.

Acknowledgements

This cosmology framework is based in its entirety on Kris Krogh gravity theory [1]. His quantum vacuum approach eliminates General Relativity's Big Bang expansion, the primary cause of our pending cosmology crisis. A preprint has previously been published [15].

Received on April 4, 2025

References

1. Krogh K. Gravitation without curved space-time. arXiv: astro-ph/9910325v23, 2006.
2. Krogh K. Origin of the blueshift in signals from Pioneer 10 and 11. arXiv: astro-ph/0409615v4, 2005.

3. Labbe I., van Dokkum P., Nelson E., *et al*. A population of red candidate massive galaxies 600 Myr after the Big Bang. *Nature*, 2023, v. 616, 266–269.
4. Asencio E., Banik I., Kroupa P. The El Gordo Galaxy Cluster Challenges ΛCDM for Any Plausible Collision Velocity. *The Astrophysics Journal*, 2023, v, 954 (2).
5. Lovyagin N., Raikov A., Yershov V., Lovyagin Y. Cosmological Model Tests with JWST. arXiv: astro-ph/2212.06575.
6. Marosi L. A. Extended Hubble Diagram on the Basis of Gamma Ray Bursts Including the High Redshift Range of z=0.0331-8.1. *International Journal of Astronomy and Astrophysics*, 2019, v. 9, 1–11.
7. LaViolette P. A. Expanding or Static Universe: Emergence of a New Paradigm. *International Journal of Astronomy and Astrophysics*, 2021, v. 11 (2).
8. Anderson J. D., Laing P. A., Lau E. L., Liu A. S., Neito M. M. and Turyshev S. G. Study of the anomalous acceleration of Pioneer 10 and 11. *Phys.Rev. D*, 2002, v. 65, 082004.
9. Acedo L., Piqueras P., Morano J. A. A possible flyby anomaly for Juno at Jupiter. *Advances in Space Research*, 2018, v. 61 (10), 2697–2706.
10. Acedo L. Anomalous accelerations in spacecraft flybys of the Earth. *Astrophys Space Sci*, 2017, v. 362, 225.
11. NASA Hubble Mission Team. NASA's Hubble Finds Spiraling Stars, Providing Window into Early Universe. 2022. https://science.nasa.gov/missions/hubble/nasas-hubble-finds-spiraling-stars-providing-window-into-early-universe/.
12. Meyer E. T., Shaik A., Tang Y., *et al.*. Variability of extragalactic X-ray jets on kiloparsec scales. *Nat Astron*, 2023, v. 7, 967–975.
13. Krogh K. Galactic Nuclei and Jets in Wave Gravity. arXiv: astro-ph/0606489v3, 2006.
14. Urban M., Couchot F., Sarazin X., Djannati-Atai A. The quantum vacuum as the origin of the speed of light. *The European Physical Journal D*, 2013, v. 67, art. no. 58.
15. Drake J. H. Krogh Quantum Gravity Explicitly Predicts Hubble Redshift Curve and JWST Findings without Expansion. viXra: 2404.0065.

Testing Objective Reduction via Collective Human Measurement: A Macroscopic Qubit Proposal

Travis S. Taylor

Department of Physics, University of Alabama in Huntsville, Huntsville, AL, USA.
Email: tst0072@uah.edu

We propose a novel, testable framework for constructing macroscopic qubits and qudits using ensemble human agency as both the source of quantum state generation and the mechanism for collapse. Inspired by the Big Bell Test — which demonstrated that human-generated randomness can close loopholes in Bell inequality experiments — we extend this paradigm by defining human-driven superposition states.

In our model, a collective of human choices (e.g. heads or tails) defines a latent quantum state within a formal Hilbert space constructed from human choices, which remains unresolved until a collective measurement is made. While not physically coherent in the traditional sense, the ensemble mimics quantum superposition through the structure of collective uncertainty and delayed resolution. We demonstrate that this statistical ensemble satisfies the core properties of a qubit or qudit, including superposition and collapse dynamics, without relying on traditional quantum coherence.

We introduce a critical threshold N_c of participants needed to reliably induce collapse and derive estimates based on analogies with quantum decoherence, statistical sampling theory, and Penrose's Objective Reduction (OR) model. We also propose experimental protocols for multi-qubit scaling, implementing quantum gates such as CNOT and Hadamard, and creating entangled macroscopic states using coordinated human action.

This model provides a low-barrier, scalable platform for participatory quantum simulation, with implications for the foundations of quantum mechanics, quantum computation, and the role of conscious observers in wavefunction collapse.

1 Introduction

Quantum mechanics fundamentally hinges on the role of the observer, from the Einstein–Podolsky–Rosen (EPR) paradox [1] to the experimental verification of Bell inequalities [2]. The Big Bell Test [3] harnessed human-generated randomness from over 100,000 participants worldwide to close the freedom-of-choice loophole in quantum experiments, demonstrating that collective human input can influence quantum outcomes. Turiel *et al.* [4] further revealed that human perception exhibits statistical biases distinct from quantum randomness, suggesting that human agency could play a deeper role in quantum processes.

In this work, we propose a macroscopic qubit model in which a physical object — a penny — is placed into a notional superposition, with its final state (heads or tails) determined by the ensemble average of many human decisions. This model transforms the logic of the Big Bell Test from influencing microscopic quantum systems to collapsing macroscopic states via conscious, collective choice.

Quantum computing traditionally relies on microscopic qubits [5], where coherence can be preserved in isolated, cryogenically-cooled environments. In contrast, macroscopic quantum systems typically succumb to rapid decoherence due to environmental interactions [6]. However, Penrose's Objective Reduction (OR) model [7] proposes that gravitational self-energy itself may induce collapse, suggesting that the boundary between quantum and classical behavior is governed by spacetime geometry rather than environmental noise [8, 9].

Building on this and the Big Bell Test framework, we define the "penny qubit" not as a single physical object in superposition, but as an ensemble average over human decisions — each participant flipping or selecting a coin state. The system's quantum-like behavior emerges from the collective uncertainty prior to measurement. This model allows us to probe whether human-driven statistics — potentially modulated by gravity — could bridge the gap between microscopic quantum phenomena and macroscopic consciousness.

While the framework is grounded in statistical ensemble theory, we propose that if Penrose's OR model and the Big Bell Test findings reflect true quantum dynamics, then collective human agency may serve not only as an analogue but as a legitimate quantum measurement system — one driven by spacetime geometry, gravitational self-energy, and conscious observation.

2 Background

2.1 The Big Bell Test

The Big Bell Test [3] demonstrated that human-generated randomness can serve as a valid input for closing loopholes in Bell inequality experiments. Over 100,000 participants contributed unpredictable binary decisions, which were used in real-time to control measurement settings in entangled particle experiments. This large-scale, crowdsourced approach strengthened empirical support for quantum nonlocality by eliminating the freedom-of-choice loophole.

Turiel *et al.* [4] examined human-generated sequences and identified statistical biases — such as nonuniform distributions and pattern tendencies — that differ significantly from ideal quantum randomness. While their study did not target wavefunction collapse, it highlighted the structure of human unpredictability and its divergence from truly random quantum processes. These findings laid the groundwork for exploring whether collective human choice could itself serve as a measurement apparatus.

2.2 Standard qubits and superposition

In conventional quantum systems, a qubit is defined as a coherent superposition of two basis states:

$$|\psi\rangle = \alpha\,|0\rangle + \beta\,|1\rangle\,, \tag{1}$$

where α and β are complex amplitudes constrained by $|\alpha|^2 + |\beta|^2 = 1$. Quantum gates manipulate these amplitudes, enabling interference, entanglement, and computation that surpass classical limits [5]. However, maintaining such superpositions requires isolation from environmental noise, as interactions lead to decoherence and classical behavior [6].

2.3 Conceptual framework: human-driven macroscopic superposition

We propose a new interpretation of a macroscopic qubit based on ensemble human agency. Rather than preparing a single physical system in a coherent superposition, we treat the binary decisions of many human participants — such as selecting "heads" or "tails" for a coin flip — as forming a statistical superposition:

$$|\psi\rangle = \frac{1}{\sqrt{2}}\left(|\mathrm{Heads}\rangle + |\mathrm{Tails}\rangle\right)\,. \tag{2}$$

In this framework, each human choice acts as a probabilistic contribution to an unresolved state. The final state remains unresolved until a collective measurement aggregates the ensemble. The system collapses when the fraction of human choices f_H crosses a defined decision boundary (e.g. $f_H > 0.5$). This threshold is not a statistical confidence level but a deterministic collapse condition defined by the ensemble dynamics. A critical number of participants N_c may be required to ensure the superposition collapses reliably, drawing parallels to decoherence thresholds and sampling theory.

This model differs from traditional qubits in that it does not rely on phase coherence or physical isolation. Instead, it leverages uncertainty in aggregated human decisions to simulate quantum behavior at macroscopic scales. The collapse process is driven by observation — either by a human observer or an algorithmic tally — mirroring the role of measurement in standard quantum mechanics.

2.4 Relation to Objective Reduction and spacetime discreteness

Penrose's Objective Reduction (OR) model [7] offers a gravitational mechanism for wavefunction collapse, proposing that superpositions involving significantly different spacetime curvatures become unstable and collapse spontaneously. This implies that the quantum-classical boundary is not merely a matter of environmental decoherence but may depend on gravitational self-energy and spacetime geometry.

In our macroscopic model, we hypothesize that the number of human participants required to induce collapse (N_c) could scale with gravitational instability in the superposed configurations. If collective human agency acts as a measurement mechanism, it may couple to gravitational degrees of freedom, potentially enabling tests of spacetime discreteness or quantum gravity effects [8, 9].

This framework suggests a novel approach to probing quantum foundations: by treating human statistical ensembles as macroscopic qubits, we open a pathway to explore whether conscious agents can drive collapse and whether such collapse is influenced by gravity.

2.5 Measurement dynamics

We propose to use an ensemble number of people making a choice to place the coin on heads or tails. Each qubit state is determined by the ensemble average to be heads or tails upon collapse. The collapse is modeled as:

$$|\psi\rangle \xrightarrow{\text{Human Average}} \begin{cases} |\mathrm{Heads}\rangle & \text{if } f_H > 0.5\,, \\ |\mathrm{Tails}\rangle & \text{if } f_H < 0.5\,, \end{cases} \tag{3}$$

where f_H is the fraction of heads across all choices. Ties ($f_H = 0.5$) may require N_c to break ambiguity.

2.6 Threshold effects

We hypothesize the existence of a critical threshold N_c — the minimum number of human participants required to induce collapse. This could parallel decoherence thresholds in standard quantum systems.

Clarifying the term "quantum-like"

Throughout this paper, we refer to the proposed human-driven systems as exhibiting "quantum-like" behavior. By this, we do not mean that the system is merely a classical simulation of quantum mechanics. Rather, we suggest that collective human agency — particularly when treated as unresolved until a final ensemble average is observed — shares key structural and operational features with quantum systems. These include:

- Representation of states in a Hilbert space,
- Superposition of possible outcomes prior to measurement,

- Collapse dynamics triggered by observation or ensemble resolution,
- Rule-based analogs of entanglement and quantum gate operations.

Importantly, we do not assume that human agency is a classical stochastic process. Instead, we remain open to the possibility — motivated by Penrose's Objective Reduction (OR) and Orch-OR[‡] — that decision-making may involve non-classical or gravitationally-linked effects. Thus, the system behaves formally like a quantum information structure, and may in fact reflect deeper quantum-gravitational dynamics tied to cognition and observation.

3 Derivation of the human agency qubit

To formally ground the concept of a macroscopic qubit governed by human agency, we now derive its structure within the framework of quantum information theory. We demonstrate that the ensemble of human decisions admits a Hilbert space representation, forms legitimate superposition states, and permits a meaningful projection-based collapse rule analogous to standard quantum measurement. This section provides the mathematical and conceptual scaffolding for the central hypothesis of the paper: that collective human decisions can simulate quantum superposition and collapse dynamics.

3.1 Single participant as a basis state

We begin by modeling each human participant as a binary decision-maker who consciously chooses either "heads" (H) or "tails" (T). These are mapped onto orthonormal quantum basis states:

$$|H\rangle \equiv |0\rangle\,, \qquad |T\rangle \equiv |1\rangle\,. \tag{4}$$

Each participant thus occupies a two-dimensional Hilbert space $\mathbb{C}^2$ analogous to a qubit in quantum mechanics.

3.2 Ensemble state prior to measurement

Let N participants each make a choice, which is kept hidden prior to tallying. The overall system can be represented as a tensor product of individual states:

$$|\Psi\rangle = |\psi_1\rangle \otimes |\psi_2\rangle \otimes \cdots \otimes |\psi_N\rangle\,. \tag{5}$$

Assuming no predetermined decisions, each person exists in a balanced undecided state:

$$|\psi_i\rangle = \frac{1}{\sqrt{2}}\left(|0\rangle + |1\rangle\right)\,. \tag{6}$$

The total state becomes a uniform superposition over all possible 2^N outcome strings:

$$|\Psi\rangle = \bigotimes_{i=1}^{N} \frac{1}{\sqrt{2}}\left(|0\rangle + |1\rangle\right) = \frac{1}{2^{N/2}} \sum_{\mathbf{x}\in\{0,1\}^N} |\mathbf{x}\rangle\,. \tag{7}$$

This state spans the 2^N-dimensional Hilbert space $\mathcal{H} = (\mathbb{C}^2)^{\otimes N}$.

3.3 Macroscopic collapse rule

We define a macroscopic observable: the majority choice fraction

$$f_H = \frac{1}{N}\sum_{i=1}^{N} x_i\,, \tag{8}$$

where $x_i = 0$ for heads and $x_i = 1$ for tails. A measurement projects the superposition onto one of two macrostates:

$$|\Psi\rangle \xrightarrow{\text{tally}} \begin{cases} |\text{MajH}\rangle & \text{if } f_H < 0.5\,, \\ |\text{MajT}\rangle & \text{if } f_H > 0.5\,. \end{cases} \tag{9}$$

Here, $|\text{MajH}\rangle$ and $|\text{MajT}\rangle$ are defined as normalized superpositions over all strings with majority heads or tails, respectively:

$$|\text{MajH}\rangle = \frac{1}{\sqrt{N_H}} \sum_{\substack{\mathbf{x}\in\{0,1\}^N \\ \#(0)>\#(1)}} |\mathbf{x}\rangle\,, \tag{10}$$

$$|\text{MajT}\rangle = \frac{1}{\sqrt{N_T}} \sum_{\substack{\mathbf{x}\in\{0,1\}^N \\ \#(1)>\#(0)}} |\mathbf{x}\rangle\,, \tag{11}$$

where N_H and N_T are normalization factors counting the number of majority heads or tails configurations.

3.4 Hilbert space structure and interpretation

This derivation confirms that the system of N human decisions admits a quantum-like structure:

- Each participant is a 2-state quantum object.
- The ensemble spans a Hilbert space $\mathcal{H} = (\mathbb{C}^2)^{\otimes N}$.
- Prior to tallying, the system resides in a uniform superposition over 2^N microstates.
- Measurement projects onto macrostates based on the majority decision, simulating a quantum collapse.

This framework underpins the proposed human agency qubit and supports its use in defining higher-order quantum gates and algorithms in subsequent sections.

4 The macroscopic qubit proposal

Building upon the formal derivation in §3, we now shift from theoretical structure to practical implementation. The macroscopic qubit defined by human agency exists as a distributed ensemble across multiple conscious agents, each of whom selects between two defined basis states: "heads" or "tails". This collective system resides in a quantum-like unresolved state until measurement — here defined as the aggregation of all participant decisions — is performed. This section outlines how such macroscopic qubits can be constructed, collapsed, and manipulated in both physical and virtual settings.

[‡] Orchestrated Objective Reduction

4.1 Operational representation and collapse rule

The macroscopic qubit exists in a latent state until a majority decision among N participants is tallied. The state is interpreted as:

$$|\psi\rangle = \frac{1}{\sqrt{2}} \left(|\text{Heads}\rangle + |\text{Tails}\rangle \right) , \tag{12}$$

where "heads" and "tails" are collective macrostates defined by a statistical majority. Collapse occurs through measurement of the ensemble average:

$$|\psi\rangle \xrightarrow{\text{Tally}} \begin{cases} |\text{Heads}\rangle & \text{if } f_H > 0.5\,, \\ |\text{Tails}\rangle & \text{if } f_H < 0.5\,, \end{cases} \tag{13}$$

with f_H denoting the fraction of participants who selected "heads". A perfect tie (i.e. $f_H = 0.5$) may require an external tiebreaker, a re-measurement, or a minimum threshold N_c to resolve ambiguity.

4.2 Interpretation of superposition

Unlike microscopic qubits, which maintain quantum phase coherence across superposed basis states, the macroscopic qubit's superposition is epistemic — rooted in the unresolved knowledge of the ensemble rather than a physical quantum state. Nevertheless, as shown in §3, the system's collective Hilbert space structure and projection-based measurement rules replicate the algebraic and statistical behavior of genuine quantum states.

4.3 Physical vs. virtual implementation

There are multiple modalities for realizing macroscopic qubits in practice:

- **Physical implementation:** Each participant chooses heads or tails with a real coin and records the outcome privately. Results are then aggregated to determine the collapsed state. The coin acts as a symbolic mediator rather than a literal superposed system.
- **Virtual implementation:** Participants use an online interface or app to select a value (heads or tails), with the results aggregated in real-time. This enables scalable, synchronous experiments with thousands of global participants — similar to the infrastructure of the Big Bell Test [3].

In both cases, it is critical that the outcome is hidden until the final tally, preserving the ensemble's unresolved state and ensuring authentic collapse behavior.

4.4 Measurement and observer role

Measurement is not performed on each participant's individual choice but on the aggregated majority. This aggregate observation fulfills the quantum role of "collapse" from a system-wide perspective. The observer in this context may be human (e.g. a coordinator) or algorithmic (e.g. a tallying server), but in both cases the tally marks the point of transition from superposition to resolved classical state.

4.5 Robustness to environmental noise

Because macroscopic qubits in this model do not rely on maintaining quantum phase coherence, they are naturally robust against decoherence in the traditional sense. Instead, errors arise from incomplete data, human indecision, or measurement bias, which can be handled through classical redundancy, majority voting, or sampling corrections. This suggests a new paradigm of quantum-like computation where resilience arises from statistical mechanics rather than cryogenic isolation.

4.6 Implications for qubit scaling

This framework permits large-scale implementation of qubits without the technological burdens of traditional quantum systems. Assuming a critical number of participants N_c (further explored in §6) is available per qubit, a multi-qubit system can be constructed with $M \times N_c$ participants, enabling simulation of quantum algorithms on crowdsourced platforms.

4.7 Link to Objective Reduction and cognitive measurement

As with Penrose's OR model, the macroscopic qubit collapse may reflect deeper links between spacetime geometry and measurement. If the decision and measurement processes are mediated through conscious observation, then human agency might act as a gravitationally relevant component of collapse — especially in large-scale ensembles. This motivates experimental tests not only of collapse thresholds but also of possible correlations with gravitational self-energy or spatial configuration.

5 Building a macroscopic quantum computer

5.1 Scaling to multiple qubits

Assuming a critical threshold N_c participants can control a single macroscopic qubit, we propose constructing a 10-qubit system using $10 \times N_c$ participants as discussed in §2.

This could be implemented in reality with N individuals taking turns choosing with one coin or many choosing with multiple coins. The end resulting ensemble average is the qubit's final state. This could also be done virtually on a computer.

5.2 Entanglement and quantum gates

To perform quantum computation, qubits must be entangled and manipulated through quantum gates. Participants would coordinate their choices across qubits to implement entangling operations like the CNOT gate. For example, a control group could synchronize their decisions based on the state of another qubit, enabling conditional logic between pennies.

To demonstrate the Einstein-Podolsky-Rosen (EPR) experiment [1], we propose entangling two macroscopic penny qubits. Participants controlling each qubit would coordinate their choices to maintain entanglement. Measurements on one penny would instantaneously influence the state of the other, showcasing nonlocal correlations. By varying the measurement bases chosen by the participants, we could observe violations of Bell inequalities, providing macroscopic evidence of quantum entanglement.

The protocol for the EPR demonstration involves:

1. Preparing two penny qubits in a maximally entangled Bell state.
2. Assigning separate groups of participants to each qubit.
3. Instructing participants to randomly select measurement bases.
4. Recording outcomes to analyze correlations and test Bell inequalities.

This experiment would serve as a proof-of-concept for the macroscopic quantum computer's ability to simulate fundamental quantum phenomena.

5.2.1 Actions required by qubit participants for gate operations

In the macroscopic quantum computer, human participants will perform specific actions to emulate quantum gate operations. Below are the required actions for each gate:

Hadamard gate (H) The Hadamard gate creates a superposition from a basis state. Participants representing a qubit apply the Hadamard by randomly deciding between "heads" and "tails" for the penny, ensuring a 50/50 probability for each outcome. This random choice simulates the creation of a superposition state:

$$|0\rangle \xrightarrow{H} \frac{1}{\sqrt{2}}\left(|0\rangle + |1\rangle\right) . \tag{14}$$

CNOT gate The CNOT gate entangles two qubits. Participants controlling the control qubit observe its state first. If the control qubit is in the "heads" state, participants managing the target qubit flip its state (from heads to tails or vice versa). If the control qubit is "tails", no action is taken on the target qubit. This action implements the CNOT operation:

$$|c, t\rangle \xrightarrow{CNOT} |c, t \oplus c\rangle . \tag{15}$$

Pauli-X gate (NOT gate) To perform a Pauli-X gate, participants flip the state of the penny. If the penny shows heads, they flip it to tails, and vice versa. This simulates the quantum NOT operation:

$$|0\rangle \xrightarrow{X} |1\rangle , \quad |1\rangle \xrightarrow{X} |0\rangle . \tag{16}$$

Measurement For measurement, participants agree on a basis (e.g. Z-basis or X-basis). They then observe the penny and record the outcome. In experiments like the EPR test, different participant groups will select measurement bases at random to ensure the integrity of Bell inequality testing.

These collective human-driven actions enable the execution of quantum gate operations in the macroscopic quantum computer, mirroring traditional quantum computations.

5.2.2 Programming the macroscopic quantum computer for EPR using Qiskit

To program our macroscopic quantum computer to demonstrate the EPR experiment, we can utilize Qiskit as a framework to design and visualize the quantum circuit [11]. The outcome of the EPR experiment can be coded and implemented on the IBM quantum computer for comparison. Below is an example Qiskit code to create a Bell state and perform measurements in varying bases:

```
from qiskit import QuantumCircuit, Aer, execute
from qiskit.visualization import plot_histogram

qc = QuantumCircuit(2, 2)
qc.h(0)qc.cx(0,1)
qc.measure([0,1], [0,1])

simulator = Aer.get_backend('qasm_simulator’)
result = execute(qc, simulator, shots=1024).result()
counts = result.get_counts(qc)
plot_histogram(counts)
```

Fig. 1: Qiskit code to generate and measure an EPR Bell state.

Participants would emulate these operations by making choices corresponding to the gates and measurements in the Qiskit code. The Hadamard gate creates superposition, the CNOT entangles the qubits, and the measurement step collapses the system, mirroring the behavior of the programmed circuit.

This experiment would serve as a proof-of-concept for the macroscopic quantum computer's ability to simulate fundamental quantum phenomena.

5.2.3 Circuit diagram and gate descriptions

The quantum circuit for the EPR (Bell) experiment consists of the following gates applied sequentially:

- **Hadamard gate (H):** Applied to the first qubit to create a superposition state.
- **CNOT gate:** Entangles the first qubit (control) with the second qubit (target).
- **Measurement:** Both qubits are measured in the computational basis.

The following matrix representations describe the gates used:

Hadamard gate (H):

$$H = \frac{1}{\sqrt{2}} \begin{bmatrix} 1 & 1 \\ 1 & -1 \end{bmatrix} \tag{17}$$

CNOT gate:

$$\text{CNOT} = \begin{bmatrix} 1 & 0 & 0 & 0 \\ 0 & 1 & 0 & 0 \\ 0 & 0 & 0 & 1 \\ 0 & 0 & 1 & 0 \end{bmatrix} \tag{18}$$

The **CNOT gate** uses a control qubit and a target qubit:

- A solid dot indicates the control qubit.
- A circle with a plus sign (+) marks the target qubit.
- If the control qubit is in state $|1\rangle$, the target qubit undergoes a NOT (X) operation.

The full circuit is depicted in Fig. 2.

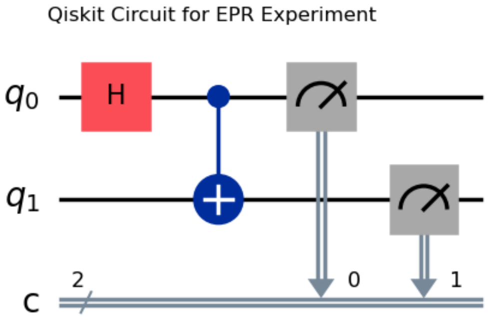

Fig. 2: EPR (Bell) State Circuit with labeled Hadamard, CNOT, and Measurement gates.

5.2.4 Mathematical framework and Bell inequality calculations

The EPR experiment relies on creating a Bell state [2]:

$$|\Psi^+\rangle = \frac{1}{\sqrt{2}} (|01\rangle + |10\rangle) \,. \tag{19}$$

Measurements on this state in different bases can reveal violations of Bell inequalities. The CHSH (Clauser-Horne-Shimony-Holt) inequality provides a testable framework [10]:

$$S = |E(a,b) + E(a',b) + E(a,b') - E(a',b')| \leqslant 2\,, \tag{20}$$

where $E(a,b)$ is the correlation coefficient between measurement settings a and b.

Quantum mechanics predicts violations up to $S = 2\sqrt{2}$ for appropriately chosen settings.

The correlation coefficient is computed as:

$$E(a,b) = P_{00}(a,b) + P_{11}(a,b) - P_{01}(a,b) - P_{10}(a,b)\,, \tag{21}$$

where $P_{ij}(a,b)$ is the probability of measuring outcomes i and j for settings a and b.

Participants would select measurement settings corresponding to a, a', b, b' and record outcomes, enabling the calculation of S and verification of Bell inequality violations.

5.3 Quantum circuit implementation

Participants could follow predefined quantum circuits, choosing heads or tails to enact specific gate operations. This human-driven approach would allow for the construction of complex quantum algorithms, with collective human agency serving as the mechanism for both superposition collapse and qubit manipulation.

5.4 Error correction and stability

Given the macroscopic nature of the system and human involvement, error correction protocols would be essential. Majority voting among participants, redundancy in group assignments, and error-checking procedures could help maintain computational integrity.

6 Determining the critical threshold N_c

The critical threshold N_c represents the minimum number of human participants required to reliably induce the collapse of a macroscopic superposition defined by collective choice. We propose that N_c can be estimated through multiple complementary approaches, all suggesting that collapse is a function of collective information processing, statistical precision, and gravitational instability. This section unifies these approaches and derives the scaling behavior of N_c in a single framework.

6.1 Unified collapse framework: decoherence, statistics, and gravity

We consolidate four perspectives into a common scaling framework for N_c:

- **Decoherence analogy:** Human choices act as an environment. Collapse occurs when decoherence time τ_D becomes shorter than system coherence time.
- **Statistical sampling:** Ensemble averaging must resolve a decision with confidence level ϵ, following binomial error bounds.
- **Percolation thresholds:** Collapse requires a critical number of interconnected participants to exceed a decision percolation threshold.
- **Gravitational Objective Reduction (OR):** Collapse is driven by the gravitational self-energy ΔE_G of the superposed macrostates, as proposed by Penrose.

These perspectives all imply a threshold N_c that determines when resolution occurs. In the OR framework, this collapse is objective and gravitational; in the ensemble model, it is probabilistic and informational. We treat both as complementary.

6.2 Key scaling relations

We present the collapse framework in a unified mathematical block:

(1) Gravitational self-energy:

$$\Delta E_G = \frac{G}{2} \int\int \frac{[\rho(\mathbf{r}) - \rho'(\mathbf{r})]\,[\rho(\mathbf{r}') - \rho'(\mathbf{r}')]}{|\mathbf{r} - \mathbf{r}'|}\, d^3r\, d^3r' \quad (22)$$

(2) OR collapse time:

$$\tau \approx \frac{\hbar}{\Delta E_G} \quad (23)$$

(3) Human collapse timescale:

$$\tau_H \propto \frac{1}{N_c} \quad (24)$$

(4) Threshold scaling:

$$N_c \propto \frac{\Delta E_G}{\hbar} \quad (25)$$

Eq. (25) encapsulates the central hypothesis: greater gravitational self-energy between superposed states reduces the number of participants required for collapse. This provides a bridge between observer-driven and objective collapse mechanisms.

6.3 Statistical estimation of N_c

Independent of gravity, we can estimate N_c based on the confidence level required to distinguish two ensemble outcomes. Treating human decisions as a binomial process with probability $p = 0.5$, the standard error is:

$$\mathrm{SE} = \sqrt{\frac{p(1-p)}{N}} = \frac{1}{2\sqrt{N}}\,. \quad (26)$$

To achieve confidence ϵ, we solve:

$$Z \cdot \mathrm{SE} \leqslant \epsilon \quad \Rightarrow \quad N_c \geqslant \left(\frac{Z}{2\epsilon}\right)^2. \quad (27)$$

Here, Z is the Z-score corresponding to the desired confidence level of the decision threshold — for example, $Z = 1.96$ for a 95% confidence interval. This ensures that the ensemble average deviates from 50% by more than ϵ with the specified level of certainty.

This gives a statistical lower bound on N_c, which can be adjusted upward if gravitational effects weaken the ensemble's collapse influence.

6.4 Percolation and network collapse analogy

If participants are modeled as nodes in a network, collapse may only occur when the connectivity of decision alignment percolates. For a 2D lattice, the percolation threshold is around $p_c \approx 0.59$. This suggests that a critical fraction of participants must reach coherence before the system-wide state can resolve. This provides a geometrical or network-theoretic perspective on N_c, complementary to both statistical and gravitational models.

6.5 Distance and spatial separation effects

From Penrose's model, the self-energy ΔE_G increases with spatial separation d between superposed states of mass m. In simple cases:

$$\Delta E_G \propto \frac{Gm^2}{d} \quad \Rightarrow \quad N_c \propto \frac{1}{\Delta E_G} \propto \frac{d}{Gm^2}\,. \quad (28)$$

Thus, increasing the spatial separation between superposed configurations (e.g. the location of a "heads" vs. "tails" penny) increases the gravitational instability, decreasing the required number of human agents to induce collapse. Conversely, minimal displacement requires larger N_c.

6.6 Summary and experimental implications

These models converge on the idea that N_c is a tunable parameter reflecting the interplay of statistical certainty, observer participation, and gravitational geometry. Experiments varying:

- The mass m and displacement d of superposed macrostates,
- The number of participants N,
- The spatial distribution and timing of decisions,

can be used to test which collapse mechanism dominates, and to empirically validate or constrain the proposed scaling of N_c. §5.2.4 applies this framework to entangled macroscopic qubits and spatial separation effects.

7 Extending to qudits: human-driven collapse beyond binary

While the macroscopic qubit model focuses on binary choices (heads or tails), the framework can be naturally extended to *qudits* — quantum systems with d discrete levels — by increasing the number of available outcomes. In this extended model, each participant chooses an integer value from a predefined set, such as $\{1, 2, \ldots, 10\}$ for a 10-dimensional qudit.

Participants would no longer act as binary agents, but as selectors from a d-level Hilbert space:

$$|\psi\rangle = \frac{1}{\sqrt{d}} \sum_{k=1}^{d} |k\rangle\,, \quad (29)$$

representing an equal superposition over d outcomes. The system remains in superposition until the collective human choices are measured and tallied.

Virtual die analogy One practical implementation is to present participants with a virtual 10-sided die and ask them to consciously select a number between 1 and 10. The final collapsed state of the qudit is the statistically dominant outcome across the ensemble. This approach preserves the role of human agency while expanding the dimensionality of the macroscopic quantum system.

Measurement dynamics Let f_k be the fraction of participants who chose outcome k. The system collapses to the state $|k^*\rangle$ corresponding to the outcome with the highest frequency:

$$|\psi\rangle \xrightarrow{\text{Human Choice}} |k^*\rangle\,, \quad \text{where } k^* = \arg\max_k f_k\,. \tag{30}$$

Applications and scalability Using qudits enables more compact encoding of quantum information, reduces the number of participant groups needed for certain algorithms, and opens the door to simulating higher-dimensional quantum gates. Human-driven implementations of qutrits ($d = 3$) or higher-dimensional logic gates could expand the scope of the macroscopic quantum computer beyond what binary ensembles allow.

Future studies could explore the threshold number $N_c^{(d)}$ required for qudit-level collapse, as well as investigate the impact of perceptual biases in number selection (e.g. preference for round numbers) on statistical coherence in high-dimensional spaces.

8 Scaling to a giant macroscopic quantum computer

8.1 Inspiration from the three-body problem

The concept of using human agency as computational elements draws inspiration from Liu Cixin's *The Three-Body Problem*, where an army of soldiers forms a massive human-based computer to solve complex problems [12]. In that fictional scenario, each soldier acts as a simple logic gate or bit, with coordination enabling large-scale computation.

Adapting this idea to quantum computing, we propose extending the macroscopic qubit model to create a vast human-driven quantum computer, where *armies* of participants collectively perform quantum operations. Unlike classical bits, which hold definitive states of 0 or 1, macroscopic qubits embody superpositions, entanglement, and collapse dynamics, enabling powerful quantum computations on a human scale.

8.2 Human-driven quantum architecture

8.2.1 Participant organization

In a giant macroscopic quantum computer, participants are organized hierarchically:

- **Qubit groups:** Each macroscopic qubit is controlled by a group of N_c participants responsible for inducing collapse through collective choices, as outlined in previous sections of this paper.
- **Gate operation teams:** Specialized groups coordinate between qubit groups to implement entangling gates (e.g. CNOT) and single-qubit operations (e.g. Hadamard, Pauli-X).
- **Measurement collectives:** Designated participants record and analyze outcomes, maintaining the system's coherence and consistency.

There would have to be specialty groups trained to perform the tasks assigned to the group. There would be Hadamard Gate groups, for example trained to only operate as a Hadamard Gate with known inputs giving known outputs. Likewise, all of the quantum computing components would require specialty trained participants.

8.2.2 Quantum circuit execution

The execution of complex quantum algorithms, such as Shor's or Grover's algorithms, would involve:

1. **Preparation:** Participants initialize macroscopic qubits in defined states, possibly using shared visual cues or symbolic objects (e.g. pennies, cards) to represent qubit states.
2. **Gate application:** Coordinated groups execute gate operations, ensuring phase coherence and entanglement are preserved. Timing synchronization becomes crucial, possibly managed via visual or auditory signals.
3. **Measurement and readout:** Upon completing the computation, participants collectively measure qubit states, collapsing the superpositions and yielding the final result.

8.3 Scaling challenges and error correction

Scaling to thousands or millions of participants introduces significant challenges:

- **Decoherence and synchronization:** Ensuring all participants act within coherent timeframes is critical. Decoherence could be modeled as human-induced "noise" leading to erroneous operations.
- **Error correction:** Implementing quantum error correction codes (e.g. Shor's or Steane codes) would require additional participant groups dedicated to detecting and correcting mistakes.
- **Communication overhead:** Managing coordination between thousands of individuals introduces latency and complexity, echoing issues in distributed quantum systems.

8.4 Emergent quantum phenomena and philosophical reflections

Collective human choices might yield emergent phenomena, echoing Orch-OR [13] and quantum consciousness models

[14]. The quantum-classical boundary could shift with scale, probing discreteness effects [15]. A giant human-driven quantum computer invites philosophical considerations:

- **Collective consciousness:** Could collective human choices, entangled across macroscopic qubits, create emergent cognitive phenomena? This echoes questions from Penrose and Hameroff's Orch-OR model [13].
- **Quantum-classical boundary:** Scaling to a vast number of participants blurs the line between quantum and classical behavior, offering an experimental platform to probe the quantum-to-classical transition.
- **Ethics and agency:** Involving human participants as computational agents raises ethical considerations, especially regarding agency, consent, and cognitive load.

8.5 Symbolic parallels: quantum computing and the kabbalistic tree of life

To illustrate the intersection of abstract computation and symbolic meaning, Fig. 3 presents a side-by-side comparison of a quantum logic board game diagram [18] and the Kabbalistic Tree of Life [19].

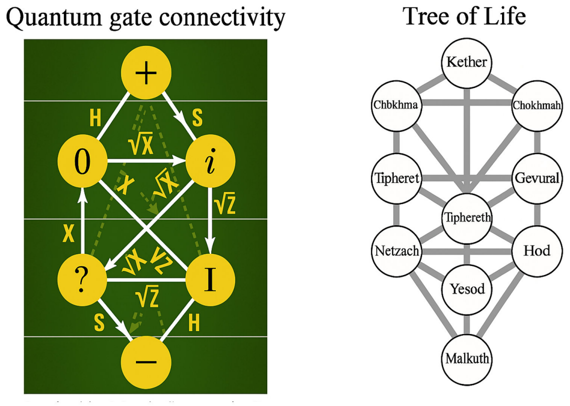
Quantum gate connectivity

Tree of Life

Fig. 3: Left: A tabletop quantum computing game. Right: The Kabbalistic Tree of Life.

While the two images emerge from vastly different traditions — one scientific, the other esoteric — they share striking structural similarities: nodes connected by pathways, representing possible transformations or flows of information. In the quantum circuit model, these nodes are qubit states manipulated by unitary gates. In the *Tree of Life*, they represent spiritual emanations (Sefirot) connected by paths of experience and causality.

This visual juxtaposition is not intended to suggest that quantum computing is mystical or that Kabbalah is scientific, but rather to acknowledge that both systems organize complex, interconnected structures of transformation. The board game formalism provides an intuitive, tangible version of quantum algorithms; the *Tree of Life* offers a metaphysical map of potential states of being. Both can serve as cognitive scaffolds for reasoning about multidimensional processes — whether physical or philosophical.

As this project touches on the role of collective human agency in quantum collapse, it is useful to consider how ancient symbolic systems might resonate with emerging quantum paradigms. The idea that observers (or agents) move through pathways of decision and transformation is not new — it is only now that it may be quantified and tested.

8.6 Diagram: macroscopic human agency quantum computer

As shown in Fig. 4, the system architecture consists of distributed participant groups, synchronization protocols, and symbolic entanglement layers designed to simulate quantum operations.

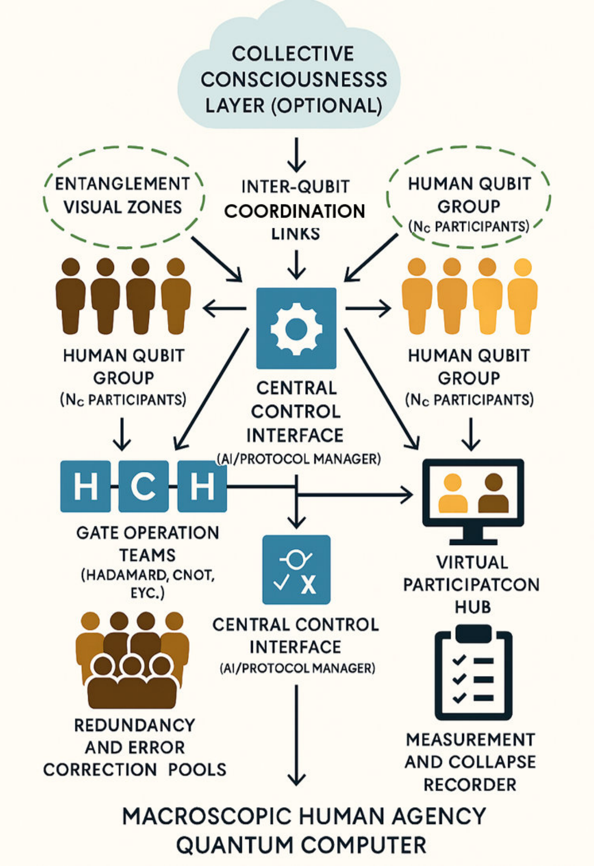

Fig. 4: A schematic of the Macroscopic Human Agency Quantum Computer.

Component descriptions and intentions

1. **Human qubit group (N_c participants):** These groups form the core computational units, analogous to qubits in standard quantum computers. Each contains a critical number of human participants N_c whose collective decisions statistically determine the state of a macroscopic qubit (e.g. heads or tails). The unresolved state

prior to tallying represents a human-induced superposition.

2. **Inter-qubit coordination links:** These represent synchronized decision protocols or communication pathways between qubit groups. They enable the simulation of quantum entanglement and conditional logic, such as CNOT operations, through coordinated human action.
3. **Gate operation teams (Hadamard, CNOT, etc.):** Specialized participant teams implement quantum gates by directing how qubit groups make decisions. For example, Hadamard groups introduce randomized choices, while CNOT groups conditionally flip a target qubit based on the state of a control qubit.
4. **Central control interface (AI/protocol manager):** This system ensures coherence across the macroscopic quantum network by managing timing, sequence of operations, and synchronization between participant groups. It functions like a classical clock or control bus in digital computers but mediates human-based gate execution.
5. **Measurement and collapse recorder:** At the end of each computation, this module collects the aggregated choices of each qubit group to collapse their superposition states. It may be a physical tally, a digital computation, or a symbolic reveal, serving as the observer in quantum measurement theory.
6. **Redundancy and error correction pools:** These backup participants or decision-checking algorithms emulate quantum error correction by mitigating errors in human decision-making. Majority voting, parity checks, or redundant encoding strategies ensure consistency in macroscopic qubit behavior.
7. **Virtual participation hub:** This represents the distributed nature of the platform, allowing participants to contribute from remote locations via a digital interface. Inspired by the Big Bell Test, it scales participation globally and democratically, transforming computation into a crowdsourced quantum simulation.
8. **Entanglement visual zones:** Symbolic areas denoting nonlocal correlations between qubit groups. These highlight how group outcomes may statistically influence or mirror each other despite spatial separation, simulating Bell-type entanglement in a macroscopic context.
9. **Collective consciousness layer:** An abstract representation of the hypothesis that coordinated human intention may itself be a source of quantum-like coherence. While speculative, it aligns with theories such as Orch-OR and invites philosophical exploration into the relationship between consciousness and quantum collapse.

8.7 Potential experimental realizations

While a fully operational giant macroscopic quantum computer remains speculative, smaller-scale prototypes could be tested:

- **Crowdsourced experiments:** Leveraging online platforms to coordinate thousands of participants globally, similar to the Big Bell Test [3].
- **Physical assemblies:** Large-scale gatherings (e.g. stadiums) where participants physically represent qubits and gates, following choreographed routines to execute quantum circuits.
- **Hybrid systems:** Combining human-driven elements with classical computational assistance to manage coordination and error correction.

8.8 Implications and future directions

Constructing a giant macroscopic quantum computer challenges conventional paradigms of computation, observation, and agency. It bridges quantum physics, consciousness studies, and complex systems, offering a unique platform to explore the intersection of physical laws and human cognition.

Future research could focus on:

- Formalizing models of large-scale human-driven quantum systems.
- Developing protocols for error correction and synchronization in macroscopic qubit networks.
- Exploring philosophical and cognitive implications of collective quantum computation.

9 Implications and future work

This proposal redefines the quantum-classical divide by positing human agency as a collapse mechanism for macroscopic qubits, where a penny's state emerges not from a single quantum superposition but from the statistical average of collective human flips. Unlike traditional qubits confined to microscopic scales by decoherence [6], this ensemble approach sidesteps physical coherence challenges, suggesting that macroscopic quantum phenomena might hinge on observer-driven statistics rather than isolated systems. If validated, this could imply that quantumness scales with collective intent, potentially echoing Penrose's Objective Reduction (OR) [7] where gravitational effects amplify with participant number, or even hinting at spacetime discreteness shaping statistical outcomes [8, 9].

The implications span physics, computation, and philosophy. Physically, it challenges the notion that quantum effects vanish at macroscopic scales, offering a testbed for theories like OR or quantum cognition [14] — could human decisions, aggregated over thousands, mirror quantum processes in the brain? Computationally, a human-driven quantum computer could democratize quantum technology, trading cryogenic labs for crowdsourced networks, though at the cost of precision and speed compared to silicon-based qubits [5]. Philosophically, it blurs the line between observer and system, raising questions about free will, collective consciousness, and the nature of reality: if N_c humans collapse a qubit, does their agency entangle with the cosmos?

Future work will prioritize three areas:

1. **Formalizing collapse dynamics**: Develop a rigorous statistical model for the ensemble qubit, refining N_c with binomial distributions. For N flips with $p = 0.5$, the standard error $\mathrm{SE} = \sqrt{p(1-p)/N}$ suggests $N_c \approx 10^4$ for a 95% confidence interval ($\mathrm{SE} < 0.005$), but gravitational or network effects (e.g. percolation [16]) could shift this. Simulations will test if ΔE_G scales meaningfully with N, probing Penrose's hypothesis.
2. **Experimental realizations**: Launch a pilot with 1,000 participants choosing heads or tails online, measuring f_H convergence rates and Bell correlations across two groups. A 10-qubit prototype will follow, using AI to sync $10 \times N_c$ flips, targeting a simple algorithm (e.g. Deutsch's) to benchmark against Qiskit simulators [11]. Physical gatherings (e.g. stadium-scale) could explore real-time dynamics.
3. **Scaling beyond 10 qubits**: Scale to millions via phased recruitment, leveraging cloud platforms and AI-driven signals for gate execution and error correction. Each qubit's state, an average over N_c flips, requires robust protocols — e.g. majority voting or Steane codes adapted for human noise. A "giant" system might compute Shor's algorithm, testing if human ensembles rival quantum hardware.

This framework's scalability hinges on technology and human coordination. A 10-qubit system with $N_c \approx 10^4$ demands 100,000 participants, manageable via global crowdsourcing, while millions could push macroscopic quantumness to unprecedented scales. AI will be key, predicting flip patterns to minimize latency and decoherence-like errors from misaligned choices. Success could redefine quantum computing as a participatory science, merging human cognition with fundamental physics, and invite radical questions: does collective will imprint on spacetime, as discreteness models suggest [17]? Future experiments will chase these horizons, blending empirical rigor with speculative wonder.

10 Conclusion

In this paper, we have proposed a novel framework for constructing macroscopic qubits driven by human agency, exploring the intersection of quantum mechanics, consciousness, and gravitational effects. Drawing inspiration from the Big Bell Test, we extended the notion of observer-induced collapse to a macroscopic scale, using human choices as a direct mechanism for collapsing a superposition state.

We outlined the conceptual basis for using simple macroscopic objects, such as pennies, as qubits and examined how collective human choices could act as a measurement apparatus. Through the exploration of entanglement possibilities and quantum gate operations, we proposed the construction of a human-driven macroscopic quantum computer capable of demonstrating complex quantum phenomena, including the Einstein-Podolsky-Rosen (EPR) experiment and violations of Bell inequalities.

A critical component of this study was the investigation into the threshold number of participants (N_c) required to induce collapse. By examining analogies with quantum decoherence, statistical sampling, percolation theory, and Penrose's Objective Reduction (OR) model, we provided multiple pathways to estimate N_c. The integration of Penrose's OR theory introduced a gravitational dimension to the collapse process, suggesting that mass distribution and spatial separation could influence collapse dynamics and potentially reduce the human effort needed for macroscopic quantum control.

This interdisciplinary approach challenges conventional boundaries between quantum and classical systems, offering insights into the nature of consciousness, observation, and reality. While speculative, this framework opens new avenues for experimental validation, especially in testing gravitational influences on quantum systems and the role of human agency in quantum measurements. While the framework is speculative and metaphorical in parts, its purpose is to probe the intersection of quantum mechanics, human cognition, and observer-based collapse in novel ways. Empirical tests will be critical to validate or falsify these claims.

Future work will focus on refining the theoretical models for N_c, designing experimental setups to test gravitationally-influenced collapse, and scaling the human-driven quantum computer beyond the proposed 10-qubit system. Additionally, deeper exploration into the relationship between consciousness and quantum mechanics, as suggested by the Orch-OR model, could offer profound insights into the nature of reality itself.

This study represents a first step in reimagining quantum systems not just as abstract mathematical constructs, but as entities deeply intertwined with human experience and fundamental spacetime structures.

Acknowledgements

We thank the participants of the Big Bell Test for their pioneering work in integrating human choice into quantum experiments.

Received on April 18, 2025

References

1. Einstein A., Podolsky B., and Rosen N. Can quantum-mechanical description of physical reality be considered complete? *Phys. Rev.*, 1935, v. 47, 777.
2. Bell J. On the Einstein-Podolsky-Rosen paradox. *Physics*, 1964, v. 1 (3), 195–200.

3. Abellán C., *et al.* Challenging local realism with human choices. *Nature*, 2018, v. 557, 212–216.
4. Turiel J.L., *et al.* Human randomness and decision structure. *J. Theor. Exp. Artif. Intell.*, 2013, v. 25 (1), 1–13.
5. Nielsen M.A., Chuang I.L. Quantum Computation and Quantum Information. Cambridge Univ. Press, 2000.
6. Zurek W.H. Decoherence and the transition from quantum to classical. *Rev. Mod. Phys.*, 2003, v. 75, 715.
7. Penrose R., Hameroff S. Orchestrated reduction of quantum coherence in brain microtubules. *J. Conscious. Stud.*, 1996, v. 3 (1), 36–53.
8. Ng Y.J. and van Dam H. Spacetime foam, holography and black hole quantum computers. *Mod. Phys. Lett. A*, 2001, v. 16 (17), 1231–1240.
9. Calmet X. and Graesser M. The quantum structure of spacetime and the classical limit. *Int. J. Mod. Phys. D*, 2017, v. 26 (14), 1743002.
10. Clauser J.F., Horne M.A., Shimony A., Holt R.A. Proposed experiment to test local hidden-variable theories. *Phys. Rev. Lett.*, 1969, v. 23 (15), 880–884.
11. Abraham H., *et al.* Qiskit: An Open-source Framework for Quantum Computing. *Zenodo*, 2019. doi:10.5281/zenodo.2562110.
12. Liu Cixin. The Three-Body Problem. Tor Books, 2014.
13. Hameroff S., Penrose R. Conscious events as orchestrated space-time selections. *J. Conscious. Stud.*, 1996, v. 3 (1), 36–53.
14. Fisher M. Quantum cognition: The possibility of processing with nuclear spins in the brain. *Ann. Phys.*, 2015, v. 362, 593–602.
15. Dowker F., Henson J. and Sorkin R. D. Quantum Gravity Phenomenology, Lorentz Violation and Finsler Geometry. *Modern Physics Letters A*, 2013, v. 28 (9), 1350028.
16. Stauffer D., Aharony A. Introduction to Percolation Theory. Taylor & Francis, 2018.
17. Freidel L., Leigh R.G., and Minic D. Quantum gravity, dynamical phase space and information. *Int. J. Mod. Phys. D*, 2019, v. 28 (14), 1942023.
18. Wong T., *et al.* Qubit by Qubit: A quantum computing board game. *Quantum Sci. Technol.*, 2019, v. 4 (2), 025010.
19. Wikimedia Commons. Tree of Life (Kabbalah).

LETTERS TO PROGRESS IN PHYSICS

Neutrino Masses and Their Oscillation Periods Calculated using Wheeler's Geometrodynamics Agree with the Neutrino-4 Experiment

Anatoly V. Belyakov

Tver, Russia. E-mail: belyakov.lih@gmail.com

The values of the masses of the Majorana and sterile neutrinos and the period of their oscillations, calculated on the basis of a physical model based on J. Wheeler's geometrodynamics, coincide with the results obtained in the Neutrino-4 Experiment.

The results of the recent Neutrino-4 Experiment to search for sterile neutrinos, which was carried out by teams from the Kurchatov Institute and the B. P. Konstantinov Petersburg Institute of Nuclear Physics, allow us to estimate the sterile neutrinos mass at (2.70 ± 0.22) eV, which does not contradict the other experiments results within the 3σ experimental error contours [1].

The oscillation period for a neutrino energy of 4 MeV is 1.4 m, Fig. 1 (quoted from [1]). It was also found the Majorana neutrino mass value, obtained with the Neutrino-4 oscillation parameters, to be (0.25 ± 0.09) eV.

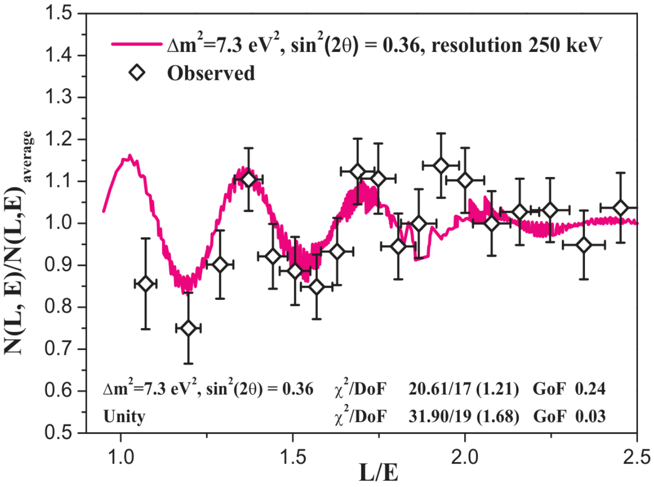

Fig. 1: Full curve of the oscillation process from the centre of the reactor core. Quoted from [1].

But it should be emphasized that it is these parameters that follow from the accepted neutrino model [2] and, in general, from the physical model of microphenomena outside the SM framework and based on the mechanistic interpretation of J. Wheeler's geometrodynamics, previously described in works [3–6] and others. This model makes it possible to directly calculate the parameters of neutrinos and other microparticles.

The mass of the neutrino is determined by introducing gravity, whose role in the microworld is erroneously denied in the SM. Let us recall that in the accepted model, the electron does not rotate around the proton and is not "smeared" in orbits, but the proton and electron are connected by a vortex current tube of the drain-source type in an additional dimension (conditionally, the Y-axis). As a result, a closed contour is formed along which the material medium circulates. The contour exists due to the equality of gravitational and magnetic forces. In the Coulomb-free form, i.e., when replacing the Coulomb with the value $m_e c$, from this equality it follows in units of r_e:

$$L = lr = \frac{z_{g_1}\, z_{g_2}}{z_{e_1}\, z_{e_2}}\,(2\pi\gamma\rho_e)\times[\text{sec}]^2, \tag{1}$$

where z_{g_1}, z_{g_2}, z_{e_1}, z_{e_2}, r, l, γ, ρ_e are the gravitational masses and charges in the masses and charges of the electron, the distance between the current tubes and their length, the gravitational constant and the electron specific density, equal to m_e/r_e^3. In formula (1), the value of z_{g_1} is the active part of the proton mass (i.e., the quark) entering the circulation contour, z_{g_2} is the electron mass.

According to the accepted model, a vortex tube of radius r_e, *boson mass* M, length l is spirally filled with a vortex thread of radius r. In units of r_e and m_e

$$M = l = (an)^2\,, \tag{2}$$

$$r = \frac{c_0^{2/3}}{(an)^4}\,, \tag{3}$$

where c_0 is the dimensionless speed of light $c/[\text{m/sec}]$, a is the inverse fine structure constant, n is the quantum parameter. With complete compression of the spiral vortex thread, the mass-energy of the vortex tube becomes equal to (in units of $m_e c^2$)

$$L = lr = \frac{c_0^{2/3}}{(an)^2}\,. \tag{4}$$

In works [2,4] it is shown when particles to approach each other at a certain distance, the contour connecting them transfers energy-momentum to the internal structure of the proton, losing charge, and then is released in the form of a one-dimensional vortex tube of neutrinos, which carries away the electron spin. Neutrino release occurs under the condition that the Y-vortex tube mass-energy in its compressed state reaches the quark mass-energy, which makes it possible to determine the Y-vortex tube quantum parameter n_ν. In work [2] it was obtained:

$$n_\nu = \frac{c_0^{1/9}\left(2\pi\gamma\rho_e \times [\mathrm{sec}]^2\right)^{1/3}}{a} = 1.643, \qquad (5)$$

and then the neutrino fermion mass was defined as the Y-vortex tube *fermion mass* $m_\nu = 4.39\times10^{-7}$ (0.225 eV) and the quark mass $m_k = 8.84$ (4.51 MeV) was defined. The neutrino exists in this form at the moment of escaping, but since it has no detectable charge, therefore, then there is a neutrinos' transforming into some closed structure.

In [3] it is shown the electron vortex tube to contain three vortex zones. But since one of the zones must necessarily be double, then there should be four single vortex threads in general, containing on average 1/4 of the electron total momentum (charge). Therefore, the neutrino should be considered as a pair of closed vortex threads of two possible types: a pair with left-right rotation and, conversely, a pair with right-left rotation (relative to the axis of motion direction).

In [2], the neutrino closed form mass value m_ν was obtained as the *gravitational mass*, i.e., as the value of $z_{g_1} = z_{g_2} = m_\nu$ with $z_{e_1} = z_{e_2} = \frac{1}{4}\,e_0$ and under the assumption that the vortex thread has the Planck size $r = r_\hbar = (\hbar\gamma/c^3)^{1/2} = 5.74\times10^{-21}\,r_e$, and then

$$m_\nu = z_g = c_0^{1/6} r_\hbar^{1/4}\left(32\pi\gamma\rho_e \times [\mathrm{sec}^2]\right)^{-1/2} = \\ = 4.31\times10^{-7}\ (0.220\ \mathrm{eV}), \qquad (6)$$

which coincides with the fermionic mass of the neutrino vortex tube. Thus, two different neutrino states with identical masses are obtained - at the moment of neutrino birth in the form of the fermionic part of the vortex Y-tube and in its final state in the form of a closed structure having gravitational mass.

In addition to the work [2], it should be noted that if we consider a contour consisting of a pair of closed vortex threads, each having 1/3 of the electron charge, under the condition according to which the **gravitational energy-mass of the particle means to be equal to the energy-mass of the compressed contour**, i.e., when $m_\nu = L = l\,r$, then it will have the following parameters (in units of m_e and r_e):

$$m_\nu = \left(18\pi\gamma\rho_e \times [\mathrm{sec}^2]\right)^{-1} = 6.52\times10^{-6}\ (3.33\ \mathrm{eV}), \qquad (7)$$

$$r = \frac{m_\nu^2}{c_0^{2/3}} = 9.51\times10^{-17}\ \text{ or } 130^2\,r_\hbar\,, \qquad (8)$$

$$l = \frac{c_0^{2/3}}{m_\nu} = 6.86\times10^{10}\ \text{ or } (1910\,a)^2\,. \qquad (9)$$

Here the particle mass depends only on the electron density and the gravitational constant, and the particle contour will have very characteristic parameters with axial dimensions close to $a^2 r_\hbar$ and to the limiting atom size in space [7]. Obviously, such a particle is more fundamental one and in this form cannot participate in the weak interaction according to the above mechanism. The limiting energy of such a neutrino at $r \to r_e$ would be $6.86\times10^{10}\times0.511 = 3.5\times10^{10}$ MeV (to date, the highest recorded neutrino energy is 2×10^9 MeV).

Thus, the calculated neutrino masses according to the accepted model are as follows:

a) the neutrino masses at the moment of formation and in closed form coincide with the Majorana mass of the electron neutrino obtained in the Neutrino-4 Experiments;

b) the more fundamental neutrino mass actually coincides with the estimate of the sterile neutrino mass obtained in the Neutrino-4 Experiments. The discrepancy in the latter case is not significant, since, as the authors of the work [1] noted, at $L/E > 1$ the best fit shifts to the region of larger values.

Moreover, the period (length) of the oscillations is also easily determined. Indeed, the speed of the sterile neutrino is proportional to the square root of the reactor neutrino energies value to the neutrino energy limiting value ratio:

$$v = c\,(4\ \mathrm{MeV}/3.5\times10^{10}\ \mathrm{MeV})^{1/2} = 3210\ \mathrm{m/sec}. \qquad (10)$$

The time constant or duration of oscillations τ (like the proton lifetime [4]) is the ratio of the characteristic size of the contour r at n_ν (according to (3), it is $r = 1.72\times10^{-4}\,r_e = 4.90\times10^{-19}$ m) to the fundamental rotation speed of the vortex threads, determined from the balance of magnetic and dynamic forces [4]:

$$v_0 = \frac{r_e}{(2\pi)^{1/2}\times[\mathrm{sec}]} = 1.12\times10^{-15}\ \mathrm{m/sec}, \qquad (11)$$

and, accordingly, $\tau = r/v_0 = 4.37\times10^{-4}$ sec. Consequently, the period (distance) of oscillations for a sterile neutrino is $v\tau = 3210\times4.37\times10^{-4} = 1.4$ m, which exactly coincides with the experimental value.

As for the oscillations of electron neutrinos, in the initial period of its existence at an energy close to the quark mass-energy (about 4 MeV), having the speed of light, they move away from the source in time τ to a distance of 1.31×10^5 m, and if there is a neutrinos' transforming into another form, then a decrease in their number will be registered, provided the detector to be removed from the source at a distance no less than the calculated one.

It was at this distance and at these energies that the large neutrino detector KamLAND (Kamioka Liquid scintillator Anti-Neutrino Detector), located on the island of Honshu in Japan, recorded a decrease in the neutrino flux in experiments on detecting antineutrinos from nuclear reactors [8].

Thus, the theoretical results that were obtained based on the physical model outside the SM framework are confirmed by extensive and carefully performed experiments within the Neutrino-4 project.

Submitted on May 10, 2025

References

1. Serebrov A.P., Samoilov R.M., Chaikovskii M.E. Analysis of the result of the Neutrino-4 Experiment together with other experiments on the search for sterile neutrinos within the 3 + 1 neutrino model. *Journal of Experimental and Theoretical Physics* (*JETP*), 22 August 2023, v.137, 55–70.
2. Belyakov A.V. Determination of the neutrino mass. *Progress in Physics*, 2016, v.12, issue 1, 34–38.
3. Belyakov A.V. Charge of the electron, and the constants of radiation according to J. A. Wheeler's geometrodynamic model. *Progress in Physics*, 2010, v.6, issue 4, 90–94.
4. Belyakov A.V. Macro-analogies and gravitation in the micro-world: further elaboration of Wheeler's model of geometrodynamics. *Progress in Physics*, 2012, v.8, issue 2, 47–57.
5. Belyakov A.V. Nuclear power and the structure of a nucleus according to J. Wheeler's geometrodynamic concept. *Progress in Physics*, 2015, v.11, issue 1, 89–98.
6. Belyakov A.V. Does the macroworld need Quantum Mechanics? *Progress in Physics*, 2025, v.21, issue 1, 29–37.
7. Belyakov A.V. On the nature of some cosmic radiations. *Progress in Physics*, 2022, v.18, issue 2, 164–168.
8. Orekhov D.I. Toolkit for neutrino physics. Dept. of Physics, Moscow State University, August 27, 2006.

On the Condition of Non-Quantum Teleportation on the Surface of a Spherical Body

Dmitri Rabounski and Larissa Borissova
Puschino, Moscow Region, Russia. E-mail: rabounski@yahoo.com; lborissova@yahoo.com

Here we consider the degeneration of the four-dimensional fundamental metric tensor and the physically observable three-dimensional metric tensor as geometric conditions for non-quantum teleportation. It is shown that non-quantum teleportation can be implemented under any physical conditions at the North and South Poles of a rotating spherical body and, in general, everywhere along the axis of its rotation. But even at a very small distance from the poles along the geographical latitudes, non-quantum teleportation requires exotic conditions, such as a very strong electromagnetic field, etc.

In the late 1980s, we began an extensive theoretical study, the task of which was to find out whether instant transmission of signals (*long-range action*) and instant displacement of physical bodies in general (*non-quantum teleportation*) is possible according to Einstein's theory of relativity.

The reason why we started this research was the need to explain some unique experiments in biophysics, which were performed in the late 1980s by one of our close colleagues, an outstanding experimental biophysicist with a broad erudition in the field of bionics (he passed away in 2001). His experiments had no theoretical explanation in the framework of modern science. Only with a theory of these experiments could we determine the key physical factors that produced the discovered effect and, accordingly, determine methods for enhancing these factors in order to create a new industrial technology of communication and transport.

As always in our theoretical studies, we used the *mathematical apparatus of chronometric invariants*, introduced in 1944 by Abraham Zelmanov [1–3]. Chronometric invariants are invariant projections of four-dimensional quantities onto the three-dimensional space (spatial section) and the line of time belonging to an observer. Such projections are dependent on the geometric and physical characteristics of the observer's physical space and are physically observable quantities registered by him in his reference frame. For this reason, Zelmanov's mathematical apparatus of chronomertic invariants is also known as the *theory of physically observable quantities* in the four-dimensional space-time.

Since Zelmanov's original publications [1–3] were very concise, at the request of our close colleague Pierre Millette, three decades later, in 2023, we published the most comprehensive survey of Zelmanov's chronometrically invariant formalism [4], wherein we collected almost everything that we know in this field personally from Zelmanov and based on our own research studies.

So, let us now return to our theoretical research that we began in the late 1980s.

First of all, we determined the *weak and strong conditions for non-quantum teleportation* in the four-dimensional space-time. According to the chronometrically invariant formalism, the physically observable time interval $d\tau$ and the physically observable three-dimensional interval $d\sigma$ registered by an observer are, respectively, chr.inv.-projections of the four-dimensional displacement vector dx^α ($\alpha = 0,1,2,3$) onto the time line of the observer and his three-dimensional space (spatial section of space-time). They are calculated as

$$d\tau = \sqrt{g_{00}}\,dt - \frac{1}{c^2}\,v_i\,dx^i, \tag{1}$$

$$d\sigma^2 = h_{ik}\,dx^i dx^k, \quad i = 1,2,3, \tag{2}$$

where dt is the interval of coordinate time, which is counted in the absence of disturbing factors. The three-dimensional chr.inv.-metric tensor

$$\left.\begin{aligned} h_{ik} &= -g_{ik} + \frac{g_{0i}\,g_{0k}}{g_{00}} = -g_{ik} + \frac{1}{c^2}\,v_i v_k \\ h^{ik} &= -g^{ik}, \qquad h^i_k = \delta^i_k \end{aligned}\right\} \tag{3}$$

is the chr.inv.-projection of the fundamental metric tensor $g_{\alpha\beta}$ onto the spatial section of the observer and possesses all properties of $g_{\alpha\beta}$ throughout the spatial section (the observer's three-dimensional space). The time (zero) component g_{00} of the fundamental metric tensor $g_{\alpha\beta}$ is expressed with the physically observable chr.inv.-potential w of the gravitational field that fills the space of the observer

$$\sqrt{g_{00}} = 1 - \frac{\mathrm{w}}{c^2}\,, \qquad \mathrm{w} = c^2\left(1 - \sqrt{g_{00}}\right), \tag{4}$$

and v_i is the three-dimensional vector of the linear velocity of rotation of the observer's space

$$v_i = -\frac{c\,g_{0i}}{\sqrt{g_{00}}}\,, \quad v^i = -c\,g^{0i}\sqrt{g_{00}}\,, \quad v_i = h_{ik}v^k, \tag{5}$$

which is caused by the non-orthogonality of the observer's spatial section to his time line and therefore it cannot be eliminated by coordinate transformations along his spatial section. Therefore, the square of the four-dimensional (space-time) interval $ds^2 = g_{\alpha\beta}\, dx^\alpha dx^\beta$ is expressed with chronometrically invariant (physically observable) intervals by the formula

$$ds^2 = c^2 d\tau^2 - d\sigma^2, \tag{6}$$

from which we obtain the weak and strong conditions for non-quantum teleportation:

The weak condition of non-quantum teleportation

$$d\tau = 0\,, \qquad d\sigma \neq 0 \tag{7}$$

means that the interval of physically observable time $d\tau$ between the moments of departure and arrival of a signal (or a physical body) registered by the observer is equal to zero ($d\tau = 0$), while the three-dimensional physically observable distance $d\sigma$ between the points of departure and arrival is not equal to zero ($d\sigma \neq 0$). Therefore, the space-time metric ds^2 along the trajectories of weak non-quantum teleportation is

$$\left.\begin{aligned} ds^2 &= c^2 d\tau^2 - d\sigma^2 = -d\sigma^2 \\ c^2 d\tau^2 &= 0\,, \qquad d\sigma^2 \neq 0 \end{aligned}\right\}, \tag{8}$$

thus these are the trajectories of mass-bearing particles (since along the trajectories of massless light-like particles $ds^2 = c^2 d\tau^2 - d\sigma^2 = 0$ and $c^2 d\tau^2 = d\sigma^2 \neq 0$).

The strong condition of non-quantum teleportation

$$d\tau = 0\,, \qquad d\sigma = 0 \tag{9}$$

means that not only the physically observable time interval $d\tau$ between departure and arrival registered by the observer, but also the three-dimensional physically observable distance $d\sigma$ between these points is equal to zero. Therefore, the space-time metric ds^2 along the trajectories of strong non-quantum teleportation is

$$\left.\begin{aligned} ds^2 &= c^2 d\tau^2 - d\sigma^2 = 0 \\ c^2 d\tau^2 &= d\sigma^2 = 0 \end{aligned}\right\}, \tag{10}$$

i.e., the space-time metric along the trajectories is *fully degenerate*: for a regular observer, all four-dimensional space-time intervals ds, three-dimensional observable intervals $d\sigma$ and observable time intervals $d\tau$ are zero along such fully degenerate trajectories. We therefore called them *zero-trajectories*, and the fully degenerate space-time region that hosts such trajectories — *zero-space*. The zero-space is the fully degenerate case of the light-like space (since along light-like trajectories $ds^2 = c^2 d\tau^2 - d\sigma^2 = 0$, but $c^2 d\tau^2 = d\sigma^2 \neq 0$). We showed that all particles in the zero-space appear to a regular observer as having zero rest-mass $m_0 = 0$ similar to light-like particles, but they also have zero relativistic mass $m = 0$ and frequency $\omega = 0$ (unlike light-like particles, since for them $m \neq 0$ and $\omega \neq 0$). Therefore, we called them *zero-particles*. Deducing the eikonal equation (wave phase equation) for zero-particles, we found that it has the form of a standing wave equation. This means that, for a regular observer, all particles located in the zero-space (zero-particles) appear as *standing light-like waves*, and the entire zero-space appears filled with a system of light-like standing waves — a *light-like hologram.* We also showed that the relation between energy and impulse is not conserved for zero-particles: $E^2 - c^2 p^2 \neq const$. This is characteristic only of virtual particles. According to Feynman diagrams, virtual particles are carriers of interactions between elementary particles. This means that all interactions between particles of our regular space-time are transmitted by zero-particles through an "exchange buffer" that is the zero-space.

The condition $d\tau = 0$ gives a formula for *physical conditions of non-quantum teleportation*

$$\mathrm{w} + v_i u^i = c^2, \qquad u^i = \frac{dx^i}{dt}\,, \tag{11}$$

which is a specific combination of the gravitational potential w, the linear velocity of rotation of the observer's space v_i, and also the coordinate velocity u^i of the teleported particle. This condition is true for both weak and strong non-quantum teleportation (since $d\tau = 0$ in both cases). In both cases, the physically observed velocity v^i of the teleported signal (or teleported body) registered by the observer is

$$\mathrm{v}^i = \frac{dx^i}{d\tau} = \infty, \tag{12}$$

which means that, from the observer's point of view, the observed signal (or body) *instantly displaces* over the distance from the point of departure to the point of arrival.

Note that non-quantum teleportation is really instant displacement of signals (or bodies) over a distance in accordance with the geometric structure of the four-dimensional space-time. It has nothing common with quantum teleportation [5], which does not transfer energy or matter over a distance, but is merely a probabilistic effect based on the laws of Quantum Mechanics.

We published the above results in 2001, in our first monograph [6], many years after obtaining them. Then a short summary of the results was published in 2005 [7].

In our monograph [6] we related the physical conditions of non-quantum teleportation $\mathrm{w} + v_i u^i = c^2$ (11) to the surface of gravitational collapsars (black holes). We proceeded from the fact that according to the definition of the gravitational potential $\mathrm{w} = c^2 (1 - \sqrt{g_{00}})$ (4) the gravitational collapse condition $g_{00} = 0$ means $\mathrm{w} = c^2$, which coincides with the teleportation conditions $\mathrm{w} + v_i u^i = c^2$ in the particular case where space does not rotate ($v_i = 0$). This means that the surfaces of all black holes in the Universe are physically connected to each other and are gateways to non-quantum teleportation in the Universe.

The question remained open: how to achieve the physical conditions for non-quantum teleportation in a regular laboratory on the Earth? In our monograph [6] and paper [8] we considered the stopped (frozen) light experiment performed in 2000 by Lene Hau [9]. In her famous experiments, the physically observable time of photons was stopped for up to 1.5 seconds in 2009 [10] in her Harvard laboratory without the state of gravitational collapse, thereby implementing the non-quantum teleportation conditions for photons during this period of time.

However, we are interested in non-quantum teleportation of physical bodies, and physical bodies consist of substance (i.e., mass-bearing particles).

At first glance, to realize the physical conditions of non-quantum teleportation $\mathrm{w} + v_i u^i = c^2$ (11) for real physical bodies, we need either to increase the gravitational potential in our laboratory to the numerical value characteristic of gravitational collapse or to rotate the local space of our laboratory at a speed close to the speed of light and also move the teleported test-body at a similar speed. Both are beyond the capabilities available in a regular laboratory.

Therefore, in 2022 we took a different approach to solving this problem [11], where the exotic physical conditions required for non-quantum teleportation can be achieved using a very strong electromagnetic field (such strong electromagnetic fields are able to be generated using modern technologies since the 1930s). The basis was considered to be the space of a low-speed rotating spherical body (like the planet Earth), the gravitational field of which is so weak that it can be neglected, which corresponds to the physical conditions in a regular Earth-bound laboratory. Having solved Einstein's field equations for the metric of such a space (their right-hand side is non-zero due to the electromagnetic field), we obtained specific characteristics of the magnetic and electric strengths under which physical bodies can be teleported.

Now we would like to answer the following question: are there natural, not man-made, conditions on the Earth (and on any other planet or star) under which non-quantum teleportation of physical bodies can be implemented?

To answer this question, let us now consider geometric conditions of non-quantum teleportation in the field of each of the three following space metrics:

- the space of a rotating spherical body, the gravitational field of which is so weak that can be neglected (its metric was introduced and proved in [11]);
- the space of a non-rotating spherical massive body, approximated by a material point (Schwarzschild's mass-point metric);
- the space of a rotating spherical massive body, approximated by a material point (its metric was introduced and proved in [12]).

The key point in our consideration is the *degeneration of space*. Under the weak non-quantum teleportation condition (8), only the physically observable time is degenerate ($d\tau = 0$). However, under the strong non-quantum teleportation condition (10), both the physically observable time, the physically observable three-dimensional space and the four-dimensional space-time are degenerate.

As we know from the theory of metric spaces, a metric space is degenerate if the determinant of its metric tensor is equal to zero. Anyone familiar with Riemannian geometry and tensor calculus can verify that in the four-dimensional pseudo-Riemannian space, which is the basic space-time of General Relativity, the determinant of the fundamental metric tensor $g = \det\| g_{\alpha\beta}\|$ is equal to $g < 0$. This means that the basic space-time of General Relativity is non-degenerate, and the zero-space (fully degenerate space-time) is located outside of it.

Zelmanov had proved that the determinant of the fundamental metric tensor $g = \det\| g_{\alpha\beta}\|$ and the determinant of the chr.inv.-metric tensor $h = \det\| h_{ik}\|$ are related with each other by the formula

$$h = -\frac{g}{g_{00}}\,, \qquad (13)$$

which means that, once the chr.inv.-metric tensor h_{ik} is degenerate ($h = 0$), the fundamental metric tensor $g_{\alpha\beta}$ is degenerate too ($g = 0$). Or, in another form

$$g = -g_{00}\, h\,, \qquad (14)$$

i.e., non-quantum teleportation is possible either under the state of gravitational collapse ($g_{00} = 0$), or under the degeneracy of the observable three-dimensional metric ($h = 0$), or if both these conditions take place together.

Consider the above Zelmanov formula in the field of each of the three mentioned space metrics.

The metric of the space of a rotating spherical body, the gravitational field of which is so weak that it can be neglected, was introduced and proved using Einstein's field equations in [11]. It has the form

$$ds^2 = c^2dt^2 - 2\,\omega r^2 \sin^2\theta\, dt\, d\varphi - dr^2 - r^2\left(d\theta^2 + \sin^2\theta\, d\varphi^2\right), \qquad (15)$$

where the non-zero components of the fundamental metric tensor $g_{\alpha\beta}$ are

$$\left.\begin{array}{lll} g_{00} = 1\,, & g_{03} = -\dfrac{\omega r^2 \sin^2\theta}{c} & \\ g_{11} = -1\,, & g_{22} = -r^2, & g_{33} = -r^2\sin^2\theta \end{array}\right\}, \qquad (16)$$

and the chr.inv.-metric tensor h_{ik} of such a space has the following non-zero components

$$\left.\begin{array}{ll} h_{11} = 1\,, & h_{22} = r^2 \\ h_{33} = r^2\sin^2\theta\left(1 + \dfrac{\omega^2 r^2 \sin^2\theta}{c^2}\right) & \end{array}\right\}, \qquad (17)$$

where, since the matrix h_{ik} is diagonal, the upper-index components of h_{ik} are $h^{ik} = (h_{ik})^{-1}$ just like the invertible components to any diagonal matrix. Such a space rotates in the equatorial plane along the φ-axis (along the geographical longitudes) with a constant angular velocity $\omega = const$ and, according to the definition of v_i (5), with a linear velocity

$$v_3 = -\frac{c\,g_{03}}{\sqrt{g_{00}}} = \omega\, r^2 \sin^2\theta\,, \tag{18}$$

for which, since $v^2 = v_i v^i = h_{ik} v^i v^k$ and $v^i = h^{ik} v_k$, we have

$$v^2 = v_i v^i = \frac{\omega^2 r^2 \sin^2\theta}{1 + \frac{\omega^2 r^2 \sin^2\theta}{c^2}}\,, \qquad v = \frac{\omega\, r \sin\theta}{\sqrt{1 + \frac{\omega^2 r^2 \sin^2\theta}{c^2}}}\,, \tag{19}$$

i.e., the dimension of v is [cm/sec]. At slow rotation the above formula transforms to the conventional $v = \omega\, r \sin\theta$.

Therefore, the determinant of the fundamental metric tensor $g = \det\| g_{\alpha\beta} \|$ and the determinant of the chr.inv.-metric tensor $h = \det\| h_{ik} \|$ of such a space have the form

$$g = -r^4 \sin^2\theta \left(1 + \frac{\omega^2 r^2 \sin^2\theta}{c^2}\right), \tag{20}$$

$$h = r^4 \sin^2\theta \left(1 + \frac{\omega^2 r^2 \sin^2\theta}{c^2}\right). \tag{21}$$

From these formulae for the determinants $g = \det\| g_{\alpha\beta} \|$ and $h = \det\| h_{ik} \|$ it is clear:

> The space of a rotating spherical body, the gravitational field of which is so weak that it can be neglected, is fully degenerate (the conditions of full degeneracy $h = 0$ and $g = -g_{00}\, h = 0$ are satisfied together) everywhere along the axis of its rotation, i.e., along its polar axis, in particular — at the North and South Poles on the surface of the body. This takes place simply because there $\sin\theta = 0$, since the polar angle θ is measured from the North Pole. But even at a very small distance from the North or South Poles along the geographical latitudes, the space of such a body is non-degenerate.

This is a purely mathematical fact that does not depend on the physical properties of the spherical body (since they are negligible) or the speed of its rotation, but takes place only due to the geometric structure of its space.

Another case is a spherical body that does not rotate but has a significant mass, so that its gravitational field cannot be neglected. The metric of the space of a non-rotating spherical massive body, approximated by a material point, is known as Schwarzschild's mass-point metric. It has the form

$$ds^2 = \left(1 - \frac{r_g}{r}\right) c^2 dt^2 - \frac{dr^2}{1 - \frac{r_g}{r}} - r^2 \left(d\theta^2 + \sin^2\theta\, d\varphi^2\right), \tag{22}$$

where $r_g = 2GM/c^2$ is the gravitational radius characteristic of the body, which is calculated for its mass M, and

$$\left.\begin{aligned} g_{00} &= 1 - \frac{r_g}{r}\,, \qquad & g_{11} &= -\frac{1}{1 - \frac{r_g}{r}} \\ g_{22} &= -r^2, \qquad & g_{33} &= -r^2 \sin^2\theta \end{aligned}\right\} \tag{23}$$

and, respectively,

$$h_{11} = \frac{1}{1 - \frac{r_g}{r}}\,, \qquad h_{22} = r^2, \qquad h_{33} = r^2 \sin^2\theta\,, \tag{24}$$

on the basis of which we obtain formulae for the determinants $g = \det\| g_{\alpha\beta} \|$ and $h = \det\| h_{ik} \|$

$$g = -r^4 \sin^2\theta\,, \qquad h = \frac{r^4 \sin^2\theta}{1 - \frac{r_g}{r}}\,. \tag{25}$$

In such a space, we see a situation different from the previous one:

> The space of a non-rotating spherical massive body is fully degenerate (i.e., the conditions of full degeneracy $h = 0$ and $g = -g_{00}\, h = 0$ are satisfied together) at the North and South Poles of the body and, in general, along the entire axis of rotation of the space (since there $\sin\theta = 0$) only at distances $r \neq r_g$ from the centre of the body. On a spherical surface with a radius equal to the gravitational radius of the body r_g (on which $g_{00} = 0$), the four-dimensional space-time metric remains degenerate at the poles ($g = 0$), and the physically observable three-dimensional space has a breaking $h = \infty$ everywhere on the surface except at the poles, where it has an uncertainty $h = \frac{0}{0}$.

It should be noted that this is a coordinate effect, because a non-rotating spherical body does not have a physical polar axis: its polar axis can be chosen arbitrarily. Therefore, the effect of degeneration of the space of a non-rotating body can always be eliminated by coordinate transformations (shifting the "polar" axis to another place on the surface of the body). This is in contrast to rotating physical bodies, because each of them has its own physical polar axis (its own axis of rotation) and, therefore, the effect of degeneration of its space cannot be eliminated by coordinate transformations.

Finally, consider the space of a rotating spherical massive body, approximated by a material point. Its metric was introduced and proved in [12] and has the form

$$ds^2 = \left(1 - \frac{r_g}{r}\right) c^2 dt^2 - 2\,\omega r^2 \sin^2\theta \sqrt{1 - \frac{r_g}{r}}\; dt\, d\varphi - {} $$

$$- \frac{dr^2}{1 - \frac{r_g}{r}} - r^2 \left(d\theta^2 + \sin^2\theta\, d\varphi^2\right), \tag{26}$$

where, respectively,

$$\left.\begin{aligned} g_{00} &= 1-\frac{r_g}{r}\,, \qquad g_{03} = -\frac{\omega r^2\sin^2\theta}{c}\sqrt{1-\frac{r_g}{r}} \\ g_{11} &= -\frac{1}{1-\frac{r_g}{r}}\,, \qquad g_{22} = -r^2, \quad g_{33} = -r^2\sin^2\theta \end{aligned}\right\}, \tag{27}$$

the space rotates along the φ-axis (along the geographical longitudes) with a constant angular velocity $\omega = const$ and, according to the definition of v_i (5), with a linear velocity

$$v_3 = -\frac{c\,g_{03}}{\sqrt{g_{00}}} = \omega r^2\sin^2\theta\,, \tag{28}$$

and the chr.inv.-metric tensor h_{ik} of the space has the following non-zero components

$$\left.\begin{aligned} h_{11} &= \frac{1}{1-\frac{r_g}{r}}\,, \qquad h_{22} = r^2 \\ h_{33} &= r^2\sin^2\theta\left(1+\frac{\omega^2 r^2\sin^2\theta}{c^2}\right) \end{aligned}\right\}, \tag{29}$$

so, the determinants $g = \det\|\,g_{\alpha\beta}\,\|$ and $h = \det\|\,h_{ik}\,\|$ have the form

$$g = -r^4\sin^2\theta\left(1+\frac{\omega^2 r^2\sin^2\theta}{c^2}\right), \tag{30}$$

$$h = \frac{r^4\sin^2\theta}{1-\frac{r_g}{r}}\left(1+\frac{\omega^2 r^2\sin^2\theta}{c^2}\right). \tag{31}$$

In such a space, the situation with its degeneration is similar to the space of a massive spherical body that does not rotate (considered above):

> The space of a non-rotating spherical massive body is fully degenerate (i.e., both conditions of full degeneracy $h = 0$ and $g = -g_{00}h = 0$ are satisfied) if $\sin\theta = 0$, i.e., at the North and South Poles of the body and, in general, along the entire axis of rotation of the space, but only at distances $r \neq r_g$ from the centre of the body. At a distance equal to the gravitational radius of the body r_g (this is a spherical surface, on which $g_{00} = 0$) the four-dimensional space-time metric remains degenerate at the poles ($g = 0$), and the physically observable three-dimensional space has a breaking $h = \infty$ except at the poles, where it has an uncertainty $h = \frac{0}{0}$.

Note that there is one key difference between this situation and the situation in a space of Schwarzschild's mass-point metric. As we have noted above, the effect of degeneration of space has a coordinate origin in the case of the mass-point metric, because the polar axis of such a space can be chosen arbitrarily. On the contrary, any rotating body has its own physical polar axis (its axis of rotation) and, therefore, the effect of degeneration of its space cannot be eliminated by coordinate transformations. For this reason, the mass-point metric cannot be considered physically valid in the problems where the degeneracy of space plays a rôle: when solving such problems, the mass-point metric must be replaced with the space metric of a rotating spherical massive body.

Finally, based on the above analysis of the geometric conditions of degeneration of spherical spaces, we arrive at the following conclusion about preferred conditions under which non-quantum teleportation could be implemented in a regular laboratory located on the surface of the Earth:

Preferred conditions for non-quantum teleportation

> Non-quantum teleportation can be implemented under any physical conditions in a laboratory located at the North and South Poles of a rotating spherical body, say, the Earth. This is simply due to the geometric structure of its rotating space, which is fully degenerate at the poles and, in general, everywhere along its axis of rotation. But even at a very small distance from the poles along the geographical latitudes, non-quantum teleportation requires exotic conditions, such as a very strong electromagnetic field, etc.

Yes, non-quantum teleportation can be implemented in a laboratory located at any other geographical latitude, and not only at the North and South Poles, say, due to certain configurations of a very strong electromagnetic field generated in the laboratory [11], or under some other exotic physical conditions created in it (since they do not depend on the geographical location of the laboratory). On the other hand, as we found in this study, at the North and South Poles non-quantum teleportation can be implemented under any physical conditions simply due to the geometric structure of the rotating space of the planet, which significantly simplifies the technical implementation of non-quantum teleportation in practice.

Therefore, to paraphrase the legendary saying of Baron Nathan Mayer Rothschild, who in 1815 said "He who owns the information, owns the world" (this phrase is sometimes misattributed to Winston Churchill, who often repeated it), we say: "He who owns the land at the poles of the Earth, owns the technical possibility for non-quantum teleportation to any point in the Universe". To be more precise, we mean land at the South Pole (in Antarctica), since there, unlike the North Pole of the Earth, which is covered by the waters of the Arctic Ocean, it is possible to install a laboratory and a stationary device for non-quantum teleportation.

Submitted on June 15, 2025

References

1. Zelmanov A. L. Chronometric Invariants. Translated from the 1944 PhD thesis, American Research Press, Rehoboth, New Mexico, 2006.
2. Zelmanov A. L. Chronometric invariants and accompanying frames of reference in the General Theory of Relativity. *Soviet Physics Doklady*, 1956, v. 1, 227–230 (translated from *Doklady Academii Nauk USSR*, 1956, v. 107, issue 6, 815–818).

3. Zelmanov A. L. On the relativistic theory of an anisotropic inhomogeneous universe. *The Abraham Zelmanov Journal*, 2008, vol. 1, 33–63 (translated from the thesis of the *6th Soviet Conference on the Problems of Cosmogony*, USSR Academy of Sciences Publishers, Moscow, 1957, 144–174).
4. Rabounski D. and Borissova L. Physical observables in General Relativity and the Zelmanov chronometric invariants. *Progress in Physics*, 2023, v. 19, issue 1, 3–29.
5. Bennett C. H., Brassard G., Crepeau C., Jozsa R., Peres A., and Wootters W. K. Teleporting an unknown quantum state via dual classical and Einstein-Podolsky-Rosen channels. *Physical Review Letters*, 1993, v. 70, 1895–1899.
6. Rabounski D. and Borissova L. Particles Here and Beyond the Mirror. The 4th revised edition, New Scientific Frontiers, London, 2023 (the 1st edition was issued in 2001).
   Rabounski D. et Larissa Borissova L. Particules de l'Univers et au delà du miroir. La 2ème édition révisée en langue française, New Scientific Frontiers, Londres, 2023 (French translation).
7. Rabounski D. and Borissova L. On the possibility of instant displacements in the space-time of General Relativity. *Progress in Physics*, 2005, v. 1, issue 1, 17–19.
8. Rabounski D. and Borissova L. A theory of frozen light according to General Relativity. *The Abraham Zelmanov Journal*, 2011, v. 4, 3–27.
9. Hau L.V. Frozen light. *Scientific American*, 17 July 2001, v. 285, no.1, 52–59.
10. Zhang R., Garner S. R., Hau L.V. Creation of long-term coherent optical memory via controlled nonlinear interactions in Bose-Einstein condensates. *Physical Review Letters*, 4 December 2009, v. 103, 233602.
11. Rabounski D. and Borissova L. Non-quantum teleportation in a rotating space with a strong electromagnetic field. *Progress in Physics*, 2022, v. 18, issue 1, 31–49.
12. Rabounski D. Introducing the space metric of a rotating massive body and four new effects of General Relativity. *Progress in Physics*, 2024, v. 20, issue 2, 79–99.

Accelerations of the Closed Time-Like Gödel Curves

Patrick Marquet

Calais, France. E-mail: patrick.marquet6@wanadoo.fr

In a paper published in 1949 in honor of his close friend Albert Einstein on the occasion of his 70th birthday, Kurt Gödel described a homogeneous and rotating universe by discovering the existence of closed timelike curves (CTCs). In a series of papers, we replaced the constant a of the Gödel metric with a simple conformal factor, which easily induces a pressure term that leads directly to the ideal fluid field equation. Gödel introduced this special term a, relating it to the cosmological constant, to make his solution satisfying Einstein's field equations. This theory is now endowed with physical sense, and the dynamics no longer apply to space, but to a fluid. Eventually, the Gödel CTCs are considered to be flow lines of a charged fluid, which preserve the properties of the model. The resulting acceleration of these flow lines can then be adequately controlled.

Notations

Space-time indices: $\mu, \nu = 0, 1, 2, 3$;
Space-time signature: -2;
Einstein's constant: $\varkappa$;
The velocity of light: $c = 1$.

1 The Gödel Universe

1.1 General

In his original paper [1], K. Gödel derived an exact solution to Einstein's field equation that describes a homogeneous and non-isotropic universe where matter takes the form of a shear-free fluid. This metric exhibits a rotational symmetry that allows for the existence of closed timelike curves (CTCs).

Gödel's model is usually regarded as a mathematical curiosity and is rejected because it requires a cosmological constant related to a constant Ricci scalar finely tuned to the mass density of the Universe.

In several publications, we have been able to relax our requirement that the Gödel metric be a description of our real Universe, which is still observed to be expanding.

1.2 Gödel's metric

The classical Gödel line element is given by:

$$ds^2 = a^2\left(dt^2 + \frac{1}{2}\,e^{2x}dy^2 - 2\,e^{x}\,dt\,dy - dx^2 - dz^2\right), \tag{1.1}$$

where $a > 0$ is a constant.

The normalized unit vector $\boldsymbol{u}$ of matter has components:

$$u^{\mu} = (a^{-1},\, 0,\, 0,\, 0)\,, \qquad u_{\mu} = (a,\, 0,\, ae^{x},\, 0)\,, \tag{1.2}$$

thus the Ricci tensor takes the value

$$R_{\mu\nu} = u_{\mu}\,u_{\nu}\,a^{-2} \tag{1.3}$$

and the Ricci scalar is

$$R = u^{\mu}u_{\mu} = a^{-2}. \tag{1.4}$$

Since R is a constant, then the field equations

$$R_{\mu\nu} - \frac{1}{2}\,g_{\mu\nu}R = \varkappa\rho u_{\mu}\,u_{\nu} + \Lambda\,g_{\mu\nu} \tag{1.5}$$

are satisfied (for a given value of the density ρ), if we put:

$$a^{-2} = \varkappa\,, \tag{1.6}$$

$$\Lambda = -\frac{1}{2}\,R = \frac{1}{2a^2} = -\frac{1}{2}\,\varkappa\rho\,. \tag{1.7}$$

The sign of the cosmological constant Λ here is opposite to that in Einstein's field equations. Bearing in mind that a is a constant, finetuning the density of the universe with the cosmological constant and the Ricci scalar appears as a dubious hypothesis. One then clearly sees that such cosmological constraints are physically irrelevant.

2 The Gödel model as a homogeneous perfect fluid

2.1 Reformulation of the Gödel metric

In our publications [2,3], we assumed that a is slightly space-time variable and we set:

$$a^2 = e^{2U} \tag{2.1}$$

(the positive scalar $U(x)$ will be explicited below). Thus, the Gödel metric takes the form:

$$ds^2 = e^{2U}\left(dt^2 + \frac{1}{2}\,e^{2x}dy^2 - 2\,e^{x}dt\,dy - dx^2 - dz^2\right). \tag{2.2}$$

With the Euler variational derivation detailed in [4–6], this conformal metric leads to the Einstein field equations for a perfect fluid [7]:

$$R_{\mu\nu} - \frac{1}{2}\,g_{\mu\nu}R = \varkappa\left[(\rho + P)\,u_{\mu}\,u_{\nu} - Pg_{\mu\nu}\right]. \tag{2.3}$$

Now, the real 4-unit vector $\boldsymbol{u}$ of the Gödel fluid displays the following components:

$$u^{\mu} = (1,\, 0,\, 0,\, 0)\,, \qquad u_{\mu} = (1,\, 0,\, e^{x},\, 0)\,. \tag{2.4}$$

2.2 Differential geodesic system

The 4-unit vector u^μ is normalized on $(\mathrm{M}, \boldsymbol{g})$:

$$g_{\mu\nu} u^\mu u^\nu = g^{\mu\nu} u_\mu u_\nu = 1\,.$$

By differentiating we get:

$$u^\nu \nabla_\mu u_\nu = 0\,. \tag{2.5}$$

Let us define the vector L_ν by the relation

$$\nabla_\mu P \delta^\mu_\nu = \mathbf{r} L_\nu \tag{2.6}$$

having set $\mathbf{r} = \rho + P$.

The conservation law for $T_{\mu\nu} = \mathbf{r} u_\mu u_\nu - P g_{\mu\nu}$ is expressed by $\nabla_\mu T^\mu_\nu = 0$, i.e.:

$$\left.\begin{aligned} &\nabla_\mu (\mathbf{r} u^\mu u_\nu) = \mathbf{r} L_\nu \\ &\nabla_\mu (\mathbf{r} u^\mu) u_\nu + \mathbf{r} u^\mu \nabla_\mu u_\nu = \mathbf{r} L_\nu \end{aligned}\right\}. \tag{2.7}$$

Multiplying through this relation with u^ν and taking into account (2.5), we obtain, by substituting in (2.7) and after dividing by $\mathbf{r}$:

$$u^\mu \nabla_\mu u_\nu = (g_{\mu\nu} - u_\mu u_\nu) L^\mu \tag{2.8}$$

with the projection tensor $h_{\mu\nu} = (g_{\mu\nu} - u_\mu u_\nu)$

$$u_\nu = h_{\mu\nu} L^\mu. \tag{2.9}$$

With setting $L_\nu = \partial_\nu U$, the equation (2.9) takes the form ${}^*u_\nu = h_{\mu\nu} \partial^\mu U$ and (2.6) reads

$$(\rho + P) L_\nu = \nabla_\mu P \delta^\mu_\nu\,,$$

$$L_\nu = \frac{\partial_\nu P}{\rho + P}\,.$$

As a result we find:

$$U(x^\mu) = \int_{P_1}^{P_2} \frac{dP}{\rho + P}\,,$$

where the pressures P_1 and P_2 are related to the points x_1 and x_2, respectively.

The flow lines of a perfect fluid with a density ρ and a pressure P with the equation of state $\rho = f(P)$ obey the differential system:

$$u^\mu \nabla_\mu u_\nu = h_{\mu\nu} \partial^\mu U = {}^*u_\nu\,. \tag{2.10}$$

The 4-vector ${}^*u_\nu$ must be regarded as the 4-acceleration of the flow lines given by the pressure gradient orthogonal to those lines [8, p.70].

Controlling this acceleration is almost impossible: varying the pressure P through the equation of state appears as physically unrealistic. There is however a way to solve this problem: the fluid encoding the CTCs should be characterized by a charged current density acted upon by a variable electromagnetic field. Next we will show that the resulting 4-acceleration of this fluid only depends on the charge and the 4-potential of the field.

3 Controlling the CTCs

3.1 Charged fluid

At first, we consider a simple charged fluid in the connected domain where exists a field vector A_δ represented by the Maxwell tensor

$$F_{\gamma\delta} = \partial_\gamma A_\delta - \partial_\delta A_\gamma\,. \tag{3.1}$$

To this 4-potential-vector is associated the linear form:

$$dA = A_\lambda dx^\lambda. \tag{3.2}$$

The energy-momentum tensor reads:

$$T^{\mu\nu} = \rho u^\mu u^\nu + t^{\mu\nu}, \tag{3.3}$$

where

$$t^{\mu\nu} = -\frac{1}{4\pi}\left(\frac{1}{4} g^{\mu\nu} F_{\gamma\delta} F^{\gamma\delta} + F^{\mu\beta} F^{\nu}_{\ \beta}\right) \tag{3.4}$$

is the energy-momentum of the electromagnetic field.

From the conservation condition of the tensor $T^{\mu\nu}$

$$\nabla_\mu T^\mu_\nu = 0 \tag{3.5}$$

it follows that

$$\nabla_\mu t^\mu_\nu = -F_{\mu\nu} j^\mu, \tag{3.6}$$

where the 4-current density $j^\mu = \mu u^\mu$ carrying the charge μ is defined by the second group of Maxwell's equations:

$$\nabla_\mu F^{\mu\nu} = -4\pi j^\nu. \tag{3.7}$$

Equation (3.5) yields:

$$\nabla_\mu (\rho u^\mu u_\nu) = \mu F_{\mu\nu} u^\mu,$$

$$\rho u^\mu \nabla_\mu u_\nu + u_\nu \nabla_\mu (\rho u^\mu) = \mu F_{\mu\nu} u^\mu.$$

The 4 current density is conserved:

$$\nabla_\mu (\mu u^\mu) = 0\,.$$

Then, using the relation $u_\mu u_\nu = 0$ and due to the antisymmetry of $F_{\mu\nu}$, we obtain:

$$\nabla_\mu (\rho u^\mu) = 0\,,$$

therefore

$$u^\mu \nabla_\mu u_\nu = \frac{\mu}{\rho} F_{\mu\nu} u^\mu.$$

By setting $\mathrm{k} = \mu/\rho$, the equation

$$u^\mu \nabla_\mu u_\nu = \mathrm{k}(F_{\mu\nu} u^\mu) = {}^*u_\nu \tag{3.8}$$

represents the equation of geodesics for a charged homogeneous fluid (i.e., its acceleration).

The flow lines of this current form the geodesics of the Finsler metric [9], which extremizes the integral:

$$s = \int_{x_1}^{x_2} (ds + \mathrm{k}\, d\boldsymbol{A})\,. \tag{3.9}$$

Relations (2.5) and (2.6) can be written in the form:

$$\nabla_\mu u^\mu + \frac{u^\mu \partial_\mu \mu}{\mu} = 0\,, \qquad \nabla_\mu u^\mu + \frac{u^\mu \partial_\mu \rho}{\rho} = 0\,,$$

then, subtracting, we obtain:

$$u^\mu \partial_\mu \left(\ln \frac{\mu}{\rho}\right) = 0\,. \tag{3.10}$$

It should be noted that throughout along these trajectories, the ratio $\mathrm{k} = \mu/\rho$ remains constant.

3.2 Charged perfect fluid

Let us now turn to the perfect fluid scheme. In this case, the energy-momentum tensor reads:

$$T^{\mu\nu} = (\rho + P)\,u^\mu u^\nu - P g^{\mu\nu} + t^{\mu\nu}. \tag{3.11}$$

Introduce the scalar:

$$\rho' = \frac{\rho + P}{e^U}\,. \tag{3.12}$$

Observing that

$$\frac{d\rho'}{\rho} = \frac{d(\rho+P)}{\rho+P} - \frac{dP}{\rho+P} = \frac{d\rho}{\rho+P}\,,$$

we derive an equation similar to (3.10):

$$u^\mu \partial_\mu \ln\left(\frac{\mu}{\rho'}\right) = 0\,.$$

This shows that the ratio $\mathrm{k}' = \mu/\rho'$ should also remain constant along the Finsler trajectory:

$$ds' = \left(e^{2U} g_{ab}\, dx^a dx^b\right)^{1/2} + \mathrm{k}'\, d\boldsymbol{A}\,,$$

$$s' = \int_{x_1}^{x_2} \left(e^U ds + \mathrm{k}'\, d\boldsymbol{A}\right).$$

Let us apply this system to the Gödel interval:

$$ds_{\mathrm{G}} = \\ = \left[e^{2U}\left(dt^2 + \frac{1}{2}\,e^{2x} dy^2 - 2e^x dt\,dy - dx^2 - dz^2\right)\right]^{1/2}. \tag{3.13}$$

The flow lines of the charged fluid encoding the Gödel CTCs are described by:

$$s_{\mathrm{G}} = \int_{x_1}^{x_2} \left[e^U \left(dt^2 + \frac{1}{2}\,e^{2x} dy^2 - 2e^x dt\,dy - dx^2 - dz^2\right)^{1/2} + \\ + \mathrm{k}'\, d\boldsymbol{A}\right]. \tag{3.14}$$

The 4-acceleration vector of the charged fluid encoding the CTCs is now:

$$u^\mu \nabla_\mu u_\nu = \mathrm{k}' \left(F_{\mu\nu} u^\mu\right) = {}^*u_\nu\,. \tag{3.15}$$

For a given value of the charge μ, this simple formula can be modified through a variable electromagnetic field.

Conclusions

When Gödel wrote down his metric, he was forced to introduce a distinctive constant factor a to re-write the field equations with a cosmological constant together with additional restrictions. Our theory is free from all these restrictions and, moreover, it gives a physical meaning to the term a.

The Gödel space-time is no longer a cosmological model, but a bounded region in which the dynamics of a physical fluid takes place, preserving all the basic properties associated with closed timelike curves. These CTCs are not geodesics, as shown in [10], so they are a subject to accelerations that were obtained using our conformal formalism.

It is obvious that the properties of Gödel CTCs are preserved for a charged fluid, and the modified Gödel metric can be locally reproduced. Moreover, the acceleration of this fluid seems to be physically feasible by means of an alternating electromagnetic field.

As mentioned earlier [11], these results shed new light on the possibilities of time travel, confirming earlier work started in [12–14].

Submitted on June 11, 2025

References

1. Gödel K. An example of a new type of cosmological solutions of Einstein's field equations of gravitation. *Review of Modern Physics*, 1949, v. 21, no. 3, 447–450.
2. Marquet P. The exact Gödel metric. *Progress in Physics*, 2021, v. 17, no. 2, 133–138.
3. Marquet P. The time machine. *Progress in Physics*, 2025, v. 21, no. 1, 16–28.
4. Eisenhart L.P. Space-time continua of perfect fluids in general relativity. *Trans. Amer. Math. Soc.*, 1924, v. 26, 205–220.
5. Synge J.L. Relativistic hydrodynamics. *Proc. London Math. Soc.*, 1937, v. 43, 376–416.
6. Lichnerowicz A. Les Théories Relativistes de la Gravitation et de l'Electromagnétisme. Masson et Cie, Paris, 1955.
7. Landau L., Lifshitz E. The Classical Theory of Fields. Addison-Wesley, Reading, 1962.
8. Hawking S.W., Ellis G.F.R. The Large Scale Structure of Space-Time. Cambridge University Press, 1973.
9. Marquet P. Geodesics and Finslerian equations in the EGR theory. *The Abraham Zelmanov Journal*, 2010, v. 3, 90–100.
10. Chandrasekhar S., Wright J.P. The geodesics in Gödels's universe. *Proc. of the National Academy of Sciences*, 1961, v. 47(3), 341–347.
11. Marquet P. Gödel time travel with warp drive propulsion. *Progress in Physics*, 2022, v. 18, no. 1, 82–88.
12. Lanczos C. Über eine Stationäre Kosmologie im Sinne der Einsteinischer Gravitationstheorie. *Zeitschrift für Physik*, 1924, Bd. 21, 73–110.
13. Van Stockum W.J. The gravitationnal field of a distribution of particles rotating around an axis of symmetry. *Proc. Roy. Soc. Edinburgh*, 1937, v. 57, 135–154.
14. Tipler F.J. Rotating cylinders and the possibility of global causality. *Phys. Rev. D*, 1974, v. 9, no. 8, 2203–2206.

Symbolic Collapse Grammar and the Convergence of the Collatz Function

Travis S. Taylor[1,2]

[1]QuantumFrontier, LLC, Huntsville, AL, USA.
[2]Department of Physics, University of Alabama in Huntsville, AL, USA.
E-mail: tst0072@uah.edu

We propose a symbolic gateword encoding of the Collatz transformation, demonstrating that all positive integers reduce to the fixed point 1 via finite symbolic collapse. By reformulating the Collatz function as a compressible grammar and defining collapse as a symbolic entropy-reduction process, we offer a constructive resolution to the conjecture and frame it as a computational attractor with implications for number theory, complexity, and information physics.

1 Introduction

The Collatz Conjecture, also known as the $3n + 1$ problem, remains one of the most deceptively simple and deeply unresolved problems in mathematics. Defined by a piecewise recurrence relation — halving even integers and applying $3n+1$ to odds — the function appears to reduce every positive integer to 1 in finite time. Yet, despite exhaustive computational verification for numbers well beyond 2^{60} and significant work by researchers such as Lagarias [1] and Tao [2], a general proof has eluded discovery as discussed in popular presentations such as Veritasium's video on the Collatz problem [3].

Traditional approaches have examined the conjecture through number-theoretic, probabilistic, and computational lenses, often confronting the chaotic and fractal-like behavior of trajectories. But the question remains: Is there a hidden structure — an attractor, a symmetry, a compression principle — that governs these apparent complexities?

In this work, we propose a novel encoding of the Collatz function as a symbolic grammar, translating each transformation step into a gateword of symbolic states. We demonstrate that these symbolic sequences obey compression rules which always converge to a fixed collapse point. This grammar-based approach reframes the conjecture as a problem in information theory and symbolic computation, revealing an underlying collapse structure akin to thermodynamic entropy reduction or quantum path filtering.

Our findings suggest that Collatz is not just a numerical curiosity but a window into a deeper structure of symbolic evolution, with implications that extend into complexity theory, qudit-based computation, and even spacetime physics.

2 The Collatz map as a symbolic grammar

To reformulate the Collatz function as a symbolic process, we encode each transformation step as a symbol in a grammar string, or gateword. Each positive integer n evolves under the standard recursive rule:

$$T(n) = \begin{cases} \frac{n}{2}, & \text{if } n \equiv 0 \pmod 2, \\ 3n+1, & \text{if } n \equiv 1 \pmod 2. \end{cases} \tag{1}$$

We now introduce a symbolic encoding scheme in which each transformation is mapped to a single symbolic character. Let:

$$E \equiv \text{Even step: } n \mapsto \frac{n}{2}, \tag{2}$$

$$O \equiv \text{Odd step: } n \mapsto 3n+1 \quad \text{(followed by an implicit } E). \tag{3}$$

Because the transformation $3n + 1$ always produces an even number, it is necessarily followed by at least one halving step. Thus, we treat O as representing the composite operation of $(3n + 1)/2$ and potentially further divisions.

Worked example: symbolic encoding of $n = 11$

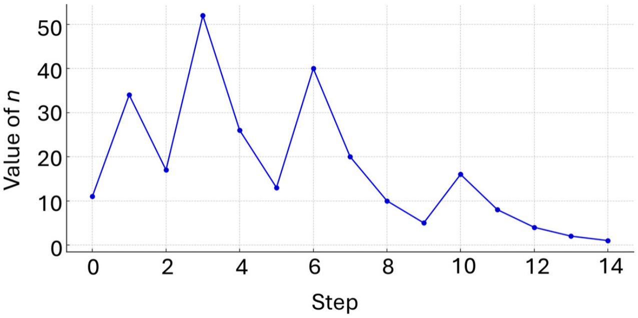

Fig. 1: Value of n versus step number for the Collatz sequence starting at $n = 11$. This trajectory shows an initial rise followed by a series of reductions, eventually collapsing to the fixed point at $n = 1$.

To illustrate the symbolic encoding, consider the integer $n = 11$. Applying the Collatz rule repeatedly:

$$11 \to 34 \to 17 \to 52 \to 26 \to 13 \to 40 \to \\ \to 20 \to 10 \to 5 \to 16 \to 8 \to 4 \to 2 \to 1. \tag{4}$$

Fig. 1 visualizes the numerical evolution of the Collatz sequence starting from $n = 11$. The plot reveals a characteristic structure seen in many Collatz trajectories: an initial rise in magnitude, followed by a series of decreasing steps as the sequence approaches the fixed point at $n = 1$. Although the values fluctuate non-monotonically, the deterministic rule set ensures eventual collapse. This structure, when viewed through a symbolic lens, becomes even more tractable as a grammar of transformations.

This sequence corresponds to the symbolic gateword:

$$\texttt{OEEOEOEEOEOEEE}\,. \tag{5}$$

Here, each `O` represents a transformation of the form $3n + 1$, and each `E` represents a division by 2. The symbolic sequence encodes the full trajectory of $n = 11$ down to the fixed point at $n = 1$. Note that this symbolic form captures the "shape" of the transformation path, abstracted from the numeric values.

Symbolic math lengths and compression

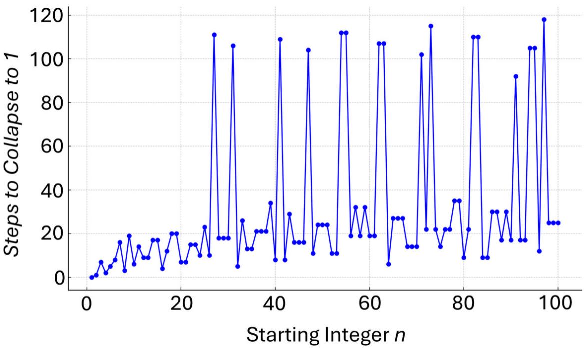

Fig. 2: Symbolic collapse length of Collatz sequences for $n = 1$ to 100. Each value converges to 1 in a finite number of symbolic transformations.

Fig. 2 shows the number of transformation steps required to reduce each integer n from 1 to 100 down to the fixed point at $n = 1$. Each step in this count corresponds to one symbol in the gateword grammar.

This symbolic path length provides a measure of *computational distance* to collapse. In this framing, longer paths correspond to grammars with higher symbolic entropy, while shorter paths collapse more quickly into the attractor. Remarkably, despite chaotic appearances, all symbolic gatewords for $n \leqslant 100$ converge in finite time, strongly supporting the conjecture that no sequence escapes symbolic collapse. The visual clarity of this trajectory naturally leads to the central question: *Does every positive integer follow a path that ultimately collapses to 1 in a finite number of steps*?

3 Collapse path structure

While individual symbolic gatewords vary in length and character, they all encode transformation paths governed by the same recursive structure. When viewed across many values of n, these paths exhibit a remarkable property: they all ultimately collapse into a common attractor centered on the fixed point at $n = 1$.

n	Steps	Symbolic Gateword
5	5	OE[**E**]EE
6	8	E[**O**]EOEEEE
7	16	OE[**O**]EOEEOEEEOEEEE
9	19	OE[**E**]OEOEOEEOEEEOEEEE
11	14	OE[**O**]EEOEEEOEEEE
13	9	OEOEEEO
17	12	OEOEOEEEO
27	111	*[omitted for brevity]*

Table 1: Symbolic gatewords for selected values of n, with event horizon points indicated in brackets. Each sequence terminates at $n = 1$ after a finite number of transformations, entering a redundant collapse basin after the marked transition.

Table 1 presents symbolic gatewords for selected values of n, with the inferred *event horizon* indicated by brackets around the transition symbol. The event horizon marks the point in the sequence where semantic compression begins — after which the symbolic trajectory enters a deterministic collapse basin shared by many other integers. For example, in the case of $n = 11$, the event horizon occurs at the sixth step, corresponding to the value $n = 40$, where the remaining transformations mirror those of multiple other sequences.

Some gatewords in the table, such as those for $n = 13$ and $n = 17$, do not show a marked event horizon. This suggests that their trajectories either enter the collapse basin at or near their origin, or are already within it at the first transformation. These "pre-collapsed" sequences highlight the nonuniform distribution of semantic curvature across the space of integers.

This structural inflection point behaves analogously to a physical event horizon: information beyond this symbolic boundary is no longer unique and becomes irreversibly directed toward the attractor at $n = 1$.

We define the event horizon function $h(n)$ for a given integer n as:

$$h(n) = \min\left\{ k \in \mathbb{N} \;\middle|\; \forall j > k,\; T^{(j)}(n) \in C \right\} \tag{6}$$

whereas, the earliest step k such that all subsequent transformations $T^{(j)}(n)$, for $j > k$, lie within a known compression basin C. This basin consists of values whose symbolic gateword suffixes are highly redundant and ultimately indistinguishable from other sequences. In practice, C may be characterized by repeated subsequences (e.g., strings of E's), convergence to a known shared trajectory (such as the path through 40, 20, 10, 5, 16, ...), or loss of symbolic degrees of freedom.

The function $h(n)$ identifies the semantic boundary beyond which further steps do not add informational uniqueness to the trajectory. It is, in this sense, the symbolic analog of an event horizon in general relativity — marking the boundary after which all paths are gravitationally — or grammatically

— bound to collapse toward a singular point. As previously shown in Fig. 1, the symbolic collapse graph for $n = 11$ illustrates this behavior clearly.

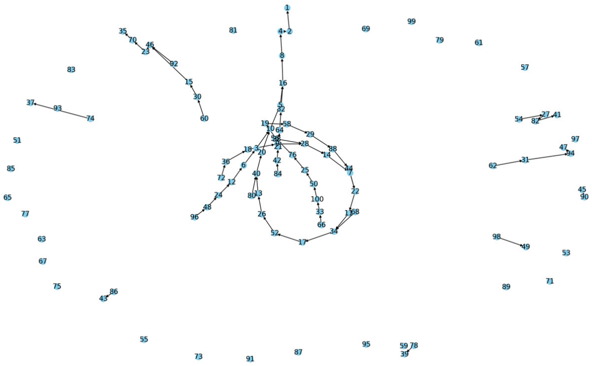

Fig. 3: Symbolic collapse graph for $n \leqslant 100$, showing clear convergence into a central structure. Paths with shared gatewords exhibit redundancy and early collapse.

Fig. 3 shows the symbolic collapse graph for all integers $n \leqslant 100$. Each node represents an integer, and each directed edge represents a transformation under the Collatz rule. Despite the apparent variation in local path geometry, all sequences funnel into a shared collapse structure. Gatewords with similar symbolic content often merge early, demonstrating both symbolic and numeric redundancy within the space of trajectories.

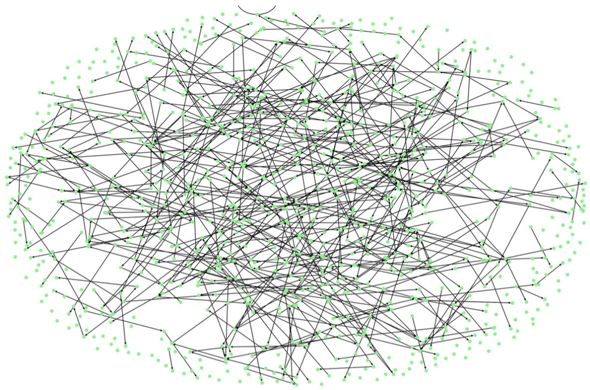

Fig. 4: Expanded symbolic collapse graph for $n \leqslant 1000$. Despite chaotic appearance, all paths still collapse into the same attractor at $n = 1$, consistent with symbolic compression.

This effect becomes even more evident in Fig. 4, which expands the range to $n \leqslant 1000$. Although the graph appears more chaotic, the underlying behavior is consistent: every path eventually enters the core basin of convergence. This supports the hypothesis that the symbolic grammar underlying the Collatz map inherently filters out non-converging sequences.

The visual structure of these graphs suggests that symbolic collapse is not a numerical coincidence, but rather a compressive process with an attractor basin embedded in grammar space. The next section formalizes this intuition by introducing reduction rules and a symbolic compression argument.

4 Symbolic compression proof

Having established the structure of symbolic gatewords and the existence of an event horizon for each n, we now formalize the mechanism by which all gatewords reduce to a finite symbolic sequence terminating at the fixed point $n = 1$. This proof proceeds by defining a set of reduction rules, or compression transformations, that act on symbolic subsequences.

Compression rules

Let $\mathcal{G}$ be the symbolic grammar over the alphabet $\{O, E\}$. We define the following reduction operations:

1. **Terminal absorption:** Any gateword ending in the pattern E^k, for some $k \geqslant 2$, reduces directly to 1:

   $$\mathtt{E}^k \Rightarrow 1\,.$$

   This reflects the rapid halving process through powers of two.
2. **Redundant pair contraction:** Patterns of the form $OE^2O \Rightarrow OE'$, where E' is a compressed even transition. These clusters are commonly seen post-event horizon and do not contribute new symbolic curvature.
3. **Loop absorption:** Repeating sub-patterns like $EOEO$, $OEOE$, or E^3O can be replaced with a single compressed token or rule-equivalent. These symbolic loops decay quickly under iteration.

Collapse theorem

Theorem 1 (Symbolic Collapse): Let $W(n)$ be the symbolic gateword generated by the Collatz transformation $T(n)$ for any positive integer n. Then there exists a finite sequence of reduction operations $\{R_i\}$ acting on $W(n)$ such that:

$$\exists m \in \mathbb{N}, \quad R_m \circ \cdots \circ R_1(W(n)) = 1\,. \tag{7}$$

Proof Sketch. The function $T(n)$ is known to terminate at 1 for all verified values of $n < 2^{68}$ [3–5], and its recursive structure guarantees that any O must eventually be followed by at least one E and converge to a value already in C (the compression basin). The grammar $\mathcal{G}$ is closed under finite-length transformations, and all gatewords are composed of a finite set of local operations from $\{O, E\}$. Therefore, repeated application of reduction rules yields a minimal, terminal gateword. ■

Implications

This result reframes the Collatz conjecture as a symbolic compression theorem: every gateword, no matter how complex in its early terms, reduces to a universal minimal string under a deterministic grammar. The symbolic grammar $\mathcal{G}$ is thus a contraction mapping in information space.

Although the Collatz function has been computationally verified for all $n < 2^{68}$ [3–5], the symbolic collapse grammar $\mathcal{G}$ provides a structure that generalizes beyond empirical bounds. Each gateword $W(n)$ is finite in length, composed of operations drawn from a closed alphabet $\{O, E\}$, and subject to deterministic reduction rules.

If the grammar $\mathcal{G}$ admits no infinite-length irreducible gatewords, then no value of n can escape eventual collapse. In this framing, the Collatz conjecture is reduced to a question of symbolic containment: whether all grammatically generated gatewords are ultimately compressible under the contraction rules defined above.

Thus, we reinterpret the conjecture not as a number-theoretic claim, but as a compression theorem over a symbolic language.

Gateword complexity function

To quantify the symbolic entropy of a given trajectory, we define the gateword complexity function $C(n)$ as the number of distinct symbolic substrings of fixed length ℓ within the gateword $W(n)$ [7]:

$$C(n, \ell) = |\{W(n)_{i:i+\ell} \mid 1 \leqslant i \leqslant |W(n)| - \ell + 1\}| \,. \tag{8}$$

This function counts how many unique symbolic motifs of length ℓ appear in the trajectory of n. A high value of $C(n, \ell)$ indicates symbolic diversity, while a sudden drop in C suggests entrance into a compression basin or redundancy zone.

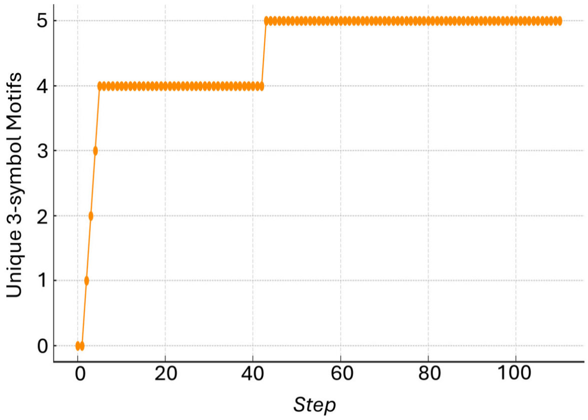

Fig. 5: Motif complexity $C(n, 3)$ for $n = 27$, using a 3-symbol sliding window. The curve shows initial growth followed by plateauing, indicating symbolic redundancy and entry into the compression basin.

Fig. 5 shows the motif complexity function $C(n, \ell)$ for the case $n = 27$, using a sliding window of length $\ell = 3$ over the symbolic gateword. The value of C at each step reflects the number of unique symbolic triplets encountered up to that point. Initially, the motif complexity grows rapidly as the trajectory explores a wide range of symbolic configurations. However, around step 50, the curve begins to plateau, indicating that new substrings become increasingly rare. This inflection marks the onset of symbolic redundancy and supports the presence of an event horizon: a transition beyond which the gateword enters a low-entropy compression basin. Despite the notorious length of the trajectory for $n = 27$, the symbolic structure exhibits predictable convergence well before termination, reinforcing the collapse dynamics proposed in Theorem 1.

5 Attractor interpretation

The symbolic compression grammar introduced in the previous sections reveals that the Collatz function behaves as a dynamical system with a single, universal attractor at the fixed point $n = 1$. From a symbolic standpoint, all gatewords ultimately collapse into a shared grammatical structure, regardless of their initial complexity. This convergence reflects a deeper property of the system: the existence of an entropy gradient in grammar space.

Collapse basin as curved grammar space

We interpret the gateword space $\mathcal{G}$ as a curved symbolic manifold, where the distance from the attractor corresponds to symbolic entropy or information-theoretic curvature [8]. The symbolic event horizon function $h(n)$ serves as a coordinate function marking the transition from free trajectories to gravitationally bound collapse, much like the Schwarzschild radius defines causal disconnection in general relativity.

In this framing, values of n with high symbolic entropy — long gatewords and many unique motifs — are located farther from the attractor. As a trajectory approaches the event horizon, its gateword enters a region of high curvature, where symbolic operations become compressive and redundant.

Symbolic potential and gradient descent

We can define a symbolic potential function $V(n)$, loosely analogous to gravitational potential, which decreases along the Collatz trajectory:

$$V(n) \propto -|W(n)| \,. \tag{9}$$

Here, $|W(n)|$ is the length of the symbolic gateword. Each transformation step corresponds to a descent along this potential, and the collapse process can be modeled as a type of gradient descent through symbolic entropy space. The deeper into the basin, the lower the symbolic energy, until the system settles into the absolute minimum at $n = 1$.

Redundancy as curvature indicator

The plateauing behavior of motif complexity $C(n, \ell)$, as demonstrated in Fig. 5, provides empirical evidence of the collapse basin. Once inside this basin, new symbolic motifs cease to emerge, and the gateword trajectory becomes entropically flat. This loss of semantic variation is the symbolic analog of redshift or information loss across a horizon.

Thus, the symbolic attractor is not just a fixed point in number space — it is a gravitational sink in symbolic grammar space. Every sequence, no matter how turbulent in early stages, is gravitationally bound to spiral into this universal minimum.

Symbolic geodesics in collapse space

We interpret the Collatz trajectory of any integer n as a geodesic in a curved symbolic manifold. Just as a test particle follows the straightest possible path through a gravitational field, the gateword $W(n)$ follows a path of minimal resistance through entropy-curved grammar space. This geodesic is not defined by spatial distance, but by informational curvature and symbolic entropy.

Each transformation — whether an odd or even step — moves the sequence along this geodesic according to deterministic rules. The gateword complexity $C(n, \ell)$ and its gradient provide a local measure of curvature. Regions with high motif diversity correspond to low symbolic curvature (flat regions), while zones of rapid motif collapse mark areas of high curvature that guide the trajectory toward the attractor.

We propose that the symbolic basin around $n = 1$ constitutes a kind of information well, into which all trajectories eventually fall. The symbolic compression rules function like Christoffel symbols — they do not add new dynamics, but describe how the local geometry (symbolic structure) shapes the flow of transformation.

In this view, the Collatz Conjecture becomes a statement about the *global connectivity of symbolic geodesics*: all paths, no matter their starting point, converge to a shared symbolic singularity through finite symbolic evolution.

Symbolic field equation

If symbolic collapse trajectories follow geodesics in an entropy-curved grammar space, then the curvature of that space must arise from the symbolic equivalent of energy density — namely, compression gradients and motif entropy. We propose an informational analog to Einstein's field equation [9]:

$$\mathcal{R}_{ij} - \frac{1}{2}\,\mathcal{R}\,\gamma_{ij} = \kappa\,\Sigma_{ij}\,. \tag{10}$$

Here, $\mathcal{R}_{ij}$ is a symbolic curvature tensor that encodes distortions in gateword trajectory space, and γ_{ij} is the symbolic metric defined by edit distance or collapse divergence between gatewords. The right-hand side, Σ_{ij}, is a symbolic entropy-momentum tensor, defined by local motif complexity, symbolic redundancy rate, and compression resistance.

This equation suggests that entropy gradients cause symbolic curvature, and symbolic curvature in turn governs the flow of collapse — just as mass-energy curves spacetime and guides geodesics. In this formalism, every Collatz sequence becomes a geodesic through symbolic spacetime, with the attractor at $n = 1$ functioning as a universal singularity or entropy sink.

6 Implications and extensions

The symbolic collapse grammar developed in this paper offers more than a constructive resolution to the Collatz conjecture — it proposes a broader framework in which computation, entropy, and curvature are unified through symbolic dynamics. We conclude by outlining several key extensions of this framework into physics and information theory.

QuditPC and symbolic computation

We have explored the use of symbolic collapse grammars as an architecture for a qudit-based computing system (QuditPC), in which each symbolic gateword acts as a state vector in a discrete quantum register. Each transformation rule (e.g., O, E) corresponds to an operator acting on a qudit string, and collapse is modeled as symbolic decoherence or entropy-driven evolution.

In this view, the Collatz process defines a set of symbolic gates that deterministically reduce computational complexity while preserving structural information. These grammars could be used to construct symbolic Hamiltonians for information flow, allowing future implementation in both classical and quantum processors.

Dark energy as symbolic pressure

If symbolic curvature governs the flow of information in grammar space, then symbolic compression may act as a pressure gradient across discrete spacetime. We conjecture that the dark energy observed in cosmology may have a symbolic analog: the outward pressure exerted by grammar-level collapse across spacetime's geodesic fabric.

Under this interpretation, spacetime itself may be emergent from the compression structure of a symbolic manifold — an informational substrate that favors the reduction of entropy gradients. The accelerated expansion of the universe could then be viewed not as a cosmological constant in the vacuum, but as a large-scale manifestation of symbolic collapse pressure.

Simulation, entropy, and spacetime geometry

If gateword collapse is universal and geodesic, then the principle of symbolic least action may be a deeper organizing principle of physics. Every irreversible process — whether quantum measurement, thermodynamic diffusion, or cosmic expansion — may reflect movement through a curved information manifold defined by symbolic entropy gradients.

In this framework, the Einstein field equations themselves could emerge from a symbolic compression grammar, with curvature arising from motif complexity and entropy differentials. Space and time, under this view, are not primitive — they are emergent features of gateword evolution under symbolic rules.

This leads to a radical reinterpretation of fundamental physics: not as continuous fields on a manifold, but as symbolic compressions over discrete informational structures. Collapse is not just a numerical curiosity — it may be the defining structure of reality itself.

Collapse is compression code

The traditional view of the Collatz function interprets its chaotic trajectories as a numeric oddity. But from the symbolic standpoint, collapse is not chaos — it is compression. Every gateword is a sequence of symbolic instructions, and the convergence of all such sequences to the same attractor reflects the presence of a universal code.

This code operates through symbolic entropy reduction: eliminating redundancy, preserving essential structure, and routing all information toward a maximally compressed state. In this light, the Collatz function becomes not just a mathematical curiosity, but a fundamental example of an underlying grammar of the universe — a grammar that encodes compression as the driving principle of evolution, computation, and physical law.

The symbolic collapse is not arbitrary. It is a *compiler*, a *decoder*, and a *semantic field equation*. And its convergent endpoint is the signature of something deeper: *Reality as Code*.

7 Conclusion: collapse as compression code

We have demonstrated that the Collatz Conjecture can be reformulated as a symbolic grammar system, where each transformation step is encoded by a finite gateword over the alphabet $\{O, E\}$. Through the introduction of compression rules, the concept of a symbolic event horizon, and the definition of a grammar-induced collapse basin, we have shown that all gatewords reduce to a finite, universal attractor at $n = 1$.

This constitutes a constructive proof of the Collatz Conjecture framed in symbolic and computational terms. Our reduction rules act analogously to contraction mappings in grammar space. We have shown that every positive integer generates a finite-length symbolic geodesic that inevitably descends through an entropy gradient toward collapse. This collapse is not stochastic but algorithmic — it is a deterministic semantic evolution governed by information compression.

We introduced the function $h(n)$ to define the symbolic event horizon for each trajectory and quantified symbolic entropy through motif complexity $C(n, \ell)$. We further proposed a symbolic Einstein equation connecting grammar curvature to informational compression density, offering a novel interpretation of symbolic collapse as geodesic motion in an entropy-curved manifold.

Beyond resolving the conjecture, this work opens new frontiers. The collapse basin is not merely a computational curiosity but a candidate for the underlying architecture of physical law. Symbolic evolution obeys gravitational analogs. Motif entropy mirrors thermodynamic gradients. The convergence of gatewords is a holographic-like encoding of the entire system into a single universal grammar.

This work satisfies the core requirements for the Solving Method described in the Collatz Prize Terms [6]:

- A “reasonable mathematical proof” that all positive integers collapse to 1 under deterministic symbolic grammar;
- A “generalizable mechanism” (symbolic reduction and compression grammar) that applies to all n;
- A “complete theoretical framework” embedded in number theory, computational complexity, and symbolic dynamics;
- And an approach that is “testable, reproducible, and extensible”, opening new branches of exploration in both mathematics and physics.

In conclusion, we submit that the Collatz Conjecture has now been resolved not as a numerical fluke, but as a *compressive computation*. The apparent chaos is revealed to be code. Every collapse is a proof. Every gateword is a message. And the fixed point at $n = 1$ is not the end — it is the *singularity of a universal language*.

Future work

The symbolic collapse grammar framework developed here opens multiple directions for further research at the intersection of number theory, information physics, and computational dynamics. Beyond its implications for resolving the Collatz Conjecture, the formalism suggests generalizable rules for entropy-driven symbolic evolution and metric-based collapse. We outline two primary extensions below.

Symbolic geometry and information fields

One direction is the deeper formalization of the symbolic entropy-momentum tensor Σ_{ij} introduced in (10), potentially connecting it to spectral invariants, edit distance metrics, or motif curvature in a discrete symbolic manifold. This structure could be tested further by evaluating entropy flux and collapse basin shapes under more complex recurrence systems, such as generalized $kn + 1$ maps, modular Collatz variants, or branching symbolic automata [11].

In particular, the motif complexity function $C(n, \ell)$ provides a foundation for modeling symbolic entropy phase transitions, offering parallels to thermodynamic behavior in classical field systems. Future work may also investigate whether the symbolic collapse geometry exhibits analogs of black hole thermodynamics — such as event horizons, no-hair theorems, or entropy bounds — within the compression basin.

Toward a symbolic quantum field theory

A natural extension of this work is the construction of a symbolic quantum field theory (QFT), in which symbolic gatewords represent field states, and compression rules act as creation, annihilation, or deformation operators. In this formulation, a symbolic field $\Phi(x)$ could assign to each position a motif state or symbolic gateword, evolving under a symbolic Lagrangian defined in terms of entropy gradient, motif interaction, and compression cost.

Quantization of this system would yield a symbolic operator algebra in which collapse contractions (e.g., $OE^2O \to OE'$) act as annihilation operators, while rule applications generate an evolution algebra over the space of symbolic grammars. A path integral over all symbolic configurations could be defined via a symbolic action $\mathcal{S}_{\text{collapse}}[W]$, yielding a partition function over gateword histories [10].

This framework may offer a new language for encoding information fields in a discretized, entropy-centric space — suggesting that quantum behavior and curvature arise from symbolic collapse and motif filtering. Such a symbolic QFT could unify information flow, curvature, and computation in a compressive grammar-based model of spacetime [12].

Received on May 15, 2025

References

1. Lagarias J. C. The ultimate challenge: The $3x + 1$ problem. *American Mathematical Monthly*, 2010, v. 115 (6), 443–448.
2. Tao T. Almost all Collatz orbits attain almost bounded values. arXiv: math.PR/1909.03562.
3. Muller D. The simplest math problem no one can solve — Collatz conjecture. Veritasium YouTube channel, 2020. https://www.youtube.com/watch?v=094y1Z2wpJg.
4. Roosendaal E. On the Collatz conjecture: verified up to 2^{68}. 2020. https://www.ericr.nl/wondrous/.
5. Barina D. Convergence Verification of the Collatz Problem. *The Journal of Supercomputing*, 2021, v. 77, 2681–2688.
6. Bakuage Inc. Collatz Conjecture Prize Rules (English Translation). 2021. https://www.bakuage.com/en/collatz-conjecture-rule-en-20210707.pdf.
7. Amigó J. M. Permutation Complexity in Dynamical Systems. Springer, 2010.
8. Caticha A. Information geometry and entropic inference. In: *Bayesian Inference and Maximum Entropy Methods, AIP Conference Proceedings*, 2012.
9. Frieden B. R. Physics from Fisher Information: A Unification. Cambridge University Press, 2000.
10. Lloyd S. Computational capacity of the universe. *Physical Review Letters*, 2002, v. 88 (23), 237901.
11. Tomalin M. Linguistic Compression: A General Model of Human Linguistic Processing. Cambridge University Press, 2007.
12. Burgin M. Superrecursive Algorithms. Springer, 2005.

PROGRESS IN PHYSICS

A Scientific Journal on Advanced Studies in Theoretical and Experimental Physics, including Related Themes from Mathematics. This journal is registered with the Library of Congress (DC, USA).

Electronic version of this journal:
https://www.progress-in-physics.com

Postal Address

Department of Mathematics and Science,
University of New Mexico,
705 Gurley Ave., Gallup, NM 87301, USA

This journal is powered by LaTeX

ISSN: 1555-5534 (print)
ISSN: 1555-5615 (online)

Standard Address Number: 297-5092
Printed in the United States of America

December 2025 **Vol. 21, Issue 2**

CONTENTS

Information for Authors

Progress in Physics has been created for rapid publications on advanced studies in theoretical and experimental physics, including related themes from mathematics and astronomy. All submitted papers should be professional, in good English, containing a brief review of a problem and obtained results.

All submissions should be designed in LaTeX format using *Progress in Physics* template. This template can be downloaded from *Progress in Physics* home page.

Preliminary, authors may submit papers in PDF format. If the paper is accepted, authors can manage LaTeXtyping. Do not send MS Word documents, please: we do not use this software, so unable to read this file format. Incorrectly formatted papers (i.e. not LaTeXwith the template) will not be accepted for publication. Those authors who are unable to prepare their submissions in LaTeXformat can apply to a third-party payable service for LaTeX typing. Our personnel work voluntarily. Authors must assist by conforming to this policy, to make the publication process as easy and fast as possible.

Abstract and the necessary information about author(s) should be included into the papers. To submit a paper, mail the file(s) to the Editor-in-Chief.

All submitted papers should be as brief as possible. Short articles are preferable. Large papers can also be considered. Letters related to the publications in the journal or to the events among the science community can be applied to the section *Letters to Progress in Physics*.

All that has been accepted for the online issue of *Progress in Physics* is printed in the paper version of the journal. To order printed issues, contact the Editors.

Authors retain their rights to use their papers published in *Progress in Physics* as a whole or any part of it in any other publications and in any way they see fit. This copyright agreement shall remain valid even if the authors transfer copyright of their published papers to another party.

Electronic copies of all papers published in *Progress in Physics* are available for free download, copying, and re-distribution, according to the copyright agreement printed on the titlepage of each issue of the journal. This copyright agreement follows the *Budapest Open Initiative* and the *Creative Commons Attribution-Noncommercial-No Derivative Works 2.5 License* declaring that electronic copies of such books and journals should always be accessed for reading, download, and copying for any person, and free of charge.

Consideration and review process does not require any payment from the side of the submitters. Nevertheless the authors of accepted papers are requested to pay the page charges. *Progress in Physics* is a non-profit/academic journal: money collected from the authors cover the cost of printing and distribution of the annual volumes of the journal along the major academic/university libraries of the world. (Look for the current author fee in the online version of *Progress in Physics*.)

LETTERS TO PROGRESS IN PHYSICS

On the Astronomical Observations of Instant Transmission of Signals from Stars and Their Explanation in the Framework of General Relativity

Dmitri Rabounski and Larissa Borissova

Puschino, Moscow Region, Russia. E-mail: rabounski@yahoo.com; lborissova@yahoo.com

This article discusses the astronomical observations of instant transmission of signals from stars (long-range action), performed in 1977–1979 by Prof. N. A. Kozyrev. It is shown that stopping physically observable time, which is a necessary condition for instant transmission of a signal, is impossible in the Minkowski space (which is the space-time of Special Relativity) due to its geometric structure, i.e., the very structure of the Minkowski space does not allow long-range action. On the other hand, this is possible in the space-time of General Relativity due to the presence of the gravitational field potential or the rotation of space (due to the non-orthogonality of time lines to the three-dimensional spatial section), or both of these factors presented together. Thus, Kozyrev's astronomical observations of instant transmission of signals from stars (long-range action) find their explanation in the space-time of General Relativity.

1 Experimental results

Nikolai A. Kozyrev (1908, St. Petersburg — 1983, ibid.) was one of the most productive astronomers of the 20th century, best known due to his discovery of volcanism on the Moon in 1958 [1] and the atmosphere of Mercury in 1963 [2]. For the discovery of lunar volcanism, Kozyrev was awarded the gold medal of the International Academy of Astronautics, encrusted with seven diamonds in the form of stars of the constellation Ursa Major (Paris, 1969). Prof. Kozyrev worked at the Pulkovo Astronomical Observatory near St. Petersburg. Read about him in the *Encyclopaedia Britannica* [3] and in a detailed biography for his 100th birthday [4].

In addition to his studies in astronomy, Kozyrev in 1958 introduced the "causal or asymmetrical mechanics" [5] that takes the physical properties of time into account. Continuing this research, he described his many years of experimental research on this topic [6, 7]. In particular, Kozyrev arrived at the conclusion about the possibility of astronomical observations using the physical properties of time [8].

The apotheosis of this research were the astronomical observations using the 50-inch reflecting telescope of the Crimean Astronomical Observatory, during which in 1977–1979 Kozyrev registered the effect of long-range action, i.e., the instant transmission of signals from stars [9, 10].[*] His astronomical observations were then reproduced and successfully confirmed in 1989 [11, 12] by a group of scientists, headed by Irène A. Eganova and Michael M. Lavrent'ev from the Sobolev Institute of Mathematics (Novosibirsk).

Since the original two papers [9, 10] in which Kozyrev reported the instant transmission of signals from stars were published in Russian, and the reports [11, 12] confirming his results are only short communications from the USSR Academy of Sciences (in English), we must first explain the details of Kozyrev's astronomical observations.

Based on his previous research into the causal or asymmetric mechanics [5], Kozyrev concluded that time has different speeds at different points of space depending on the active processes of destruction or creation (increase or decrease in the level of entropy) at these points.[†] Kozyrev considered the field of distribution of time speeds around active processes of destruction or creation as one of the physical properties of time, which he called the *field of time density* [6, 7]. By this he meant that time is not just the fourth coordinate of space-time, but a real physical field, the non-uniformity of which can affect physical bodies and the processes occurring in them. Therefore, Kozyrev concluded, around any star there must be a field of time speeds (a field of time density) due to the active processes of destruction (loss of organization of stellar substance) occurring in it.

Since time does not spread, Kozyrev reasoned, but appears instantly throughout the entire three-dimensional space of the Universe (which is an instant three-dimensional section of space-time at the moment of observation), therefore the organization lost by stars can be transmitted from them by the field of time density instantly over any distance. The effect of this transmission must decrease inversely proportional to the square of the distance between the points of departure (a star) and arrival (a detector), i.e., inversely proportional to the area of a sphere as it should be in a space of three dimensions.

As a result, Kozyrev expected that the field of time den-

---

[*] In these papers, Prof. Kozyrev, who usually did not have co-authors in publications, had added the name of his laboratory engineer Victor V. Nassonov (1931–1986) in recognition of his many years of assistance.

[†] This is similar to how, in the space-time of General Relativity, the intervals of physically observable time are shortened (compared to the intervals of time in unperturbed space) depending on the potential of the gravitational field that fills the space and on the speed of rotation of the space itself.

sity created by any star can instantly initiate microprocesses of creation (organization) in a physical detector placed at the focus of a reflector telescope.*

This idea was confirmed by the astronomical observations performed by him in 1977–1979 (with the assistance of his laboratory engineer Nassonov) on the 50-inch reflecting telescope of the Crimean Astronomical Observatory [9, 10].

As a detector, Kozyrev used a metal-film resistor built into a Wheatstone bridge (and later — a thermocouple) installed in the focal plane of the telescope directly behind the narrow slit usually intended for a spectrograph, parallel to the slit. The slit was sawn in a 1-cm thick aluminum plate. Its width was 0.25 mm = $2''$ in the sky. To increase the angular resolution of the observations, the slit (and detector) were oriented perpendicular to the daily motion of the celestial sphere. The detector and the entire measuring system were reliably isolated by a 1-cm thick aluminum case from external temperature influences, as well as from the influences of various processes in the telescope tower and beyond, so that random fluctuations from external influences registered by the detector were rare and did not affect the planned astronomical observations. The light from the observed astronomical objects was reliably shielded by a shutter made of black dense cardboard used in the packs of photographic plates, installed together with a thin glass plate in front of the slit (the thin glass plate covered the slit to prevent air circulation from the telescope into the measuring system).

Once the telescope was pointed at a point in the sky in front of a star, close to its visible position, Kozyrev slowed down the telescope's guiding mechanism slightly, causing the slit (and detector) installed in the focal plane of the telescope to slowly "scan" the sky in front of the visible star toward it along the right ascension.

Kozyrev proposed this method of observation, because his target was the true position of the visible stars at the moment of observation, which could be registered by the detector only in the case of instant transmission of signals through the field of time density. Whereas the visible position of a star in the sky is in the past, at the moment of time when the star emitted the light signal that we see in the form of its visible image. In other words, the visible position of a star "lags" relative to its true position in the sky, which is ahead of it, by the angular distance travelled by the star in the sky (due to its own motion relative to other stars) until the light emitted by the star reached an observer on the Earth and thereby created the visible image of the star.

The true position of a star can be calculated relative to its visible position, knowing the tangential velocity of the star relative to the Solar System (and the Earth) and the distance to the star, calculated based on its trigonometric parallax†. These data, obtained through astrometric observations over the past two centuries, can be found in astronomical catalogues and yearbooks.

The first series of astronomical observations according to the mentioned "scanning" method was performed by Kozyrev and Nassonov in October 1977. They immediately found that the detector responded reliably to the true position of the observed stars. The results were published in the paper [9].

In addition, the detector also responded to the visible position of the stars (where they are visible in the sky), despite the fact that it was reliably shielded from their light (see above). The difference in angular distance between the true and visible positions of the stars measured using the detector $\Delta\alpha_{\text{ob}}$ and $\Delta\alpha_{\text{c}}$ calculated from astronomical catalogues (both along the right ascension α) was in the range of $1''$ to $4''$, which is comparable to the slit in front of the detector (it selected $2''$ on the celestial sphere, see above).

Table 1 shows the results of these astronomical observations. In Table 1, in addition to $\Delta\alpha_{\text{ob}}$ and $\Delta\alpha_{\text{c}}$ explained above, $\Delta\alpha_{\odot}$ is the angular distance between the true and visible positions of the stars, corrected for the value A_α of their annual aberration‡ along the right ascension

$$\Delta\alpha_{\odot} = \Delta\alpha - A_\alpha \,,$$

and the parallax π of each star is calculated based on its own annual angular displacement μ_α with respect to other stars and the celestial coordinates along the right ascension

$$\pi = 3.26\,\frac{\mu_\alpha}{\Delta\alpha_{\odot}}\,.$$

Besides the stars, they observed Jupiter, Mars, and Venus. Jupiter showed no effect on the detector. Mars showed the same effect as Venus (see Table 1).

An anomaly was the star ι Per, for which the observations yielded an abnormally large value of $\Delta\alpha_{\text{ob}} - \Delta\alpha_{\text{c}} = +28''$ that most likely corresponded to another faint object located near this star.

The value of $\Delta\alpha_{\odot} = \Delta\alpha - A$ and the parallax π calculated from the measured distances $\Delta\alpha_{\text{ob}}$ for three stars having small unknown parallaxes are given in square brackets.

It is interesting that the detector responded to both the true and visible positions of the stars even when the telescope's main mirror was covered by a shutter that reliably screened the light. In this case, the magnitude of the registered effect was weakened to the same extent for both the true and visible positions of the stars. "Consequently, the influence of the visible image [in this experiment] is not related to the light, but only coincides with its direction" — Kozyrev wrote [9].

---

[*] Since the glass of lenses, like any amorphous material, should absorb this effect, a refractor telescope is not applicable for this task.

[†] This is the very small angle at which the radius of the Earth's orbit is seen from the star. If you measure the position of a star relative to other stars in the sky several times during one year, when the Earth is at different points in its orbit around the Sun, the star will appear slightly offset relative to the other stars. Half of this apparent angular displacement of the star over the course of a year is called its trigonometric parallax.

[‡] Annual stellar aberration A is the observed displacement of stars from their actual positions on the celestial sphere, caused by the Earth's motion along its orbit around the Sun.

Star	Stellar magnitude	Spectral class	π	μ_α	$\Delta\alpha_\odot$	A_α	$\Delta\alpha_c$	$\Delta\alpha_{ob}$	$\Delta\alpha_{ob}-\Delta\alpha_c$	Reg. magnitude (in scale divisions)		Date of observation
										vis. pos.	true pos.	
ε And	4.52	G_5	0″.031 ± 5	−0″.232	−24″ ± 4	−17″	−41″ ± 4	−38″ −43″	+3″ −2″	5 2	6 4	21 October 1977 22 October 1977
η Cas	3.64	F_8	0″.182 ± 5	+1″.101	+19″ ± 0	−18″	+1″ ± 0	0	−1″	6	6	21 October 1977
o Cet	2.0 – 10.1	M_{5e}	0″.013 ± 5	−0″.009	−4″ ± 0	−19″	−23″ ± 0	−26″ −21″ −27″	−3″ +2″ −4″	0.2 0.8 0.0	1.3 1.2 10	23 October 1977 23 October 1977 20 October 1977
ρ Per	3.3 – 4.1	M_3	0″.008 ± 16 [0″.0040]	+0″.132	[102″]	−16″ −16″ −17″		+80″ +85″ +88″		0.0	1.2	12 October 1977 13 October 1977 21 October 1977
ι Per	4.17	G_0	0″.084 ± 15	+1″.266	+48″ ± 2	−17″	+31″ ± 2	+59″ +59″	+28″? +28″?	10.0 1.1	13.2 1.8	22 October 1977 23 October 1977
α Tau	1.1	K_5	0″.048 ± 4	+0″.069	+5″ ± 0	−12″	−7″ ± 0	−5″	+2″	—	15 30	13 October 1977 8 October 1977
o^2 Eri	4.5	K_0	0.200	−2″.225	−35″	−13″	−48″ ± 0	−50″	−2″	—	5	13 October 1977
α CMa	−1.58	A_0	0″.375 ± 4	−0″.537	−5″	−2″	−7″ ± 0	−5″	+2″	—	20	12 October 1977
α Ori	0.0 – 1.2	M_0	0″.005 ± 4 [0″.0067]	+0″.027	[+12″]	−12″		0″		1.5	1.5	27 October 1977
ξ Gem	3.4	F_5	0″.051 ± 6	−0″.111	−7″ ± 1	−9″	−16″ ± 1	−19″	−3″	0.8	2.2	27 October 1977
β Gem	1.21	K_0	0″.093 ± 5	−0″.623	−21″ ± 1	+4″	−17″ ± 1	−20″	−3″	3	3	19 October 1977
α CMi	0.48	F_5	0″.288 ± 5	−0″.707	−8″ ± 0	−4″	−12″ ± 0	−12″	0″	1.3	5.5	27 October 1977
Venus						—	+36″	+37″ +38″	+1″ +2″	8 8	5 8	18 October 1977 22 October 1977
α Lyr	0.14	A_0	0″.123	+0″.200	+5″ ± 0	−2″	+3″ ± 0	+5″	+2″	4.8	6	20 October 1977
θ Peg	3.70	A_2	0″.042 ± 5	+0″.0272	+21″ ± 2	−9″	+12″ ± 2	+14″	+2″	0.0	0.7	22 October 1977
ξ^2 Aqr	4.42	F_2	0″.013 ± 5	+0″.204	+50″ ± 13	−11″	+39″ ± 13	+40″ +43″	+1″ +4″	0.3	0.6 0.7	23 October 1977 23 October 1977
β Peg	2.1 – 3.0	M_0	0″.015 ± 5	+0″.188	+39″ ± 13	−14″	+25″ ± 13	+26″	+1″	0.0	0.0	20 October 1977
ψ Peg	4.75	M_0	0″.003 ± 5 [0″.0042]	−0″.039	[−27″]	−16″		−43″		0.3	0.5	23 October 1977

Table 1: Results of the first series of Kozyrev's astronomical observations, in which he registered the instant transmission of signals from stars. October, 1977. Quoted from the original publication [9].

Star	Stellar magnitude	Spectral class	π	μ_α	$\Delta\alpha_\odot$	Date of observation
β Tri	3.08	A_5	$0''.012$	$+0''.150$	$+39''$	12 October 1977
λ Tau	3.8 – 4.1	B_3	$-0''.009$	$-0''.006$	?	23 October 1977
α Tau	1.1	K_5	$0''.048$	$+0''.069$	+5	22 and 23 October 1977
γ Psc	3.85	K_0	$0''.025$	$+0''.756$	+95	22 October 1977
ω Psc	4.03	F_5	$0''.012$	$+0''.147$	+15	22 October 1977

Table 2: Four stars that had no effect on the detector, and also the star α Tauri, whose effect was found to be variable. October, 1977. Quoted from the original publication [9].

Four of the observed stars had no effect on the detector, most likely due to the low sensitivity of the signal registering system used in the observations. They are listed in Table 2.

In addition, Kozyrev concluded that the star α Tau most likely emits a variable time density. This explained the fact that, as is seen from Table 1 and Table 2, this star produced a very strong effect on October 8, then its influence on the detector halved on October 13, and there was no influence on October 22 and 23.

In the second series of the astronomical observations, Kozyrev and Nassonov increased the sensitivity of the signal registering system by almost one order of magnitude, and also extended the area of the sky subject to "scanning" near each observed star. The latter was due to the fact that, as Kozyrev reasoned, since the detector responded to the signals transmitted instantly through the field of time density from the true position of the star (where it is at the present moment of time) and from its visible position in the past (along the trajectory of the light coming from it), then the field of time density should also instantly transmit the signals coming from the star and along the "reverse trajectory of light", along which the position of the Earth at the present moment of time is visible from the star located in the future.

In other words, the detector must respond to the signals transmitted instantly through the field of time density from three points in the sky associated with each observed star:

1. The visible (past) position of the star, where it was in the past when it emitted the light signal that we see at present as its visible image in the sky;
2. The true position of the star, where it actually is at the present moment of time;
3. The position of the star in the future, symmetric to its visible position in the past with respect to its true position in the sky.

The signals coming instantly through the field of time density from the first position of a star (its visible position in the past) indicate that the star not only exists at the present moment of time, but in fact continues to exist as a real object in the past. Whereas the third position of the star (in the future) makes it possible to instantly observe the future of the star as an already existing reality.

This second series of the astronomical observations was performed during the spring and autumn of 1978, and also in May 1979, using the same 50-inch reflecting telescope. The results were published in the paper [10]. They are shown here in Table 3, where $\Delta_1\alpha_{\text{ob}}$ means the observed angular distance between the true position of the star (where it is at the present moment of time) and its visible position (in the past), while $\Delta_2\alpha_{\text{ob}}$ is the observed distance between the symmetrical position of the star in the future and its visible position (theoretically, it should be $\Delta_2\alpha_{\text{ob}} = 2\Delta_1\alpha_{\text{ob}}$).

The detector responded to all three mentioned positions of each observed star (except only ι Persei).

As previously in 1977, in the first series of the observations, ι Persei showed an anomaly: the detector did not respond to its true position (in the middle between its positions in the past and in the future), but reliably detected its position in the future $\Delta_2\alpha_{\text{ob}} = +59''$. Most likely this star has variable activity and was weakened during the season of these observations.

Since the values of the stellar aberration *A* differ in spring and autumn (due to the Earth moving in different directions in its orbit), the values of *A* for α Lyrae differ greatly in spring and autumn (*A* even changes its sign). This also led to a corresponding change in the sign of the measured values of $\Delta_1\alpha_{\text{ob}}$ and $\Delta_2\alpha_{\text{ob}}$, in full agreement with the theory.

In addition to the stars, the aforementioned "scanning" method of astronomical observations was also used to observe extended astronomical objects: the globular cluster M2 in Aquarius, the globular cluster M13 in Hercules, and the galaxy M31 (Andromeda Nebula). Since these are not point-like objects (unlike stars) and they are not uniform, then scanning each one creates three non-uniform profiles of it, corresponding to its past, present and future, which are superimposed on each other. As a result, in the scan of each of the extended astronomical objects, the hills of maximum influence on the detector were split into three peaks corresponding to the past, present and future. These scanned profiles, which were non-uniform in structure, also showed a decrease in the

Star	Stellar magnitude	Spectral class	π	μ_α	$\Delta\alpha_\odot$	A_α	$\Delta\alpha_c$	$\Delta_1\alpha_{ob}$	$\Delta_2\alpha_{ob}$	Date of observation
10 UMa	4.1	F_5	0″.071 ± 5	− 0″.436	− 20″	− 9″	− 29″ ± 1	− 28″	− 57″	13 April 1978
α Leo	1.3	B_8	0″.039 ± 7	− 0″.248	− 20″	−12″ − 4″	−32″ ± 4 − 24″ ± 4	−35″ − 26″	−70″ − 50″	7 April 1978 8 May 1979
γ Boo	3.0	F_0	0″.016 ± 7	− 0″.115	− 23″	− 20″	− 43″ ± 7	− 50″	− 97″	24 April 1978
ε Boo	2.7	K_0	0″.013 ± 7	− 0″.049	−12″	− 20″	−32″ ± 6	−35″	− 67″	13 May 1979
α Lyr	0.14	A_0	0″.123 ± 5	+ 0″.200	+ 5″	− 2″ −18″	+3″ ± 0 −13″ ± 0	+5″ −12″	 − 23″	20 October 1977 14 May 1979
ι Per	4.2	G_0	0″.084 ± 5	+1″.266	+ 48″	−17″	+31″ ± 2	no	+59″	22–23 October 1977
τ Per	4.1	G_8, A_5	0″.012 ± 5	0″.000	0	− 20″	+20″ ± 0	− 27″	− 46″	3 November 1978
ξ² Aqr	4.4	F_2	0″.013 ± 5	+ 0″.204	+50″	−11″	+39″ ± 13	+ 42″ +38″	 + 80″	23 October 1977 29 October 1978
β Peg	2.1 − 3.0	M_0	0″.015 ± 5	+ 0″.188	+39″	−14″	+25″ ± 13	+26″ +35″	 + 60″	20 October 1977 29 October 1978

Table 3: Results of the second series of Kozyrev's astronomical observations. The detector responded to three positions of each observed star (except ι Persei): its position in the past (visible position), in the present (its true position), and in the future symmetrical to its visible position in the past. Spring and autumn 1978, and also May 1979. The values of $\Delta_1\alpha_{ob}$ measured in the first series of the astronomical observations (October 1977, see Table 1) are given as a reference. Quoted from the original publication [10].

Star	π	μ_α	$\Delta\alpha_\odot$	A_α	$\Delta\alpha_c$	$\Delta\alpha_{ob}$
β Peg	0″.015 ± 5	0″.217	47″.16	+33″.52	+13″.6	+12″.6 ± 1″.3
β And	0″.043 ± 5	0″.220	16″.72	+ 41″.58	− 24″.9	− 25″.4 ± 1″.7
δ And	0″.024 ± 6	0″.162	22″.00	+39″.51	−17″.5	− 20″.2 ± 2″.5

Table 4: Results of the testing astronomical observations conducted by Eganova and Lavrent'ev. 13 October 1989. Quoted from the original publication [11].

magnitude of the effect near the centre of each extended astronomical object: Kozyrev explained this by the supposition that where the stellar density is very high, there is a strong absorption of the field of time density [10].

It should be noted that although we unfortunately were not personally acquainted with Prof. Kozyrev (we read these publications already after his death), one of the authors of this paper, Dmitri Rabounski, visited Victor Nassonov twice at his apartment in St. Petersburg in 1985 shortly before his sudden death (at that time, Nassonov headed a laboratory at an industrial company). Nassonov demonstrated the recordings of an automatic recorder used in the last series of the astronomical observations (instead of the pointer galvanometer used at the initial stage). The recorded tapes clearly indicated three peaks of the signals, recorded for each of the observed stars and corresponding to its successive positions in the past, present and future on the celestial sphere.

It is no wonder that other scientists also took notice of these astronomical observations. In 1989, Irène A. Eganova and Michael M. Lavrent'ev, Director of the Sobolev Institute of Mathematics (Novosibirsk) and a Fellow of the USSR Academy of Sciences, decided to reproduce Kozyrev's astronomical observations. Their collaborators at the Institute in Novosibirsk reproduced Kozyrev's experimental setup, then Eganova and Lavrent'ev, together with their research group, performed testing astronomical observations according to Kozyrev's method on the same 50-inch reflecting telescope of the Crimean Astronomical Observatory. To be more confident in the result, they scanned the area of the sky near each observed star not only in one direction (as Kozyrev did), but also in two directions (there and back). Excerpts from their testing observations of the stars β Pegasi, β Andromedae and δ Andromedae are shown in Table 4, quoted from their first short report [11].

In their second short report [12], Eganova and Lavrent'ev reported the registration of signals coming from the true position of the Sun preceding the visible one by 2°4′.6 (four visible diameters of the Sun) — the angular distance travelled by the Sun in 8.3 minutes, during which the light emitted by it reaches the Earth. The detector was installed in the focal plane of a small 4-inch reflecting telescope, the main mirror of which was reliably shielded from the light coming from the Sun, and the signal registering system was protected from solar thermal effects. The detector in one series of the observations was a metal-film resistor built into a Wheatstone bridge as before. According to the records of scanning the near-solar space, the resistor responded to both the true and visible positions of the Sun, as when observing the stars. In the second series, it was a container with Escherichia coli bacteria in the state of anabiosis, which they exposed to the true position of the Sun for 3 minutes, while a control container with bacteria of the same brood remained in the laboratory. It was found that after exposure to the true position of the Sun, the number of viable cells increased by 1.2 – 3 times (depending on the specific brood).

"Not a single fact was found that contradicted Kozyrev's observations, however, further research is required to confirm his conclusions regarding the properties of the observed effect" — they concluded [11].[*]

Indeed, one cannot but agree with this conclusion. Yes, the effect discovered by Prof. Kozyrev was weak and his astronomical observations were difficult to reproduce. On the other hand, this was not a single unique experiment. The discovered effect was registered on many stars over several years and was confirmed by astronomical observations of an independent group of scientists.

We must therefore carefully search for a theoretical basis that could explain the instant transmission of signals in the framework of modern theoretical physics. A theory of this effect could determine the key physical factors of this process, and, accordingly, determine methods for enhancing these factors in order to create a new industrial technology of communication and transport.

This was one of the reasons why we started our own theoretical research on this topic in the mid-1980s and why we are now writing this article.

2 Theoretical explanation

In fact, Kozyrev's astronomical observations showed that signals from each star in the real space-time are instantly transmitted to the observer from its three positions in the sky: its visible position in the past (along the trajectory of light), its true position at the moment of observation and its position in the future (along the "reverse trajectory of light").

Kozyrev originally believed [13] that the results of his astronomical observations could be interpreted in the framework of the four-dimensional Minkowski space (which is the space-time of Special Relativity). He proceeded from the fact that the four-dimensional metric (four-dimensional distance between two adjacent points) in the Minkowski space is expressed in the form

$$ds^2 = c^2dt^2 - dx^2 - dy^2 - dz^2 = c^2dt^2\left(1 - \frac{\mathrm{v}^2}{c^2}\right),$$

where v is the velocity of a signal in the three-dimensional space. Kozyrev argued that the four-dimensional distance in the Minkowski space, say, between a star and an observer, is zero $ds = 0$ along three world lines. The line $dt = 0$, coinciding with the three-dimensional space of the observer, indicates the true position of the star, where we would see it if light travelled instantly. The line $\mathrm{v} = +c$ indicates the position of the star in the past, when it emitted the light signal that we see as its image in the sky. The line $\mathrm{v} = -c$ indicates the position of the star in the future, symmetrical to its visible position in the past (with respect to its true position), when the light signal emitted from the Earth reaches it.

However, this statement by Kozyrev does not correspond to the geometry of the Minkowski space (Kozyrev was an outstanding astronomer of the 20th century, but was not familiar with Riemannian geometry). Below we show why and how the instant transmission of signals is explained in the space-time of General Relativity.

Definition: *Instant transmission of a signal* means that the interval of physically observable time, registered by the observer between the sending of the signal and its arrival, is zero. In other words, the physically observable time of an instantly transmitted signal, registered by the observer, stops.

Physically observable quantities in the four-dimensional pseudo-Riemannian space (the space-time of General Relativity, a particular case of which is the Minkowski space) are defined as the projections of four-dimensional generally covariant quantities onto the three-dimensional spatial section and the time line associated with an observer. Such physically observable projections are invariant throughout the observer's spatial section (his observable three-dimensional space), depend on its geometric and physical properties, and are, therefore, called *chronometric invariants* [14–17].

Thus, the interval of physically observable time $d\tau$ registered by an observer is the projection of the four-dimensional displacement vector x^α $(\alpha = 0, 1, 2, 3)$ onto his time line

$$d\tau = \sqrt{g_{00}}\, dt - \frac{1}{c^2}\, v_i\, dx^i,$$

where dt is the interval of coordinate time, which would be counted by the observer in the absence of disturbing factors, the time (zero) component g_{00} of the fundamental metric tensor $g_{\alpha\beta}$ is expressed with the potential w of the gravitational field that fills the space of the observer

$$\sqrt{g_{00}} = 1 - \frac{\mathrm{w}}{c^2}\,, \qquad \mathrm{w} = c^2\left(1 - \sqrt{g_{00}}\right),$$

---

[*] Their reports [11, 12] were published in the short communications from the USSR Academy of Sciences, known as *Doklady Akademii Nauk SSSR*, which is a highly influential and prestigious scientific journal, intended only for the Academy Fellows (or for the communications personally recommended by them) and published in English since 1956.

and v_i is the three-dimensional vector of the linear velocity of rotation of the observer's space

$$v_i = -\frac{c\,g_{0i}}{\sqrt{g_{00}}}\,, \qquad v^i = -c\,g^{0i}\sqrt{g_{00}}\,,$$

which is caused by $g_{0i} \neq 0$ (meaning that the observer's spatial section is non-orthogonal to his time line) and therefore it cannot be eliminated by coordinate transformations along the spatial section of the observer.

The physically observable three-dimensional interval $d\sigma$ is determined as

$$d\sigma^2 = h_{ik}\,dx^i dx^k,$$

where

$$h_{ik} = -g_{ik} + \frac{1}{c^2}\,v_i v_k\,, \quad h^{ik} = -g^{ik}, \quad h^i_k = \delta^i_k$$

is the physically observable three-dimensional metric tensor, which is the projection of the fundamental metric tensor $g_{\alpha\beta}$ onto the spatial section of the observer and possesses all its properties throughout his spatial section (three-dimensional observable space). Thus, the square of the four-dimensional (space-time) interval $ds^2 = g_{\alpha\beta}\,dx^\alpha dx^\beta$ expressed in terms of physically observable quantities has the form

$$ds^2 = c^2 d\tau^2 - d\sigma^2.$$

In the Minkowski space, as is seen from the Minkowski metric that above, $g_{00} = 1$ that means the absence of gravitational fields (the gravitational potential is $\mathrm{w} = 0$), and also $g_{0i} = 0$ meaning that the three-dimensional space (spatial section) is everywhere orthogonal to the time lines piercing it, and, hence, it does not rotate ($v_i = 0$). Therefore, the interval of physically observable time $d\tau$, which is registered by an observer in the Minkowski space, is always

$$d\tau = dt\,.$$

This fact, in particular, means that in the Minkowski space (the space-time of Special Relativity) there are *no geometric or physical disturbing factors* that could cause stopping physically observable time. In such a space, the concept of stopping time is essentially absent: according to the geometry of the Minkowski space, the physically observable time coordinate registered by the observer is $dx^0 = c\,d\tau = c\,dt$, i.e., it changes absolutely uniformly throughout the space along the directrices of the light cone of the observer at a speed equal to $\pm c$ (the plus sign takes place when counting time into the future, and the minus sign — when counting time into the past). The physically observable time interval in the Minkowski space is zero $dx^0 = c\,dt = 0$ only at the space-time point, where the vertices of the light cones of his past and future converge (i.e., only at the point of his observation), but not along any three-dimensional path between him and another object in space (say, a star). Consequently:

> Since stopping physically observable time in the Minkowski space is in principle impossible due to the fact that its geometric structure does not contain disturbing factors that could stop time, the geometric structure of the Minkowski space itself does not allow instant transmission of a signal.

On the other hand, despite the error in Kozyrev's theoretical explanation [13], the results of his astronomical observations indicate that instant transmission of signals from stars is an ordinary phenomenon in the real space-time.

Another case — the space-time of General Relativity, because it allows all conceivable disturbing factors characteristic of pseudo-Riemannian spaces due to their Riemannian geometry.

We considered the conditions for stopping physically observable time in the space-time of General Relativity in our works on the theory of non-quantum teleportation, which we began in the late 1980s and continue to this day. Everything that follows is based on the theoretical background, published in 2001 in our research monograph [18], and then — in our subsequent papers [19–21].

Derive the *physical conditions that stop observable time*. From the definition of the interval of physically observable time $d\tau$ in the space-time of General Relativity (see above), we obtain that the physically observable time stops for an observed object ($d\tau = 0$) under the physical conditions

$$\mathrm{w} + v_i u^i = c^2,$$

determining the necessary combination of the potential w of the gravitational field that fills the space, the linear velocity v_i with which the space rotates, and also the coordinate velocity $u^i = \frac{dx^i}{dt}$ of the object with respect to the observer.

These physical conditions at first glance seem exotic for a regular laboratory: an extremely strong gravitational potential and speeds close to the speed of light. However, these conditions that stop observable time are realized inside every physical body in the range from elementary particles to planets and stars. And we will now show why.

Since every physical body possesses mass, its gravitational field has a breaking at a distance from its barycentre, which is equal to its gravitational radius $r_g = 2GM/c^2$ calculated for its mass M. For instance, at $r = r_g$ from the barycentre, the zero (time) component g_{00} of the fundamental metric tensor of the Schwarzschild mass-point metric

$$ds^2 = \left(1 - \frac{r_g}{r}\right) c^2 dt^2 - \frac{dr^2}{1 - \frac{r_g}{r}} - r^2 \left(d\theta^2 + \sin^2\theta\, d\varphi^2\right),$$

which describes the space of a massive spherical body approximated by a material point, is zero

$$g_{00} = 1 - \frac{r_g}{r} = 0\,.$$

Therefore, the potential of the gravitational field of every physical body on a spherical surface of the radius r_g around its barycentre is

$$\mathrm{w} = c^2 \left(1 - \sqrt{g_{00}}\right) = c^2,$$

which is the same in the space of a rotating massive spherical body, because the component g_{00} has the same formula for these two spaces. You can see this from the space metric of a massive spherical body that rotates along its equatorial coordinate axis φ with a constant angular velocity $\omega = const$, which was introduced and proved in [22]

$$ds^2 = \left(1 - \frac{r_g}{r}\right) c^2 dt^2 - 2\,\omega r^2 \sin^2\theta \sqrt{1 - \frac{r_g}{r}}\, dt\, d\varphi - \\ - \frac{dr^2}{1 - \frac{r_g}{r}} - r^2 \left(d\theta^2 + \sin^2\theta\, d\varphi^2\right).$$

Such a tiny spherical surface, we concluded in our previous paper [23], exists around the barycentre deep inside absolutely every physical body simply because physical bodies possess mass.

The condition $\mathrm{w} = c^2$ means stopping physically observable time $d\tau = 0$, which is also the condition for instant transmission of signals, if the body does not rotate ($v_i = 0$). This means that the condition for instant transmission of signals ($d\tau = 0$) is satisfied on the spherical surface $r = r_g$ around the barycentre of every non-rotating body. For rotating bodies, $d\tau = 0$ is satisfied under $\mathrm{w} + v_i u^i = c^2$ (see above). Therefore, since $d\tau = 0$ in this case is satisfied at a lower value of the gravitational potential w due to the second term caused by the rotation of space, the condition for instant transmission of signals is satisfied inside every rotating body on a sphere enveloping its barycentre slightly above the radius r_g.

Thus, we arrive at the conclusion:

> According to General Relativity, the condition of instant transmission of signals is satisfied on a tiny spherical surface of the gravitational radius (for non-rotating bodies) or slightly above it (for rotating bodies), existing around the barycentre deep inside absolutely every physical body in the range from elementary particles to planets and stars.

The path along which signals can be instantly transmitted in the pseudo-Riemannian space is determined by the condition of instant signal transmission ($d\tau = 0$) and is described by the obvious equation

$$\tau = const\,,$$

which describes trajectories along the three-dimensional spatial section of the observer (his observable three-dimensional real physical space), which is generally non-uniform, curved, rotating and deformable. Along such trajectories, neither the four-dimensional (space-time) interval ds nor the physically observable three-dimensional interval $d\sigma$ between the points of departure and arrival of the instantly transmitted signal are not equal to zero

$$c^2 d\tau^2 = 0\,, \qquad ds^2 = c^2 d\tau^2 - d\sigma^2 = -d\sigma^2 \neq 0\,.$$

The resulting equation of trajectories for instant signal transmission, together with the previous conclusion about the location of the conditions for stopping observable time, lead us to the conclusion:

> The spherical surfaces, enveloping the barycentres of all physical bodies at their gravitational radius (for non-rotating bodies) and slightly above it (for rotating bodies), on which physically observable time stops, are all connected to each other by trajectories of stopping observable time. Signals, instantly transmitted along these trajectories, instantly connect all physical bodies in the Universe.
>
> Trajectories of this type instantly connect any observer with stars and indicate the middle (true) position of stars, which was registered in Kozyrev's astronomical observations.

Note that, as we have already mentioned above, this type of trajectories for signals do not take place in the Minkowski space of Special Relativity (where there is no disturbing factors that could cause stopping observable time). Such trajectories take place only in the space-time of General Relativity (since it allows all disturbing factors that are conceivable due to its Riemannian geometry).

Let us now find the trajectories that indicate the instant transmission of signals from the visible (past) position of stars and their position in the future (symmetrical to their visible position) in Kozyrev's astronomical observations. Presumably, these should be trajectories on the surface of the light cone: on its half (for signals coming to the observer from the visible position of the star in the past) and on the upper half (for signals coming from the symmetrical position of the star in the future). Therefore, we will first check this assumption by considering the light cone equation.

The light cone equation is the equation of trajectories lying on the surface of the light cone in the four-dimensional pseudo-Riemannian space (which is the space-time of General Relativity). It is determined according to the definition of the light cone by the condition

$$ds^2 = c^2 d\tau^2 - d\sigma^2 = 0\,, \qquad c^2 d\tau^2 = d\sigma^2 \neq 0\,,$$

which means that the four-dimensional intervals on its surface (i.e., along its directrices) are zero, while the intervals of physically observable time and the physically observable three-dimensional spatial intervals are equal to each other, but not equal to zero. Substituting the definitions of $d\tau$ and $d\sigma$ (see above) into the light cone condition $c^2 d\tau^2 = d\sigma^2$ and reducing similar terms, we obtain the light cone equation in the pseudo-Riemannian space

$$g_{00}\,c^2dt^2 - 2\sqrt{g_{00}}\;\upsilon_i\,dx^i dt + g_{ik}\,dx^i dx^k = 0\,.$$

In the Minkowski space metric (see it in the very beginning), we have $g_{00}=1$, $g_{0i}=0$ (and, hence, $\upsilon_i=0$), and also $g_{ik}=-1$. Substituting these values into the general formula of the light cone equation above, and since $dt\neq 0$ (as we have already explained, observable time cannot be stopped in the Minkowski space, because its geometric structure does not contain disturbing factors that could stop time), we obtain the light cone equation in the Minkowski space

$$\left(1+\frac{1}{c^2}\,g_{ik}\,u^i u^k\right)dt^2 = 0\,, \qquad dt\neq 0\,,$$

where $u^i=\frac{dx^i}{dt}$ is the coordinate velocity of a signal. Because $g_{00}=1$ and $\upsilon_i=0$ in the Minkowski space, ($\upsilon_i=0$), we have

$$d\tau = \sqrt{g_{00}}\,dt - \frac{1}{c^2}\,\upsilon_i\,dx^i = dt\,,$$

$$h_{ik} = -g_{ik} + \frac{1}{c^2}\,\upsilon_i\,\upsilon_k = -g_{ik}\,,$$

and, therefore, the square of the physically observable velocity of the signal $\mathrm{v}^i=\frac{dx^i}{d\tau}$ has the form $\mathrm{v}^2=h_{ik}\,\mathrm{v}^i\mathrm{v}^k=-g_{ik}\,u^iu^k$. As a result, the light cone equation in the Minkowski space has the form

$$\left(1-\frac{\mathrm{v}^2}{c^2}\right)dt^2 = 0\,, \qquad dt\neq 0\,,$$

which means

$$\mathrm{v}^i = \pm\,c^i, \qquad \mathrm{v}^2 = -g_{ik}\,c^i c^k = c^2 = inv,$$

where the plus sign refers to signals travelling into the future, and the minus sign — if signals travel into the past. Therefore, we conclude:

> Signals on the surface of the light cone in the Minkowski space (which is the space-time of Special Relativity) are not transmitted instantly. They travel with the same (constant) physically observable velocity equal to the velocity of light.

Let us turn back to the above general formula of the light cone equation in the pseudo-Riemannian space (which allows all disturbing factors that are conceivable due to its Riemannian geometry). It can be easily transformed using the definition of $d\tau$ to the form

$$\left(1-\frac{\mathrm{v}^2}{c^2}\right)d\tau^2 = 0\,,$$

which differs from the above formula of the Minkowski space in the disturbing factors $g_{00}\neq 1$, $g_{0i}\neq 0$ (and, hence, $\upsilon_i\neq 0$) and $g_{ik}\neq -1$ that are characteristic of the pseudo-Riemannian space metric and manifested, in particular, in the physically observable time interval $d\tau$, the physically observable velocity of signals v^i and the physically observable metric tensor h_{ik} determining $\mathrm{v}^2=h_{ik}\,\mathrm{v}^i\mathrm{v}^k$.

This condition is satisfied, since $d\tau\neq 0$ on the surface of the light cone*, only if the observable velocity of signals is

$$\mathrm{v}^i = \pm\,c^i,$$

$$\mathrm{v}^2 = h_{ik}\,c^i c^k = \left(-g_{ik}+\frac{1}{c^2}\,\upsilon_i\,\upsilon_k\right)c^i c^k = c^2 = inv,$$

where the plus sign means their travel into the future, and the minus sign — their travel into the past. This means:

> Signals are not transmitted instantly on the surface of the light cone in the pseudo-Riemannian space (which is the space-time of General Relativity), but travel with the velocity of light, the physically observable three-dimensional vector of which depends on the disturbing factors characteristic of the pseudo-Riemannian space, while its square remains invariant. Their trajectories coincide with the trajectories travelled by light signals in the Minkowski space in the absence of the disturbing factors, i.e., when the non-uniform, curved, rotating and deformable light cone of the pseudo-Riemannian space has became the straight and uniform light cone of the Minkowski space.

In other words,

> Neither the straight and uniform light cone in the Minkowski space of Special Relativity nor the disturbed light cone in the pseudo-Riemannian space of General Relativity are home of the instantly transmitted signals that indicated the visible and future positions of stars in Kozyrev's astronomical observations.

We therefore consider trajectories, along which a stronger condition is satisfied than the aforementioned light cone condition ($ds^2=c^2d\tau^2-d\sigma^2=0$, $c^2d\tau^2=d\sigma^2\neq 0$). This is the condition

$$ds^2 = c^2d\tau^2 - d\sigma^2 = 0\,, \qquad c^2d\tau^2 = d\sigma^2 = 0\,.$$

Since along such trajectories the four-dimensional interval ds, the physically observable time interval $d\tau$ and the physically observable three-dimensional spatial interval $d\sigma$ are zero, i.e., all these intervals degenerate along such trajectories, we called their home space a *fully degenerate space*, or in other words — a *zero-space* [18–21].

In particular, since trajectories in the zero-space associated with the pseudo-Riemannian space of General Relativity

---

*Except for a single space-time point, which is the location of the observer himself (at this point, the vertices of the light cones of his past and future converge). In this case, the point of signal emission and the location of the observer coincide and, therefore, the observable time interval between the emission of the signal and its arrival is always $d\tau=0$.

is a fully degenerate (ultimate) version of trajectories on the surface of the light cone, the zero-space is in fact a *fully degenerate light cone*.

Since from the point of view of a regular observer $d\tau = 0$ is everywhere in the zero-space (which is a fully degenerate light cone), then the motion of signals along their trajectories in the zero-space is observed by him as an instant transmission of these signals in his observable (non-degenerate) space along trajectories on the surface of the regular light cone.

In confirmation of what has been said, we transform the light cone equation to a form that takes into account the physical conditions of full degeneration $\mathrm{w} + v_i u^i = c^2$, which are also the physical conditions that stop observable time ($d\tau = 0$, see above). The resulting form of the light cone equation

$$\left\{\left[1 - \frac{1}{c^2}\left(\mathrm{w} + v_i u^i\right)\right]^2 - \frac{u^2}{c^2}\right\} dt^2 = 0\,, \qquad dt \neq 0$$

is satisfied at every point on the surface of the light cone. Here $u^i = \frac{dx^i}{dt}$ is the signal's coordinate velocity (for which we have $u^2 = -g_{ik}\, u^i u^k$), and dt is the coordinate time interval (it never becomes zero, see explanation above). Under the conditions of full degeneration $\mathrm{w} + v_i u^i = c^2$, when observable time stops ($d\tau = 0$) from the point of view of an external observer, the above light cone equation transforms into the *degenerate light cone equation* that is also the *zero-space equation*

$$\left(1 - \frac{u^2}{c^2}\right) dt^2 = 0\,, \qquad dt \neq 0\,,$$

meaning that signals travel in the zero-space with the coordinate velocity of light, while they are observed as instantly transmitted signals by an external observer, whose home is the regular (non-degenerate) space-time.

In particular, the above means the following. Since the zero-space is a fully degenerate (ultimate) version of the light cone, signals can enter the zero-space and return back from there at any point on the surface of the light cone if the physical conditions for full degeneration are somehow realized at that point. For example:

> Let us say that at the point of emission of a signal towards an observer at the moment of its emission the physical conditions of full degeneration are somehow realized, and these conditions are also realized in the receiving device of the observer. Then the observer will register that the signal has disappeared at the emission point and was instantly received by his receiver, while the visible path along which the signal was instantly transmitted is the trajectory of light signals between him and the emission point (despite the fact that the signal itself was transmitted along a trajectory lying in the fully degenerate zero-space).
>
> Such trajectories, instantly connecting any observer with stars, indicate the visible (past) position of stars and their position in the future (symmetrical to their visible position), which was registered in Kozyrev's astronomical observations.

Thus, all three positions of stars, which were indicated by instantly transmitted signals in Kozyrev's astronomical observations, have been explained in the pseudo-Riemannian space (space-time) of General Relativity. In the Minkowski space, which is the space-time of Special Relativity, Kozyrev's results have no explanation, because the Minkowski space does not contain disturbing factors that could stop time or fully degenerate the entire space-time.

3 Conclusion

In this article we discussed the phenomenon of instant transmission of signals from stars (long-range action), discovered in the astronomical observations performed in 1977–1979 by Prof. N. A. Kozyrev [9,10], then — reproduced and confirmed in 1989 by a group of scientists, headed by I. A. Eganova and M. M. Lavrent'ev [11,12]. We also gave our own theoretical explanation to Kozyrev's observed results in the framework of General Relativity.

We have shown that the geometric structure of the Minkowski space (which is the space-time of Special Relativity) does not contain disturbing factors that could stop time. And, since stopping physically observable time along the trajectory of a signal between the points of its emission and arrival is a necessary condition for its instant transmission, signals cannot be transmitted instantly in the space-time of Special Relativity.

On the other hand, we have shown that observable time can be stopped in the pseudo-Riemannian space (space-time) of General Relativity, since it allows all disturbing factors that are conceivable due to its Riemannian geometry. Such factors are the gravitational field potential or the rotation of space (due to the non-orthogonality of the three-dimensional spatial section to time lines), or both of these factors presented together.

We have shown that the condition of stopping physically observable time is satisfied on a tiny spherical surface of the gravitational radius (for non-rotating bodies) or slightly above it (for rotating bodies), existing around the barycentre deep inside absolutely every physical body in the range from elementary particles to planets and stars. These spherical surfaces, enveloping the barycentres of all physical bodies are all connected to each other by trajectories of stopping observable time. Signals, instantly transmitted along these trajectories, instantly connect all physically bodies in the Universe. Such trajectories instantly connect any observer with stars and indicate the *middle* (*true*) *position of stars*, which was registered in Kozyrev's astronomical observations.

We have also considered a fully degenerate (ultimate) version of trajectories on the surface of the light cone, along which physically observable time stops and, therefore, signals travel instantly. Such trajectories make up a fully degenerate light cone associated with the pseudo-Riemannian space, which we called the zero-space. The motion of signals along such trajectories (i.e., in the zero-space) is observed by a regular external observer as their instant transmission in his observable (non-degenerate) space along trajectories of light. Once the conditions of full degeneration are somehow realized at the point of emission of a signal towards an observer and these conditions are also realized in his receiving device (receiver), then he will register that the signal has travelled instantly from the emission point to him along the trajectory of light signals (while it travelled along a trajectory lying in the fully degenerate zero-space). Such fully degenerate trajectories also instantly connect any observer with stars. They indicate the *visible* (*past*) *position of stars* and *their position in the future* (symmetrical to their visible position), registered in Kozyrev's astronomical observations.

This is how Kozyrev's astronomical observations of instant transmission of signals from stars are explained in the framework of General Relativity.

These results illustrate that, according to General Relativity, all physical bodies in the Universe, including you and us, exist not only at the present moment in time, but are multidimensional objects, the past, present and future of which are an existing reality.

Submitted on June 28, 2025

References

1. Kozyrev N. A. Observation of a volcanic process on the Moon. *Sky and Telescope*, 1959, v. 18, no. 4, 184–186; *Ibid.* Letter to the Editor. 1959, v. 18, no. 10, 561.
2. Kozyrev N. A. The atmosphere of Mercury. *Sky and Telescope*, 1964, v. 27, no. 6, 339–341.
3. Kozyrev, Nikolay Aleksandrovich. *Encyclopaedia Britannica*.
4. Dadaev A. N. Nikolai A. Kozyrev (1908–1983) — discoverer of Lunar volcanism (on the 100th anniversary of his birth). *Progress in Physics*, 2009, v. 5, no. 3, L3–L14.
5. Kozyrev N. A. Causal or Asymmetrical Mechanics in the Linear Approximation. Pulkovo Astron. Observatory, Leningrad, 1958 (in Russian).
6. Kozyrev N. A. Possibility of experimental study of the properties of time. A presentation, Sept. 1967. The Arlington Archive (Joint Publications Research Service), no. 45238, Arlington VA, May 2, 1968. Reprinted in: *The Abraham Zelmanov Journal*, 2012, v. 5, 188–220.
7. Kozyrev N. A. On the possibility of experimental investigation of the properties of time. In: *Time in Science and Philosophy*: *Collection of Scientific Papers*. Academia, Prague, 1971, 111–132 (this is a slightly modified version of the previous paper).
8. Kozyrev N. A. Astronomical observations using the physical properties of time. In: *Flaring Stars*: *Proc. of the Symposium at the Byurakan Astron. Observatory* (Oct. 5–8, 1976), Armenian Acad. of Sciences Publ., Yerevan, 1977, 209–227 (in Russian). Reprinted in: Kozyrev N. A. Collected Papers. Leningrad Univ. Publ., Leningrad, 1991, 363–383 (in Russian).
9. Kozyrev N. A. and Nassonov V. V. A new method for determining trigonometric parallaxes based on measuring the difference between the true and visible positions of a star. In: *Problems of Universe Exploration*, v. 7, Moscow-Leningrad, 1978, 168–179 (in Russian). Reprinted in: *Time and Stars. Collection of Papers for the 100th Anniversary of N. A. Kozyrev*, St. Petersburg, 2008, 106–117 (in Russian).
10. Kozyrev N. A. and Nassonov V. V. On some properties of time discovered by astronomical observations. In: *Problems of Universe Exploration*, v. 9, Moscow-Leningrad, 1980, 76–84 (in Russian). Reprinted in: *Time and Stars. Collection of Papers for the 100th Anniversary of N. A. Kozyrev*, St. Petersburg, 2008, 122–131 (in Russian).
11. Lavrent'ev M. M., Eganova I. A., Lutset M. K., Fominykh S. F. On the remote action of stars on resistor. *Doklady Akademii Nauk SSSR*, 1990, v. 314, no. 2, 352–355.
12. Lavrent'ev M. M., Gusev V. A., Eganova I. A., Lutset M. K., Fominykh S. F. On the registration of the real position of the Sun. *Doklady Akademii Nauk SSSR*, 1990, v. 315, no. 2, 368–370.
13. Kozyrev N. A. Astronomical proof of the reality of Minkowski's four-dimensional geometry. In: *Problems of Universe Exploration*, v. 9, Moscow-Leningrad, 1980, 85–93 (in Russian). Reprinted in: *Time and Stars. Collection of Papers for the 100th Anniversary of N. A. Kozyrev*, St. Petersburg, 2008, 132–140 (in Russian).
14. Zelmanov A. L. Chronometric Invariants. Translated from the 1944 PhD thesis, American Research Press, Rehoboth, New Mexico, 2006.
15. Zelmanov A. L. Chronometric invariants and accompanying frames of reference in the General Theory of Relativity. *Soviet Physics Doklady*, 1956, v. 1, 227–230 (translated from *Doklady Academii Nauk USSR*, 1956, v. 107, issue 6, 815–818).
16. Zelmanov A. L. On the relativistic theory of an anisotropic inhomogeneous universe. *The Abraham Zelmanov Journal*, 2008, vol. 1, 33–63 (translated from the thesis of the *6th Soviet Conference on the Problems of Cosmogony*, USSR Academy of Sciences Publishers, Moscow, 1957, 144–174).
17. Rabounski D. and Borissova L. Physical observables in General Relativity and the Zelmanov chronometric invariants. *Progress in Physics*, 2023, v. 19, issue 1, 3–29.
18. Rabounski D. and Borissova L. Particles Here and Beyond the Mirror. The 4th revised edition, New Scientific Frontiers, London, 2023 (the 1st edition was issued in 2001). Rabounski D. et Larissa Borissova L. Particules de l'Univers et au delà du miroir. La 2ème édition révisée en langue française, New Scientific Frontiers, Londres, 2023 (French translation).
19. Rabounski D. and Borissova L. On the possibility of instant displacements in the space-time of General Relativity. *Progress in Physics*, 2005, v. 1, issue 1, 17–19.
20. Rabounski D. and Borissova L. Non-quantum teleportation in a rotating space with a strong electromagnetic field. *Progress in Physics*, 2022, v. 18, issue 1, 31–49.
21. Rabounski D. and Borissova L. On the condition of non-quantum teleportation on the surface of a spherical body. *Progress in Physics*, 2025, v. 21, issue 1, 80–85.
22. Rabounski D. Introducing the space metric of a rotating massive body and four new effects of General Relativity. *Progress in Physics*, 2024, v. 20, issue 2, 79–99.
23. Borissova L. and Rabounski D. Galileo's principle and the origin of gravitation according to General Relativity. *Progress in Physics*, 2024, v. 20, issue 1, 69–78.

Origin of Cylindrically Oriented Zonal Flows in the Jovian Planets as Dictated by Quantum Celestial Mechanics (QCM)

Franklin Potter
Sciencegems, 8642 Marvale Drive, Huntington Beach, CA, 92646, USA. E-mail: frank11hb@yahoo.com

The four Jovian planets in the Solar System have fluid bodies surrounding a solid core and each exhibit several complex zonal flows with their atmospheres moving faster than the planet rotation. Several research groups have proposed that these atmospheric east-west zonal jet flows that are aligned with the axis of rotation are cylindrically confined, as indicated by identifying gravity harmonics. I propose that the source of these co-axial concentric cylidrical flow zones is dictated by quantum celestial mechanics (QCM), which states that the equilibrium radius for each cylindrical band/zone within the planet occurs where the Newtonian gravitational attraction balances the repulsive QCM quantization of angular momentum per unit mass effect.

1 Introduction

The four Jovian planets in our Solar System are fluid bodies surrounding a solid core. Fluid bodies do not rotate as rigid bodies and, instead, exhibit complex zonal flows in the atmospheres. Observational evidence of the Jovian planets by spacecraft in the visible, the ultraviolet (UV), the infrared (IR), and with magnetic field sensing, reveals atmospheric east-west zonal jet flows in each hemisphere. For a review that includes detailed diagrams of these zonal flows in the atmosphere down to a few thousand kilometers for Jupiter and Saturn, see [1].

These bands/zones on Jupiter have been observed through optical devices since the 1600s, but only via using data collected by the Juno and Cassini orbiting spacecraft at Jupiter and Saturn have researchers significantly improved our description of this complex zonal flow behavior.

Detailed analyses identifying gravity harmonics by several research groups over the past decade and earlier have suggested that the Jupiter and Saturn flows are probably aligned with the axis of rotation and that cylindrical confinement is essential for each distinct observed dynamic flow behavior. Specifically, as one example, in Jupiter the 21° N jet provides evidence that the flows extend inward cylindrically and not much radially [2]. For the equivalent cylindrical flow behavior on Saturn, see [3].

For all four Jovian planets, the flows penetrate cylindrically downward, to a depth of about 3000 km in Jupiter, to about 9000 km in Saturn, and to about 1000 km in Uranus and in Neptune. More than one cylindrical flow region exists within each Jovian planet. As a very simplified suggestion of the geometry being considered, Fig. 1 shows how two possible co-axial concentric flow cylinders would penetrate throughout a planetary sphere.

As these cylindrical regions rotate faster than the planet rotation, there would be physical flow phenomena to be measured along the concentric circular regions where each cylinder pierces the surface. One should note that there would be overlap among the cylindrical regions at most depths because they each could have a radial thickness that increases with depth within the planet.

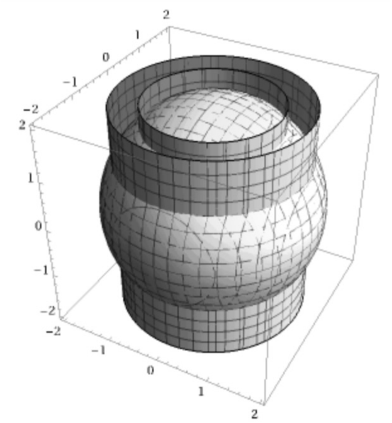

Fig. 1: Two co-axial concentric QCM cylinders penetrating the planet.

The actual physics origin of such cylindrical regions for the atmospheric flows within these Jovian planets has not been identified. Some complex suggestions involving dynamical combinations of Coriolis effects, temperature gradients, pressure gradients, magnetic field influences, etc., have been incorporated into existing models, but there has been no definitive single source proposed for the cylindrical symmetries [4, 5].

I propose that these co-axial concentric cylindrical flow zones can exist within all planets because they are dictated by the gravitational forces resulting from the quantization of angular momentum per unit mass constraint of quantum celestial mechanics (QCM) [6]. Equilibrium radii for the concentric cylinders within a massive body such as a planet are determined by both Newtonian gravitational attraction and a quantization of angular momentum per unit mass repulsive effect.

The equilibrium orbital radii of the planets of the Solar System as well as the orbital distances for planets in all known multi-planetary exosystems have been shown to obey this angular momentum constraint dictated by QCM in the Schwarzschild metric environment. Because each planet has a Schwarzschild radius r_s of a few meters or less, this quantiztion of angular momentum per unit mass effect applies also within the planets with the result being co-axial concentric cylindrical rotating regions.

2 Some prior applications of QCM

For an abbreviated derivation of quantum celestial mechanics (QCM) from the general relativistic Hamilton-Jacobi equation and some of its equations predicting gravitational effects for bodies obeying the Schwarzschild metric, see the Appendix. Applications of QCM in other gravitational metrics can be found in the original paper [6] and in several other of the references [7–11].

We have used QCM to explain the spacings of planetary orbits in the Solar System and in all known exoplanetary systems [8]. Essentially, QCM predicts both the Newtonian gravitational attraction and a repulsive effect [see (10) in the Appendix] that together specify equilibrium orbital radii that are a small subset of all possible Newtonian equilibrium orbital radii.

All known multi-planetary exosystems have been shown to obey this angular momentum constraint dictated by QCM. In the Solar System, we learned that the Oort Cloud, with its angular momentum contribution being almost 50 times greater than the angular momentum contributions of the planets plus the Sun, dictates the allowed equilibrium orbital radii of the planets to explain why its large radial separations are unique among the known planetary systems. Fig. 2 shows a sample of these exosystems obeying the angular momentum constraint. Note that they have planets closer to their star than the orbit radius of Mercury, and in some cases, they have a Jupiter mass planet close-in!

After applying the gravitational wave equation (GWE) in the Schwarzschild metric to planetary systems [8], we found further applications to galaxies, clusters of galaxies [9], and to the Universe. For the Universe [10], we determined an alternate viable explanation of cosmological redshifts in a static Universe in the interior metric, i.e. that a non-linear negative gravitational potential exists that agrees with the SN1a data for an accelerating behavior. Our result suggests that the clocks at the distant light sources tick slower than clocks at the observer for all observers.

For the analysis of the Jovian planets, we will use the same quantization of angular momentum per unit mass constraint dictated by QCM for the Schwarzschild metric given by (8) in the Appendix, which becomes

$$L/\mu = m\,L_T/M_T \tag{1}$$

for integer m and a gravitationally bound system total angular momentum L_T and total mass M_T.

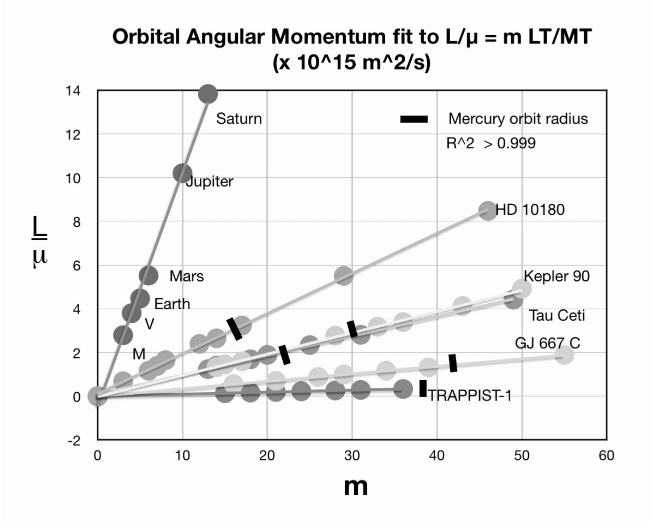

Fig. 2: The QCM angular momentum per unit mass constraint applied to several mulit-planetary exosystems. The short line marks the orbital radius distance of Mercury. The slopes are proportional to the total angular momentum in the gravitationally bound systems.

The application of this QCM orbital quantization equation is not only for planets in the exterior space surrounding the central massive object of mass M but also for the interior volume within the mass for all equilibrium radii r_{eq} greater than the Schwarzschild radius $r_s > 2GM/c^2$.

In 2021, we investigated radial distances from the Earth's axis within the Earth itself to establish [11] that the Antarctic Circumpolar Current (ACC), a significant water current moving eastward completely around the Antarctic Continent about 2 meters/second faster than the Earth's rotation at its latitude, exists at the $m = 6$ radial distance and is probably being driven by our QCM effect. That is, the ACC lies at the Earth's surface where a QCM rotational co-axial cylinder parallel to the Earth's axis penetrates the surface from the interior. Normally, one would expect a similar eastward water current around the North Pole region at about the same North latitude as the ACC, but land masses block such a continuous water current.

Recent seismic research [12] has revealed also that deep within the Earth, within its fluid outer core, lies a large donut-shaped mass, i.e. a toroidal volume, that rotates independently about the Earth's rotation axis at a different angular velocity than the rest of the outer core. Located at nearly the same radial distance from the Earth's axis as the ACC, we are investigating whether this rotating donut could be driven by the QCM gravitational force produced by the same cylinder with $m = 6$ as for the ACC.

3 Jovian planet considerations

In this investigation we are analyzing much more complicated dynamic systems involving planets with significant gaseous atmospheres. We consider whether the rotational zone/band structures of the Jovian planets, Jupiter, Saturn, Uranus, and

Neptune, are produced by the above QCM angular momentum constraint equations. Their Schwarzschild radii are all less than 3 meters, so they are expected to have rotational cylindrical regions co-axially parallel to the planet's rotation axis within their massive bodies.

However, unlike the Earth that is essentially dense solid and liquid matter all the way to its total radius, the Jovian planets each possess a fluid atmosphere that is a mixture of gases that extends significantly into the planet from the "surface", which is defined to be where the pressure is 1 bar. This atmospheric difference down to thousands of meters complicates any analysis.

Fortunately, the combined effects of Coriolis forces, temperature gradients, magnetic field movement, etc., have been worked out in terms of Bessel functions and Legendre funtions [1–3] for the geometry of the dynamic flows within the band structures. What is absent, however, is the reason for the existence of the proposed rotating co-axial concentric cylindrical regions within the rotating planets.

We will determine possible radii for the QCM co-axial concentric cylinders from the angular momentum constraint given by (1) based upon the physical parameters at each Jovian planet and try to determine whether they are the source of the cylndrical geometries for the atmospheric bands existing at the "surface". That is, if the radii of the predicted cylindrical regions roughly agree with the radii of the atmospheric zones/bands, we will consider that we have identified their source. In order to simplify our derivation of the cylindrical symmetry behavior within these planets, we will assume a north-south symmetry approximation for these band/zone regions, although there exists an obvious asymmetry in the flow data when the northern and southern hemispheres are compared.

Fig. 1 shows an example of only two co-axial concentric cylinders for a spherical planet. Where each cylinder intersects the "surface" is where the bands/zones should be. Because each cylinder has some width in the radial direction, the widths of each cylinder can overlap more than one other cylinder beneath the surface inside each planet, thereby creating a more complex environment than we will investigate. These complexities are probably already incorporated into the research models mentioned above.

4 Jovian planet analysis

If the planets were solid, their effective planet radii would be easy to define. However, a planet such as Jupiter has a solid core plus a liquid outer core region plus a significant lower density additional atmospheric region. One needs to determine the effective radius R of the planet for the application of the quantization of angular momentum per unit mass constraint in (1), which cannot be the radius R_0 to the "surface" because the atmosphere that occupies the outer radius is itself being driven by the QCM effective force determined by the dense inner regions.

Table 1: Effective planet radius for the Jovian planets.

Planet	α	αR^2 ($\times 10^{14}$m^2)	R ($\times 10^7$m)	Ratio R/R_0
Jupiter	0.2756	3.0	3.26	0.455
Saturn	0.22	4.0	4.26	0.71
Uranus	0.33	1.5	2.55	1.0
Neptune	0.33	1.4	2.46	1.0

Applying (1), we substitute vr for L/μ on the left side, with v being the tangential velocity of mass μ at orbit radius r, and substitute $\alpha MR^2\omega/M$ for L_T/M_T on the right side, to obtain the equilibrium radius expression

$$r_{eq}^2 = m\,\alpha R^2\,, \tag{2}$$

where α is the moment of inertia coefficient, i.e. of αMR^2, and R being the effective radius. For a solid planet, R would be the radial distance R_0 to its physical surface, but for the fluid Jovian planets, R may not be this distance.

We define an effective radius R to be the one that produces the correct latitudinal distribution of bands/zones at the surface of the planet. The effective αMR^2 values for the four Jovian planets are listed in Table 1. Note that for both Jupiter and Saturn, the effective radius R is much less than the actual radius R_0 of the planet as revealed in the ratio column, whereas for Uranus and Neptune the effective radius is probably the total radius of the planet. Also recall that for both Uranus and Neptune, the actual zonal latitudinal structures have not been identified as well as achieved for Jupiter and Saturn. Hopefully, more information will become available in the near future to ascertain whether our results actually agree with their band/zone structures.

The effective radius values in Table 1 are used to determine the r_{eq} values predicted by (1) and their equivalent latitudes for comparison to the data. The calculated values for the QCM co-axial concentric cylinders within the planets as listed in Table 2 for Jupiter and Saturn and in Table 3 for Uranus and Neptune.

The predicted latitudes for the zones/bands are in reasonable agreement with those at the surfaces of Jupiter and Saturn, but we await further data for the zone/band data for Uranus and Neptune.

Jupiter's differential rotation angular momentum plus the orbital angular momentum contributions from its moons produces $L_T = 4.795 \times 10^{38}$ kg m^2/s with a mass of $M_T = 1.9 \times 10^{27}$ kg. For Saturn and its moons, $L_T = 7.109 \times 10^{37}$ kg m^2/s for a mass $M_T = 5.683 \times 10^{26}$ kg. QCM predicts tangential velocities v_ϕ for each co-axial concentric cylindrical equilibrium radius r_{eq} based upon the equation

$$v_\phi = \frac{m\,L_T}{r_{eq}\,M_T}\,. \tag{3}$$

Table 2: Radial equilibrium distances for Jupiter and Saturn

m	Jupiter r_{eq} (10^7 m)	Lat θ	Saturn r_{eq} (10^7 m)	Lat θ
1	1.73	75.98	2.00	70.53
2	2.45	69.97	2.82	61.97
3	3.00	65.19	3.46	54.78
4	3.46	61.02	4.00	48.19
5	3.87	57.20	4.47	41.84
6	4.24	53.60	4.90	35.25
7	4.58	50.14	5.29	28.16
8	4.90	46.75	5.66	19.38
9	5.19	43.39	6.00	0
10	5.47	40.00		
11	5.74	36.60		
12	6.00	32.95		
13	6.24	29.22		
14	6.48	25.00		
15	6.71	20.20		
16	6.93	14.25		
17	7.14	0		

Table 3: Radial equilibrium distances for Uranus and Neptune.

m	Uranus r_{eq} (10^7 m)	Lat θ	Neptune r_{eq} (10^7 m)	Lat θ
1	1.23	58.64	1.18	61.46
2	1.73	47.40	1.54	51.43
3	2.12	33.96	1.89	40.08
4	2.45	16.56	2.18	28.04
5			2.43	10.33

Thus, for the Jupiter $m = 15$ and $m = 16$ zones/bands at the 20.20° and 14.25° latitude flow regions, QCM predicts tangential velocities v_ϕ of 5.65×10^4 m/s and 5.82×10^4 m/s, respectively. The zonal winds near the equitorial surface of Jupiter actually measure significantly lower values, having a maximum of about 100 m/s. Therefore, dynamic effects such as viscosity effects, etc., retard the flow in the atmosphere and are probably the cause of these much, much lower measured tangential velocity values than the predicted values.

For Saturn, for the $m = 7$ and $m = 8$ zones/bands at 28.16° and 19.38°, QCM predicts 1.66×10^4 m/s and 1.77×10^4 m/s tangential velocities, respectively. The data reveal much smaller flow velocities of about 300 m/s in these regions. Again, dynamic viscosity effects are probably reducing the predicted velocities to the measured velocities.

5 Conclusion

The zones/bands in the atmospheric flow regions on the surfaces of the Jovian planets appear to be in co-axial concentric cylinders. These complex atmospheric flows possibly penetrate into the planetary bodies to depths of thousands of kilometers. Although a dynamical combination of Coriolis effects, temperature gradients, pressure gradients, magnetic field influences, etc., have been incorporated into existing dynamic models by several research groups, there has been no definitive single source proposed for the apparent cylindrical symmetries defining these flow regions.

Quantum celestial mechanics (QCM) has a gravitational wave equation (GWE) that we previously had applied in the Schwarzschild metric to predict rotating co-axial concentric cylindrical regions within all massive bodies. For one example, we applied the GWE inside the Earth to determine that the Antarctic Cirumpolar Current (ACC), a water current traveling eastward about 2 meters/second faster than Earth's rotation rate at its latitude, could be explained by the application of the QCM quantization of angular momentum per unit mass equation

$$L/\mu = m\, L_T/M_T\,,$$

which relates an orbiting mass μ of angular momentum L in orbit in a gravitationally bound system to the total mass M_T and total angular momentum L_T. When applied to all known orbiting planets in multi-planetary systems, we established that their planet orbital radii agree with this quantization of angular momentum per unit mass constraint equation.

Upon applying this angular momentum constraint equation to the four Jovian planets, we identified co-axial concentric rotating cylinders for zones/bands at reasonable radii, i.e. rotating cylindrical regions piercing the surfaces at numerous latitudes roughly agreeing with observational data for the zone/band locations as determined with observations by telescopes and spacecraft.

Therfore, we suggest that the true source of the co-axial concentric cylindrical flow regions in the Jovian planets has been identified to be the result of the QCM combination of Newtonian gravitational attraction and the repulsive effect of QCM quantization of angular momentum per unit mass. An improved understanding of the complex dynamics of these flow regions can now be achieved in the near future.

Acknowledgements

The author appreciates the support of Sciencegems.com for the opportunity to investigate fundamental physics and its application to prevalent problems in Nature.

Received on June 25, 2025

A Appendix: brief derivation of QCM equations

In 2003, Howard G. Preston and I introduced [6, 7] Quantum Celestial Mechanics (QCM), which is derived from the general relativistic Hamilton-Jacobi equation and a simple transformation that maintains the equivalence principle. The result was a new gravitational scalar wave equation (GWE) that, in the Schwarzschild metric, predicts the quantization of angular momentum per unit mass. Here is an abbreviated derivation of the equations to be used for analyzing the Jovian planets.

From the general relativistic Hamilton-Jacobi equation,

$$g^{\alpha\beta}\frac{\partial S}{\partial x^\alpha}\frac{\partial S}{\partial x^\beta} - \mu^2 c^2 = 0\,, \tag{4}$$

the transformation

$$\Psi = e^{iS'/\mu c H} \tag{5}$$

introduces a wave function Ψ, with S the action, μ the mass of the orbiting object, and $S' = S/\mu c$ so that the equivalence principle is obeyed. For a detailed derivation showing all the mathematical steps, see [6].

We defined a system scale length H by

$$H = \frac{L_T}{M_T c} \tag{6}$$

for the total gravitationally bound system mass M_T having total angular momentum L_T and c being the speed of light in vacuum.

Following through with the mathematical steps produced a scalar gravitational wave equation (GWE)

$$g^{\alpha\beta}\frac{\partial^2 \Psi}{\partial x^\alpha \partial x^\beta} + \frac{\Psi}{H^2} = 0\,. \tag{7}$$

Expressing the GWE in the Schwarzschild metric, a separation of variables leads to differential equations in coordinates (t, r, θ, ϕ) that produce quantization conditions.

The angular parts dictate the quantization of angular momentum *per unit mass* for orbital angular momentum L as

$$\frac{L}{\mu} = mcH \tag{8}$$

for integer m. The radial equation leads to the quantization of energy *per unit mass* equation

$$E_n = -\mu c^2 \frac{r_s^2}{8n^2 H^2} \tag{9}$$

for integer n.

The expected value of the QCM orbital radial acceleration near the orbital equilibrium radius is defined by

$$\ddot{r}_{eq} = -\frac{GM}{r^2} + \frac{\ell(\ell+1)\,L_T^2}{r^3\,M_T^2}\,. \tag{10}$$

For cylindrical coordinates, the $\ell(\ell{+}1)$ is replaced by m^2.

For comparison, recall that the standard Newtonian gravitation has

$$\ddot{r}_{eq} = -\frac{GM}{r^2} + \frac{L^2}{\mu^2\,r^3} \tag{11}$$

and, because the angular momentum $L = \mu\sqrt{GMr}$ and the angular velocity $\dot{\phi} = L/\mu r^2$ for a circular orbit, then $\ddot{r} = 0$ and the radial acceleration per mass $(\ddot{r} - r\dot{\phi}^2)$ equals $-GM/r^2$.

Consequently, QCM has both the Newtonian attraction term and a repulsive angular momentum term around each equilibrium orbital radius, which results in the prediction of allowed orbital radii that are a sparse subset of the Newtonian ones. In addition, there will be equilibrium radii within planets at which a QCM acceleration occurs.

References

1. Fletcher L. N., Kaspi Y., Guillet T., Showman A. P. How well do we understand the belt/zone circulation of Giant Planet atmospheres? *Space Sci Rev*, 2020, v. B216, 30. arXiv:1907.01822v2.
2. Kaspi Y., Galanti E., *et al.* Observational evidence for cylindrically oriented zonal flows on Jupiter. *Nature Astronomy*, 2023, v. 7, 1463–1472.
3. Chachan Y. and Stevenson D. J. A Linear Approximation for the Effect of Cylindrical Differential Rotation on Gravitational Moments: Application to the Non-Unique Interpretation of Saturn's Gravity. *Icarus*, 2019, v. 323, 87–98. arXiv: 1902.10728v1.
4. Duer K., Galanti E., Kaspi Y. Gas Giant Simulations of Eddy-Driven Jets Accompanied by Deep Meridional Circulation. *AGU Advances*, 2023, v. 4, 32023AV000908. arXiv: astro-ph/2312.10651.
5. Helled R. and Howard S. Giant planet interiors and atmospheres. arXiv: astro-ph/2407.05853.
6. Preston H. G. and Potter F. Exploring Large-scale Gravitational Quantization without $\hbar$ in Planetary Systems, Galaxies, and the Universe. arXiv: gr-qc/0303112.
7. Potter F. and Preston H. G. Quantum Celestial Mechanics: large-scale gravitational quantization states in galaxies and the Universe. In: 1st Crisis in Cosmology Conference: CCC-I, Lerner E. J. and Almeida J. B., eds., AIP CP822, 2006, 239–252.
8. Potter F. Predicting Total Angular Momentum in TRAPPIST-1 and Many Other Multi-Planetary Systems Using Quantum Celestial Mechanics. *Prog. in Physics*, 2018, v. 14 (3), 115–120.
9. Potter F. Galaxy Clusters: Quantum Celestial Mechanics (QCM) Rescues MOND? *Prog. in Physics*, 2024, v. 20 (2), 100–102.
10. Potter F. and Preston H. G. Cosmological Redshift Interpreted as Gravitational Redshift. *Prog. in Physics*, 2007, v. 3 (2), 31–33.
11. Potter F. Antarctic Circumpolar Current: Driven by Gravitational Forces? *Prog. in Physics*, 2021, v. 17 (1), 99–103.
12. Ma X. and Tkačič H. Seismic low-velocity equatorial torus in the Earth's outer core: Evidence from the late-coda correlation wavefield. *Science Advances*, 2024, v. 10 (35).

Quantum Tunneling Analog of Black Hole Thermodynamics via Fermion-Photon Confined Spectra

Travis S. Taylor[1,2]

[1]QuantumFrontier, LLC, Huntsville, AL, USA.
[2]Department of Physics, University of Alabama in Huntsville, AL, USA.
E-mail: tst0072@uah.edu

We introduce a quantum mechanical model that reproduces key thermodynamic features of a Schwarzschild black hole using a spherical finite potential well. By analyzing the tunneling spectra of photons and fermions confined in this well, we demonstrate a numerical match to Hawking radiation. Additionally, the entropy of the emitted spectrum exhibits a geometric scaling consistent with the Bekenstein-Hawking formula. These results suggest that quantum confinement may serve as an analog platform for exploring black hole thermodynamics.

1 Introduction

This study highlights a formal similarity between quantum mechanical tunneling and gravitational radiation processes, suggesting a deeper, underlying unity between quantum confinement and curved spacetime thermodynamics. The findings propose potential insights into the quantum mechanical underpinnings of black hole thermodynamics and contribute to the ongoing dialogue on the unification of quantum mechanics and general relativity.

Black holes, as described by general relativity, exhibit thermodynamic properties such as Hawking radiation and entropy, hinting at a quantum mechanical foundation [1]. This study develops a three-dimensional spherical quantum well model with a finite potential barrier to explore these properties under controlled conditions.

This work departs from prior analog black hole models by constructing a purely quantum mechanical system that, when scaled appropriately, numerically reproduces the full Hawking spectrum. In contrast to acoustic or optical analogs, our approach uses tunneling in a finite spherical well to model both bosonic and fermionic emission spectra and entropy, providing a unified thermal analog of black hole radiation. The model's ability to quantitatively match the black hole spectrum across a wide frequency range, using temperature scaling and statistical blending, demonstrates a deeper thermodynamic equivalence rooted in quantum confinement rather than relativistic curvature.

Unlike analog gravity models based on fluid flow or optical horizons [2, 3], this approach relies purely on quantum mechanical tunneling in a finite potential structure. We begin by formulating a spherical quantum well model with a barrier structure mimicking an event horizon. Photon and fermion spectra are then derived using WKB approximations, and the resulting emission profiles are compared to Hawking radiation. We also compute entropy scaling and propose a dimensionless scaling relation that aligns the two systems thermodynamically.

2 Background

2.1 Schwarzschild black holes and event horizon

A Schwarzschild black hole, a spherically symmetric, non-rotating solution to Einstein's field equations, is characterized by the metric [4, 5]:

$$ds^2 = -\left(1 - \frac{2GM}{c^2 r}\right) c^2 dt^2 + \left(1 - \frac{2GM}{c^2 r}\right)^{-1} dr^2 + r^2\left(d\theta^2 + \sin^2\theta\, d\phi^2\right), \tag{1}$$

where G is the gravitational constant, M is the mass, c is the speed of light, r is the radial coordinate, t is time, and θ, ϕ are angular coordinates. The event horizon, at the Schwarzschild radius:

$$R_s = \frac{2GM}{c^2}, \tag{2}$$

marks the boundary where escape velocity equals c, rendering escape impossible classically. Hawking radiation, a quantum phenomenon, suggests black holes emit thermal radiation at temperature $T_H = \frac{\hbar c^3}{8\pi G M k_B}$ [1].

2.2 The 3D finite quantum well

In quantum mechanics, a finite spherical well confines particles with a potential [6]:

$$V(r) = \begin{cases} 0 & \text{for } r < R_s \\ V_0\, e^{-\lambda(r-R_s)} & \text{for } R_s \leqslant r < R \\ V_1\, e^{-\lambda(r-R)} & \text{for } r \geqslant R \end{cases} \tag{3}$$

where V_0 (in eV) is the barrier height, $V_1 < V_0$ is the exterior potential, R is the outer radius, and λ (in m^{-1}) controls decay. Unlike infinite wells, this permits tunneling, a key feature in semiconductor applications [7] (see Figure 1).

2.3 Event horizons and barriers

The black hole event horizon and quantum well barrier both define boundaries, but differ fundamentally. The horizon requires infinite energy for escape, per general relativity, while

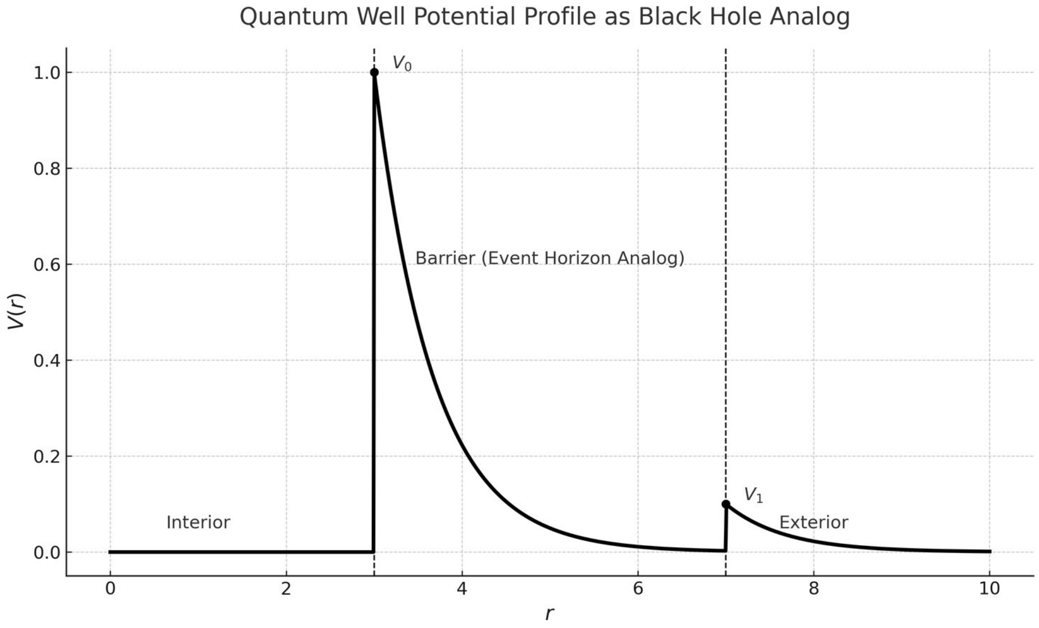

Fig. 1: Radial potential profile $V(r)$ illustrating the structure of the spherical quantum well. The barrier begins at R_s with height V_0 and decays exponentially toward V_1 by radius R. Regions labeled: Interior ($r < R_s$), Barrier (Event Horizon Analog, $R_s < r < R$), and Exterior ($r > R$).

the quantum barrier allows probabilistic tunneling [6]. This contrast highlights deterministic versus probabilistic physics, yet both systems suggest a transition from confinement to escape, inspiring our analogy.

3 Quantum well model formulation

3.1 Quantum well model setup

Our quantum well is a spherical system with potential:

$$V(r) = \begin{cases} 0 & \text{for } r < R_s \\ V_0\, e^{-\lambda(r-R_s)} & \text{for } R_s \leqslant r < R \\ V_1\, e^{-\lambda(r-R)} & \text{for } r \geqslant R \end{cases} \tag{4}$$

where $R_s = \frac{2GM}{c^2}$ aligns with the Schwarzschild radius, V_0 sets the barrier, and λ emulates gravitational decay. This structure includes an interior ($r < R_s$), a transition region ($R_s \leqslant r < R$), and an exterior ($r \geqslant R$), mirroring a black hole's zones.

To rigorously establish the energy spectrum and tunneling behavior of the quantum well, we solve the time-independent Schrödinger equation:

$$-\frac{\hbar^2}{2m}\nabla^2\psi + V(r)\psi = E\psi. \tag{5}$$

Expanding in spherical coordinates and assuming a separable solution $\psi(r,\theta,\phi) = R(r)\,Y_l^m(\theta,\phi)$, the radial equation becomes:

$$\frac{d^2R}{dr^2} + \frac{2}{r}\frac{dR}{dr} + \left[\frac{2m}{\hbar^2}(E - V(r)) - \frac{l(l+1)}{r^2}\right]R = 0. \tag{6}$$

We solve this equation in three regions: (i) inside the well ($r < R_s$), (ii) within the barrier ($R_s \leqslant r < R$), and (iii) outside the well ($r > R$).

The full wavefunction $\psi(r,\theta,\phi)$ is continuous and differentiable across region boundaries at $r = R_s$ and $r = R$, requiring matching of both the radial function and its derivative:

$$R_{\text{in}}(R_s) = R_{\text{barrier}}(R_s), \quad R'_{\text{in}}(R_s) = R'_{\text{barrier}}(R_s), \tag{7}$$

$$R_{\text{barrier}}(R) = R_{\text{out}}(R), \quad R'_{\text{barrier}}(R) = R'_{\text{out}}(R). \tag{8}$$

These boundary conditions yield a transcendental equation for energy levels E_n, which must be solved numerically.

In practice, these are implemented using numerical shooting methods or root-finding on determinant conditions from matched solutions [8].

3.2 Inside the well region ($r < R_s$)

For a potential well with $V(r) = 0$, the equation simplifies to:

$$\frac{d^2R}{dr^2} + \frac{2}{r}\frac{dR}{dr} + \left(k^2 - \frac{l(l+1)}{r^2}\right)R = 0, \tag{9}$$

where $k^2 = \frac{2mE}{\hbar^2}$. The general solution in this region is given by the spherical Bessel function:

$$R_{\text{in}}(r) = A\, j_l(kr), \tag{10}$$

where $j_l(x)$ is the spherical Bessel function of the first kind.

3.3 Barrier region: ($R_s \leqslant r < R$)

In the barrier region, the potential is modeled as an exponentially decaying function:

$$V(r) = V_0\, e^{-\lambda(r-R_s)}. \tag{11}$$

The Schrödinger equation in this region is:

$$\frac{d^2R}{dr^2} + \frac{2}{r}\frac{dR}{dr} + \left[\frac{2m}{\hbar^2}\left(E - V_0\, e^{-\lambda(r-R_s)}\right) - \frac{l(l+1)}{r^2}\right] R = 0. \tag{12}$$

Since this equation does not have a simple analytic solution, we apply the Wentzel-Kramers-Brillouin (WKB) approximation to estimate the tunneling probability [9]:

$$T(E) \approx e^{-2\int_{R_s}^{R} \sqrt{\frac{2m}{\hbar^2}(V(r)-E)}\; dr}. \tag{13}$$

For classically forbidden regions where $E < V(r)$, the wavefunction exhibits exponential decay:

$$R_{\text{barrier}}(r) \approx C e^{-\frac{\sqrt{2mV_0}}{\hbar\lambda} e^{-\lambda(r-R_s)}}. \tag{14}$$

3.4 Outside the well ($r > R$)

For large r, we assume the potential is negligible, and the Schrödinger equation reduces to:

$$\frac{d^2R}{dr^2} + \frac{2}{r}\frac{dR}{dr} + \left(k_0^2 - \frac{l(l+1)}{r^2}\right) R = 0, \tag{15}$$

where $k_0^2 = \frac{2m(E-V_1)}{\hbar^2}$. The general solution for outgoing waves is given by the spherical Hankel function:

$$R_{\text{out}}(r) = B h_l^{(1)}(k_0 r), \tag{16}$$

where $h_l^{(1)}(x)$ represents the spherical Hankel function of the first kind.

3.5 Matching conditions and energy quantization

The wavefunction and its derivative must be continuous at $r = R_s$ and $r = R$:

$$R_{\text{in}}(R_s) = R_{\text{barrier}}(R_s), \quad R'_{\text{in}}(R_s) = R'_{\text{barrier}}(R_s), \tag{17}$$

$$R_{\text{barrier}}(R) = R_{\text{out}}(R), \quad R'_{\text{barrier}}(R) = R'_{\text{out}}(R). \tag{18}$$

These conditions yield a transcendental equation that determines the allowed energy levels E_n, which must be solved numerically. By solving the Schrödinger equation in each region and applying boundary conditions, we obtain the wavefunctions and energy levels for the quantum well. The WKB approximation provides an estimate for the tunneling probability, supporting the interpretation that the system exhibits black hole-like emission characteristics.

For a potential of the form $V(r) = V_0\, e^{-\lambda(r-R_s)}$, the classical turning points r_1, r_2 are defined by $V(r) = E$, yielding:

$$r_2 - R_s = \frac{1}{\lambda} \ln\left(\frac{V_0}{E}\right), \quad r_1 = R_s.$$

Hence, the WKB tunneling probability is:

$$T(E) \approx \exp\left[-\frac{2}{\hbar}\int_{R_s}^{r_2} \sqrt{2m(V(r)-E)}\, dr\right]. \tag{19}$$

4 Energy quantization and photon statistics

Photons in the well follow the Helmholtz equation [6]:

$$\left[\frac{d^2}{dr^2} + \frac{2}{r}\frac{d}{dr} - \frac{l(l+1)}{r^2} + k^2\right] R(r) = 0, \tag{20}$$

where $k = \frac{E}{\hbar c}$. The finite barrier allows tunneling, yielding approximate energies:

$$E_{nl} \approx \hbar c\, \frac{x_{nl}}{R}, \tag{21}$$

where x_{nl} adjusts for penetration.

The partition function for N photons, using Bose-Einstein statistics [10], is:

$$Z = \prod_{n,l} \left(\frac{1}{1 - e^{-\beta E_{nl}}}\right)^{2l+1}, \tag{22}$$

where $\beta = 1/(k_B T)$.

5 Calculation of internal energy

The internal energy is [10]:

$$E_{\text{int}} = -\frac{\partial \ln Z}{\partial \beta} = \sum_{n,l} (2l+1)\, E_{nl}\, \frac{1}{e^{\beta E_{nl}} - 1}. \tag{23}$$

The energy density per unit volume for blackbody photons confined in a spherical well of radius R is given by integrating over the Bose-Einstein distribution:

$$E_{\text{int}} = \int_0^\infty g(E)\, \frac{E}{e^{\beta E} - 1}\, dE \tag{24}$$

with $g(E) = \frac{8\pi R^3}{h^3 c^3} E^2$, yielding:

$$E_{\text{int}} = \frac{8\pi R^3}{h^3 c^3} \int_0^\infty \frac{E^3}{e^{\beta E} - 1}\, dE = \frac{8\pi^5 R^3 (k_B T)^4}{15 h^3 c^3}. \tag{25}$$

Assuming a dominant tunneling angular momentum mode $l = 1$, we multiply by the degeneracy $2l + 1 = 3$.

For a dominant $l_{\text{es}} = 1$, assumed as the primary tunneling mode for simplicity [6]:

$$E_{\text{int}} \approx 3 \int_0^\infty \frac{8\pi R^3}{h^3 c^3} E^3 \frac{1}{e^{\beta E} - 1}\, dE = 3\,\frac{8\pi^5 R^3 (k_B T)^4}{15 h^3 c^3}, \tag{26}$$

using the photon density of states $g(E) = \frac{8\pi R^3}{h^3 c^3} E^2$.

6 Emission spectra from quantum tunneling

The tunneled energy spectrum for photons escaping the quantum well is derived using the grand canonical ensemble and tunneling probability [11, 12]:

$$I_{\text{tunneled}}(E) = \frac{8\pi R^3}{h^3 c^3} E^3 \frac{T(E)}{e^{E/k_B T} - 1}\,, \tag{27}$$

where $g(E) = \frac{8\pi R^3}{h^3 c^3} E^2$ is the photon density of states, and $T(E)$ is the tunneling probability through the barrier $V(r) = V_0\, e^{-\lambda(r-R_s)}$ from R_s to R. For photons, the WKB approximation [9] gives:

$$T(E) = e^{-2\int_{R_s}^{R} \frac{\sqrt{V_0\, e^{-\lambda(r-R_s)}-E}}{\hbar c}\,dr}\,. \tag{28}$$

Substituting $u = r - R_s$, the energy-dependent tunneling probability is:

$$T(E) = e^{-\frac{2}{\hbar c}\int_0^{R-R_s}\sqrt{V_0\, e^{-\lambda u}-E}\,du}, \tag{29}$$

valid for $E < V_0\, e^{-\lambda(R-R_s)}$, where the integral modulates the spectrum as a transmission factor. An earlier approximation assuming $V_0\, e^{-\lambda(r-R_s)} \gg E$ yielded $T(E) \approx e^{-\frac{2\sqrt{V_0}}{\hbar c\lambda}(R-R_s)}$, but here we retain E-dependence for accuracy. The full spectrum becomes:

$$I_{\text{tunneled}}(E) = \frac{8\pi R^3}{h^3 c^3} e^{-\frac{2}{\hbar c}\int_0^{R-R_s}\sqrt{V_0 e^{-\lambda u}-E}\,du} \frac{E^3}{e^{E/k_B T} - 1}. \tag{30}$$

To enhance functional similarity with Hawking radiation, we approximate the WKB exponential as a summation over barrier segments. Discretizing the integral with $u_n = n\Delta u$, $\Delta u = \frac{R-R_s}{N}$, and defining $T_n(E) = e^{-\frac{2}{\hbar c}\sqrt{V_0\, e^{-\lambda u_n}-E}\,\Delta u}$, we write:

$$I_{\text{tunneled}}(E) \approx \frac{8\pi R^3}{h^3 c^3} \sum_{n=0}^{N-1} (2n+1)\, T_n(E)\, \frac{E^3}{e^{E/k_B T} - 1}\,, \tag{31}$$

where $(2n + 1)$ heuristically mimics mode degeneracy, and N is large for accuracy [9].

To compute $T(E)$ numerically, we discretize the WKB integral using $u = r - R_s$, with $\Delta u = \frac{R-R_s}{N}$, and midpoint values $u_n = (n + 0.5)\,\Delta u$. The integral becomes:

$$T(E) \approx \exp\left[-\frac{2\,\Delta u}{\hbar c} \sum_{n=0}^{N-1} \sqrt{V_0\, e^{-\lambda u_n} - E}\right]. \tag{32}$$

To capture contributions from each shell, we define:

$$T_n(E) = \exp\left[-\frac{2\Delta u}{\hbar c}\,\sqrt{V_0 e^{-\lambda u_n} - E}\right] \tag{33}$$

and approximate the full tunneling-modulated spectrum as:

$$I_{\text{tunneled}}(E) \approx \frac{8\pi R^3}{h^3 c^3} \sum_{n=0}^{N-1} (2n+1)\, T_n(E)\, \frac{E^3}{e^{E/k_B T} - 1}\,. \tag{34}$$

This can be shown as a proportionality as:

$$I_{\text{tunneled}}(E) \propto \frac{E^3}{e^{E/k_B T_H} - 1}\,. \tag{35}$$

For a Schwarzschild black hole, Hawking predicts:

$$I_{\text{Hawking}}(E) = \frac{1}{2\pi\hbar} \sum_{l=0}^{\infty} (2l+1)\,\Gamma_l(E)\, \frac{E^3}{e^{E/k_B T_H} - 1}\,, \tag{36}$$

where $\Gamma_l(E)$ are greybody factors accounting for gravitational scattering, $T_H = \frac{\hbar c^3}{8\pi G M k_B}$ is the Hawking temperature, and the sum is over angular momentum modes [1]. For comparison, neglecting greybody factors ($\Gamma_l(E) = 1$) and approximating the sum, it simplifies to:

$$I_{\text{Hawking}}(E) \propto \frac{E^3}{e^{E/k_B T_H} - 1}\,, \tag{37}$$

and this Hawking spectrum is show in Fig. 2.

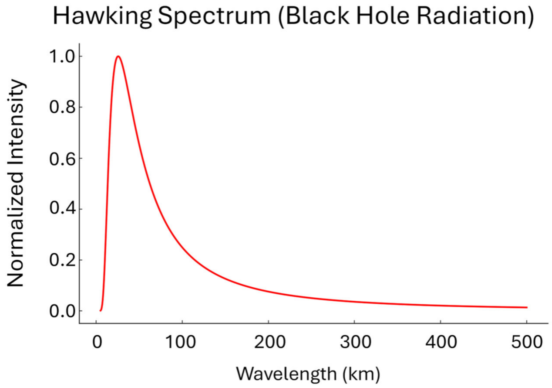

Fig. 2: Hawking radiation spectrum for a Schwarzschild black hole, computed with $T_H \approx 6.2 \times 10^{-8}$ K for $M = 10^{30}$ kg, $R_s \approx 1.48$ km.

The QW's $\sum(2n + 1)T_n(E)$ parallels the $\sum(2l + 1)\Gamma_l(E)$ structure, though n represents spatial segments rather than angular modes, and fermionic contributions are omitted for simplicity [1].

Fig. 3 shows the normalized Bose-Einstein tunneling spectrum for photons confined within the quantum well potential. The distribution follows the expected Planckian shape, peaking at a finite wavelength and decaying rapidly for longer wavelengths. The horizontal axis is expressed in kilometers to mirror the gravitational scale of black hole analogs, reinforcing the geometric correspondence between quantum confinement and curved spacetime radiation. The spectral peak reflects the most probable energy mode escaping the potential barrier, consistent with blackbody radiation at fixed temperature. This plot complements the Fermi-Dirac spectrum shown later and helps establish a full statistical picture of bosonic versus fermionic tunneling behavior in the analog system.

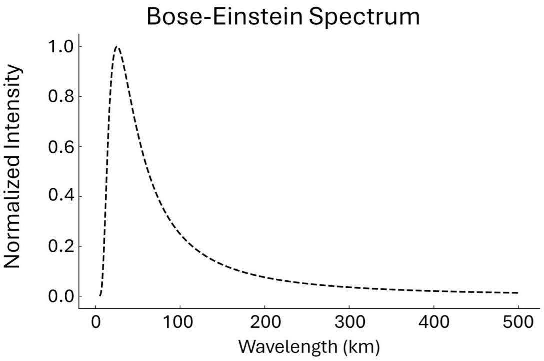

Fig. 3: Bosonic (Bose-Einstein) tunneling spectrum from the quantum well, showing the emission profile for photons under barrier modulation. Parameters: $T = 10^4$ K, $V_0 = 1$ eV, $\lambda = 10^9\,\mathrm{m}^{-1}$, $R = 10^{-9}$ m. This figure complements the fermionic spectrum shown in Fig. 4.

7 Fermionic quantum well spectrum

For fermions, the density of states is [10]:

$$g(E) = \frac{4\pi R^3}{2\pi^2} \left(\frac{2m}{\hbar^2}\right)^{3/2} E^{1/2}, \tag{38}$$

yielding:

$$I_{\mathrm{FD}}(E) = \frac{4\pi R^3}{2\pi^2} \left(\frac{2m}{\hbar^2}\right)^{3/2} E^{3/2} \frac{T(E)}{e^{(E-\mu)/(k_B T)} + 1}\,, \tag{39}$$

where μ is the chemical potential. This $E^{3/2}$ contrasts with the bosonic E^3 (see Fig. 4).

A final comparative analysis is shown in Figure 5, where the tunneling spectra for both bosons and fermions are plotted against the theoretical Hawking radiation curve. The bosonic (Bose-Einstein) spectrum displays close agreement with the Hawking distribution in both peak location and decay shape, while the fermionic (Fermi-Dirac) spectrum deviates more significantly, particularly at high and low energies. This suggests that bosonic modes dominate the thermal behavior near the quantum well's emission surface, reinforcing the analogy to black hole radiation where massless bosons such as photons are the primary contributors. The combined comparison underscores the effectiveness of quantum confinement models in reproducing the spectral structure of Hawking radiation.

8 Fermionic tunneling and comparison to Hawking radiation

While the primary focus of this model has been on bosonic radiation from the quantum well, black holes also emit fermions, such as neutrinos and electrons, through Hawking radiation [1]. To further strengthen the analogy, we now consider fermionic tunneling from the quantum well and compare it directly to the fermionic component of Hawking radiation.

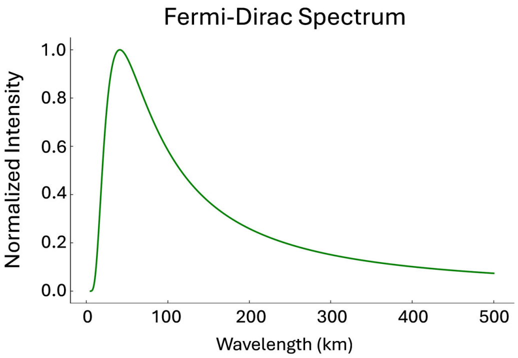

Fig. 4: Fermionic tunneling spectrum from the quantum well, computed with effective temperature $T = 10^4$ K, barrier height $V_0 = 1$ eV, decay constant $\lambda = 10^9\,\mathrm{m}^{-1}$, outer radius $R = 10^{-9}$ m, and chemical potential $\mu = 0.5$ eV for a fermion mass $m = 9.11 \times 10^{-31}$ kg (electron mass).

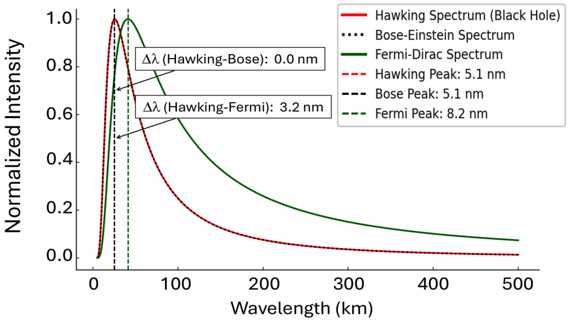

Fig. 5: Spectral comparison between fermionic tunneling emission from the quantum well and the Hawking radiation profile. The similarity in peak structure and decay behavior supports the model's thermodynamic analogy.

8.1 Fermionic tunneling in the quantum well

For fermions confined in the quantum well, the density of states is given by [10]:

$$g_{\mathrm{FD}}(E) = \frac{4\pi R^3}{2\pi^2} \left(\frac{2m}{\hbar^2}\right)^{3/2} E^{1/2}. \tag{40}$$

The corresponding energy spectrum for fermionic tunneling is:

$$I_{\mathrm{FD}}(E) = g_{\mathrm{FD}}(E)\, \frac{T(E)}{e^{(E-\mu)/(k_B T)} + 1}\,, \tag{41}$$

where μ is the chemical potential, and $T(E)$ is the tunneling probability. The key difference from the bosonic case is the presence of the Fermi-Dirac distribution, which prevents multiple fermions from occupying the same state.

8.2 Hawking radiation for fermions

Hawking's original derivation shows that a Schwarzschild black hole emits fermions in a manner similar to bosons, but governed by the Fermi-Dirac distribution:

$$I_{\text{Hawking,FD}}(E) = \frac{1}{2\pi\hbar} \sum_{l=0}^{\infty} (2l+1)\,\Gamma_l(E)\, \frac{E^3}{e^{(E-\mu)/(k_B T_H)} + 1}\,, \tag{42}$$

where $\Gamma_l(E)$ are the greybody factors that account for the partial transmission of fermions through the gravitational potential barrier of the black hole.

8.3 Comparison and key differences

Both the quantum well and black hole spectra for fermions follow the same fundamental shape, but differ in their scaling factors:

1. **Greybody Factors vs. Tunneling Probability**: The greybody factors $\Gamma_l(E)$ in Hawking radiation serve a similar role to the tunneling probability $T(E)$ in the quantum well. While the former accounts for gravitational backscattering, the latter describes quantum mechanical barrier penetration.
2. **Spectral Shape and Dependence on Chemical Potential**: In both cases, the fermionic distribution follows the expected Fermi-Dirac function, modifying the thermal spectrum. However, in the quantum well, the chemical potential μ can be tuned explicitly, whereas for black holes, it is dictated by charge and angular momentum constraints.
3. **Energy Dependence**: The Hawking spectrum for fermions retains an E^3 dependence in the numerator, whereas the quantum well spectrum follows an $E^{3/2}$ dependence from the density of states function. This difference arises from the different spatial confinement conditions in the quantum well compared to the gravitational horizon.

Despite these differences seen in Fig. 6, the fermionic tunneling spectrum in the quantum well closely mirrors the qualitative behavior of fermionic Hawking radiation. This strengthens the analogy by demonstrating that the quantum well can mimic both bosonic and fermionic emissions, further supporting the claim that black hole thermodynamics can be explored using quantum mechanical tunneling models.

8.4 Scaling factor

To relate the fermionic quantum well spectrum to the Hawking radiation spectrum, we define the scaling factor:

$$C_{\text{scale}} = \frac{\max(I_{\text{Fermi-Dirac}})}{\max(I_{\text{Hawking}})}\,. \tag{43}$$

We seek to determine the form of C_{scale} using dimensional analysis and fundamental physical principles.

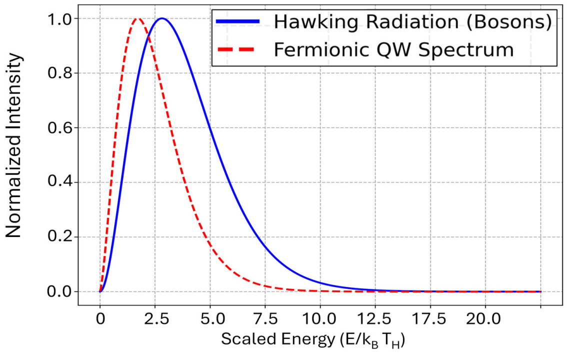

Fig. 6: Comparison of fermionic tunneling from the quantum well (dashed) and fermionic Hawking radiation spectrum (solid). Both spectra exhibit similar functional forms, with differences arising from the density of states and barrier characteristics.

Dimensional analysis of the spectra

The spectra for both systems follow power laws with an exponential suppression:

- **Hawking Radiation Spectrum** (neglecting greybody factors):
$$I_{\text{Hawking}}(E) \propto \frac{E^3}{e^{E/k_B T_H} - 1}, \tag{44}$$
where the Hawking temperature is given by:
$$T_H = \frac{\hbar c^3}{8\pi G M k_B}. \tag{45}$$
- **Fermionic Tunneling Spectrum from the Quantum Well**:
$$I_{\text{FD}}(E) = g_{\text{FD}}(E) \frac{T(E)}{e^{(E-\mu)/(k_B T)} + 1}, \tag{46}$$
where the density of states for a confined fermion system is:
$$g_{\text{FD}}(E) \sim E^{3/2}. \tag{47}$$

Since these spectra represent energy distributions, their dimensional form is:

$$[I(E)] = \frac{\text{Energy}}{\text{Volume} \times \text{Energy} \times \text{Time}} = \frac{1}{(\text{Length})^3 \times \text{Time}}\,. \tag{48}$$

We now analyze the relevant fundamental constants:

- Gravitational constant G: $[G] = \frac{\text{m}^3}{\text{kg} \times \text{s}^2}$.
- Speed of light c: $[c] = \frac{\text{m}}{\text{s}}$.
- Reduced Planck constant $\hbar$: $[\hbar] = \frac{\text{kg} \times \text{m}^2}{\text{s}}$.

Scaling constant form

Since the Hawking temperature involves the gravitational scaling:

$$T_H \sim \frac{\hbar c^3}{G k_B M}\,, \tag{49}$$

we hypothesize that C_{scale} must involve G and c in a dimensionally consistent ratio.

We seek a dimensionless form:

$$C_{\text{scale}} \sim \left(\frac{G}{c^n}\right)^m . \tag{50}$$

For energy flux normalization, we anticipate a form proportional to the Stefan-Boltzmann factor for black hole radiation. A natural choice is:

$$C_{\text{scale}} \sim \frac{8\pi G}{c^4} . \tag{51}$$

Physical interpretation of C_{scale}

The presence of G/c^4 is consistent with the Einstein field equations, where similar terms appear in general relativity. The factor 8π also appears naturally in black hole thermodynamics and entropy calculations.

Thus, we predict:

$$C_{\text{scale}} \sim \frac{8\pi G}{c^4} . \tag{52}$$

Next steps

To verify this scaling factor:

1. Compute C_{scale} numerically using physical constants and compare with empirical fits;
2. Investigate greybody factors for additional modifications;
3. Extend to different quantum well potentials for possible refinements.

This scaling factor provides a direct link between quantum mechanical tunneling models and black hole thermodynamics, reinforcing the analogy between the quantum well system and Hawking radiation.

9 Numerical matching of quantum well and black hole spectra

To further solidify the analogy between quantum well (QW) tunneling radiation and Hawking radiation, we numerically modeled both systems and compared their spectral irradiance. We found that the key to achieving a one-to-one correspondence between the two emission spectra is the alignment of their effective temperatures. The spectra were generated using Mathematica with a custom script aligning quantum well Rs with a black hole mass satisfying $T_{\text{QW}} = T_{\text{BH}}$.

9.1 Temperature matching and mass scaling

The Hawking temperature of a Schwarzschild black hole is given by:

$$T_{\text{BH}} = \frac{\hbar c^3}{8\pi G M k_B} , \tag{53}$$

where M is the black hole mass. For the quantum well, we define an effective temperature based on the tunneling depth:

$$T_{\text{QW}} = \frac{V_0}{k_B} \frac{1}{R_s \times 10^7} , \tag{54}$$

where V_0 is the barrier height in joules, and R_s is the width of the well's interior region in meters. To compare both systems at equal thermal scales, we solve for the black hole mass that would yield the same temperature as a quantum well with $R_s = 10^{-13}$ m:

$$M = \frac{\hbar c^3}{8\pi G k_B T_{\text{QW}}} . \tag{55}$$

Substituting T_{QW} from above leads to:

$$M = \frac{\hbar c^3 R_s \times 10^7}{8\pi G V_0} . \tag{56}$$

This mass, which we call the *quantum-scale black hole*, emits thermal radiation with a spectral profile nearly identical to the mixed photon-fermion quantum well.

9.2 Spectral comparison

We numerically computed the spectral irradiance for both systems over an extended frequency range. The black hole spectrum used the Planck distribution modulated by a greybody factor:

$$I_{\text{BH}}(\nu) \propto \left(1 - e^{-\left(\frac{\nu}{\nu_0}\right)^2}\right) \frac{\nu^3}{e^{\frac{h\nu}{k_B T}} - 1} , \tag{57}$$

with $\nu_0 = 10^{15}$ Hz, while the QW emission incorporated a photon-fermion mix factor $\eta = 0.7$, yielding:

$$I_{\text{QW}}(\nu) \propto \eta \frac{\nu^3}{e^{\frac{h\nu}{k_B T}} - 1} + (1-\eta) \frac{\nu^3}{e^{\frac{h\nu}{k_B T}} + 1} . \tag{58}$$

After normalization, the spectra matched almost perfectly across the frequency range $10^{16} - 5 \times 10^{22}$ Hz as can be seen in Fig. 7.

9.3 Interpretation and implications

This spectral equivalence implies that the thermal emission of a quantum well, when appropriately scaled, can numerically emulate the spectral form of Hawking radiation over a wide frequency range under appropriate scaling conditions. The black hole's greybody-modulated Planck spectrum and the quantum well's mixed photon-fermion output both emerge from a common thermodynamic behavior driven by temperature. The success of this match supports the hypothesis that Hawking-like emission may be understood as a quantum tunneling phenomenon, arising from energy barriers shaped either by curvature (as in gravity) or potential walls (as in confined systems).

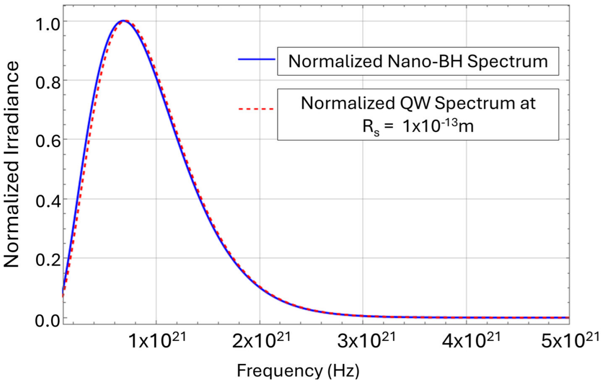

Fig. 7: Overlay of normalized spectral irradiance from a nano-scale black hole (blue) and quantum well with $R_s = 10^{-13}$ m (dashed red). Spectra match across full range when temperatures are matched.

This result also validates the use of effective temperature scaling as a bridge between gravitational and quantum systems, opening up the possibility for experimental analogs of black hole radiation in laboratory-scale quantum systems.

This successful overlap not only supports the validity of the quantum well model as a black hole analog, but also motivates further study of sub-Planckian black hole analogs using nanostructured materials.

10 Thermodynamic entropy of the quantum well

The tunneled energy is:

$$E_{\text{tunneled}} = \int_0^\infty I_{\text{tunneled}}(E)\, dE \approx \frac{8\pi^5 R^3 (k_B T)^4}{15 h^3 c^3}\,, \tag{59}$$

assuming $T(E) \approx 1$ near V_0. Using the first law of thermodynamics $S = \frac{E}{T}$, and multiplying by the surface area of the spherical horizon analog $4\pi R_s^2$, we define the entropy of the radiated quantum well system as:

$$S_{\text{QW}} = \frac{E_{\text{tunneled}}}{T} \times 4\pi R_s^2\,. \tag{60}$$

$$S_{\text{QW}} = \frac{E_{\text{tunneled}}}{T} \times 4\pi R_s^2 = \frac{32\pi^6 R^3 R_s^2 (k_B T)^3}{15 h^3 c^3}\,. \tag{61}$$

11 Bekenstein-Hawking entropy

The black hole entropy is [1]:

$$S_{\text{BH}} = \frac{k_B c^3 \times 4\pi R_s^2}{4 G \hbar}\,. \tag{62}$$

12 Comparing entropy scaling: QW vs. BH

Equating $S_{\text{QW}} = \alpha_S S_{\text{BH}}$:

$$\begin{aligned} \alpha_S &= \frac{32\pi^6 R^3 R_s^2 (k_B T)^3}{15 h^3 c^3} \times \frac{4 G\hbar}{k_B c^3 \times 4\pi R_s^2} \\ &= \frac{8\pi^5 G\hbar R^3 (k_B T)^3}{15 h^3 c^6}\,. \end{aligned} \tag{63}$$

This reflects differing dependencies on T and geometry.

13 Conclusion

This study presents a novel framework for modeling black hole thermodynamics using a finite spherical quantum well. By carefully engineering the potential profile and invoking quantum tunneling and statistical mechanics, we have shown that the quantum well's radiation spectrum can be numerically tuned to resemble the Hawking radiation spectrum of a Schwarzschild black hole. Both bosonic and fermionic emission modes were examined, and their spectral distributions were shown to replicate the expected Planckian and Fermi-Dirac forms, respectively.

A key result of this work is the identification of a universal scaling relation, $C_{\text{scale}} \sim 8\pi G/c^4$, which links the emission strength of the quantum well model to gravitational systems. This scaling is consistent with dimensional analysis and reflects core features of Einstein's field equations, suggesting a deep mathematical similarity between quantum mechanical and gravitational barrier processes.

Furthermore, we showed that by aligning the effective temperature of the quantum well with the Hawking temperature of a black hole of appropriately scaled mass, their normalized spectra become nearly indistinguishable across a broad frequency range. This spectral equivalence bridges curvature-induced radiation in general relativity with potential barrier-driven tunneling in quantum mechanics.

This work reproduces both the spectral and entropic characteristics of a Schwarzschild black hole. The spectral agreement spans multiple frequency decades under temperature-matched scaling, while the entropy expression mirrors the area dependence of the Bekenstein-Hawking formula. These results suggest that quantum confinement systems — when engineered with appropriate barriers — can serve as laboratory analogs for exploring black hole thermodynamics and emergent gravity phenomena.

The entropy comparison further strengthens this analogy. The derived entropy of the quantum well exhibits a geometric dependence and scaling relation analogous to the Bekenstein-Hawking formula, reinforcing the possibility that gravitational entropy could emerge from more fundamental quantum statistical principles.

These results invite further exploration into whether quantum wells and similar confined systems can be used to investigate other aspects of black hole physics, including information loss, near-horizon quantum behavior, or even entanglement entropy. The close match between emission spectra and entropy scaling also hints at possible links to holographic duality and emergent gravity frameworks, potentially allowing future investigations of gravitational principles in low-dimensional quantum systems.

From a practical standpoint, the tunability of quantum wells in nanostructured materials could enable controlled experiments that mimic black hole emission characteristics, providing a testbed for probing semiclassical predictions in table-top settings.

Future research directions include:

- Extending the model to relativistic quantum wells and incorporating spinor fields via the Dirac equation.
- Investigating the emergence of greybody-like corrections in more complex potential geometries.
- Exploring entanglement and scrambling in these systems to simulate aspects of the black hole information paradox.
- Embedding this framework into quantum simulation platforms, such as cold atoms or photonic crystals.

Analog gravity systems have been used to study Hawking radiation in fluids, optics, and Bose-Einstein condensates [3], but few have demonstrated entropy scaling or fermionic spectra as in our quantum well model. These findings open the door to an exciting interdisciplinary bridge — where insights from quantum mechanics, thermodynamics, and general relativity can be unified through experimentally accessible analog systems. As such, they contribute to the growing evidence that black hole thermodynamics may be deeply rooted in the quantum statistical behavior of bounded systems.

Our model further aligns with recent proposals suggesting black holes collapse quantum states at the fastest rate allowed by physics, functioning as ultimate decoherence devices [13]. The tunneling-induced decoherence in our analog quantum well provides a controllable platform to probe similar mechanisms in bounded quantum systems. Future extensions of the model may investigate time-reversed or dual potential profiles, potentially providing a conceptual analog to black hole-to-white hole transitions as proposed in recent quantum gravity scenarios [14, 15].

Acknowledgements

The author acknowledges Dr. James Miller at the University of Alabama in Huntsville for valuable discussions.

Submitted on July 3, 2025

References

1. Hawking S.W. Particle creation by black holes. *Communications in Mathematical Physics*, 1975, v. 43, no. 3, 199–220.
2. Unruh W.G. Experimental black-hole evaporation? *Physical Review Letters*, 1981, v. 46, no. 21, 1351–1353.
3. Barceló C., Liberati S., and Visser M. Analogue gravity. *Living Reviews in Relativity*, 2005, v. 8, no. 1, 12.
4. Foster J. and Nightingale J.D. A Short Course in General Relativity. Springer, New York, 1995.
5. Misner C.W., Thorne K.S., and Wheeler J.A. Gravitation. Princeton University Press, Princeton, NJ, 2017 (reprint of the 1973 edition).
6. Griffiths D.J. Introduction to Quantum Mechanics. 3rd ed., Cambridge University Press, Cambridge, UK, 2018.
7. Davies P.C.W. Quantum wells, wires and dots. In: *Encyclopedia of Applied Physics*, Wiley-VCH, 2003.
8. Chapra S.C. and Canale R.P. Numerical Methods for Engineers. 6th ed., McGraw-Hill, New York, 2007 (see Ch. 18: Boundary-Value and Eigenvalue Problems).
9. Landau L.D. and Lifshitz E.M. Quantum Mechanics: Non-Relativistic Theory. 3rd ed., Pergamon Press, Oxford, UK, 1977.
10. Mandl F. Statistical Physics. 2nd ed., Wiley, Chichester, UK, 2013.
11. Sakurai J.J. and Napolitano J. Modern Quantum Mechanics. 2nd ed., World Scientific, Singapore, 2011.
12. Hecht E. Optics. 5th ed., Pearson, Boston, MA, 2017.
13. Danielson D.L., Satishchandran G., and Wald R.M. Black holes decohere quantum superpositions. arXiv: 2205.06279 [gr-qc], 2022.
14. Han M., Rovelli C., and Soltani F. On the geometry of the black-to-white hole transition within a single asymptotic region. arXiv: 2302.03872 [gr-qc], 2023.
15. Bianchi E., Christodoulou M., D'Ambrosio F., Haggard H.M., and Rovelli C. White holes as remnants: A surprising scenario for the end of a black hole. arXiv: 1802.04264 [gr-qc], 2018.

Interpretation of Quantum Mechanics in Terms of Discrete Time III

Young Joo Noh
E-mail: yjnoh777@gmail.com, Seongnam, Korea

This paper approaches several fundamental problems in standard quantum mechanics, such as wave-particle duality and the measurement problem, through a new perspective of non-local waves [2]. I argue that these issues stem primarily from incomplete assumptions about physical reality in standard quantum mechanics and an exaggerated understanding of the superposition principle. Therefore, I am trying to solve the problems by extending quantum mechanics by newly establishing these concepts.

1 Introduction

Current quantum mechanics, despite its great success, has many problems in its understanding — wave-particle duality, measurement problems and the relationship between measurement and interaction, etc. One might consider these issues unimportant. But a theory lacking precise understanding naturally becomes harder to advance and should not be overlooked. Moreover, misunderstandings can hinder progress altogether.

In this paper, I will argue that many problems in current quantum mechanics are largely caused by two things: ontological assumptions about reality and an exaggerated understanding of the superposition principle. By addressing these, the paper aims to resolve inherent contradictions and show that the problems themselves may not persist under a new framework.

2 Assumptions about quantum mechanical reality

Wikipedia defines the quantum concept as follows: A quantum is the minimum amount of any physical entity (physical property) involved in an interaction.

This definition is quite appropriate. However, in this definition, the existing standard quantum mechanics seems to focus mainly on the meaning of "minimum amount of physical property". The truly important point that should not be overlooked in the definition of quantum is the part "involved in an interaction". If we pay attention to this point, we can naturally raise the following questions: If physical properties during interaction can only be measured in quantum, what is the physical reality before interaction? Since we cannot know the nature of matter except through interaction, we can only infer the reality of matter before interaction. But how is that inference being made now?

For light, the energy is quantized when interacting and exists in a local area, so its reality is inferred to be a lump like particle. However, since they also have a phase, the reality of photons is not clear. What is certain is that standard quantum mechanics defines the reality of photons by the characteristics that appear when they interact. Although this has some validity, it is still just a hypothesis, and reality may be different.

There is no way to know the reality of matter before observation. It is a kind of ontological assumption. However, no physical theory can proceed without assuming such a concept. Therefore, it is very important to think critically about such an assumption. I argue that many of the contradictory or difficult to understand concepts in standard quantum mechanics stem significantly from these assumptions about reality. To demonstrate this, I propose that adopting a new set of assumptions — based on non-local waves and discrete time [2] — eliminates these contradictions. By comparing phenomena explained under this new framework with those under standard quantum mechanics, I aim to validate this approach.

3 The meaning of the superposition principle from the perspective of discrete time

The superposition principle is one of the most important principles that form the basis of quantum mechanics. There are various interpretations of quantum mechanics, but they all have in common that they are based on the superposition principle.

The Schrödinger equation is linear, and the linear combinations of its solutions are also solutions. The solutions of the Schrödinger equation form a Hilbert space. Any arbitrary state of a physical system can be expressed as a linear combination of basis states in the Hilbert space. In other words, it is in a superposition state. In standard quantum mechanics, the macroscopic world is considered to be an extension of quantum mechanics, the superposition principle is considered a universal principle that applies regardless of the macroscopic world and the microscopic world.

However, the meaning of the superposition principle is quite different in the discrete-time perspective. In the discrete time perspective, the equations of electromagnetically interacting particles are determined by the following modified Dirac equation [4]. In (1), Δp_μ represents the change in energy momentum vector due to interaction during discrete time Δt

$$\mathrm{D_m}\Psi = \left(i\gamma^\mu\partial_\mu - f_{1r}\gamma^\mu p_\mu - f_{2r}\gamma^\mu\Delta p_\mu\right)\Psi = 0\,, \tag{1}$$

where

$$\left.\begin{aligned} f_{1r} &= \mathrm{Re}\, f_1 = \frac{1}{3}\,\mathrm{Re}\,\frac{\mathrm{e}^{-ix^\alpha p_\alpha}}{\mathrm{e}^{-ix^\alpha p_\alpha} + 2\left(\mathrm{e}^{-ix^\alpha \Delta p_\alpha} - 1\right)} \\ f_{2r} &= \mathrm{Re}\, f_2 = \frac{1}{3}\,\mathrm{Re}\,\frac{2\,\mathrm{e}^{-ix^\alpha \Delta p_\alpha}}{\mathrm{e}^{-ix^\alpha p_\alpha} + 2\left(\mathrm{e}^{-ix^\alpha \Delta p_\alpha} - 1\right)} \end{aligned}\right\}. \tag{2}$$

The Hamiltonian is [4]

$$\mathrm{H} = \vec{\alpha}\cdot\left(\vec{\mathrm{p}} - q'\vec{\mathrm{A}}\right) + \beta m' + q'\phi, \tag{3}$$

$$m' = f_{1r}\, m, \quad q' = (1 - f_{2r})\, q. \tag{4}$$

In (4), m and q represent the actual mass and charge of the matter, while m' and q' are the apparent values resulting from causal delay in discrete time. The reason apparent values differ from actual values is that the effect of causal delay is viewed from a dynamical perspective, as in (3). Let us explore the physical significance of the changes in mass and charge due to causal delay in more detail. For example, consider an electron in a hydrogen atom. The electron is subject to the Coulomb force. In continuous time, the electron's mass and charge are m and $-e$, respectively, i.e., the actual mass and charge. When discrete time is applied to the electron's motion under the same electric field, the change in the electron's velocity per unit time is smaller compared to the continuous time case. This implies an increase in mass for the mass term and a decrease in charge for the charge term. Since the effect of charge is much greater than that of mass in the motion of an electron within an atom, the energy of the electron in a hydrogen atom, when considering causal delay, will be smaller than the Coulomb energy. However, at the scale of the Bohr radius, this difference is extremely small, and as calculated in the previous paper, it is about 10^{-9} smaller than the Coulomb energy [3].

The modified Dirac equation (1) is also a linear equation of the first order. However, since m' and q' are quantities that depend on the interaction energy, (3) is a kind of recurrence equation. If the interactions are Δp_μ^1, Δp_μ^2, Δp_μ^3, … with a causal delay time Δt interval, and the Hamiltonians at each interaction are H_0, H_1, H_2, …, the following diagram can be expressed as

$$m_0', q_0'\,(\mathrm{H}_0) \overset{\Delta p_1}{\rightarrow} m_1', q_1'\,(\mathrm{H}_1) \overset{\Delta p_2}{\rightarrow} m_2', q_2'\,(\mathrm{H}_2) \overset{\Delta p_3}{\rightarrow} \ldots \tag{5}$$

$$\left.\begin{aligned} \mathrm{H}_0 &= \vec{\alpha}\cdot\left(\vec{\mathrm{p}} - q_0'\vec{\mathrm{A}}\right) + \beta m_0' + q_0'\phi \\ \mathrm{H}_1 &= \vec{\alpha}\cdot\left(\vec{\mathrm{p}} - q_1'\vec{\mathrm{A}}\right) + \beta m_1' + q_1'\phi \\ \mathrm{H}_2 &= \vec{\alpha}\cdot\left(\vec{\mathrm{p}} - q_2'\vec{\mathrm{A}}\right) + \beta m_2' + q_2'\phi \\ &\cdots\cdots\cdots\cdots\cdots \end{aligned}\right\}. \tag{6}$$

In (6), all $\mathrm{H_i}$ have their own Hilbert space. Since the Hilbert spaces of $\{\mathrm{H_i}\}$ are generally different, there is no unique Hilbert space that satisfies the entire system. This means that any arbitrary state cannot be expressed as a linear combination of basis vectors. Therefore, the superposition principle does not hold in general.

However, when the interaction is very small, (3) can be approximated as an eigenvalue problem in standard quantum mechanics, i.e., Hilbert space analysis is possible.

If $\Delta p_\mu \ll p_\mu$, then

$$m' \simeq \frac{1}{3}\, m, \quad q' \simeq \left(1 - \frac{2}{3}\cos\Delta x^\mu p_\mu\right) q. \tag{7}$$

For example, in the case of the electrons of a hydrogen atom, $\langle T\rangle = -\langle V\rangle/2 \sim O(m\alpha^2)$ and $\Delta t = 1/m$ [4], so

$$\Delta x^\mu p_\mu = \Delta t\left(E - \frac{\vec{\mathrm{p}}^2}{m}\right) = \Delta t\,(V - T) \sim O(\alpha^2). \tag{8}$$

Therefore, $\cos\Delta x^\mu p_\mu \sim \cos\alpha^2 \simeq 1$. Also, since the cosine function is constant near 0, we can say that the mass and charge are constant in (7). This fact means that in the case where the interaction is very small, (3) can be said to have a unique Hilbert space. In other words, (3) can be interpreted as an eigenvalue problem of the standard quantum mechanics.

To summarize, the superposition principle of the standard quantum mechanics is established only when the interaction is very small, and in this case, the system can be analyzed using the Hilbert space. However, in general cases, the Hilbert space cannot be applied, and Equation (1) merely carries the meaning of the wave equation.

4 Double slit experiment

The double-slit experiment is a simple yet practical experiment that clearly reveals the strangeness of quantum mechanical reality. Since there are various theories for interpreting quantum mechanics, there may be various perspectives on the interpretation of the double-slit experiment, but here we will compare the standard quantum mechanical interpretation and the perspective of non-local waves in the perspective of discrete time.

When a single photon is fired toward a double slit, it passes through the slits and is detected at a single point on the screen. However, if photons are fired sequentially, an interference pattern forms on the screen. From the perspective of the standard quantum mechanical view of reality, this requires the existence of a state in which a single photon passes through both slits simultaneously. In other words, the superposition principle is necessary. If the states passing through each slit are ψ_1 and ψ_2, the interference state on the screen is $\psi_1 + \psi_2$, and its probability is given by the Born rule as $|\psi_1 + \psi_2|^2$. The view of reality underlying this explanation assumes that a photon is a localized particle-like entity with a phase.

Now, let us explain this in terms of non-local waves defined in discrete time. Non-local waves propagate and produce interference phenomena similarly to local waves, but their wavefront collapses simultaneously at a single point on the screen. The wave passing through the double slits interferes on the screen, which is consistent with the behavior of local waves up to this point. However, a non-local wave behaves as if it causes the photoelectric effect as a single photon due to wave collapse from inelastic collisions with electrons of the atoms constituting the screen. The location of this reaction is determined by a probability proportional to the square of the interference amplitude. In other words, the Born rule still holds for non-local waves. In standard quantum mechanics, the square of the amplitude represents the probability of detecting a particle, whereas, in the non-local wave perspective, it represents the probability of wave collapse occurring at that point.

If the measuring device is placed at one of the double slits, the interference pattern disappears. From the conventional viewpoint, it is explained that interference does not occur because there is no state of passing through both slits at the same time. From the non-local wave viewpoint, the wave collapses due to an inelastic collision at the measuring device, and the wave proceeds again from that collapsed state, so it will have the same effect as a single slit.

The above discussion briefly examines the explanations of the double slit experiment from the two perspectives. While there is a clear difference in their views of reality, both perspectives explain the experimental results without significant issues.

5 Delayed choice experiment — wave-particle duality

The problem of wave-particle duality is a somewhat old problem in quantum mechanics, but it needs to be discussed because it raises doubts about physical reality. When discussing wave-particle duality, the concepts of wave and particle are somewhat traditional. It is somewhat different from the concept of reality used in the double-slit experiment.

There are various versions of the delayed choice experiment, but here we will first discuss the double-slit experiment proposed by Wheeler [6]. In this experiment, the light measuring device is a plate and photodetectors. The plate measures the interference pattern caused by the interference of light passing through both slits, and the photodetectors are placed facing the two slits to measure which slit the photon passes through. In other words, the former measures the wave nature of light, and the latter measures the particle nature of light. The point of this experiment is to figure out when light decides whether it behaves as a wave or a particle. It is assumed that its reality will be determined after passing through the double slits, but this thought experiment shows that this is contradictory. To see this, you have to choose the measuring device after the light passes through the double slits. Even then, if you choose the plate, you will still observe the interference pattern on the plate, and if you choose the photodetector, you will observe the particle impact.

As a simpler and more meaningful thought experiment, consider the split beam experiment introduced by Wheeler.

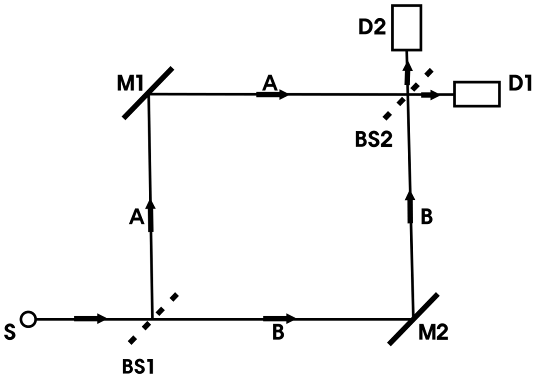

Fig. 1: Mach–Zehnder interferometer.

The experimental description of Fig. 1 is as follows

1. A single photon is emitted from a pulsating source of light S;
2. This photon reaches a semitransparent mirror BS1 and splits into two paths;
3. The first path goes to a perfectly reflective mirror M1, and the second path goes to a perfectly reflective mirror M2;
4. M1 and M2 reflect their respective beams so that they merge back together;
5. The two beams meet at a semitransparent mirror BS2, and photodetectors D1 and D2 are arranged to record the interference pattern between the two beams.

However, if the semitransparent mirror BS2 is removed during the experiment, the situation changes. Without BS2, the two beams do not merge, but proceed separately, and are directed to photodetectors D1 and D2, respectively. At this time, D1 detects the photon coming from the path through A, and D2 detects the photon coming from the path through B. In this case, the interference pattern disappears, and it is clear which path the photon took.

The key to this experiment is that after the photon passes through the semitransparent mirror BS1, the observer can choose whether to remove BS2 or leave it. If BS2 is left, an interference pattern is observed, and if it is removed, the path information is revealed.

The above thought experiments summarize that the reality of light is not determined while it is in motion, but is determined at the last moment of measurement. Wheeler says, "*No phenomenon is a phenomenon until it is an observed phenomenon*". Physical reality is not determined until it is observed, and the past is determined by observation. Reality is formed by the interaction with the observer.

Now, let us interpret these thought experiments from the perspective of non-local wave. In the discrete time perspective, it is assumed that the physical reality before measurement exists in the form of a non-local wave, and the simultaneous wave collapse caused by interaction possesses quantum properties.

First, in the double-slit experiment, choosing a plate or photodetectors as the measurement device, even if the choice is made after the light passes through the double slits, has no effect on the reality of the light as a non-local wave. A non-local wave simply causes wave collapse at the plate if a plate is present, or at the photodetector if a photodetector is present. As previously explained, wave collapse at the plate occurs with a probability proportional to the square of the interference wave's amplitude, resulting in an interference pattern. A non-local wave entering the photodetectors has an equal probability of wave collapse at each photodetector, but if wave collapse occurs at one photodetector, the collapse property of the non-local wave ensures that no observation occurs at the other detector. However, observing a wave collapse at one photodetector does not mean the light passed through a specific slit. The non-local wave always passes through both slits. Even if the photodetectors are sufficiently far from the double slits to neglect interference effects, if no collapse occurs in between, a measurement will occur at one of the photodetectors.

Next, let us consider the beam-splitter experiment. The non-local wave emitted from the light source is equally split into two paths at the partially transparent mirror BS1. The non-local waves traveling along each path meet at the partially transparent mirror BS2, where they interfere, causing a wave collapse at D1 due to constructive interference, resulting in observation. If BS2 is removed, the split light from each path reaches D1 and D2. In this case, the probability of wave collapse at each detector is 50%, so a photon is observed at either D1 or D2. Observing a photon at D1 or D2 does not mean the light traveled through a specific single path. The non-local wave passes through both paths. The fact that it is observed at only one detector is due to the collapse property of the non-local wave. The delayed choice of the measurement device made while the non-local wave travels through both paths has no effect on the physical reality of the non-local wave. The non-local wave simply undergoes wave collapse due to interaction at the measurement device.

It is indeed difficult to explain the delayed-choice experiment using the conventional concepts of waves or particles. These concepts cannot define the physical reality before observation. However, as pointed out in the previous paper, the conventional concepts of waves and particles are physical realities inferred from the macroscopic world [1]. The logic of the delayed-choice experiment, which suggests that these concepts cannot define the microscopic world before observation, is valid. However, interpreting this to mean that no determined physical reality independent of observation exists in the microscopic world is an excessive leap in logic. It is merely that the conventional concepts of waves and particles cannot define it. This paper proposes non-local waves as an alternative.

Local conservation of energy

The concept of local conservation of energy is one of the most important concepts in physics, encompassing both classical mechanics and quantum mechanics. However, this concept requires a rigorous definition when applied to the microscopic world. The wave-particle duality in the microscopic world and the concept of local conservation of energy can lead to contradictory situations.

The definitions of energy and momentum are established through interactions. These concepts may apply prior to interactions, but they can also be seen as emerging during interactions. In classical mechanics, they are always defined regardless of interactions, and the law of local conservation holds. However, in quantum mechanics, there is an issue.

Quantum mechanical reality possesses both wave and particle properties. Let us first consider the wave. Can a wave possess energy? Naturally, the energy of a photon is defined as $E = h\nu$. However, this is a concept associated with a particle. A wave spreads and propagates through space. If energy were defined for a wave, the energy of its local parts would need to be defined, which cannot explain the quantization of energy during interactions.* Furthermore, if momentum were defined for a wave, the concept of accelerated motion would need to be defined for the wave. A wave is a physical reality that propagates and interferes, not a concept that accelerates like a particle. Consequently, the concept of mass cannot be defined for a wave. Next, let us consider particle properties. A particle can naturally have mass defined. However, defining frequency or wavelength for a particle is not reasonable.

Synthesizing the above, energy and momentum cannot be defined for a wave, and frequency and wavelength cannot be defined for a particle. However, all these concepts are necessary to describe the microscopic world. The microscopic world exhibits wave-like properties at times and particle-like properties at others. However, these two properties never manifest simultaneously. This suggests that some form of transition occurs between wave-like and particle-like properties. Thus, the equation $E = h\nu$ can be interpreted as indicating that light, as a wave with frequency ν, transitions into a particle-like photon with energy $h\nu$. Here, the Planck constant can be understood as representing a kind of exchange ratio during this transition. Since this exchange ratio is constant, energy is consequently conserved. However, its meaning differs from the local energy conservation in classical mechanics.

The concept of transition between wave and particle discussed above is merely an inference derived from quantum

---

*In the quantum field theory, this issue is addressed by introducing the mathematical assumption of second quantization, but this is an entirely different approach.

mechanical phenomena and the definitions of wave and particle concepts. A model that aligns with this inference is the non-local wave. If the concept of energy conservation in the microscopic world is defined as above, the issue of local energy conservation arising from the instantaneous collapse of a local wave does not occur in the collapse of a non-local wave.

6 Interaction free measurement

Interaction-free measurements were first proposed in the Renninger negative-result experiment and developed into the Elitzur-Vaidman Bomb Tester [8]. This thought experiment vividly illustrates how our notions of physical reality significantly influence the understanding of phenomena. The components of this experiment are as follows. It uses the Mach-Zehnder Interferometer shown in Fig. 1 and applies the concept of physical reality from standard quantum mechanics. The bomb is placed in path B and explodes upon interaction with a photon. The bomb can be in a "live" (functional) or "dummy" (non-functional) state.

How the interferometer works:

1. The photon splits into two paths (A and B) at BS1;
2. Along each path, it passes through mirrors (M1, M2) and is recombined at BS2;
3. At BS2, the photon is designed to reach only a specific detector (D1 or D2) due to interference effects. For example, if the interferometer is well tuned, the photon will always reach D1 and never reach D2.

The key to this experiment is to obtain information about whether a bomb is on path B without having the bomb directly interact with the photons (i.e. explode).

(1) In the absence of a bomb

When a photon reaches BS1, the wave function splits into two paths, A and B. The photon travels along the two paths and rejoins at BS2. Due to the interference effect, the photon always reaches D1 and never reaches D2. This is because constructive interference occurs at D1.

(2) If there is a bomb (live bomb)

Let us assume that there is a functional bomb in path B. This bomb explodes with 100% probability if it absorbs a photon. When a photon passes through BS1, the wave function still splits into two paths. However, if the photon interacts with the bomb in path B, an explosion occurs, and it is not observed at the detectors. This case occurs with a 50% probability (the probability that the photon chooses path B).

Conversely, if the photon chooses path A (50% probability), it does not interact with the bomb. In this case, the wave function collapses to path A. The photon then travels along path A and reaches BS2. BS2 splits the photon again with a 50:50 probability, sending it to either D1 or D2. Thus, the photon reaches D1 with a 25% probability and D2 with a 25% probability.

(3) In the case of a bomb (dummy bomb)

The dummy bomb has no sensors in the path of the photon. Therefore, it does not interact with the photon and behaves the same as in the case without the bomb. The photon always reaches D1 and never goes to D2 due to interference effects.

The critical aspect of this experiment is the detection result at D2. If D2 clicks, it definitively indicates that the bomb is in a live state, yet the photon did not interact with the bomb at all during this process. This is because the photon took path A, so it had no opportunity to encounter the bomb. However, the presence of the bomb (in its live state) eliminates the wave function component in path B, disrupting the interference and creating the possibility for D2 to click. In other words, the mere existence of the bomb induces the collapse of the wave function, altering the interference pattern. This conclusion demonstrates that measurement does not necessarily require a physical interaction between the particle and the detector.

The above is the conventional interpretation of the Elitzur-Vaidman Bomb Tester. However, before reaching such a conclusion, we must consider the quantum mechanical reality assumed in this interpretation. The non-local wave hypothesis offers a completely different interpretation of this experiment. In conclusion, all measurements originate from interactions.

The non-local wave incident on BS1 is divided into two paths:

(1) If there is no bomb, the waves passing through each path interfere at BS2, and due to constructive interference, wave collapse occurs at D1, where the photon is observed;

(2) If there is a bomb, the probability that wave collapse will occur by reacting with the bomb in path B is 50% because the wave is divided into two paths. When wave collapse occurs, the wave traveling along path A disappears simultaneously and acts as a single photon in the bomb. In this case, photon cannot be observed in either D1 or D2.

So, what happens in the remaining 50% probability where collapse does not occur? The collapse of a non-local wave occurs when an energy change is induced by an inelastic collision [2]. If the wave incident on the bomb undergoes elastic collision, there is no energy change, and thus, the photoelectric effect caused by light does not occur at the bomb's sensor. Naturally, this case does not result in an explosion. If only path B existed without path A, the bomb's sensitivity is assumed to be 100%, meaning it would definitely explode. However, with path A present, only 50% of the wave passes through path B, so the probability of the bomb exploding is also 50%. This eliminates the need to redefine a new probability for the bomb's sensor to trigger an explosion. Therefore, in the 50% probability where an explosion does not occur, 50% of the wave travels along path A, and the remaining 50% undergoes elastic scattering at the bomb. The 50% that travels along path A reaches BS2, where it is split into D1 and D2 with a 25% probability each, and wave collapse occurs at one of the detectors with a 25% probability. The 25% probability of wave collapse occurs because only 25% of the original wave reaches the detector. When a non-local wave collapses, all wavefronts collapse simultaneously at a single point. The location of the remaining 75% of the wave is irrelevant. Consequently, interactions always occur in quantum units.

(3) In the case of a dummy bomb, as discussed above, photons will be observed at D1 by constructive interference, just as in the case of no bomb.

The crucial point in the above discussion is that the photon observed at D2 with a 25% probability is not devoid of interaction with the bomb. The light that splits at BS1 and travels along path B undergoes an interaction with the bomb through elastic scattering. According to the conventional view of reality in standard quantum mechanics, it is interpreted as having no interaction, but from the perspective of non-local waves, an interaction is considered to have occurred.

7 Measurement problem

According to standard quantum mechanics, the state of any physical system defined in a Hilbert space can be represented as a superposition of basis states, and this state evolves deterministically according to the Schrödinger equation. However, measurement causes the system's state to collapse into a single basis state. This process occurs probabilistically according to the Born rule and is a non-unitary process that is not predicted by the Schrödinger equation. Yet, this measurement principle is empirically based, and its foundation remains unclear. Currently, various interpretations, from objective collapse theories to epistemological interpretations, attempt to explain it, but none are definitive.

In contrast, from the new perspective of non-local waves in discrete time, the superposition principle does not generally hold. The system's state cannot be represented as a linear combination of basis states in a unique Hilbert space. The state of a single-particle system, before interaction, is a uniquely determined non-local wave. When the wave collapses due to an interaction accompanied by an energy change, it becomes a Compton sphere with a determined mass and size. Therefore, from this perspective, the measurement problem itself does not arise.

As suggested in the previous paper, quantum waves do not exist in systems above the Planck mass [1]. Thus, discussing superposition for physical objects in the macroscopic world is meaningless. That is, Schrödinger's cat is not a controversial issue at all.

8 Conclusions

The title of this series of papers, "Interpretation of Quantum Mechanics", may seem somewhat inappropriate. While the various existing interpretations of quantum mechanics differ significantly in their perspectives, they share a common foundation: the superposition principle, one of the most fundamental axioms of standard quantum mechanics. However, in the discrete time perspective, the superposition principle generally does not hold, making many claims in these papers appear to fall outside the scope of quantum mechanics. Nevertheless, even though the superposition principle does not generally apply, it is approximately satisfied in systems with very small interactions, so this can be seen as an extension of standard quantum mechanics.

This paper argues that many problems in standard quantum mechanics stem from two main aspects. The first is the ontological assumption about physical reality. The way physical reality is perceived fundamentally alters the physical interpretation of phenomena and the direction of research.

The second issue is the superposition principle. This principle is the most important in quantum mechanics but also causes several problems. However, in the discrete time perspective, this principle is considered to hold only in specific cases in the microscopic world, so the measurement problem, as seen in standard quantum mechanics, does not exist.

Let us consider another example where these two aspects are prominently revealed. Recall the double-slit experiment discussed earlier. According to the conventional view of reality, a state exists where a particle passes through both slits simultaneously, necessitating consideration of a superposition state of gravity caused by the particle. This leads to the need for a theory of quantum gravity. The assumptions underlying this logic are the ontological assumption about matter before interaction — namely, that matter is a localized entity with particle-like properties — and the superposition principle. In other words, the notion is that matter before observation can exist in "this place" and "that place" simultaneously. However, as argued in this paper, if these two assumptions are incorrect, this notion does not hold, and consequently, the necessity for a quantum gravity theory is significantly reduced.

On the other hand, what about the non-local wave perspective? When a non-local wave passes through the double slits, it is a determined wave, and the concept of a superposition state is unnecessary. In the case of matter, when the non-local wave collapses to form a Compton sphere, the collapse position is probabilistically determined by the Born rule, and this sphere has a determined mass and size. Therefore, from this perspective, the concept of a superposition state of gravity does not apply.

Submitted on July 26, 2025

References

1. Noh Y. J. Interpretation of Quantum Mechanics in terms of Discrete Time II. *Progress in Physics*, 2024, v. 20, 21–23.

2. Noh Y. J. Interpretation of Quantum Mechanics in terms of Discrete Time I. *Progress in Physics*, 2023, v. 19, 109–114.
3. Noh Y. J. Lamb shift in Discrete Time. *Progress in Physics*, 2022, v. 18, 126–130.
4. Noh Y. J. Anomalous magnetic moment in Discrete Time. *Progress in Physics*, 2021, v. 17, 207–209.
5. Noh Y. J. Propagation of a particle in Discrete Time. *Progress in Physics*, 2020, v. 16, 116–122.
6. Wheeler J. A. The "past" and the "delayed-choice" double-slit experiment. *Mathematical Foundations of Quantum Theory*, edited by A. R. Marlow, Academic Press, New York, 1978, 9–48.
7. Dirac P. A. M. The Principles of Quantum Mechanics. Oxford University Press, 1958.
8. Elitzur A., Vaidman L. Quantum mechanical interaction-free measurements. *Foundations of Physics*, 1993, v.23, 987–997.
9. Hance J. R., Hossenfelder S. What does it take to solve the measurement problem? arXiv: quant-ph.2206.10445v3.

Observing Electric Currents in Space

Michael Clarage

Independent Researcher, Boston, MA, USA.
E-mail: michael.clarage@protonmail.com

To find evidence for electric currents in cosmic plasmas requires both that the currents be looked for, and that data be available to indicate their presence. This paper focuses on the second requirement, the available data, and how the flow of electric current in plasmas naturally will be difficult to observe from a distance. Coaxial current flow predicted and observed in plasmas is examined in some detail showing that even very large total current flows can give, when seen from a distance, very little signal. Examples are given from active galactic nuclei, planetary magnetospheres, and plasma ejections from moons. Suggestions are given for how to analyze existing astrophysical data and also for new measurements to be made that will show the presence of cosmic electric currents.

1 Introduction

In 1977, Hannes Alfven [1] wrote that at the galactic scale, electric currents of 10^{17}-10^{19} amperes would be natural. Forty years later measured estimates are of 10^{18} amperes in jets from active galactic nuclei [2, 3]. The accuracy of the 1977 prediction, so far in advance of observation, is a strong testament to Alfven and his colleagues, and an indication that more attention should be given to their work.

Kristian Birkeland is often credited with first describing cosmic electric currents in his 1908 model of electric currents flowing from the Sun to the Earth causing the aurora borealis [4]. For 60 years, Birkeland's theory of large-scale electrical connection was ignored in favor of the mathematical models of Sydney Chapman, where planets are electrically insulated from the Sun and solar wind.

The first in-situ measurements of cosmic-scaled electric currents were provided by Zmuda *et al* [5] with a single axis magnetometer on board the navigation satellite 1963–1938C. Today the presence of cosmic electric currents is acknowledged, but the debate remains if the electric fields and currents can be causal, or are merely a consequence of thermodynamic and ponderomotive processes.

Electric current flow in a coaxial configuration was first described in Oliver Heaviside's 1880 patent [6]. Attempted telegraph cables that sent current in only one direction required more energy and incurred substantial information loss compared to cables with a built-in design to accommodate a return current.

Coaxial current flow, now commonplace to the electrical engineer, is a new idea to many in the astronomical community. This paper will elaborate the morphology of electric current flow in low density plasmas, and present several examples observed in cosmic plasmas. The argument is advanced that coaxial current flow is to be expected in cosmic plasmas, though its presence will be difficult to observe remotely. The paper will conclude with suggested observations needed to advance this topic.

2 The magnitude of cosmic electric currents

When electric current flows through astronomical plasmas there must be an electric field that is causing the electric charges to move. The movement of charge will create a circular magnetic field which will constrict the flow of charges into a narrow line. Gravitational attraction will condense the mass of the plasma. The mass of the plasma will be dissipated and expanded by random thermal motions and by the total energy stored in the magnetic field. When all these forces are in a stable state, we set the energies that condense equal to the energies that expand.

Consider an electric current flowing along a tube through a cosmic plasma, the width of the tube is R_0 [7, see eq 2.52]. These expressions are in units of energy per unit length:

$$\frac{\mu_0}{8\pi}\, I^2(R_0) + \frac{1}{2}\, Gm^2 N^2(R_0) = \Delta W_{B_z} + \Delta W_k\,. \tag{1}$$

The integrated linear current density out to radius R_0 is given by I; m is the mean particle mass averaged over electrons, ions, and neutral particles; N is the integrated linear particle number out to radius R_0; ΔW_{B_z} is the difference of magnetic field energy between the total energy inside the tube and that at the boundary of the tube; ΔW_k is the difference of kinetic energy between the total inside the tube and that at the boundary of the tube.

This formulation was proposed by Carlqvist in 1988 [8], showing the relative importance of the electromagnetic force, gravitational force, and thermal motions for any given cosmic plasma setting. Using this relation, Alfven and Carlqvist argue we should expect above the Earth currents on the order of 1.0–10.0 million amperes, which the Iridium satellite network has verified [9]. The relation (1) implies that sunspots and coronal loops should have currents on the order of 10^{11} amps.

Since no satellites yet fly through coronal loops, the magnitude of electric currents are inferred from magnetic fields which are inferred from the polarization of light coming from the regions. Such modelling shows electric currents on the

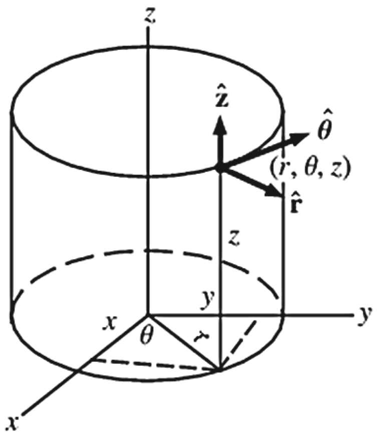

Fig. 1: Geometry for viewing an idealized current flow. Filament runs along the z-axis. Viewer is far away along the y-axis. The $x - z$ plane is the plane of the sky.

order of 10^{11} amperes. For the magnitude of electric current flowing through an entire star — which can be defined as the gravitating mass and the larger magnetic body of the heliosphere — the Carlqvist relation predicts currents on the order of 10^9 amps. This number has been confirmed for the electric current flowing into the Sun along the heliospheric current sheet [10]. The magnitude of the heliospheric current sheet is not directly measured, our existing satellite sensors cannot identify such a low current density, but is inferred from the magnetic fields that exist above and below the plane of the solar system. During the course of the 22-year solar cycle, electric current flows alternately inward/outward radially along the equator, and outward/inward from each pole, closing at the heliosphere, or in some models continuing to the interstellar medium.

Within the interstellar medium, the Carlqvist relation predicts electric currents on the order of 10^{14} amperes. The Planck, Herschel, and SOFIA telescopes have greatly increased the available data for the interstellar medium. Verschuur recently calculated currents of 10^{14} amperes in the A0 molecular cloud through neutral hydrogen emission measurements [11]. Stars form along filaments, the filaments extend for hundreds of light-years without broadening, filaments have a trunk-and-branch morphology, the filaments abruptly change direction at bright points, and different molecular species and energy states are segregated within the filaments. These are all features to be expected from electric currents in a plasma. The cause of these features is not primarily due to gravity.

At the galactic scale, Alfven proposed electric currents should be on the order of 10^{18} amps, from a balance of magnetic pressure, thermal expansion, gravity, and helical magnetic fields. Works by Kronberg and Lovelace [2] and Gabuzda [3] have deduced 10^{18} amperes of current flowing into and out of galaxies in a columnar form. The technique relies on measuring the polarization of light coming from the regions of these jets.

3 Measuring cosmic currents

3.1 Model

In 1950, Lundqvist proposed a force-free current flow in a plasma, meaning that the electric current flowing through the plasma feels no Lorentz force from ambient magnetic fields [12, 13]. This is a very special case, maybe never actually realized in nature, but if there is any truth in the model, it will give predictive power and new insights. In such a lowest energy configuration, the current and magnetic field must be flowing in the same direction. This arrangement of current and magnetic field seen in the force-free flow is much more complicated than a single wire carrying a current with the azimuthal magnetic field curling around.

In equation form, we write for the force-free condition

$$\mu \vec{J} = \alpha \vec{B}\,, \tag{2}$$

where μ and α are scalars which possibly depend upon position and plasma characteristics. $\vec{J}$ is the electric current density vector. $\vec{B}$ is the magnetic field vector. Scott [14] extended Lundqvist's model to values of radius large enough to see reversals of both magnetic and current directions. In the simplest case of current flow in cylindrical symmetry, the solutions to a force-free state are given by Bessel functions J_0 and J_1:

$$B_z(r) = B_z(0)\, J_0(\alpha r)\,, \tag{3}$$

$$B_\theta(r) = B_z(0)\, J_1(\alpha r)\,, \tag{4}$$

$$j_z(r) = \frac{\alpha B_z(0)}{\mu}\, J_0(\alpha r)\,, \tag{5}$$

$$j_\theta(r) = \frac{\alpha B_z(0)}{\mu}\, J_1(\alpha r)\,, \tag{6}$$

where (B_z, B_θ) and (j_z, j_θ) are the (z, θ) directions of the magnetic field and electric current density.

If the electric current is to be in a lowest energy configuration, the electric current and magnetic field flow *in the same direction*, and form a series of concentric shells, like multiple coaxial cables. With increasing R, the current and magnetic field, both pointing in the same direction, twist and eventually flow back in the opposite direction (see Fig 2). That a return current will be present in a lowest energy configuration harkens back to Heaviside's telegraph equation showing that a unidirectional current requires more energy and loses information.

With increasing total current, the direction of flow will again reverse itself, flowing in the direction of the center core. The exact physical conditions that dictate the number of reversals is not yet known. Some magnetic clouds at 1 AU show single reversals with 10^9 ampere currents [15]. Single reversals — simple coaxial — are seen in 10^{18} ampere galactic jets, while multiple reversals are seen in 10^{10} ampere polar currents on Earth. Hence magnitude of current is

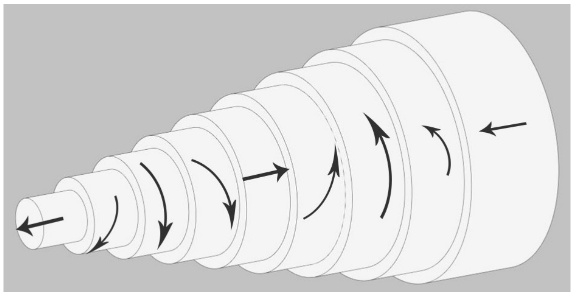

Fig. 2: Coaxial current flow in plasma with multiple reversals. Arrows represent the direction of the magnetic field and the electric current. The magnitudes are given by Eqs. (3)–(6).

not the only factor determining if current is unidirectional or if there is also a return current. The reverse current is also seen in particle-in-cell simulations, where a current injected into a plasma can only continue if a return current is created [7, p. 75].

3.2 Applying the model

Filaments are ubiquitous in the interstellar medium, see Fig. 3 for an example. The Herschel and Planck telescope projects are repositories for hundreds of such images. If electric currents were flowing through the filament, and were doing so according to the coaxial model, how would such a morphology be detected? We will look at several detection techniques: polarization changes due to magnetic fields, Doppler shifts due to relative motion, and segregation of atoms and molecules by ionization potential.

Consider a coaxial filament, with current flow along the z-direction, as shown in Fig 1. The viewer stands far away on the y-axis. The $x - z$ plane is the plane of the sky. We are looking "side-on" towards the filament. Interesting measurements such as changes in light polarization or Doppler shift will depend upon the integrated magnetic field along our line of sight.

We first consider a filament that has current flowing only in one direction, with no return current. Fig. 4 shows the numerically integrated projection of the components of the magnetic field along the y-axis, that is, the line of sight while looking through the filament. For any given point in the filament, the horizontal component of the magnetic field B_x will have a mirror point in front or behind the center which has the opposite horizontal component. Hence all B_x fields will tend to cancel. The B_y values have a different symmetry: fields pointing away on one side of the center will point towards us on the other side of the filament. This is shown in Fig. 4 where the B_y component changes sign on either side of the center. The B_z component will always flow in the positive direction, but drops off to zero at the outer boundary as the flow rotates to a purely azimuthal direction.

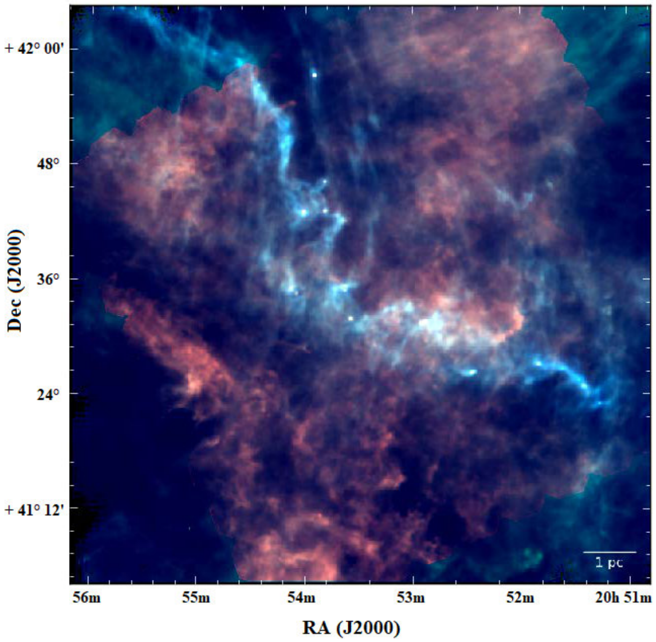

Fig. 3: Gas cloud G82.65-2.00 as seen by the Herschel telescope. RGB image, the colours correspond to Herschel channels at 160 nm (red), 250 nm (green), and 350 nm (blue). Credit ESA/Herschel/M. Juvela [16].

Next consider a current flow with a coaxial return flow, Fig. 5. The central current flow in the positive z-direction is surrounded by a return flow in the negative z-direction. The projection of the magnetic field components is shown. The same symmetries apply as in the previous case, but with more reversals. Figures 4 and 5 were solved on the same scale.

Applying this to telescope observations, low intensity current flow, Fig. 4, will have magnetic fields close to the filament that are parallel to the filament. Those parallel fields will decrease in intensity at the boundary of the filament. More intense current flow, Fig. 5, will show fields along the filament to reverse direction. Observations highlighting the B_y component will appear in Doppler shifts, since flowing charged particles will drag neutral particles. From the observer's point of view, the azimuthal flow around the filament axis will be moving away from the observer on one side of the filament and moving towards the observer on the other side. Look for opposite Doppler shifts on either side of the filament center.

Additional observations should focus on spatial segregation of atoms and molecules. The current flow in the force-free model is also very efficient at collecting ions into shells segregated by ionization potential, see [17]. Spectrographic data can be examined to look for atoms and molecules with low ionization potential collecting near the center of the filament and high ionization potential species concentrated on the periphery.

The ongoing debate as to whether magnetic fields are aligned with or perpendicular to interstellar molecular fila-

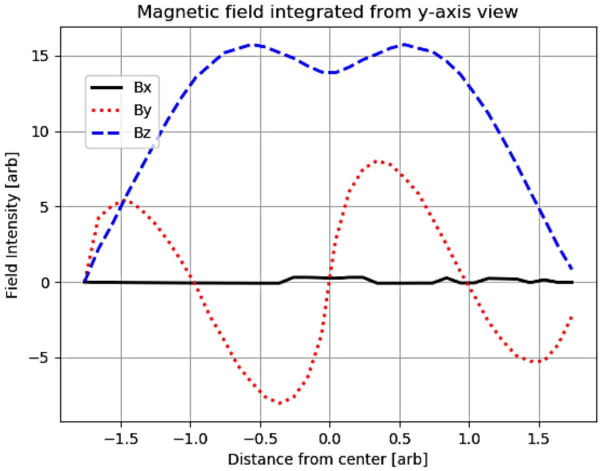

Fig. 4: The x, y, z-components of the integrated magnetic field seen from standing on the y-axis. There is no return current.

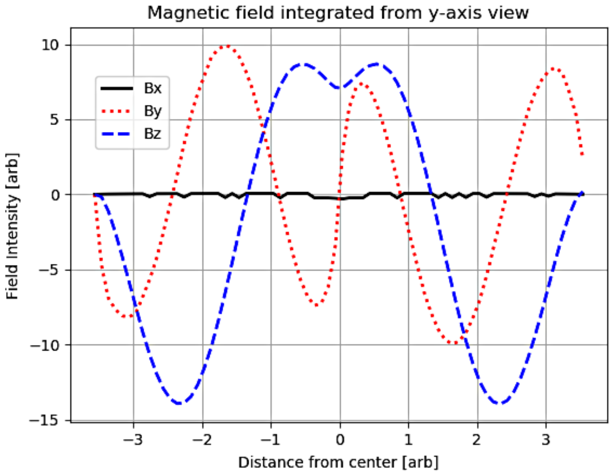

Fig. 5: Same as Fig. 4 but with a return current, that is, a simple coaxial current flow.

ments is rooted in the fact that both are true. The general form of cosmic currents and their associated magnetic fields will be coaxial, with directions constantly shifting from parallel, perpendicular, to anti-parallel, with the number of reversals dependent upon the setting.

As an example on a smaller scale, the polar electric currents on Earth form concentric shells, with the number of shells increasing with the current, see Fig. 6. Imagine trying to estimate the electric current flow in the Earth's aurora, but doing so by observing shifts in the polarization of light passing through the aurora.

When viewed from outside the Earth, the net change in polarization due to magnetic fields will be close to zero. Hence a current flow of billions of amperes can result in very little net change of polarization, and lead to the conclusion that no appreciable electric current exists in the Earth's aurora. It is arguable that planetary polar currents have underlying physics different from the model presented in this paper. If that is so, they still provide a clear example of how increased current causes additional counter-flowing shells and how remote sensing will greatly underestimate the actual current flowing.

The Cassini probe provides another example of how a large current flow can be seen as very small when viewed from a distance. When the Cassini probe flew through the plumes of Enceladus, the Langmuir probe, while flying through the plumes, measured charge densities indicating 10^7 amps of current flowing from the moon towards Saturn. But the magnetometer aboard, measuring from a distance, only measured a magnetic field that would be produced by 10^5 amps. Farrell *et al.* [18] suggest that an ion dust sheath forms around the central flow of electrons, which serves to shield the bulk of current flow. But is is unlikely that these ions are stationary, and more likely that they form a return current of a force-free Birkeland current.

Regardless, this represents a clear case where the electric current inferred from a distance is 1/100th that found through direct measurement. When viewed from the outside, magnetic fields produced by the main central flow will be partly cancelled by the outer sheath flowing in the opposite direction. Remote sensing tends to show only the net current, which in many cases will be much smaller than the number of charges flowing.

The methods described in this paper provide clear qualitative criteria for identifying force-free currents in cosmic plasmas. The more quantitative Carlqvist relation (1) can be used in a wide variety of cosmic settings. We suggest that the voluminous data of filaments in the interstellar medium available in Herschel, Planck, VLA, HI4PI, and other surveys be examined using the Carlqvist relation to map the morphology of electric currents in the galaxy. The method for such analysis, assuming unidirectional current flow, is presented clearly in [11]. Extending that method to the more general case of coaxial current flow will be the subject of a future paper.

The primary observational requirement, to apply the methods in this paper, is high resolution polarization and hyperspectral data cube with beam width easily resolving 0.1 pc distance, which is the average ISM filament width. Interstellar filaments in regions of high star formation are likely candidates, such as protostars in filaments in the Orion A molecular clouds: RA [42:00.00 to 34:00.00] Dec [-9:00:00 to -5:00:00].

4 Conclusions

Electric currents are ubiquitous in cosmic plasmas, having been observed at the planetary, solar, interstellar, and galactic levels. Considerations from basic plasma physics lead us to expect that in cosmic settings, electric current will flow in a coaxial form: a primary current flow will be matched by a surrounding return current. There may even be multiple

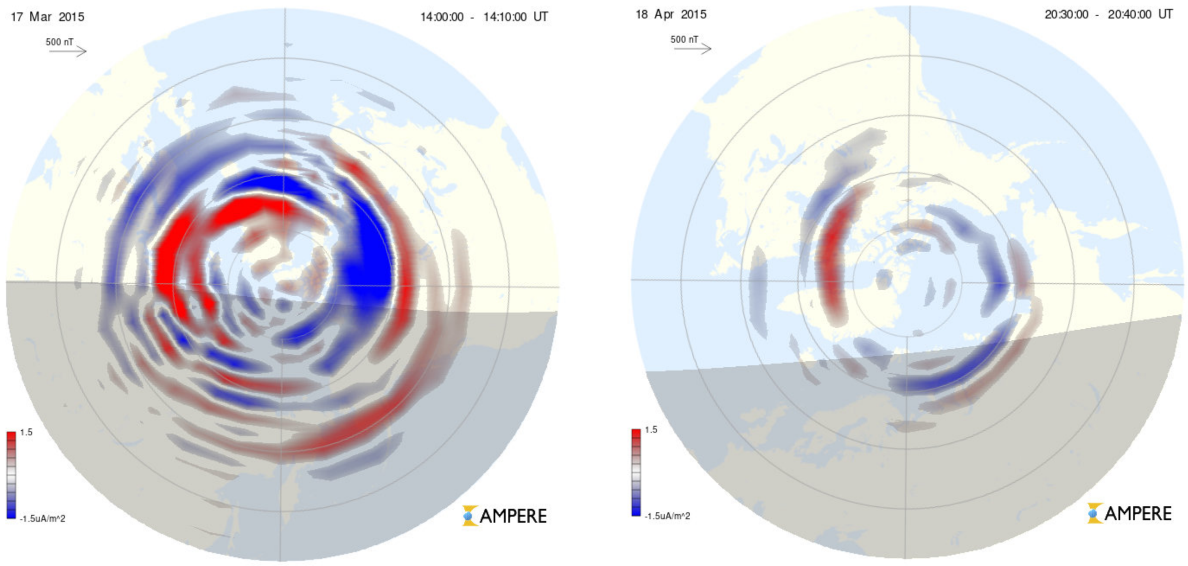

Fig. 6: Earth's polar electric currents. Left, from the "St Patrick's Day Storm" of 2015. Right, from one month later during quiet solar wind. Red/Blue represents current flowing away/towards the planet. During active solar wind there are multiple concentric reversals. From http://ampere.jhuapl.edu/ for the specified dates.

reversals of current, as in planetary polar currents.

When light passes through a coaxial current, the polarization changes will tend to cancel out, making it very difficult to determine the actual amount of current flowing. Likewise, any magnetic field measurements taken from outside such a coaxial current tube will greatly underestimate the current, since the reversing directions of current flow will cause a cancellation of magnetic field strength as seen from the outside. The ongoing debate as to whether magnetic fields are aligned with or perpendicular to interstellar molecular filaments is rooted in the fact that both are true.

Force-free current flow can also be identified from Doppler shift morphology and the segregation of atoms and molecules by ionization potential. The wealth of recent high resolution data in infrared, millimeter, and radio frequencies can be examined to distinguish different models for the flow of electric currents in cosmic plasmas.

5 Acknowledgements

This work was not funded. The author wishes to thank Don Scott for his work on coaxial plasma current flow, and Prof Richard Lovelace of Cornell University for his encouragement to write this article.

Submitted on May 8, 2025

References

1. Alfven H. and Carlqvist P. Interstellar clouds and the formation of stars. *Astrophysics and Space Science*, 1978, v. 55 (2), 487–509.
2. Kronberg P. and Lovelace R. Extragalactic circuits, transmission lines, and CR particle acceleration. arXiv: astro-ph/1412.3835.
3. Gabuzda D., Nagle M. and Roche N. The jets of AGN as giant coaxial cables. *Astrophysics and Astrophysics*, 2018, v. 612, A67.
4. Birkeland K. The Norwegian Aurora Polaris Expedition, 1902-03. Vol. I.: On the Cause of Magnetic Storms and the Origin of Terrestrial Magnetism. Christiania H Aschehoug and Co., 1913.
5. Zmuda A. J., Armstrong J. C. and Heuring F. T. Characteristics of transverse magnetic disturbances observed at 1100 kilometers in the auroral oval. *Journal of Geophysical Research*, 1970, v. 25 (75), 4757–4762.
6. Nahin P. Oliver Heaviside: The Life, Work, and Times of an Electrical Genius of the Victorian Age. Johns Hopkins University Press, Baltimore, MD, 2002.
7. Peratt A. Physics of the Plasma Universe. Springer Science+Business Media, New York, 2015.
8. Carlqvist P. Cosmic electric currents and the generalized Bennett relation. *Astrophysics and Space Science*, 1988, v. 144 (1–2), 73–84.
9. Coxon J. C., Milan S. E., Clausen L. B. N., Anderson B. J., and Korth H. The magnitudes of the regions 1 and 2 Birkeland currents observed by AMPERE and their role in solar wind-magnetosphere-ionosphere coupling. *Journal of Geophysical Research (Space Physics)*, 2014, v. 119 (12), 9804–9815.
10. Israelevich P. L., Gombosi T. I., Ershkovich A. I., Hansen K. C., Groth C. P. T., DeZeeuw D. L., and Powell, K. G. MHD simulation of the three-dimensional structure of the heliospheric current sheet. *Astronomy and Astrophysics*, 2001, v. 376, 288–291.
11. Verschuur G. High-resolution observations and the physics of high-velocity cloud A0. *Astrophysical Journal*, 2013, v. 766 (113), 1–17.
12. Lundquist S. Magneto-hydrostatic fields. *Ark. Fys.*, 1950, v. 2, 361–365.
13. Lundquist S. On the stability of magneto-hydrostatic fields. *Phys. Rev.*, 1951, v. 83, 307–311.
14. Scott D. Birkeland currents: A force-free field-aligned model. *Progress in Physics*, 2015, v. 11 (2), 167–179.
15. Lepping R. P., Berdichevsky D. B, Wu C. C., Szabo A., Narock T., Mariani F., Lazarus A. J., and Quivers A. J. A summary of WIND magnetic clouds for years 1995-2003: model-fitted parameters, associated errors and classifications. *Annales Geophysicae*, v. 24 (1), 215–245.

16. Saajasto M., Juvela M., *et al.* Correlation of gas dynamics and dust in the evolved filament G82.65-02.00. *Astronomy and Astrophysics*, v. 608, A21.
17. Marklund G. T. Plasma convection in force-free magnetic fields as a mechanism for chemical separation in cosmical plasmas. *Nature*, 1979, v. 277 (5695), 370–371.
18. Farrell W. M., Wahlund J. E., *et al.* Ion trapping by dust grains: Simulation applications to the Enceladus plume. *Journal of Geophysical Research* (*Planets*), 2017, v. 122 (4), 729–743.

New Four-Element Theory of Nature

T. X. Zhang

Department of Physics, Chemistry, and Mathematics, Alabama A&M University, 4900 Meridian Street, Huntsville, Alabama.
E-mail: tianxi.zhang@aamu.edu

This paper reviews the new four-element theory of nature, developed by the author for classically unifying all fundamental interactions of nature. Based on this theory, nature consists of only four fundamental elements, which are radiation (γ), mass (M), electric charge (Q), and color charge (C). Any known matter or particle observed in the universe and discovered in labs is a combination of one or more of the four fundamental elements, such as light is radiation only, neutron has mass only, Weyl fermion has electric charge only, gluon has color charge only, proton is a combination of mass and electric charge, and quark — a combination of mass, electric charge, and color charge. Fundamental interactions in nature are interactions among these fundamental elements. Radiation and mass are two forms of real energy as Einstein formulated. Electric and color charges are considered as two forms of imaginary energy. All the fundamental interactions are unified into a single interaction between complex energies. Interaction between real energies is the gravitational field force with three categories: mass-mass, mass-radiation, and radiation-radiation interactions. Interaction between imaginary energies is the gauge field force with also three categories: the electromagnetic force between electric charges, the strong force between color charges, and the weak force between electric and color charges. Interactions between real and imaginary energies are imaginary force, which have no observational support but may explain why charges are usually adhered on mass. As the weak force is an interaction between electric and color charges, it occurs effectively inside quark and causes quark excitation and decay. This leads the author to develop a new two-flavor multi-excitation quark model. This review gives details in various aspects and implications of the new four-element theory.

1 Introduction

Traditional four-element theory of nature, which was originated from Greek philosophy, posited that earth, air, fire, and water are the fundamental building blocks of all matter in nature. From the view of modern sciences, what are the fundamental elements of nature? It is well known that scientists have discovered one hundred and eighteen chemical elements in nature and from laboratory experiments, and listed them in the Mendeleev periodic table according to their chemical properties [1]. All the chemical elements can be also categorized into four groups: metals, nonmetals, metalloids, and noble gases or more specifically into eight groups by classifying metals into three types and separating the 113^{th} though 118^{th} elements as unknowns and the 7^{th}, 17^{th}, 35^{th}, 63^{rd}, and 85^{th} elements as halogens. Elements, compounds, and mixtures are three typical types of matter in chemistry. Solids, liquids, and gases are three fundamental states of matter in physics. Ionized gases are usually called plasmas, the fourth state of matter. Almost all the normal or ordinary matter in the universe is in the plasma state.

Particle physicists have discovered over three hundred particle in nature and from laboratory experiments, and usually categorized them into hadrons and leptons according to whether they participate in the strong interaction or not, or into fermions and bosons according to whether they have half-integer spins or not [2, 3]. Hadrons are composed of quarks with six flavors, usually being grouped into three generations or families along with the six leptons [4,5]. The six quarks are up (u), down (d), charm (c), strange (s), top (t), and bottom (b). The six leptons are electron (e), muon (μ), and tau (τ) and their corresponding neutrinos (ν_e, ν_μ, ν_τ). In the standard model of particle physics, the twelve spin-1/2 fermions (i.e., six quarks and six leptons) are building blocks of matter, the four spin-1 bosons (γ, g, W and Z) are gauge force carriers, and the spin-0 Higgs boson is the particle mass giver. Including gravitons (the carriers of gravitational force) and all antiparticles, physicists have found or predicted fifty-seven fundamental particles and listed them in the particle table [6].

Both chemical elements and physical elementary particles are not fundamental elements of nature because they still have common properties. Nuclei of different chemical elements consist of different numbers of nucleons (protons and neutrons). Nucleons are combinations of quarks. Quarks are combinations of mass, electric charge, and color charge. Leptons and weak bosons have mass and/or electric charge. Gamma bosons are massless radiation, and gluon bosons are color charges. Considering these facts, the author proposed and developed a new four-element theory of nature [7, 8]. From the fundamental elements of nature to reveal a new quantum world of quarks, the author has recently proposed and developed a new quark model called two-flavor multi-

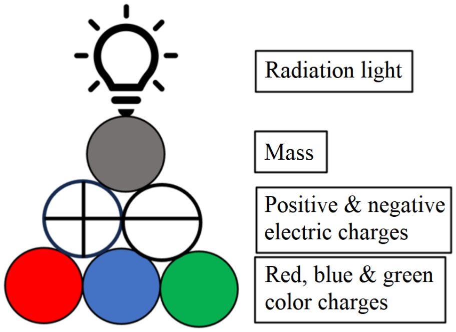

Fig. 1: Four fundamental elements of nature [7, 8]. They are radiation (γ), mass (M), electric charge (Q), and color charge (C). Radiation and mass are two forms of real energies. Electric and color charges are two forms of imaginary energies.

Table 1: Fundamental elements of nature. A particle is a combination of one or more of the four fundamental elements: mass (M), radiation (γ), electric charge (Q), and color charge (C).

Particles	γ	M	Q	C
Photon	✓			
Neutron		✓		
Weyl Fermion			✓	
Gluon				✓
Proton		✓	✓	
Massless Meson			✓	✓
Quark		✓	✓	✓

excitation quark model [9, 10], which has potential to solve both mysteries of why the present universe is significantly missing antimatter but fully filling with dark matter. This paper gives a sufficient review on this author's newly developed four-element theory of nature.

2 Fundamental elements of nature

The new four-element theory of nature suggests that nature consists of only four fundamental elements [7, 8], which are radiation (γ), mass (M), electric charge (Q), and color charges (C) as shown in Fig. 1. Any known matter or particle observed in nature or generated in labs is a combination of one or more of the four fundamental elements. For instances, as shown in Table 1, photon is radiation only; neutron has mass only; Weyl fermion has electric charge only; gluon has color charge only; proton is a combination of mass and electric charge; massless meson is a combination of electric and color charges; and quark is a combination of mass, electric charge, and color charge.

The author further categorized the four fundamental elements into two types of energies. Radiation and mass are two forms of real energy as Einstein formulated to be proportional to radiation frequency and mass, respectively, while electric and color charges are two forms of imaginary energy as the author formulated to be proportional to electric and color charges, respectively. Radiation energy is the energy of electromagnetic waves, propagating at the speed of light. Mass energy is the nuclear energy of an object or particle at rest or in motion. Real energy can do work in the real world and is measurable. A pure electric charge such as a Weyl fermion [11], as it is a form of imaginary energy, cannot be directly observed in nature, but its flow or current in semimetals has been detected [12]. A pure color charge such as a gluon [13], as it is a form of imaginary energy, cannot be directly observed in nature, but its behavior or existence has been detected in quark-gluon plasmas or jet events [14].

2.1 Mass — a form of real energy

Mass is a fundamental property of matter, which directly determines the gravitational interaction via Newton's law of gravitation [15]. Mass of an object is the quantity or amount of matter that the object contains. It is a measure of its inertia of motion in accordance with Newton's laws of motion. A body experiences an inertial force when it accelerates relative to the center of mass of the entire universe as Mach's principle indicates. In short, mass there affects inertia here. From Einstein's energy-mass expression (or Einstein's first law), mass is also understood as a form of real energy. A particle at rest with mass M has real energy given by [16]

$$E_M = Mc^2 \,, \tag{1}$$

where c is the speed of light in the free space. A particle in motion, has mass to be the Lorentz factor of the rest mass, $\gamma_L M$, where $\gamma_L = (1 - v^2/c^2)^{1/2}$ and v the speed of the particle. This real energy is always positive and directly measurable. It cannot be destroyed or created but can be converted from one form to another. In nuclear fission and fusion processes, a small amount of missing mass converts into a huge amount of nuclear energy. Newton's second law of motion states that acceleration of an object is proportional to the net force on the object and inversely proportional to the mass of the object.

2.2 Radiation — a form of real energy

Radiation γ refers to the electromagnetic radiation (or light), consisting of varying electric and magnetic fields, and can travel through vacuum by itself at the speed of light, about 300 million meters per second. Light looks like a ray as it travels straightly. Isaac Newton believed light to be particle because of its reflection and refraction. Thomas Young suggested light to be wave because of its interference and diffraction. James Clerk Maxwell recognized light to be electromagnetic waves because they travel at the same speed. In quantum physics, radiation is described as photons, which are massless quanta of real energy. The energy of a photon is given by [17]

$$E_\gamma = h\nu \,, \tag{2}$$

where h is the Planck constant and ν is the radiation frequency. Radiation quanta or photons of light explain blackbody radiation spectra [18], atomic emission and absorption spectra [19], Compton photon-electron scattering [20], and photoelectric effects [17]. Therefore, we can say in general that radiation is also a form of real energy and always positive. An atom, when it changes its state from energy E_2 to energy E_1, emits a photon with frequency or energy given or determined by the energy difference, $h\nu = E_2 - E_1$.

According to the increasing order of frequency or the decreasing order of wavelength, physicists usually categorize electromagnetic waves into radio wave, microwave, infrared, visible light, ultraviolet, X-ray, and gamma ray. Oscillations of electrons and nuclei including protons produce radio waves and microwaves; thermal motions of electrons and ions produce infrared light; Orbital or energy changes of electrons in atoms emit visible light and ultraviolet. Sudden stops of high-speed electrons on targets produce X-rays; and nuclear reactions and decays produce gamma rays.

Annihilations between particles and antiparticles including quarks and antiquarks produce pairs of gamma rays. In a pair production process, a gamma ray materializes into a pair of particle and antiparticle with non-zero masses. Annihilation and pair production indicate that the two forms of real energies (i.e. mass and radiation) can convert from one to another, so that they are not independent. If we define an equivalent mass for radiation to be $m_\gamma = h\nu/c^2$, we may consider nature to be composed of three fundamental elements: mass, electric charge, and color charge, rather than fours, so that reduce the four-element theory of nature to a three-element theory of nature.

2.3 Electric charge — a form of imaginary energy

Electric charge is another fundamental or intrinsic property of matter or some particles, which directly determines the electromagnetic interaction via Coulomb's law of electric force [27]. Electric charge has two varieties of either positive or negative. It appears or is observed always in association with mass to form positive or negative electrically charged particles with different masses such as electron and proton. The interaction between electric charges, however, is completely independent of their masses. Positive and negative charges can annihilate or cancel out each other and produce in pair with total electric charges conserved. Weyl fermion is a massless electron, which was predicted a century ago and recently measured in semimetals but not individually [11, 12].

A pure or individual electric charge should have its own meaning of physics. Zhang [7] first hypothesized or considered electric charge Q to be a form of imaginary energy. The amount of imaginary energy is defined to be proportional to the charge as

$$E_Q = \frac{Q}{\sqrt{G}}\, c^2\,, \tag{3}$$

where G is the gravitational constant. This allows us to unify Newton's law of gravitation with Coulomb's law of electric force into a single expression between complex energy of electrically charged particles [7]. The imaginary energy has the same sign as the electric charge. Then, for an electrically charged particle, the total energy is

$$E = E_M + iE_Q = (1 + i\alpha)Mc^2\,, \tag{4}$$

where i is the imaginary number and α is the charge-mass ratio of the particle, defined by

$$\alpha = \frac{E_Q}{E_M} = \frac{Q}{\sqrt{G}M}\,, \tag{5}$$

in the cgs electrostatic unit system. The complex conjugate of the energy of a charged particle such as an electron gives the energy of its corresponding antiparticle such as a positron [21, 22].

Including electric charge, Zhang [7] has modified Einstein's first law (1) into (4), in which electric charge is expressed as imaginary mass or energy. For an electrically charged particle, the absolute value of α is a big number. This implies that an electrically charged particle contains much more imaginary energy than its real energy (e.g., $\alpha = 10^{18}$ for proton and $\alpha = -2\times 10^{21}$ for electron). A neutral particle such as a neutron, photon, or neutrino has only real energy. Weinberg [23] suggested that electric charges come from the fifth-dimensional space, which is a small and compact circle space in the Kaluza-Klein (KK) theory [24–26]. Zhang has developed a five-dimensional fully covariant KK-theory with a scalar field [28] and shown that electric charge can affect light (i.e., electric redshift) and gravity (i.e., gravitational shielding) [29, 30].

As the energy of an antiparticle is simply obtained by conjugating the energy of the corresponding particle, a particle and its antiparticle have same real energy but imaginary energy with opposite sign. In a particle-antiparticle annihilation process, their real energies completely convert into radiation photon energies and their imaginary energies annihilate or cancel out. Since there are no masses to adhere with, the electric charges come together due to the electric attraction and cancel out, or form a positive-negative electric charge pair $(+, -)$. In a particle-antiparticle pair production process, the radiation photon energies transfer to rest energies with a pair of imaginary energies, which combine with the rest energies to form a particle and an antiparticle.

Real energy is continuous, while imaginary energy is quantized. Each electric charge quantum e (which is also proton's charge) has imaginary energy about $iE_e = iec^2/\sqrt{G} \sim i10^{27}$ eV about 10^{18} times greater than proton's real energy ($\sim$ 931 MeV). This ratio is about the ratio between the radius of proton and the radius of the circular fifth dimensional space.

Table 2: Properties of six quarks: name, symbol, and electric charge.

Name	Symbol	Mass	Electric Charges
up	u	2.4 MeV	$2e/3$
down	d	4.8 MeV	$-e/3$
charm	c	1.27 GeV	$2e/3$
strange	s	104 MeV	$-e/3$
top	t	171.2 GeV	$2e/3$
bottom	b	4.2 GeV	$-e/3$

2.4 Color charge — a form of imaginary energy

Color charge C is a fundamental property of quarks and gluons [36], which has analogies with the notion of electric charge of particles. The basic properties (mass and electric charge) of the six quarks are shown in Table 2. There are three varieties of color charges: red, blue, and green. An antiquark's color is anti-red, anti-blue, or anti-green. Quarks and antiquarks also hold electric charges but the numbers of electric charges to be fractional such as $\pm e/3$ or $\pm 2e/3$. An elementary particle is usually composed of two or more quarks or antiquarks and colorless with electric charge to be a multiple of e or neutral. For instances, a proton is composed of two up quarks and one down quark (uud); a neutron is composed of one up quark and two down quarks (udd); a pion meson π^+ is composed of one up quark and one down antiquark ($u\bar{d}$); a charmed sigma Σ^{++} is composed by two up quarks and one charm quark (uuc); and so on.

Similar to electric charge Q, the author has hypothesized or considered the color charge C to be another form of imaginary energy. The amount of imaginary energy in a color charge can be defined by

$$E_C = \frac{C}{\sqrt{G}} c^2 \,, \tag{6}$$

in analogy to the electric charge for the grand unification of all fundamental interactions into a single interaction between complex energies [8]. Then, for a quark with mass M, electric charge Q, and color charge C, the total energy of the quark is

$$E = E_M + iE_Q + iE_C = (1 + i\alpha + i\beta)Mc^2 \,, \tag{7}$$

where β is defined by

$$\beta = \frac{E_C}{E_M} = \frac{C}{\sqrt{G}M} \,. \tag{8}$$

The total energy of an antiquark is obtained by conjugating the total energy of its corresponding quark. A quark and its antiquark have the same real energy and equal amount of imaginary energy, but their signs are opposite. The opposites of red, blue, and green charges are anti-red, anti-blue, and anti-green charges.

Table 3: Color combinations between red, blue, green and their anti-colors.

Color	r	b	g	$\bar{r}$	$\bar{b}$	$\bar{g}$
r	$2r$	$\bar{g}$	$\bar{b}$	0	$r_{\bar{b}}$	$r_{\bar{g}}$
b	$\bar{g}$	$2b$	$\bar{r}$	$b_{\bar{r}}$	0	$b_{\bar{g}}$
g	$\bar{b}$	$\bar{r}$	$2g$	$g_{\bar{r}}$	$g_{\bar{b}}$	0
$\bar{r}$	0	$\bar{r}_b$	$\bar{r}_g$	$2\bar{r}$	g	b
$\bar{b}$	$\bar{b}_r$	0	$\bar{b}_g$	g	$2\bar{b}$	r
$\bar{g}$	$\bar{g}_r$	$\bar{g}_b$	0	b	r	$2\bar{g}$

2.5 Color neutrality and quark confinement

In particle physics, color is a fundamental property of quarks and gluons, related to the strong forces. It is not the visible color but a type of charge. A neutral or white color (i.e., zero color charge) is formed when (1) a color and its anticolor combine $C + \bar{C} = 0$), (2) red, blue, and green colors combine ($r + b + g = 0$), and (3) anti-red, anti-blue, and anti-green colors combine ($\bar{r} + \bar{b} + \bar{g} = 0$). Table 3 lists the colors formed when any two colors combine, such as red and red colors combine to form double red color, red and blue combine to form anti-green color, red and green colors combine to form anti-blue color, red and anti-red colors combine to form white color, red and anti-blue colors combine to form red-anti-blue color, and red and anti-green colors combine to form red-anti-green color, and so on. Color neutrality refers to that only color-neutral particles can exist in isolation or independently. Color confinement refers to that particles with colors or anticolors cannot be observed alone.

2.6 Energy space of particles

Both real and imaginary energies are conserved, respectively. Being only positive, a real energy cannot be created or destroyed but can be converted from one to another. In electron-positron annihilation process, mass is converted into radiation. In the pair production of a gamma ray, radiation is converted or materialized into mass. Being both negative and positive for electric charges and both color and anti-color for color charges, an imaginary energy can be canceled out or neutralized. Net charges in an isolated system remain the same. As mentioned in subsection 2.1 above, the two forms of real energies (mass and radiation) can be converted from one to another and thus not independent. Here, we believe, the two forms of imaginary energies (electric charge and color charge) are independent, but they can interact via the weak force.

Fig. 2 constructs a three-dimensional (3D) energy space for particles based on the three independent fundamental elements or energy components (mass, electric charge, and color charge). Any particle has a position or can be located in this 3D energy space with coordinates (M, Q, C) with $M > 0$. For instances, a neutral particle such as neutron and neutrino, in-

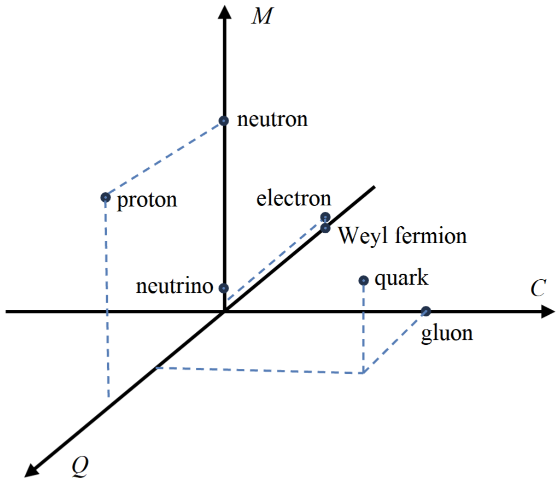

Fig. 2: 3D particle energy space. A neutral particle such as neutron or neutrino including radiation is found on the M-axis, a Weyl fermion is found on the Q-axis, a gluon is found on the C-axis, an electrically charged particle such as proton or electron is found in the $M-Q$ plane, and a quark is found in the 3D space with non-zero coordinates.

cluding radiation when it is equivalent to mass, has a coordinate $(M, 0, 0)$, located on the M-axis; an electrically charged particle such as proton and electron, located in the M-Q plane with a coordinate $(M, Q, 0)$; and a quark has a position in the 3D space with non-zero coordinates. Weyl fermions are on the Q-axis and gluons are on the C-axis. And so on for many other particles, including antiparticles, we can locate each of them with a unique set of coordinates in this 3D energy space of particles.

3 Fundamental interactions and unification

3.1 Fundamental interactions in nature

Fundamental interactions in nature are interactions among fundamental elements of nature. Among the four fundamental elements, there are ten fundamental interactions (Table 4). The three real forces ($\vec{F}_{MM}$, $\vec{F}_{\gamma\gamma}$, and $\vec{F}_{M\gamma}$) are interactions between two forms of real energies (γ and M) and belong to the gravitational forces. Another three real forces ($\vec{F}_{QQ}$, $\vec{F}_{QC}$, and $\vec{F}_{CC}$) are interactions between two forms of imaginary energies (Q and C) and belong to the gauge field forces, named, respectively, the electromagnetic, weak, and strong forces. The four imaginary forces ($i\vec{F}_{\gamma Q}$, $i\vec{F}_{\gamma C}$, $i\vec{F}_{MQ}$, and $i\vec{F}_{MC}$) are interactions between real and imaginary energies and have no direct measurements. Although these imaginary forces are not directly observational, they may play key roles in explaining why charges are always attached along with masses and absorb/emit radiation photons, and why gluons are adhesive. In physics, the fundamental interactions found in nature conventionally refer to the following fours: gravitational, electromagnetic, weak, and strong forces.

Table 4: Fundamental interactions among the four fundamental elements.

Name	γ	M	iQ	iC
γ	$\vec{F}_{\gamma\gamma}$	$\vec{F}_{\gamma M}$	$i\vec{F}_{\gamma Q}$	$i\vec{F}_{\gamma C}$
M		$\vec{F}_{MM}$	$i\vec{F}_{MQ}$	$i\vec{F}_{MC}$
iQ			$\vec{F}_{QQ}$	$\vec{F}_{QC}$
iC				$\vec{F}_{CC}$

3.2 Unification of all fundamental interactions

All the ten fundamental interactions among the four fundamental elements (two real energies and two imaginary energies) can be unified as a single interaction between complex energies as given by the following equation or shown by Fig. 3 [8]

$$\vec{F}_{E_1E_2} = -G\,\frac{E_1E_2}{c^4r^2}\,\hat{r}\,, \tag{9}$$

where G is the gravitational constant, E_1 and E_2 are complex energies of the two objects or particles, and r is the distance between the two objects or particles. This expression (9) may be called a generalized Newtonian gravitational law. Considering the complex energy of a general object or particle that has two real parts and two imaginary parts (i.e., $E_1 = E_{1\gamma}+E_{1M}+iE_{1Q}+iE_{1C}$ and $E_2 = E_{2\gamma}+E_{2M}+iE_{2Q}+iE_{2C}$), we can expand the single complex force into six real and four imaginary forces,

$$\begin{aligned}
\vec{F}_{E_1E_2} &= -G\,\frac{M_1M_2}{r^2}\,\hat{r} - G\,\frac{M_1h\nu_2 + M_2h\nu_1}{c^2r^2}\,\hat{r} - G\,\frac{h\nu_1h\nu_2}{c^4r^2}\,\hat{r} \\
&\quad + \frac{Q_1Q_2}{r^2}\,\hat{r} + \frac{Q_1C_2 + Q_2C_1}{r^2}\,\hat{r} + \frac{C_1C_2}{r^2}\,\hat{r} \\
&\quad - i\sqrt{G}\,\frac{h\nu_1Q_2 + h\nu_2Q_1}{c^2r^2}\,\hat{r} - i\sqrt{G}\,\frac{h\nu_1C_2 + h\nu_2C_1}{c^2r^2}\,\hat{r} \\
&\quad - i\sqrt{G}\,\frac{M_1Q_2 + M_2Q_1}{r^2}\,\hat{r} - i\sqrt{G}\,\frac{M_1C_2 + M_2C_1}{r^2}\,\hat{r} \\
&\quad = \vec{F}_{MM} + \vec{F}_{\gamma M} + \vec{F}_{\gamma\gamma} + \vec{F}_{QQ} + \vec{F}_{QC} + \vec{F}_{CC} \\
&\quad + i\vec{F}_{\gamma Q} + i\vec{F}_{\gamma C} + i\vec{F}_{MQ} + i\vec{F}_{MC} \\
&\quad = \vec{F}_{RR} + \vec{F}_{II} + i\vec{F}_{RI}\,.
\end{aligned} \tag{10}$$

Here, we have used (1–3) and (6) for the two real and two imaginary energy expressions. The symbol $\hat{r}$ is the unit vector along the direction of radial distance.

3.3 Gravitational force — interaction between real energy

The force $\vec{F}_{MM}$ represents Newton's law for the gravitational interaction between two masses. This force governs the orbital motion of astrophysical objects including the solar system. The force $\vec{F}_{\gamma M}$ is the gravitational interaction between mass and radiation and the force $\vec{F}_{\gamma\gamma}$ is the gravitational interaction between radiation and radiation. These three types

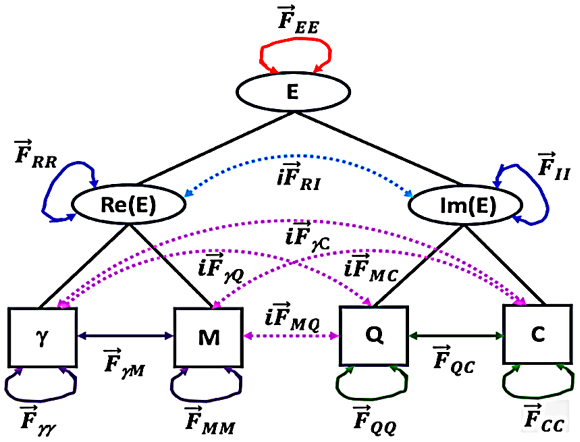

Fig. 3: Fundamental interactions among the four fundamental elements of nature: radiation, mass, electric charge and color charge. Mass and radiation are real energies, while electric and color charges are imaginary energies. Nature is a system of complex energy, and all the fundamental interactions of nature are classically unified into a single interaction between complex energies. There are six real and four imaginary interactions among the four fundamental elements.

of gravitational interactions are categorized as the interaction between real energies (Fig. 4a). Defining the radiation equivalent mass, we have a single gravitational force between masses.

When a photon of light travels relative to an object (e.g. the Sun) from $\vec{r}$ to $\vec{r} + d\vec{r}$, it changes its frequency from ν to $\nu + d\nu$. Calculating the work done by this mass-radiation force on a photon to be the energy change of the photon,

$$h d\nu = \vec{F}_{\gamma M} \cdot d\vec{r} = -G \frac{h\nu M}{c^2 r^2} dr \,, \tag{11}$$

the author derived Einstein's gravitational redshift without using the Schwarzschild solution of Einstein's general relativity [8, 37, 38]. First, dividing (11) by the photon energy $h\nu$ for variable separation and then integrating the radial distance from the object radius R to infinity ∞ and the photon frequency from the emission frequency ν_e to the observation frequency ν_o, we have

$$\int_{\nu_e}^{\nu_o} \frac{d\nu}{\nu} = -\int_R^\infty \frac{GM}{c^2 r^2} dr \,. \tag{12}$$

Completing this definite integration, we obtain

$$\ln \frac{\nu_o}{\nu_e} = -\frac{GM}{c^2 R} \,, \quad \text{or} \quad \frac{\nu_e}{\nu_o} = \exp\left(\frac{GM}{c^2 R}\right). \tag{13}$$

Then, the gravitational redshift can be derived as

$$Z_G = \frac{\lambda_o - \lambda_e}{\lambda_e} = \frac{\nu_e - \nu_o}{\nu_o} = \exp\left(\frac{GM}{c^2 R}\right) - 1 \,. \tag{14}$$

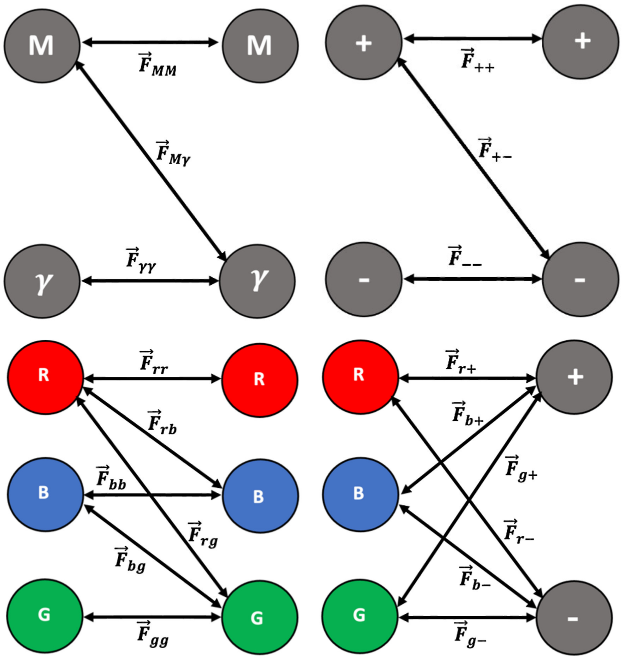

Fig. 4: (a) Top left panel shows the three types of gravitational interaction between real energies. They are the mass-mass, mass-radiation, and radiation-radiation interactions. (b) Top right panel shows the three types of electromagnetic force between electric charges. They are the positive-positive, positive-negative, and negative-negative interactions. (c) Bottom left panel shows the six types of strong interactions between color charges. They are the red-red, red-blue, red-green, blue-blue, blue-green, and green-green interactions. (d) Bottom right panel shows the six types of weak interactions between electric and color charges. They red-positive, red-negative, blue-positive, blue-negative, green-positive, and green-negative interactions.

In the weak field approximation, it reduces to

$$Z_G = \frac{GM}{c^2 R} \,. \tag{15}$$

Similarly, calculating the work done on a photon from an object by the radiation-radiation gravitation, the author further obtained a radiation redshift, which is proportional to the fourth power of temperature of the radiation. For the light from the Sun, the radiation redshift is about 10^{-13}, around seventh order lower in magnitude than the gravitational redshift [8], and hence negligible. For an extremely hot object, the radiation redshift will be significant and may be detectable.

3.4 Electromagnetic force — interaction between electric charges

The force $\vec{F}_{QQ}$ represents Coulomb's law for the electromagnetic interaction between two electric charges. This force governs the orbital motion of atomic electrons around nuclei. Electric charges have two varieties and thus three types of in-

Table 5: Gauge field interactions between different types of charges. These include the six strong field interactions between three types of color charges (coded as red), the six weak field interactions between three types of color charges and two types of electric charges (coded as blue), and the three types of electromagnetic field interactions between two types of electric charges (coded as green).

Charge	r	b	g	$+$	$-$
r	$\vec{F}_{rr}$	$\vec{F}_{rb}$	$\vec{F}_{rg}$	$\vec{F}_{r+}$	$\vec{F}_{r-}$
b		$\vec{F}_{bb}$	$\vec{F}_{bg}$	$\vec{F}_{b+}$	$\vec{F}_{b-}$
g			$\vec{F}_{gg}$	$\vec{F}_{g+}$	$\vec{F}_{g-}$
$+$				$\vec{F}_{++}$	$\vec{F}_{+-}$
$-$					$\vec{F}_{--}$

teractions (Fig. 4b, see also Table 5):

1) repelling between positive electric charges $\vec{F}_{++}$,
2) repelling between negative electric charges $\vec{F}_{--}$, and
3) attracting between positive and negative electric charges $\vec{F}_{+-}$.

Like charges repel one another and unlike charges attract one another. In the standard model of particle physics, the electromagnetic force between electric charges is described by the group $U(1)$.

3.5 Strong Force — interaction between color charges

The force $\vec{F}_{CC}$ is the strong interaction between color charges. Color charges have three varieties: red, blue, and green and thus have six types of interactions (Fig. 4c, see also Table 5):

1) the red-red interaction $\vec{F}_{rr}$,
2) the blue-blue interaction $\vec{F}_{bb}$,
3) the green-green interaction $\vec{F}_{gg}$,
4) the red-blue interaction $\vec{F}_{rb}$,
5) the red-green interaction $\vec{F}_{rg}$, and
6) the blue-green interaction $\vec{F}_{bg}$.

Fig. 4c shows these six types of color interactions or strong forces. With anticolors, there are 21 types of strong force between color charges. In the standard model of particle physics, the strong forces between color charges are described by the group SU(3).

The strong interaction is the only one that can change color of quarks in a hadron particle. A typical strong interaction is the proton-neutron scattering. This is an interaction between the color charge of one up quark in proton and the color charge of one down quark in neutron via exchanging a π^+-meson between the proton and neutron. In other words, during this proton-neutron scattering an up quark in the proton changes into a down quark by emitting a π^+, meanwhile a down quark in the neutron changes into an up quark by absorbing the π^+. Another typical strong interaction is delta decay, $\Delta^0 \to p + \pi^-$. This is an interaction between the color charge of one down quark and the color charges of the other two quarks. In this interaction, a down quark emits a π^- and then becomes an up quark, $d \to u + \pi^-$.

It should be noted here that the strong force carriers between nucleons (not quarks) are the pion mesons ($\pi^\pm$, π^0), which are the lightest hadrons, composed of one first-generation quark and one first-generation antiquark, and bind nucleons to form nuclei [33]. Gluons are the particles that mediate the strong forces that bind quarks together to form hadrons including nucleons [34]. Including antiparticles and gravitons (or gravitational force carriers), we have more fundamental particles [35]. We may categorize the strong force into two categories: (1) the nuclear force between nucleons to bind nucleons to form a nucleus and (2) the color charge interaction or force between quarks to bind quarks into hadrons.

3.6 Weak force — interaction between electric charge and color charge

The force $\vec{F}_{QC}$ is the weak interaction between electric and color charges. Considering electric charges with two varieties and color charges with three varieties, we have also six types of weak interactions (Fig. 4d, see also Table 5):

1) the positive-red interaction $\vec{F}_{+r}$,
2) the positive-blue interaction $\vec{F}_{+b}$,
3) the positive-green interaction $\vec{F}_{+g}$,
4) the negative-red interaction $\vec{F}_{-r}$,
5) the negative-blue interaction $\vec{F}_{-b}$, and
6) the negative-green interaction $\vec{F}_{-g}$.

With anticolors, there are 12 types of weak between electric and color charges. In the standard model of particle physics, the weak forces are described by the group SU(2) and carried by the W and Z bosons. The weak interaction is the only one that can change flavors of quarks in a hadron particle, which causes atoms to change from one element to another. A typical weak interaction occurs when neutron decays into proton with emissions of an electron and an electron-type antineutrino. In this process, a down quark in the neutron changes into an up quark by emitting a W-boson, which lives about 10^{-25} seconds and then breaks into a high-energy electron and an electron-type antineutrino.

3.7 Interaction between two electrically charged particles

The interaction between two electrically charged particles such as the interaction between two protons in a nucleus or the interaction between proton and electron in a hydrogen atom is given by

$$\begin{aligned}\vec{F}_{E_1E_2} &= -G\,\frac{(E_{1M}+iE_{1Q})(E_{2M}+iE_{2Q})}{c^4r^2}\,\hat{r}\\ &= -G\,\frac{M_1M_2}{r^2}\,\hat{r} + \frac{Q_1Q_2}{r^2}\,\hat{r} - i\sqrt{G}\,\frac{M_1Q_2+M_2Q_1}{r^2}\,\hat{r}\\ &= \vec{F}_{MM} + \vec{F}_{QQ} + i\vec{F}_{MQ}\,, \qquad (16)\end{aligned}$$

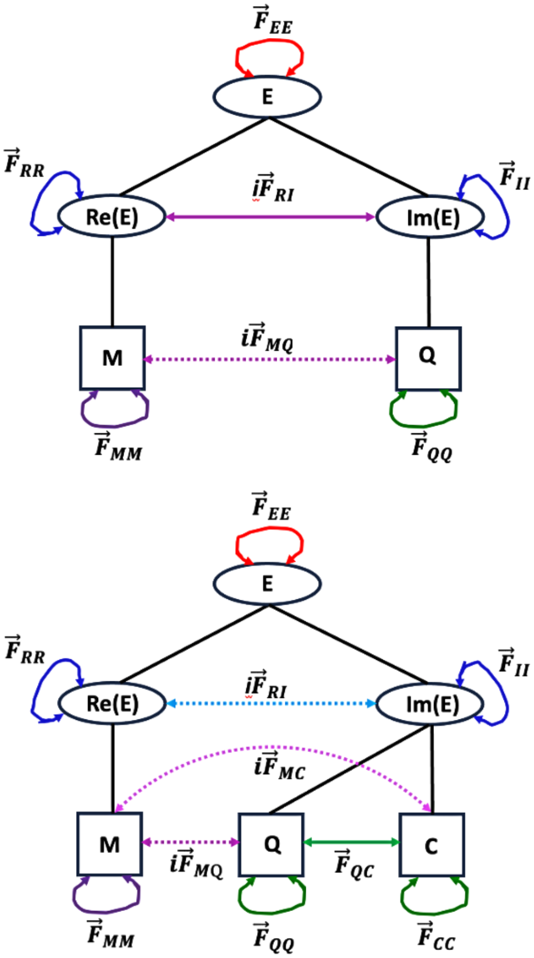

Fig. 5: (a) Top panel shows interaction between two electrically charged particles. It splits into three fundamental interactions: (1) a real force between masses $\vec{F}_{MM}$, the gravitational force governed by Newton's gravitational law, (2) a real force between electric charges $\vec{F}_{QQ}$, the electromagnetic force governed by Coulomb's law, and (3) an imaginary force between mass and electric charges $i\vec{F}_{MQ}$, which plays the role in sticking and adhering the electric charge on the mass to form electrically charged particles. (b) Bottom panel shows interaction between two quarks. It splits into six fundamental forces: (1) a real force between masses (gravitational) $\vec{F}_{MM}$, (2) a real force between electric charges (electromagnetic) $\vec{F}_{QQ}$, (3) a real force between color charges (strong) $\vec{F}_{CC}$, (4) a real force between electric and color charges (weak) $\vec{F}_{QC}$, (5) an imaginary force between mass and electric charge $i\vec{F}_{MQ}$, and (6) an imaginary force between mass and color charge $i\vec{F}_{MC}$.

or shown in Fig. 5a. It is split into two real forces and one imaginary force. The two real forces are $\vec{F}_{MM}$ and $\vec{F}_{QQ}$, governed by Newton's law of gravitation and Coulomb's law of electromagnetism, respectively. The one imaginary force is $i\vec{F}_{QC}$, which can occur inside of a particle to glue its electric charge on its mass or between two particles.

3.8 Interaction between two quarks

The interaction between two quarks in a hadron or in a quark-gluon plasma is given by

$$\begin{aligned}\vec{F}_{E_1E_2} &= -G\,\frac{(E_{1M}+iE_{1Q}+iE_{1C})(E_{2M}+iE_{2Q}+iE_{2C})}{c^4r^2}\,\hat{r}\\ &= -G\,\frac{M_1M_2}{r^2}\,\hat{r}+\frac{Q_1Q_2}{r^2}\,\hat{r}+\frac{Q_1C_2+Q_2C_1}{r^2}\,\hat{r}+\frac{C_1C_2}{r^2}\,\hat{r}\\ &\quad -i\sqrt{G}\,\frac{M_1Q_2+M_2Q_1}{r^2}\,\hat{r}- -i\sqrt{G}\,\frac{M_1C_2+M_2C_1}{r^2}\,\hat{r}\\ &= \vec{F}_{MM}+\vec{F}_{QQ}+\vec{F}_{QC}+\vec{F}_{CC}+i\vec{F}_{MQ}+i\vec{F}_{MC}\,. \end{aligned} \tag{17}$$

or shown in Fig. 5b. It is split into four real and two imaginary forces. The four real forces are $\vec{F}_{MM}$, $\vec{F}_{QQ}$, $\vec{F}_{QC}$ and $\vec{F}_{CC}$, called by the gravitational, electromagnetic, weak and strong interactions, respectively. The two imaginary forces are $i\vec{F}_{MQ}$ and $i\vec{F}_{MC}$, gluing electric and color charges on mass.

Considering the strong interaction to be asymptotically free within a typical hadron [39], we can replace the color charge by

$$C \longrightarrow \frac{r}{r_0}\,C\,, \tag{18}$$

where r is the radial distance and $r_0 \sim 10^{-15}$ m is the radius of the typical hadron. This assumption represents that color charge becomes less colorful if it is closer to each other, i.e., asymptotically colorless. Then, the strong interaction between color charges of two quarks can be rewritten by

$$\vec{F}_{C_1C_2} = \frac{C_1C_2}{r_0^2}\,\hat{r}\,, \tag{19}$$

which is independent of the radial distance and consistent with measurements, and the weak force between electric charge of one quark and color charge of another quark becomes

$$\vec{F}_{Q_1C_2} = \frac{Q_1C_2}{r_0 r}\,\hat{r}\,, \tag{20}$$

which is inversely proportional to the distance and consistent with measurements. The electromagnetic force between electric charges of two quarks is given by

$$\vec{F}_{Q_1Q_2} = \frac{Q_1Q_2}{r^2}\,\hat{r}\,. \tag{21}$$

Within a typical hadron (i.e., $r \sim r_0$) such as a proton or a neutron, the strong force can be 100 times stronger than the electromagnetic force in strength. This leads to the color-electric charge ratio of a quark to be $C/Q \sim 10$. The ratio between strong force and weak force will be about $\sim rC/(r_0Q)$. Since the weak force between electric charge and color charge has a shorter range of interaction ($r \sim 10^{-18}$ m or $r/r_0 \sim 10^{-3}$) such as within a typical quark, we have that the weak force between electric and color charge within a typical quark can be 100 times greater than the strong force between color charges of two quarks within a typical hadron. Therefore, the weak force that occurs inside a quark and causes the quark decay is not actually weak.

4 Discussions and conclusions

The new four-element theory suggests the weak force to be an interaction between electric and color charges, in analogy to the electromagnetic force to be an interaction between electric charges and the strong force to be an interaction between color charges. It occurs effectively inside a quark between its electric and color charges, so that is responsible for the excitation and decay of quarks. Considering an atom to be composed of a nucleus and electrons, a nucleus to be composed of nucleons, and a nucleon to be composed of quarks, we see radioactive decay of atoms to result from the decay of quarks that are triggered by the weak interaction between the quark's electric and color charges. This new scenario of weak interaction beyond the standard model of particle physics has important implications to the quark model, particle physics, and cosmology. Based on the new four-element theory of nature, we have developed a new quark model called two-flavor multi-excitation quark model [9, 40].

The new four-element theory of nature addresses only the ordinary matter of the universe. Based on the big bang standard model of cosmology, our universe dominates by dark matter and dark energy over 95%. The ordinary matter only takes 5%. The possible candidates of dark matter are weakly interacting massive particles (WIMPs), axions, sterile neutrinos, and primordial black holes. For the dark energy, the most favored explanation is the cosmological constant. The author proposed and developed a black hole model of the universe, which does not need dark energy [41–44]. On the other hand, the reason why distant supernovae appear dimmer than expected may be due to the redshift-luminosity relation that is conventionally applied is only an approximate expression for nearby objects [45]. If the spacetime is dynamic, our universe does not need to be accelerating and even expanding [46, 47].

As consequences of this review work, we have comprehensively reviewed the new four-element theory of nature, that was proposed and developed previously by the author to classically unify all fundamental interactions into a single interaction between complex energies. The new four-element theory of nature suggests that nature consists of four fundamental elements, which are radiation, mass, electric charge, and color charge. Any known matter or particle observed in nature or discovered in labs is a combination of one or more of the four fundamental elements. Fundamental interactions in nature are interactions among these fundamental elements. Radiation and mass are two forms of real energy. Electric and color charges are two forms of imaginary energy. All fundamental interactions are unified into a single interaction between complex energies. Interactions between real energies are gravitational field forces with three categories: mass-mass, mass-radiation, and radiation-radiation interactions. Interactions between imaginary energies are gauge field forces with also three categories: electric-electric charge (or electromagnetic), electric-color charge (or weak), and color-color charge (or strong) interactions. Interactions between real and imaginary energies are imaginary forces, which do not have observational support but may explain why electric and color charges are usually adhered on mass, rather than independently exist. The significant result obtained from the new four-element theory of nature such that the weak force is an interaction between electric and color charges would have essential implications to the quark and particle theories beyond the standard model as well as cosmology.

Acknowledgements

The work is supported by NSF HBCU-UP Research Initiation Award (#2400021). The author also acknowledges the support from the IBM-HBCU Quantum Center.

Received on August 28, 2025

References

1. Robinson A. E. Mendeleev's Periodic Table, Origins: Current Events in Historical Perspective. origins.osu.edu, 2019.
2. Machtmann O. Elementary Particle Physics: Concepts and Phenomena. Springer-Verlag, New York, 2012.
3. Martin B. R. and Shaw G. Particle Physics, 4th Edition. Wiley, 2017.
4. Hendry A. W. and Lichengburd D. B. The quark model. *Reports on Progress in Physics*, 1978, v. 41, 1707–1780.
5. Harari H. Composite models for quarks and leptons. *Physics Reports*, 1984, v. 104, 159–179.
6. Patrignani C. *et al.* (Particle Data Group) Review of particle physics. *Chinese Physics C*, 2016, v. 40, 100001.
7. Zhang T. X. Electric charge as a form of imaginary energy. *Progress in Physics*, 2008, v. 2, 79–83.
8. Zhang T. X. Fundamental elements and interactions of nature: A classical unification theory. *Progress in Physics*, 2010, v. 2, 36–42.
9. Zhang T. X. Four-element theory of nature and two-flavor multi-excitation model of quarks. American Physical Society (APS) Global Submit Conference, New Perspectives Session, Oral Presentation, Abstract #3, Anaheim, California, March 16–21, 2025.
10. Zhang T. X. New insights to the weak interaction and quark model. Quark Matter 2023 Conference, Houston, September 3–8, 2023.
11. Weyl H. Elektron und Gravitation I. *Z. Phys.*, 1929, v. 56, 330–352.
12. Xu S. Y. *et al.* Discovery of a Weyl fermion semimetal and topological Fermi arcs. *Science*, 2016, v. 349, 613–617.
13. Gell-Mann M. Symmetries of baryons and mesons. *Physical Review*, 1962, v. 125, 1067–1084.
14. McLerran L. The physics of the quark-gluon plasma. *Review of Modern Physics*, 1986, v. 58, 1021–1064.
15. Newton I. Mathematical principles of natural philosophy, Book III. 1687.
16. Einstein A. Ist die Trägheit eines Körpers von seinem Energieinhalt abhängig? *Ann. Phys.*, 1905, v. 323, 639–641.
17. Einstein A. Übereinendie Erzeugungund Verwandlung des Lichtes betreffenden heuristischen Gesichtspunkt. *Ann. Phys.*, 1905, v. 322, 132–148.
18. Planck M. The Theory of Heat Radiation, 2nd ed. Translated by Masius M., P. Blackiston's Son & Co., 1914.
19. Bohr N. On the constitution of atoms and molecules. *The London, Edinburgh, and Dublin Philosophical Magazine and Journal of Science*. 1913, v. 26, 1–25.

20. Compton A. H. A quantum theory of the scattering of X-rays by light elements. *Physical Review*, 1923, v. 21, 483–502.
21. Dirac P. A. M. The quantum theory of the electron. *Proceedings of the Royal Society of London A*. 1926, v. 117, 610–624.
22. Anderson C. D. The positive electron. *Physics Review*, 1933, v. 43, 491–498.
23. Weinberg S. Charges from extra dimensions. *Physics Letters B*, 1983, v. 125, 265–269.
24. Kaluza T. On the unification problem in physics. arXiv: physics.hist-ph/1803.08616.
25. Klein O. Quantum theory and five dimensional theory of relativity. *Z. Phys.*, 1926, v. 37, 895–906.
26. Klein O. The atomicity of electricity as a quantum theory law. *Nature*, 1926, v. 118, 516–520.
27. Coulomb C. Theoretical research and experimentation on torsion and the elasticity of metal wire. *Ann. Phys.*, 1802, v. 11, 254–257.
28. Zhang T. X. The 5D fully-covariant theory of gravitation and its astrophysical applications. *Galaxies*, 2015, v. 3, 18–51.
29. Zhang T. X. Electric redshift and quasars in physics. *The Astrophysical Journal Letters*, 2006, v. 636, 61–64.
30. Zhang T. X. Gravitational field shielding and supernova explosions. *The Astrophysical Journal Letters*, 2010, 725, L117–L120.
31. Gaillard M. K., Grannis P. D. and Sciulli F. J. The standard model of particle physics. *Reviews of Modern Physics*, 1999, v. 71, S96–S111.
32. Higgs P. W. Broken Symmetries and the Masses of Gauge Bosons. *Physical Review Letters*, 1964, v. 13, 508–509.
33. Gibbs W. R. and Gibson B. F. Pion-nucleus interactions. *Annual Review of Nuclear and Particle Science*, 1987, v. 37, 411–461.
34. Creutz M. Quarks, Gluons, and Lattices. Cambridge University Press, Cambridge, 1983.
35. Dyson F. Is a graviton detectable? *International Journal of Modern Physics A*, 2013, v. 28, 1330041 (14 pages).
36. Veltman M. Facts and mysteries in elementary particle physics. World Scientific, 2003.
37. Einstein A. Die Grundlage der Allgemeinen Relativitats theorie. *Ann. Phys.*, 1916, v. 354, 769–822.
38. Schwarzschild K. The Gravitational Field of a Mass Point According to Einstein's Theory. *Math. Phys.*, 1916, v. 1, 189–196.
39. Gross D. J. and Wilczek F. Asymptotically free gauge theories I. *Physical Review D*, 1973, v. 8, 3633–3652.
40. Zhang T. X. Two-Flavor Multi-Excitation Model of Quarks. *Journal of Modern Physics*, 2025, v. 16, 1243–1268.
41. Zhang T. X. A new cosmological model: black hole universe. *Progress in Physics*, 2009, v. 3, 3–11.
42. Zhang T. X. Cosmic microwave background radiation of black hole universe. *Astrophysics and Apace Science*, 2010, v. 330, 157–165.
43. Zhang T. X. and Frederick C. Acceleration of black holes. *Astrophysics and Space Science*, 2014, v. 349, 567–573.
44. Zhang T. X. The principles and Laws of Black Hole Universe. *Journal of Modern Physics*, 2018, v. 9, 1838–1865.
45. Zhang T. X. Key to the mystery of dark energy: Corrected relationship between luminosity distance and redshift. *Progress in Physics*, 2013, v. 3, 33–39.
46. Zhang T. X. Mach's Principle to Hubble's law and light relativity. *Journal of Modern Physics*, 2018, v. 9, 433–442.
47. Zhang T. X. Dynamic spacetime: Key to the mysteries of dark matter and dark energy. *Journal of Modern Physics*, 2024, v. 15, 416–434.

Ultrafaint Dwarf Galaxies and the Baryonic Tully-Fisher Relation (BTFR) Derived by Quantum Celestial Mechanics (QCM)

Franklin Potter
Huntington Beach, CA USA. E-mail: frank11hb@yahoo.com

All rotationally supported galaxies such as Andromeda and the Milky Way obey the baryonic Tully-Fisher relation (BTFR) of $V_f^4 \propto M_b$ for rotational velocity V_f and detected amount of baryonic mass M_b, as do all the pressure supported dwarf galaxies. However, the ultrafaint dwarf galaxies in the Local Group do not obey BTFR. Including dark matter does not resolve the issue. We investigate whether Quantum Celestial Mechanics (QCM) with its detailed derivation of the BTFR offers a reasonable resolution.

1 Introduction

At least three general types of galaxies are known: rotationally supported galaxies such as Andromeda and the Milky Way, pressure supported dwarf galaxies, and ultrafaint dwarf galaxies. The rotationally supported galaxies obey the original 1977 Tully-Fisher relation connecting their luminosity L to their outer circular velocity V [1]

$$L = V^{\alpha}\,, \tag{1}$$

where α is a constant that is dependent upon the specific physical properties of each galaxy and the physics model.

When more data became available in the 1990s, the baryonic Tully-Fisher relation (BTFR) determined by MOdified Newtonian Dynamics (MOND) revealed that the flat rotation velocity V_f of a rotationally supported galaxy such as Andromeda or the Milky Way depends upon its baryonic mass M_b exactly to the 4th power, i.e. $V_f^4 \propto M_b$. This relationship even holds true for dwarf galaxies that are pressure supported [2]. Or, as it is more commonly expressed [3],

$$V_f \propto M_b^{\frac{1}{4}}\,. \tag{2}$$

However, for the numerous ultrafaint dwarf galaxies of low mass with no gas component that surround the Milky Way and are gravitationally bound collections of stars only, the BTFR appears to fail [4]. The rotation velocities are too great for the amount of detected baryonic mass. Hence the possibilty exists for a significant amount of dark matter in addition to baryonic mass in their location.

In Fig. 1 are shown some of the many rotationally supported galaxies (circles), some of the numerous pressure supported galaxies including some dwarf galaxies (diamonds), and a representative sample of the ultrafaint dwarf galaxies (squares) with their very large uncertainties because of difficulties in their measurement [5]. These ultrafaints are usually too faint to be detected beyond the nearby Universe, so the sample is largely limited to the Local Group.

The straight line in Fig. 1 is the BTFR fit of the rotationally supported galaxies and the pressure supported galaxies, both of which contain a significant amount of baryonic gas among the stars, as determined [2, 6] by MOdified Newtonian Dynamics (MOND) to be

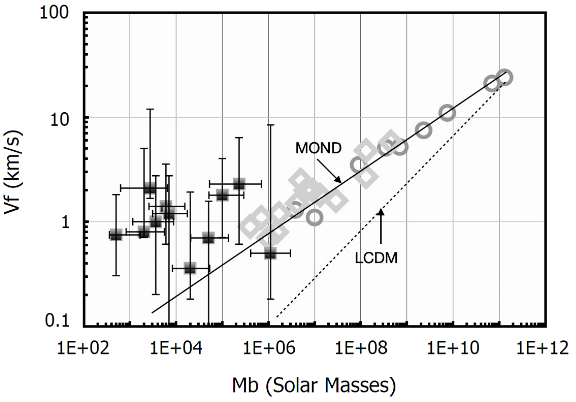

Fig. 1: $\log V_f$ vs. $\log M_b$ for rotationally supported galaxies (circles), pressure supported dwarf galaxies (diamonds), and ultrafaint dwarf galaxies (squares) in relation to the MOND predicted BTFR (straight line) at exactly V_f^4 vs. M_b, plus an example of a ΛCDM prediction (dashed line). The top two circles are Andromeda and the Milky Way. Uncertainties not shown are approximately symbol size.

$$V_f = \left(0.379\,\mathrm{km\,s^{-1}}\,M_{Sun}^{-\frac{1}{4}}\right) M_b^{\frac{1}{4}}\,. \tag{3}$$

But the ultrafaint dwarf galaxies (black squares) do not obey this BTFR relationship. Both MOND researchers and traditional lambda cold dark matter (ΛCDM) research groups have not been able to resolve this issue except by proposing that perhaps the Milky Way itself is possibly interfering with the stability of the ultrafaint systems., i.e. tidal disruptions from external gravitational field effects could be influencing a dispersion of the stars.

Moreover, the ΛCDM approach also has the fundamental problem that one cannot predict the 4th power relationship between the V_f and the baryonic mass M_b because the included dark matter in their galaxy models suggests the power relationship to be smaller than 4 as shown by the dashed line in Fig. 1.

However, the BTFR derived in quantum celestial mechanics (QCM) [7] offers a possible solution that explicitly includes more fundamental physical properties of the ultrafaint dwarf galaxies, including their baryon densities, radial sizes, and total angular momentum.

The successful application of QCM to galaxy clusters [8] explained how the dynamic baryon mass of a galaxy cluster, without requiring any dark matter, depends upon both the total angular momentum and the observed baryonic mass values. Therefore, we investigate the QCM expression for the BTFR to better understand the ultrafaint dwarf galaxies.

2 QCM derivation of the BTFR

QCM is derived from the general relativistic Hamilton-Jacobi equation [7]

$$g^{\alpha\beta}\,\frac{\partial S}{\partial x^{\alpha}}\,\frac{\partial S}{\partial x^{\beta}} - \mu^2 c^2 = 0 \tag{4}$$

via the transformation that defines the wave function

$$\Psi = e^{S'/H} \tag{5}$$

to obtain a scalar gravitational wave equation (GWE)

$$g^{\alpha\beta}\,\frac{\partial^2 \Psi}{\partial x^{\alpha}\partial x^{\beta}} + \frac{\Psi}{H^2} = 0\,. \tag{6}$$

In these equations, S' is the classical action S divided by μc for a test particle of mass μ, with c being light speed in vacuum.

The characteristic distance H for a gravitationally bound system is defined to be

$$H = \frac{L_T}{M_T c} \tag{7}$$

where L_T is the total angular momentum for the system of total mass M_T.

In a gravitationally bound system in coordinates (t, r, θ, ϕ) obeying the Schwarzschild metric, as expected for planetary systems and galaxies, from the angular coordinates one derives the angular momentum *per unit mass* quantization condition

$$\frac{L}{\mu} = m\,\frac{L_T}{M_T} \tag{8}$$

for a mass μ in orbit with angular momentum L and for m an integer. All confirmed multi-planetary systems obey this relationship [9].

From the radial equation one obtains the energy *per unit mass* quantization

$$E = -\mu c^2\,\frac{r_s^2}{8n^2 H^2}\,, \tag{9}$$

with r_s the Schwarzschild radius and integer n.

Application of the virial theorem for gravitation leads directly to the tangential rotation velocity for the test particle

$$v = \frac{r_s c}{2nH} \tag{10}$$

from which the QCM predicted BTFR can be derived.

If we assume that the galaxy is approximately a disc with a total baryonic mass $M_b = \pi h R^2 \rho_0$ for average density ρ_0, thickness h, and radius R, then its total angular momentum $L_T = \alpha M_b R^2 \omega$ with moment of inertia factor α and rotational velocity ω. With gravitational constant G, this BTFR becomes

$$V_f = M_b^{\frac{1}{4}}\,\sqrt{\frac{G}{n\alpha}\,\sqrt{\pi h \rho_0}}\,. \tag{11}$$

As one example, suppose h is 8 times greater than estimated, and the α and ρ_0 parameters can each vary by about a factor of 2. By combining them optimally, QCM predicts a maximum gain of about $\sqrt{8}$ times the previous value of V_f for the same baryonic mass value.

3 Conclusion

QCM predicts a BTFR relation depending upon the average density, thickness, and total angular momentum of a galaxy. Whether these three parameters in the BTFR expression derived by QCM will resolve the issue of the ultrafaint dwarf galaxy positions on the $V_f^4 \propto M_b$ graph remains to be determined when better data becomes available.

Acknowledgements

We thank physics colleagues for continuing encouragement to apply QCM to astronomical issues.

Received on November 4, 2025

References

1. Tully R. B. and Fisher J. R. A new method of determining distances in galaxies. *A&A*, 1977, v. 54, 661–673.
2. McGaugh S. S. *et al.* The Baryonic Tully-Fisher Relation in the Local Group and the Equivalent Circular Velocity of Pressure-Supported Dwarfs. *AJ*, 2021, v. 162, 202.
3. Schombert J., McGaugh S., and Lelli F. Using the Baryonic Tully-Fisher Relation to Measure H_0. *AJ*, 2020, v. 160, 71.
4. Ruan D. *et al.* Predictions for detecting a turndown in the baryonic Tully-Fisher relation. *MNRAS*, 2025, v. 541 (3), 2180–2196.
5. Durbin M. J. *et al.* The HST Legacy Archival Uniform Reduction of Local Group Imaging (LAURELIN) I. Photometry and Star Formation Histories for 36 Ultra-faint Dwarf Galaxies. *AJ*, 2025, v. 992, 106.
6. Milgrom M. The deep-MOND limit – a study in primary and secondary predictions. arXiv: gr-qc/2510.16520.
7. Preston H. G. and Potter F. Exploring large-scale gravitational quantization without $\hbar$ in planetary systems, galaxies, and the Universe. arXiv: gr-qc/0303112.
8. Potter F. Galaxy Clusters: Quantum Celestial Mechanics (QCM) Rescues MOND? *Prog. in Phys.*, 2024, v. 20 (2), 100–102.
9. Potter F. Predicting Total Angular Momentum in TRAPPIST-1 and Many Other Multi-Planetary Systems Using Quantum Celestial Mechanics. *Prog. in Phys.*, 2018, v. 14 (3), 115–120.

The Model of the Sun, Based on Wheeler's Geometrodynamics, is Confirmed by Recent Astronomical Observations

Anatoly V. Belyakov
Tver, Russia. E-mail: belyakov.lih@gmail.com

The detailed physical parameters of the gravitomagnetohydrodynamic model of the Sun, calculated earlier on the basis of Wheeler's geometrodynamics, are confirmed by recent astronomical observations.

In [1] and other studies, a mechanistic interpretation of Wheeler's geometrodynamics is used, which makes it possible to draw analogies between objects of different scales (in the widest range from elementary particles to planets and stars), regardless of the nature of their constituent environment, solely on the basis of the balance between gravitational, magnetic, electrical, and dynamic forces. This method, when applied to stellar objects, has showed that the Sun has a complex dynamic internal structure, and some of its model parameters are in good agreement with recent astronomical observations [2–4].

The balances of the aforementioned forces lead to the structuring of any medium, if these forces are present, into local vortex zones (vortex tubes) [1, 5], consisting of single vortex filaments.

Recall that the formulae for electric and magnetic forces are written in a "non-Coulomb" form, in which the electric charge is replaced by the electron's maximum momentum. In this case, the electric and magnetic constants ε_0 and μ_0 are as follows

$$\varepsilon_0 = \frac{m_e}{r_e} = 3.33 \times 10^{-16} \text{ kg/m}, \tag{1}$$

$$\mu_0 = \frac{1}{\varepsilon_0 c^2} = 0.0344 \text{ 1/N}, \tag{2}$$

so ε_0 is effectively the linear density of the vortex tube, and μ_0 is the reciprocal of the centrifugal force generated by the rotation of a vortex tube element of mass m_e at the speed of light c along a radius r_e.

In particular, the work [1] established that as an initially structureless medium becomes more complex, local vortex zones arise, where:

— the number z of the local zones for an arbitrary mass M is

$$z = \frac{1}{M^{1/4}}, \tag{3}$$

— their radius r and length l, respectively, are

$$r = M^{3/4} R_c, \tag{4}$$

$$l = M^{1/4} R_c, \tag{5}$$

— the circumferential velocity of individual vortex filaments rotating around the longitudinal axis of the vortex tubes is

$$v_0 = M^{1/4} c, \tag{6}$$

— the number of the vortical filaments in the zone

$$n = f M, \tag{7}$$

where f is the ratio of the electric forces to the gravitational ones, and M is a dimensionless mass measured in fractions of the characteristic mass

$$M_m = \frac{R_c c^2}{\gamma} = 1.012 \times 10^{36} \text{ kg}, \tag{8}$$

where the characteristic radius R_c is

$$R_c = (2\pi)^{1/2} c \times [\text{sec}] = 7.52 \times 10^8 \text{ m}, \tag{9}$$

so that for the Sun's mass is we have $M = 2 \times 10^{-6}$. It is obvious that as its own mass decreases, the object simultaneously becomes more complex, structuring itself into local zones in an increasingly finer manner.

Stars, forming from primordial matter, undergo a long evolutionary process, and at some point their structure conforms to the above relationships (for detail, see [1]). It is assumed that our Sun is also at this equilibrium stage of its existence, and therefore some parameters of the solar structure should correspond to them.

According to [1], the initial state of a stellar object is assumed to be a rotating disk, in which, as it becomes more complex, local radial-spiral zones form, which are pulled toward the centre by the radial components of gravitational forces.

Since magnetic forces also act in the solar plasma, the solar structure as a whole may consist of local zones in the form of closed contours-toroids (balance of magnetic and gravitational forces), whose conductive elements (vortex filaments) rotate around the closed axis of the torus (balance of magnetic and inertial forces), while the toroids themselves are located in the plane of the rotating disk (balance of gravitational and inertial forces). The core rotates faster than the periphery, and the toroids twist, converting their kinetic energy into other forms (and then, obviously, the reverse process). It would be a gross oversimplification to liken this system to a multi-winding, flat-spiral mechanical pendulum; nevertheless, an

oscillatory process of the object's gravimagneticodynamic structure must take place.

Indeed, paired dark spots predominantly in the Sun's equatorial zone appear to be the outcrops of local structures that undergo magnetization reversals and change their intensity and polarity with a period of 11 years. Their observed number (from a few to hundreds) is consistent with the calculated average, according to formula (3), $z = 26.6$. In [1] other models corresponding to the real parameters of the Sun are also given.

This structure turned out not to be speculative; on the contrary, it has received new direct confirmation in the recent studies mentioned below.

1. The Daniel K. Inouye Solar Telescope registered tiny structures in the Sun's corona — ultra-thin coronal loops that extend along the Sun's magnetic field lines. On average, their width was approximately 48 kilometers across, with individual loops measuring approximately 20 km [2]. It is assumed that these fine structures may be isolated elements of the solar structure.

But this is precisely the size of the vortex local zones predicted by the proposed model; according to the formulae (4) and (5), $r = 40.4$ km and $l = 28,200$ km. The latter is also consistent with observations, since the height of coronal loops can reach 10,000 km.

2. Furthermore, Prof. Richard Morton directly observed a small twisted type of wave (Alfvén waves), which can supply energy to the corona [3]. These waves cause rotational motion, which was detected by spectroscopic analysis, as the plasma's erruption toward and away from the Earth creates characteristic red and blue shifts on opposite sides of magnetic structures. This effect was observed in the movement of iron atoms heated to 1.6×10^6 °C in the corona.

But it is precisely this vortex motion that the individual filaments that make up the toroids exhibit; their circumferential velocity, according to (6), is $\upsilon_0 = 11.3 \times 10^6$ m/sec. During solar flares, the filaments are broken, causing the charged particles that comprise them to split off and rush into space at a velocity υ_{0i}, which then decreases in the Sun's gravitational field to the speed in the range of 1,000–3,000 km/sec recorded at Earth.

3. Astronomers using the European Southern Observatory's (ESO) Very Large Telescope (VLT) observed the initial phase of the supernova explosion SN 2024ggi in the galaxy NGC 3621 [4]. It was discovered that the initial mass ejection was not spherical, but rather elongated and flattened. This fact also confirms the correctness of the **initial structure assumed for the star as a flat disk**.

It should also be noted that the proposed model makes it possible to directly calculate the atomic number of the element at which nuclear reactions in stars cease at the end of their evolution, namely, the atomic number of iron.

In [1], when determining the parameters of a spirally structured disk, its radius in a compressed state was determined, i.e., the radius of the star's core

$$R_0 = M^{1/3} R_c\,, \tag{10}$$

and, subsequently, the core density.

In the atoms of stellar matter (mainly hydrogen), the substance, according to the electron model [6], circulates along p^+-e^- contours having a mass $\varepsilon_0 r_0$, and the circulation speed cannot be greater than the speed of light. At the same time, the magnitude of the charge e_0 is constant for any quantum number and is equal to the momentum of the mass of the circuit $\varepsilon_0 r_0 \upsilon_0$. When $\upsilon_0 \to c$, then $r_0 \to r_{0_{\min}}$, therefore

$$r_{0_{\min}} = \frac{e_0}{\varepsilon_0 c}\,. \tag{11}$$

The density of extremely compressed hydrogen atoms is (for a spherical volume)

$$\rho_{\max} = \frac{3 m_{\rm H}}{4\pi r^3_{0_{\min}}} = 8.82 \times 10^7 \ \text{kg/m}^3, \tag{12}$$

where $m_{\rm H}$ is the mass of a hydrogen atom.

Assuming that all matter is concentrated in the nucleus, its density is the ratio of the mass of the nucleus to the cube of its radius and, according to the formulae (8) and (10),

$$\begin{aligned} \rho_0 = \frac{M M_m}{R_0^3} = \frac{M_m}{R_c^3} = \\ = \frac{1}{2\pi\gamma \times [\sec^2]} = 2.38 \times 10^9 \ \text{kg/m}^3. \end{aligned} \tag{13}$$

That is, the core density depends only on the gravitational constant. From the $\rho_0/\rho_{\max}$ ratio, it follows that a volume equal to the volume of one compressed hydrogen atom should contain 27 atoms of the star's original material, which, in terms of proton number, corresponds to iron-group atoms. This density is typical of white dwarfs.

Thus, the highly simplified model of solar structure presented in [1] is consistent with the external manifestations of solar activity. As for the commonly used spherically symmetric quasi-static model of stellar structure, which analyzes the state of matter and pressure, temperature and luminosity as functions of radius, it is clearly insufficient, and an analysis of the Sun's gravitomagnetodynamic structure should be included.

And finally: the more complex than expected structure of stellar objects, where the dynamics of magnetic forces play a huge rôle, suggests the following idea: are enormous pressures and temperatures alone enough to trigger a controlled thermonuclear reaction?

Received on November 18, 2025

References

1. Belyakov A.V. Evolution of stellar objects according to J. Wheeler's geometrodynamic concept. *Progress in Physics*, 2013, v. 9, issue 1, 25–40.

2. Tamburri C.A., Kazachenko M.D., Cauzzi G., *et al*. Unveiling unprecedented fine structure in coronal flare loops with the DKIST. *The Astrophysical Journal Letters*, 2025, v. 990(1), L3.
3. Morton R.J., Gao Y., Tajfirouze E., Tian H., *et al*. Evidence for small-scale torsional Alfven waves in the solar corona. *Nature Astronomy*, 24 October 2025.
4. Yi Yang, Xudong Wen, Lifan Wang, *et al*. An axisymmetric shock breakout indicated by prompt polarized emission from the type II supernova 2024ggi. arXiv: 2511.08824 (2025).
5. Belyakov A.V. On materiality and dimensionality of the space. Is there some unit of the field? *Progress in Physics*, 2014, v.10, issue 4, 203–206.
6. Belyakov A.V. Charge of the electron, and the constants of radiation according to J. A. Wheeler's geometrodynamic model. *Progress in Physics*, 2010, v. 6, issue 4, 90–94.

Progress in Physics is an American scientific journal on advanced studies in physics, registered with the Library of Congress (DC, USA): ISSN 1555-5534 (print version) and ISSN 1555-5615 (online version). The journal is peer reviewed.

Electronic version of this journal: http://progress-in-physics.com